THE UNIVERSITY OF CHICAGO

TOPICS ON THE DETECTION OF ULTRA-HIGH ENERGY NEUTRINOS

A DISSERTATION SUBMITTED TO
THE FACULTY OF THE DIVISION OF THE PHYSICAL SCIENCES
IN CANDIDACY FOR THE DEGREE OF
DOCTOR OF PHILOSOPHY

DEPARTMENT OF PHYSICS

BY
DANIEL SMITH

CHICAGO, ILLINOIS
AUGUST 2022

TABLE OF CONTENTS

LIST OF FIGURES

LIST OF TABLES

ACKNOWLEDGMENTS

Topics on Neutrino Astronomy: The source of IceCube neutrino flux, development of RNO-G, and ANITA's anomalous events.

I first thank my thesis advisor, Prof. Abigail Vieregg. Thank you for the freedom you've afforded me to explore the broad topics of astroparticle physics detailed herein. The years of work culminating in this dissertation were not easy, but I've made it through with your guidance and support. I also thank my thesis committee members–David Schmitz, Jeff McMahon, and Damiano Caprioli–for lending their time to serve on my committee.

I want to thank my colleagues and collaborators who have worked with me on papers and projects detailed herein. I thank Cosmin Deaconu for seemingly bottomless support, a true hero of our lab. I thank Christoph Welling and Bryan Hendricks for turning amateur hour at Summit Station into a successful season of calibration. I thank Brian Clark and Christian Glaser for being wonderful teammates while running IceCube-Gen2 Radios's first full detector simulations. I thank Dave Besson for long discussions and lots of paper editing on topics of ice properties, and for generally being a great support. I thank Dan Hooper for his support in my foray into astroparticle theory analysis. I thank my groupmates Kaeli Hughes and Dan Southall for the hours spend in detector commissioning, and for being good friends and commiseraters. I thank Ilse Plaiser for all the help with NuRadioMC and antenna simulations. I thank the ANITA collaboration for fruitful discussion on FDTD simulations. I thank Patrick Allison for his work on RNO-G's digitizer board. I thank the RNO-G collaboration, particularly Steph Wissel, Anna Nelles, and Nick van Eijndhoven, for all the valuable feedback over the years.

Outside of my research, I thank the friends who have supported me the last few years, whether it be via teaching, homework or simply companionship: Sharba, Syrian, Joe, Anora, Jan, Yehuda.

Finally, I thank Melani, my beloved.

ABSTRACT

Ultra-high energy (UHE) neutrinos, produced in astrophysical sources and in the interaction of UHE cosmic rays with the cosmic microwave background, offer a unique view of processes that are inaccessible by other messenger types at energies above 10^{18} eV. In this thesis, I present work from several experiments that broadly represent the field of UHE neutrino detection, including detector commissioning, calibration, data analysis, and simulations for the development of future experiments.

For the Radio Neutrino Observatory in Greenland, I discuss the detector development and commissioning, as well as a measurement of the radio field attenuation length at Summit Station, Greenland, a measurement important to the detector's sensitivity and electric field reconstruction. For the IceCube experiment, I perform a source search using the experiment's already-measured flux of astrophysical neutrinos, placing limits on the flux contribution from blazar and non-blazar AGN sources. For the ANITA experiment, I discuss electromagnetic simulations to test the hypothesis that non-specular reflections at the ice created the experiment's 'anomalous' events. Finally, for the future IceCube-Gen2 experiment, I present simulations for the radio component of the detector, demonstrating the radio detection technique's ability to achieve the science goals of the experiment.

CHAPTER 1

INTRODUCTION & MOTIVATION

In the pursuit of understanding the universe, humanity has studied large-scale structures in astronomy and microscopic structures in particle physics. As our understanding of celestial bodies and subatomic particles has advanced, we have found that a union of the two topics gives us a deeper understanding of the universe than available from either alone. Astroparticle physics encompasses studying both the fundamental properties of particles and the mechanisms and sources that could produce such particles. A natural step addition to astroparticle physics is multi-messenger astronomy, the combination of astroparticle information from cosmically generated hadrons and neutrinos with other messenger types, primarily gravitational waves and photons at many energy scales, to develop the deepest understanding of our universe to date.

Multi-messenger astronomy requires multiple detectors and telescopes to work in unison. Neutrino observatories are particularly difficult to construct due to the expected low flux of astrophysical neutrinos at high energy ($> 10^{18}$ eV) and the low interaction cross sections of neutrinos at lower energies.

1.1 Neutrino Astronomy

Neutrinos produced in astrophysical sources offer a unique view of processes that are inaccessible by electromagnetic and ultra-high energy cosmic ray (UHECR) observations, while simultaneously being an ideal messenger particle for multi-messenger astronomy.

Neutrinos, as weakly interacting particles, have extremely long attenuation lengths through the universe, allowing, in the lower energy regime, the observation of processes that would be shrouded by matter and, in the ultra-high energy regime, the observation of the most extreme astrophysical sources outside of the reach of gamma ray and UHECR observatories.

Since neutrinos are also neutral, they propagate along straight paths and, if detected at Earth, their trajectories point directly back to their sources. This is not the case for UHECRs, which experience curved trajectories from cosmic magnetic fields, making correlation with a source impossible except for close sources and extremely energetic UHECRs [116].

Neutrino astronomy provides a unique probe into UHECRs at energies above the GZK cutoff (described in Sect. 1.3.2) and the most distant and energetic sources (described in Sect. 1.1.4). While the main body of work presented herein is on the topics of high and ultra-high energy neutrino astronomy, I present the topics of supernova and stellar neutrinos, in Sect. 1.1.2 and Sect. 1.1.1 respectively, for the historical context of the field and as case studies of the power of neutrino astronomy and multi-messenger astronomy.

1.1.1 Solar Neutrinos

Arthur Eddington suggested early in the 20^{th} century that the source of energy from stars was from fusion of hydrogen into helium [108]. In 1939, Hans Bethe calculated the rate of fusion within stars assuming that the process began with two protons fusing to form a deuteron and a positron, first proposing the proton-proton chain [78]. With the discovery and inclusion of the neutrino, the proton-proton chain starts with,

$$p + p \rightarrow D + e^{+} + \nu_e, \tag{1.1}$$

where D is deuterium. While today we know the nuclear processes within a star are much more complicated [250], it was expected early that a low energy (O(MeV)) flux of neutrinos should be emitted from the sun.

In the 1960s, Ray Davis and John Bahcall led and developed the Homestake experiment [92] to measure the solar neutrino flux using neutrino capture on chlorine,

$$\nu_e + {}^{37}\text{Cl} \rightarrow {}^{37}\text{Ar}^{+} + e^{-}. \tag{1.2}$$

The absolute number of neutrino interactions was measured by collecting and counting the argon atoms. The Homestake experiment ultimately measured a flux of ν_e much lower than predicted, between 27.5% and 33.3% of various models of nuclear interactions expected to take place in the Sun [250, 64]. Thus began the solar neutrino problem, a large discrepancy between the observed numbers of neutrinos from astroparticle experiments and the expected number of neutrinos from nuclear theory of stellar processes [64]. Many other experiments observed similar deficits, including Kamiokande-II [154], Super-Kamiokande [125], Sage [126], Gallex [144], and GNO [45], all plotted in Fig. 1.1.

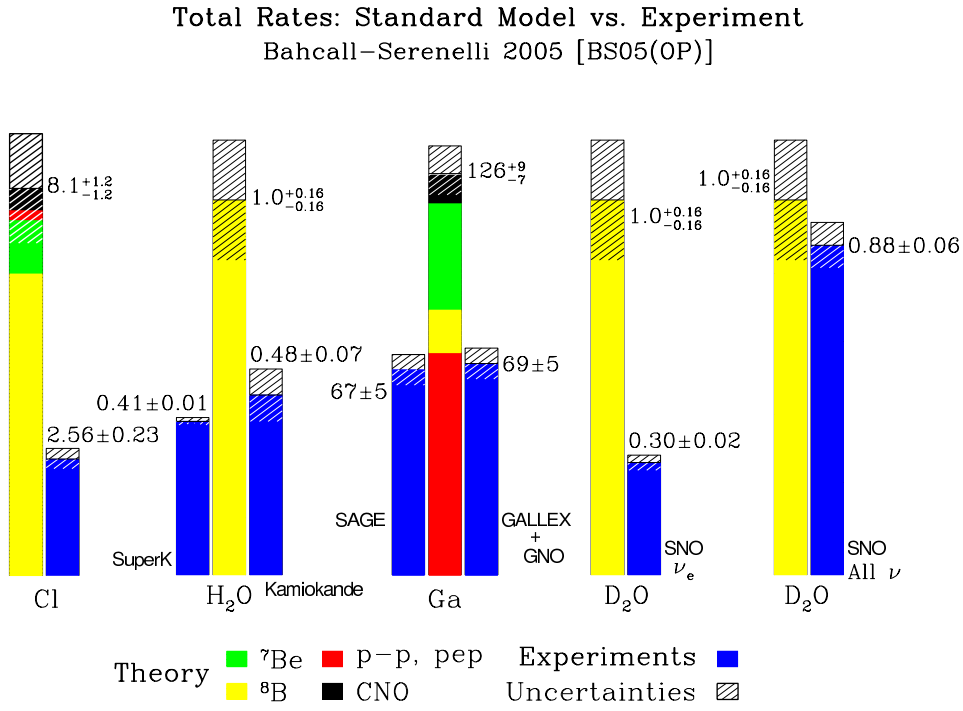

Figure 1.1: The measured flux of solar neutrinos for different target types and experiments. A deficit is shown in all experiments except for SNO, which had the unique ability to detect all three types of neutrino flavors. Figure taken from [64].

Ultimately, the theory of neutrino oscillation solved the solar neutrino problem. As directly measured by the Sudbury Neutrino Observatory (SNO) [34], a large number of elec-

tron neutrinos had oscillated in their flight to Earth into other neutrinos flavors which earlier experiments were unable to detect [215]. Notably, neutrino oscillation was first experimentally discovered by Super-Kamiokande via the measured muon neutrino flux from neutrinos produced in cosmic ray interactions with the atmosphere[124].

The observation of solar neutrinos confirmed nuclear models of the sun's fusion process while revealing the fundamental information that neutrinos have mass and oscillate. Solar neutrinos remain a case study of the power of combining multiple disciplines (astronomy, nuclear physics, and particle physics) and messenger types (photons and neutrinos) to understand the universe.

1.1.2 Astrophysical Neutrinos from Supernovas

In 1987, a Type II supernova (SN 1987A) occurred in the Large Magellanic Cloud [187]. A prompt burst of electron neutrinos was produced during the creation of a neutron star at the center of the collapse. Electrons and protons in the initial star were forced together by gravitational collapse in inverse beta decay,

$$e^{-} + p \rightarrow n + \nu_e. \tag{1.3}$$

After the initial burst, neutrinos produced in the inverse beta decay were trapped in the increasingly dense matter of the newly forming neutron star. Over a period of ~ 10 seconds, they diffused out. Ultimately, the majority (99%) of the released energy in the supernova was carried away by low energy (O(10 MeV)) electron neutrinos. There are many models and numerical simulations [203, 162, 204, 227, 206, 240] describing this process to high precision.

At Earth and before the arrival of the photons from the supernova, the Kamiokande experiment in Japan observed 12 neutrino signal events [153], IMB in the United States observed 8 [80], and Baksan in Russia observed 5 [37], in a span of less than 15 seconds. Plotted in Fig. 1.2 is the energy vs. time of arrival of all neutrino events associated with

SN 1987A.

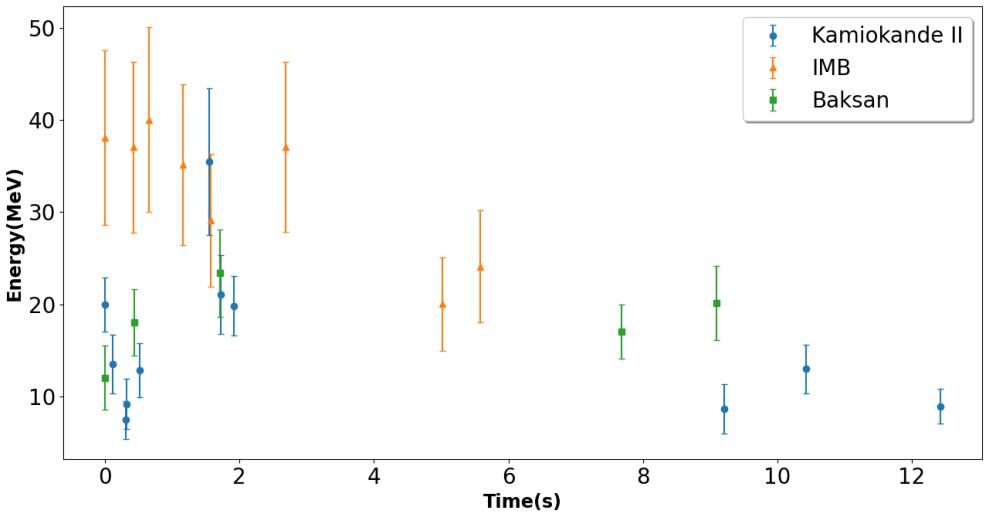

Figure 1.2: Energy vs. time of all detected neutrinos from SN1987a. Figure from [96], available under Creative Commons licensing.

This was the first spectacular observation of extra-solar neutrinos. The 28 events, in tandem with optical observations, confirmed models of supernova collapse including the large role that neutrinos play [203, 162, 204, 227, 206, 240]. In fundamental physics, the handful of events set limits on the rest mass, charge, total number of flavors, oscillation properties, and lifetime of electron neutrinos [223, 57, 58].

1.1.3 Ultra-High Energy (UHE) Neutrinos

UHE neutrinos, neutrinos with energy in excess of 10^{17} eV, are produced either directly in the universe's most distant and energetic sources (called astrophysical neutrinos) or through the interaction of UHECRs with the cosmic microwave background (CMB) (called cosmogenic neutrinos). They offer a unique view of the universe: above 10^{20} eV, the only particle messenger type available to astronomy is UHE neutrinos. UHECRs above 10^{20} eV are attenuated from interactions with the CMB and photons above 10^{12} eV are attenuated from

pair production with the CMB. Moreover, at energies above gamma ray energies, 10^{14} eV, neutrinos are the only particle messenger type that preserve their direction information. At all energies, the universe is transparent to gravitational waves [68, 24], but, as a subatomic particle, UHE neutrinos are the only messenger type that carry information of the particle interactions at the source on this energy scale. As can be seen in Fig. 1.3, large swaths of distances and energies are only available from UHE neutrinos and gravitational waves [68].

The expected flux of UHE neutrinos at Earth is small. The only measurement of the astrophysical neutrino energy spectrum to date, by the IceCube experiment (described in more detail in Sect. 1.5.2), is equal to,

$$\frac{d\Phi_{6\nu}}{dE} = \left(6.45^{+1.46}_{-0.46}\right)\left(\frac{E_\nu}{100\ \text{TeV}}\right)^{-2.89^{+0.2}_{-0.19}} \times 10^{-18}\left[\text{GeV}^{-1}\text{cm}^{-2}\text{s}^{-1}\text{sr}^{-1}\right], \tag{1.4}$$

where $\Phi_{6\nu}$ is the flux of neutrinos and E_ν is the energy of neutrinos [225, 18]. This measurement, shown in Fig. 1.10, has been made from neutrino observations up to $\sim 10^{16}$ eV in energy, but with increasingly large uncertainty on the spectral index of the spectrum due to low statistics. To consistently observe astrophysical neutrinos at higher energies than IceCube and to detect cosmogenic neutrinos, a detector volume an order of magnitude or more larger than the 1 km^3 of IceCube is required.

1.1.4 Astrophysical Neutrino Sources

The origin of the flux of astrophysical neutrinos is still unknown. However, the IceCube experiment has recorded two tantalizing coincidences between astrophysical neutrinos and their sources.

The first source, TXS 0506+056, is a blazar, a gamma ray luminous active galactic nucleus (AGN) with its relativistic jet of particles and ionized gas beamed at Earth [12]. In 2017,

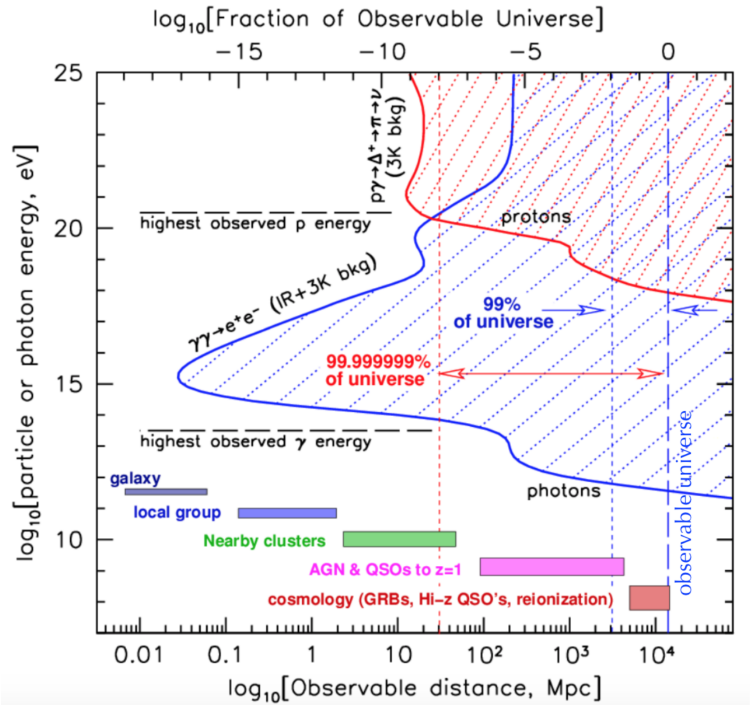

Figure 1.3: Energy vs. observation distance for different particle types. Shown are are the regions of space that are inaccessible from photons (blue) and hadrons (red, for all-proton fraction) due to interactions with the CMB via pair production and the GZK mechanism, respectively. Above 10^{20} eV, only UHE neutrinos can be used for astronomy and above 10^{14} eV, neutrinos are the only messenger type that still points to its source. The universe is transparent to gravitational waves at all energies and distance scales, with LIGO having sensitivity out to 1 Gpc [24]. Figure from Peter Gorham.

IceCube detected a 300 TeV muon neutrino that was spatially coincident with the blazar which was flaring (period of time with higher than normal gamma ray emission) at the time. The post-trial chance correlation between such a neutrino and a flaring blazar is rejected at the 3σ level. After the detection, IceCube performed a time analysis and found evidence for a flare of neutrinos in 2014–2015 from the same source at a time when the blazar was not flaring in gamma ray emission [11]. The archival time search yields a higher likelihood that the blazar is a source of astrophysical neutrinos, with the post-trial chance correlation between the neutrino burst and the blazar being rejected at the 3.5σ level. While not at the discovery-level statistical certainty used in particle physics (5σ), this is tantalizing evidence of a source of astrophysical neutrinos, the first to date at these energy scales (solar and

SN1987a neutrinos were in the MeV energy scale). This correlation does not come without its complications. The time analysis revealed a neutrino burst when the blazar was not flaring, suggesting a complicated production mechanism of high energy neutrinos produced out of time from gamma ray emission. Moreover, blazars have been ruled out as the primary source for IceCube's measured astrophysics neutrino flux, discussed more in Section 4.

The second source, AT2019dsg, is a tidal disruption event, when a star approaches close to a supermassive black hole and is pulled apart by tidal forces [237]. In 2019, IceCube detected a 200 TeV muon neutrino that was spatially coincident with the radio-detection of the tidal disruption event. The post-trial chance correlation between the neutrino and tidal disruption event is rejected at the 2.58σ and increases to 2.88σ when folding in the relatively high luminosity of the tidal disruption event. The low statistical certainty makes this a less likely coincidence than TXS 0506+056 but tidal disruption events are of interest for future source searches.

1.2 UHE Neutrino Production Mechanism

1.2.1 GZK Production

UHE neutrinos are produced, in part, from the interaction of UHECRs with the CMB. Kenneth Greisen [140], Georgiy Zatsepin, and Vadim Kuzmin [262] proposed this idea in 1966, creatively named the GZK effect or GZK limit. A sufficiently high energy cosmic ray ($> 10^{19}$ eV) will interact with a CMB photon ($\mathrm{O}(10^{-3}$ eV)) through the Δ^+ resonance,

$$\begin{aligned} p + \gamma_{CMB} \rightarrow \Delta^+ &\rightarrow p + \pi^0 \\ &\text{or} \hookrightarrow n + \pi^+ \end{aligned} \tag{1.5}$$

In the decay into a proton and a neutral pion, the proton exists as a lower energy comic ray

and the neutral pion decays into two gamma rays. In the decay into a neutron and positive pion, the neutron decays via,

$$n \to p + e^- + \bar{\nu}_e, \tag{1.6}$$

and the pion's most likely decay chain is,

$$\begin{aligned} \pi^+ &\to \nu_\mu + \mu^+ \\ \mu^+ &\to e^+ + \nu_e + \bar{\nu}_\mu. \end{aligned} \tag{1.7}$$

The resulting three neutrinos from the π^+ decay will be extremely boosted with energies around 10^{18} eV. The neutrino from the neutron decay is a small addition to the neutrino flux at 10^{15}–10^{16} eV [259]. The gamma rays from the π^0 decay and the neutron decay create an expected correlated flux of gamma ray and neutrino emission from a source.

The GZK process can also be thought of as the GZK limit. Due to the cross-section of the delta resonance and the density of CMB photons in the universe, a UHECR of energy $> 10^{19}$ eV will have an interaction length of $\sim$ 50 Mpcs, making the universe opaque to UHECRs at these energies.

This source of neutrinos is guaranteed: observed UHECRs have sufficient energy to interact with the CMB and produce GZK neutrinos. However, the mechanism of UHECR production and thus expected UHECR nuclear composition and cosmogenic neutrino flux is yet undetermined.

Models of expected GZK neutrino flux include the original source evolution and the nuclear composition of UHECRs. UHECRs composed of more than one nucleon (UHE nuclei) mainly lose energy through photodisintegration from CMB photons, reducing the energy available to any freed nucleon (proton) by the number of nucleons in the original UHE nuclei. The freed proton, if of sufficient energy, can then interact with the CMB

to produce cosmogenic neutrinos. This results in a higher UHECR energy cutoff, up to 10^{21} eV, and a suppressed GZK neutrino flux. The composition of UHECRs is expected to be between hydrogen and iron, and a discussion of the measured values of nuclear composition are available in Sect. 1.3.2.

The discovery of cosmogenic neutrinos would inform the composition and acceleration mechanism of UHECRs, their source evolution, and provide fundamental measurement of neutrinos at energy ranges far above those available at terrestrial accelerators and current neutrino observatories.

1.2.2 Direct Production

Many models of UHECR and UHE neutrinos start with lower energy charged particles that are accelerated to ultra-high energy scales through high magnetic fields and Fermi shock acceleration. After being accelerated, a charged particle either interacts with the local medium to produce UHE neutrinos or escapes and interacts with the CMB to create cosmogenic neutrinos. These so-called "bottom-up" models exist for many source types, including active galactic nuclei [194, 199, 190], pulsars [114], low-luminosity gamma ray bursts [82, 163], tidal disruption events [79, 253, 100, 202], and binary neutron star mergers [111].

First order Fermi shock acceleration occurs when a particle in a shock front continually diffuses upstream across the shock front before being scattering downstream, gaining energy each time and accelerating until the particle is boosted enough to escape the shock front. Second order Fermi shock acceleration occurs when a particle interacts with so-called "magnetic clouds", randomly moving magnetic fields. Elastic collisions within the cloud are more likely to accelerate than decelerate a particle, boosting a charged particle over time.

The maximum energy of a charged particle, E_{max}, that a source can produce is related to the source's size and present magnetic fields. The limit is expressed as the Hillas criterion

[152]:

$$E_{max} = \frac{|q|}{c} BR, \tag{1.8}$$

where B is the magnetic field of a source and R is the linear size. A figure of potential sources with their magnetic fields and linear sizes is shown in Fig. 1.4.

An example UHECR acceleration model is the so-called *espresso* acceleration [190], which provides a mechanism to produce UHECRs up to the Hillas limit (10^{20} eV) from AGN. Relatively low energy cosmic rays ($< 10^{17}$ eV) are produced from Fermi shock acceleration from supernova remnants [107, 85]. These particles, called seeds, penetrate into the relativistic jet associated with AGN and receive a single-shot boost from the magnetic fields within the jet. The now UHE cosmic rays can escape the jet off the axis of the jet and either interact with the CMB or with the local medium to produce cosmogenic or astrophysical neutrinos, respectively. Numerical simulations of seed cosmic rays in AGN jets have confirmed this effect. Studies to measure UHE neutrinos from AGN are underway and one such analysis is described in detail in Sect. 4.

While accelerating, an UHECR can interact with the local medium to produce a flux of UHE neutrinos. The two types of interactions are photo-hadronic ($p\gamma$), where the accelerated ion interacts with the intense photon field in the source, and hadronuclear (pp), where the accelerated ion interacts with hadrons in the source [195, 191, 29].

Photo-hadronic interactions create UHE neutrinos via the same process described in Sect. 1.2.1. The interaction produces an excited baryon (heavier than proton) which then undergoes a series of decays into neutrinos, gamma rays, and lower energy hadrons. Hadronuclear interactions create neutrinos via the general production of pions, via

$$p + p \rightarrow \pi^{+/-/0} + X, \tag{1.9}$$

where the pion can be any charge and the out-going X is any particle or particles that meet conservation requirements of the interaction [212]. In general, pp interactions are complicated, analogous to interactions observed at the LHC, and create gamma rays, cosmic rays and neutrinos. The Fermi diffuse isotropic gamma ray background places constraints on neutrino production from pp interactions due to the correspondingly large flux of gamma rays from the decay of π^0 [198, 191]. However, these limits can be skirted if the neutrino production occurs in an optically thick environment [233, 197].

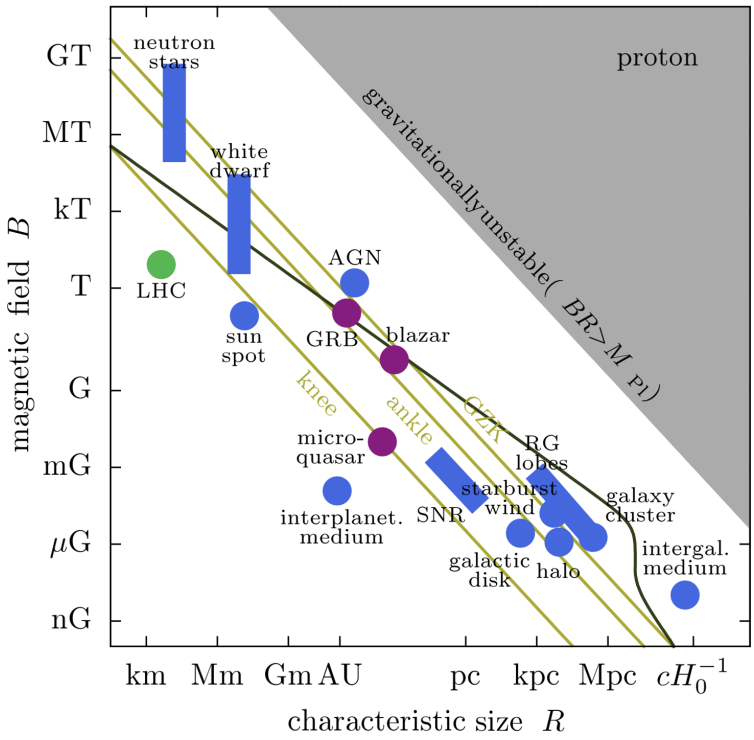

Figure 1.4: Hillas diagram, showing various cosmic ray sources (in blue) by the magnetic fields present in the source (B) vs. the radius of the source (R). Inflection points in the UHECR spectrum are drawn in gold for comparison, assuming a proton-only composition. The acceleration potential of the LHC is also included in green and the nonphysical phase space is excluded in grey. Figure from [49].

1.3 UHE Cosmic Rays (UHECR)

Due to a common origin and their role as a producer of cosmogenic neutrinos, a discussion of UHECRs (cosmic rays with energies in excess of 10^{18} eV) is required to fully understand UHE neutrino astronomy. UHECRs are messenger particles in their own right and they are the highest energy particles ever observed. While their electric charge makes pointing to a source difficult or impossible, the precise measurement of the UHECR flux is important for determining the sources and acceleration mechanisms of cosmic rays. The exact origin of UHECRs remains an open question in astronomy.

1.3.1 Cosmic Ray History

Cosmic rays were first discovered by Victor Hess in 1912 [150]. Shortly after the first invention of radioactivity measurement devices (specifically, the electrometer by Theodor Wulf in 1909), Hess measured the ionization rate at sea level and at 5,300 meters in a balloon flight, discovering a four-fold increase in ionization at altitude. Thus began the scientific field of cosmic rays, focused on discovering what the radiation was and from where it came.

1.3.2 UHECR Physics & Cosmology

The leading detectors in the field of UHECRs are the Pierre Auger Observatory in Argentina [1] and Telescope Array Project (TA) in the United States [169]. Each contains a surface array of detectors over 3000 km^2 and 762 km^2, respectively, to measure the charged particles produced in the extensive air shower (EAS) of particles induced by an UHECR that reach the surface. Each also contains a fluorescence detector, optical telescopes that detect the ultraviolet light produced by the charged particles from the EAS interacting with nitrogen in the air, causing the gas to fluoresce. The fluorescence detectors have very large simultaneous effective volumes but low detector up-times since they can only operate in the darkest and

clearest of conditions (moon-less, cloudless nights) [245].

Both observatories measure an cosmic ray flux, seen in Fig. 1.5, and cosmic ray composition, seen in Fig. 1.6.

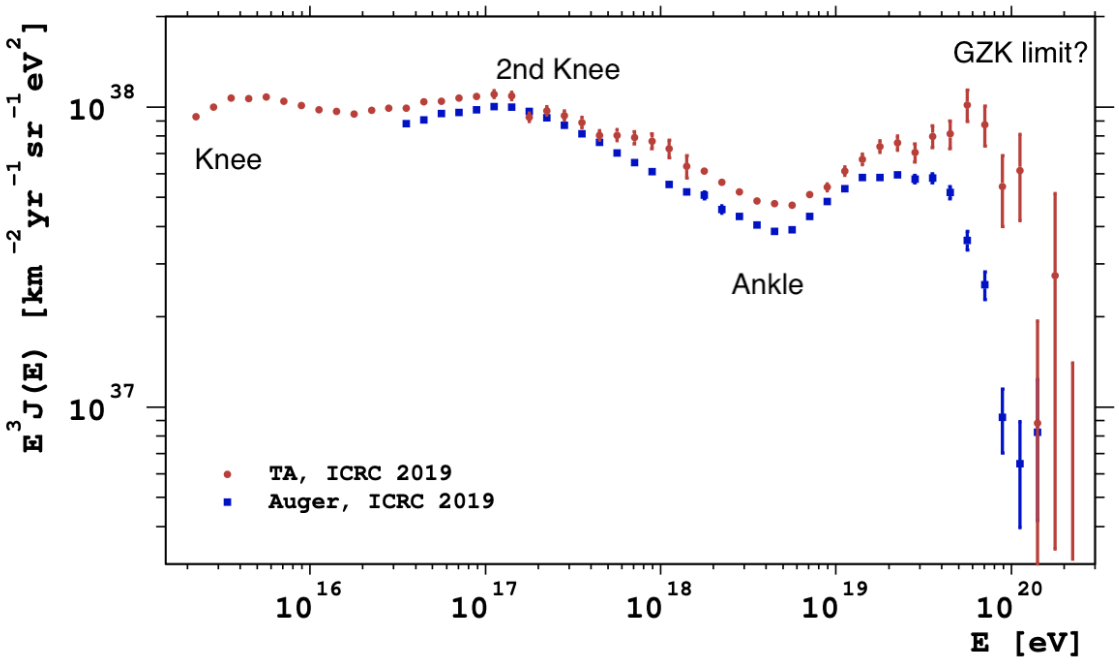

Figure 1.5: The cosmic ray flux spectrum from the TA (red) and Auger (blue) experiments. Included are inflection points and their names, each caused by a change in the energy spectrum from different acceleration mechanisms and sources. The discrepancy between the TA and Auger results is an active area of study [26] and is likely due to detector systematics. The cutoff at $\sim 10^{20}$ is either from the interaction of UHECRs with the CMB (either through direction $p\gamma$ interactions or through photodisintegration, as described in Sect. 1.2.1) or due to limitation of accelerators in the universe [152]. Figure from [103].

The shape of the cosmic ray flux is dictated by the production mechanisms of cosmic rays. At energies between the "knee" (3 PeV) and before the "ankle" (3 EeV), the spectrum falls as an $E^{-3.0}$ power law, where E is energy. Cosmic rays in this energy range are galactic in origin, thought to be primarily produced in supernova remnants via Fermi acceleration mechanisms [107, 85]. The flattening of the distribution after the ankle is thought to be due to the transition of galactic to extragalactic production of cosmic rays. The cutoff near 10^{20} eV can either be due to GZK suppression (UHECRs attenuated by interaction with

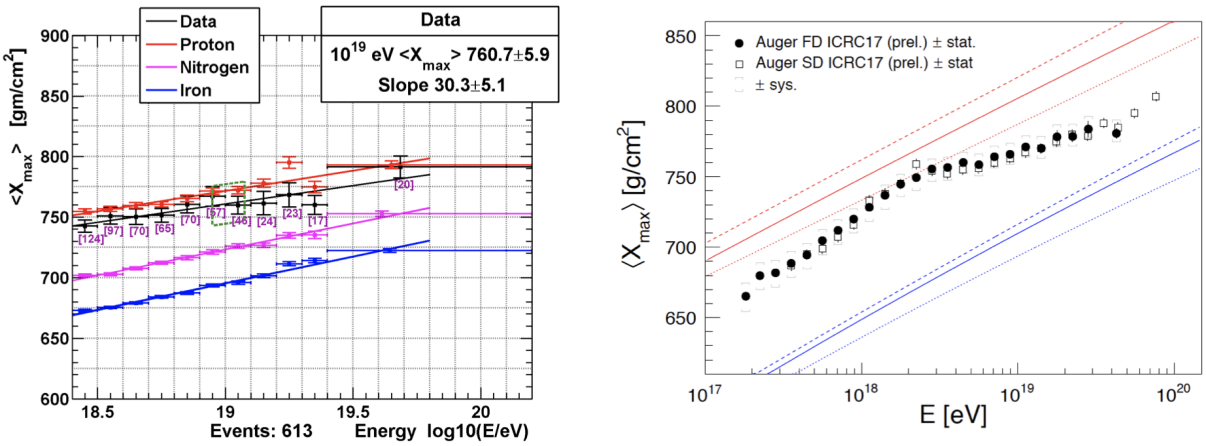

Figure 1.6: The mass composition of UHECRs as measured by the TA observatory (left) and the Auger observatory (right). In the Auger plot, red is an all-proton composition and blue is an all-iron composition. TA figure is from [145] and Auger figure is from [228]

.

the CMB, described in Sect. 1.2.1) or due to limitation of accelerators in the universe [152]. From the UHECR spectrum alone, it is impossible to determine if the cutoff is from lack of acceleration or the GZK limit: only through the observation of cosmogenic neutrinos can this be understood.

Composition of UHECRs is determined via a direct measurement of maximum shower depth into the atmosphere, X_{max}, and initial particle energy. The primary particle mass, A, is related to shower energy and maximum shower depth via,

$$\langle X_{max} \rangle = \langle X_{max} \rangle_p + f_E \langle \ln A \rangle, \tag{1.10}$$

where $\langle X_{max} \rangle_p$ is the average X_{max} of protons and f_E is determined in simulations of hadronic interactions [214].

1.4 Detection Mechanisms

1.4.1 Particle Physics Interactions

Since neutrinos are weakly interacting and neutral, all detection techniques involve a neutrino weakly interacting by exchanging $W^{\pm}$ or Z^0 bosons with fermions (electrons or quarks) within a detector volume. The outgoing particles of the interaction are then directly observed via their electromagnetic radiation.

In Charged Current (CC) interactions, there is an exchange of a $W^{\pm}$ boson, creating an outgoing lepton of the same flavor as the incoming neutrinos. In Neutral Current (NC) interactions, there is an exchange of a neutral Z^0. There is no neutrino flavor determination power in NC interactions. The Feynman diagrams of possible neutrino interactions are plotted in Fig. 1.7.

1.4.2 Particle Showers

A cascade of particles occurs when a highly energetic particle interacts with matter, causing a series of particle productions, nuclear deexcitations, scatterings, and decays.

If the interaction occurs in the Earth's atmosphere, it is called an extensive air shower (EAS). An EAS can be detected from the charged particles that reach the Earth or through the detection of electromagnetic emission created by the shower. For the experiments described herein, UHECRs are detected via the radio produced in their induced EASs (see Sect. 1.4.4 and Sect. 1.4.3).

Analogous to the air shower, a particle cascade occurs in a dense material when an UHE neutrino interacts with a target material. The interaction either releases an energetic lepton or scatters a nucleus, releasing enough energy to produce a large cascade of charged particles, similar to an EAS but with different size scale. The size of the shower is constrained by the Moliere radius ($\sim$ 10 cm in ice) and the radiation length ($\sim$ 20 m in ice). Detection of

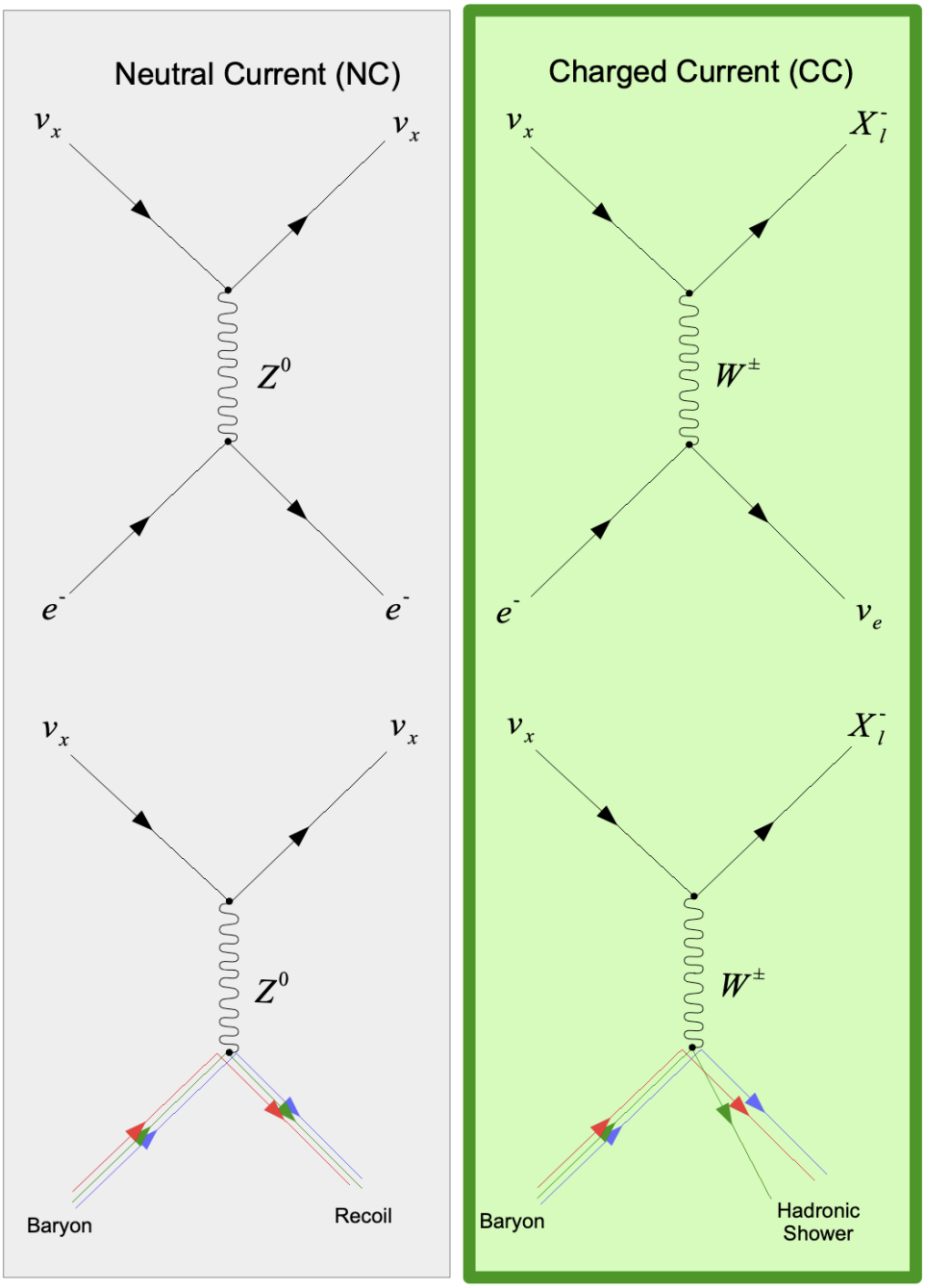

Figure 1.7: Feynman diagrams of neutral current (left) and charged current (right) interactions of neutrinos and matter. Figure from [220].

particle cascades in ice is discussed in Sec. 1.4.3.

1.4.3 Cherenkov & Askaryan Radiation

Cherenkov radiation, first observed by Pavel Cherenkov in 1934 [88, 254, 164], is electromagnetic radiation emitted when a charged particle passes through a dielectric medium faster than light in the medium. According to Maxwell's equations, moving charged particles emit moving electromagnetic waves. If the particle is traveling faster than the electromagnetic wave, a coherent wave front in a cone shape is created. The Cherenkov radiation energy E of a particle per unit length x and per frequency ω is given by the Frank-Tamm formula [242]:

$$\frac{d^2E}{dxd\omega} = \frac{q^2}{4\pi}\mu(\omega)\omega\left(1 - \frac{c^2}{v^2n^2(\omega)}\right), \tag{1.11}$$

where q is the electric charge of the particle, v is the speed of the particle, $\mu(\omega)$ is the permeability of the material, and $n(\omega)$ is the index of refraction of the material.

Many experiments detect particles from their Cherenkov radiation emission, including the Pierre Auger Observatory [1], Super-Kamiokande [252], and all experiments described herein. IceCube, discussed in Sect. 1.5.2 and Sect. 4, uses optical wavelengths of Cherenkov radiation emitted by the charged particles both in particle showers in ice and traversing muons produced from distance neutrino and cosmic ray interactions.

Askaryan radiation, theorized by Gurgen Askaryan in 1962 [60], is the radio frequency emission from a particle cascade in a dielectric material, equivalent to the radio Cherenkov emission. The electrons created in pair production are Compton scattered into the leading edge of the shower, causing a negative charge excess to build up on the leading edge. At the same time, positrons are annihilated with electrons in the medium, leading to a net negative charge within the shower. The charge imbalance and moving electron front will radiate coherently for wavelengths longer than the characteristic width (Moliere radius, ~ 10 cm in

ice) of the shower, creating a radio frequency Cherenkov cone. The resulting emitted signal is a O(ns), sharp, and broadband impulse that radiates in a cone at critical angle,

$$\cos\theta_{crit} = \frac{1}{n}\frac{c}{v}. \tag{1.12}$$

The coherence is lost at angles away from the critical angle, known as the "off-cone" angle. The pulse is linearly polarized, pointing towards the shower-axis. The level of coherence and the polarization of a given signal can be used to measure the direction of the initial particle [213, 127, 53].

Askaryan emission has been measured for ice [131], salt [130], and silica sand [222] in an electron particle beam. An example pulse in ice as measured by the ANITA experiment is plotted in Fig. 1.8 [132].

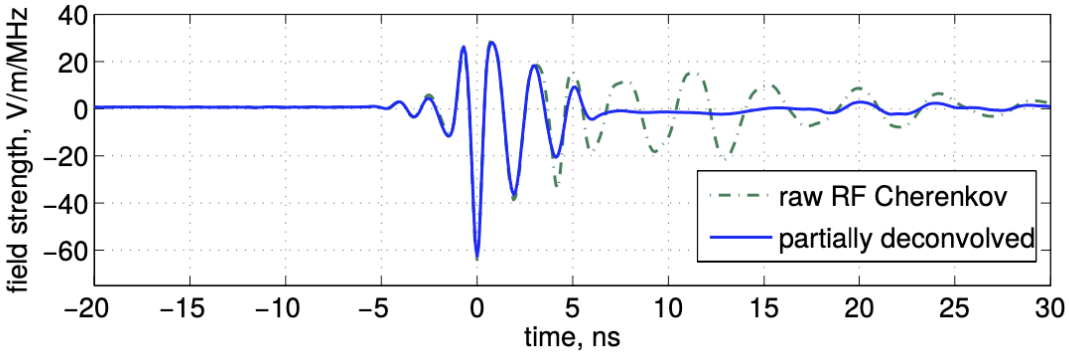

Figure 1.8: An Askaryan pulse produced via an electron beam interacting with ice. Signal includes some amount of ANITA-I electronics system response, including a high-pass filter of 200 MHz. Figure from [131].

1.4.4 Geomagnetic Radiation

Geomagnetic radiation is the radio frequency emission created by charges in a shower accelerating in the Earth's magnetic field. The electrons and positrons in an EAS experience the Lorentz force, $\vec{F} = q\vec{v} \times \vec{B}$, in the geomagnetic field, causing them to separate and spiral

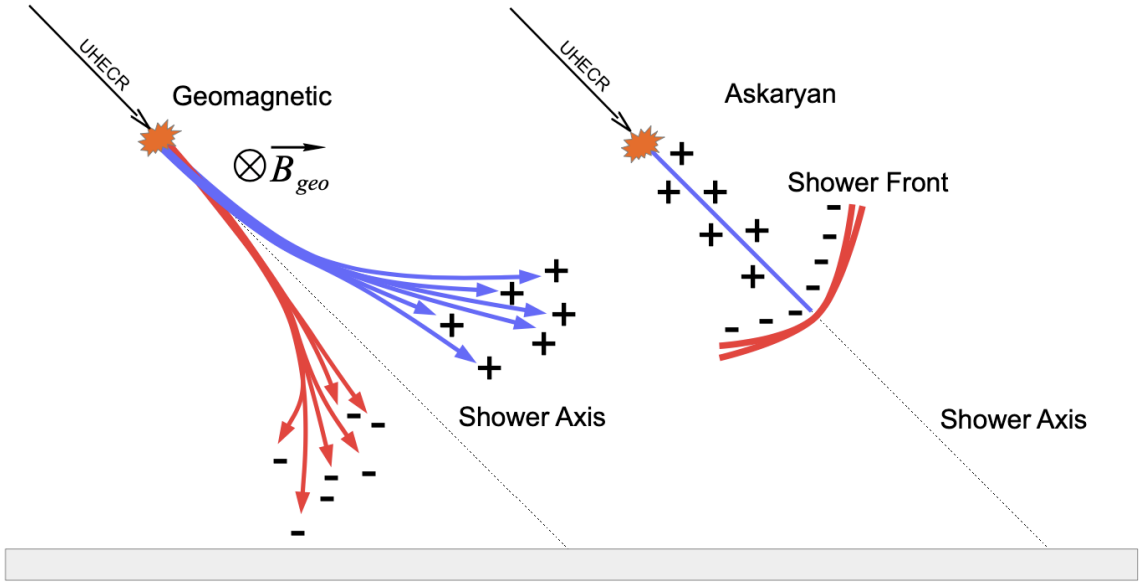

Figure 1.9: Diagram of the two radio emission mechanisms from EASs. Figure from [220].

around the magnetic field lines. The acceleration from the trajectory leads to synchrotron emission. Due to the O(m) scale of the radius of the EAS (Moliere radius in air), the shower coherently emits forward-beamed synchrotron emission in radio frequencies. This effect has been measured using an electromagnetic shower created in an electron beam traveling through a magnetic field [76]. Geomagnetic radiation is the predominate radio production mechanism for EASs.

1.4.5 Ice Properties

All detectors described herein detect neutrinos from the electromagnetic radiation from an neutrino's interaction in ice. After production, the emission must propagate from the shower to the detector.

In the case of IceCube, the optical scattering in deep glacial ice is O(100 m) [16] and optical strings are separated by 70 m, meaning the interaction vertex or secondary particles must pass through the center of the detector to be detected. For this reason, IceCube is most

sensitive to muon neutrinos as a boosted muon produced in an interaction can propagate far distances from the vertex before passing through the detector [8].

In the case of radio experiments, the radio attenuation in deep glacial ice is O(1 km) [32, 62, 69, 77], allowing for much larger detector volumes from a single string of radio antennas. A discussion of the radio frequency attenuation measurement at Summit Station, Greenland is described in Sect. 3.1. For this reason, radio detection of neutrinos is the most promising detector mechanism for the EeV energy scale.

1.4.6 Multi-messenger Astronomy

Besides being the unique messenger types for some distances and energy scales, UHE neutrinos are also powerful for their potential in multi-messenger astronomy, or astronomy that associates multiple detection types (electromagnetic detection in many frequencies, or gravitational waves) together to develop a deeper understanding of astrophysical objects [84].

For example, there is an expectation that gamma rays will be produced in tandem with UHE neutrinos within blazars. The blazar's relativistic jet is thought to have sufficiently high and extensive magnetic fields to accelerate seed cosmic rays to ultra-high energy scales [190] (described in Sect. 1.2.2). These charged hadrons can interact in the source, either through $p\gamma$ or pp, producing a corresponding flux of gamma rays from neutral pion decay, neutrinos from charged pion decay, and a flux of UHECRs. Blazars as a source of UHE neutrinos is further motivated by IceCube's coincidence observation of an high energy neutrino with TXS 0506+056, described in Sect. 1.1.4. Further observations of neutrinos and gamma rays, in either blazar or other astrophysical objects, will further inform models of astrophysical objects, including descriptions cosmic ray accelerator mechanisms, in ways unavailable to gamma ray detection alone [84, 190].

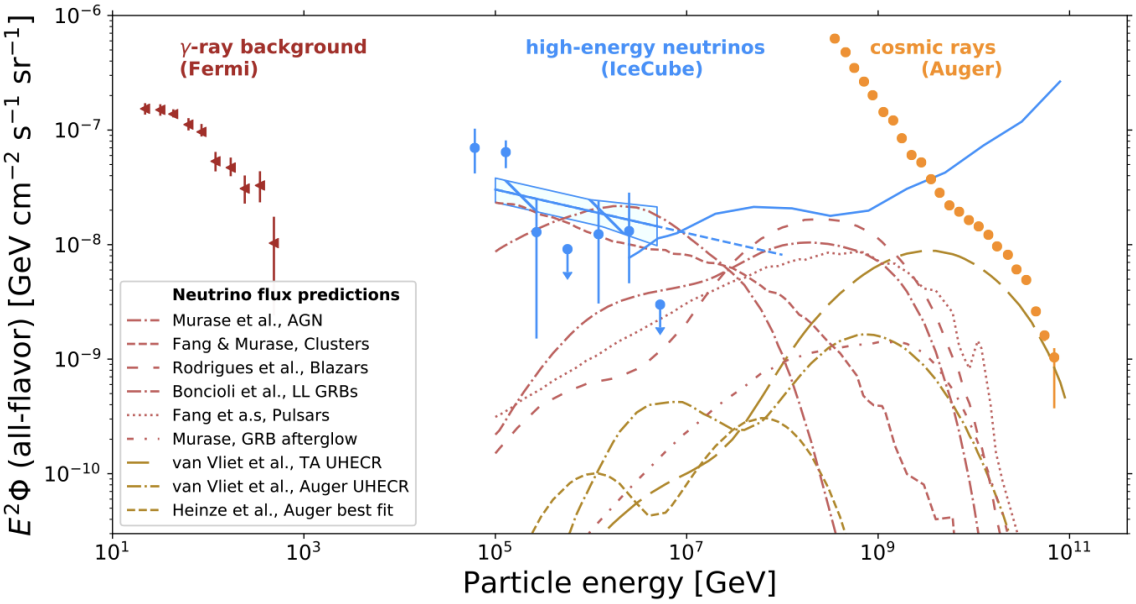

Figure 1.10: Current measurements of the flux of the highest energy gamma rays (from the Fermi telescope), cosmic rays (from Auger), and neutrinos (from IceCube). The similar flux densities among messenger types suggest a common source. Figure from [31].

1.5 Current & Future Detectors

1.5.1 RNO-G

The Radio Neutrino Observatory in Greenland (RNO-G) is an in-ice radio detector that, as of 2022, is being constructed near to the National Science Foundation's Summit Station at the highest point of the Greenlandic Ice Sheet [31]. The experiment is designed to self-trigger on the impulsive Askaryan radiation produced by a neutrino interaction of energy $> 10^{16}$ eV in the ice sheet. RNO-G is similar to the ARA [40], RICE [175] and ARIANNA [52] detectors, with expertise from all three carried forward to create the largest-volume in-ice astrophysical neutrino detector to date. An extensive discussion of the RNO-G detector is present in Chapter 2.

The science case for RNO-G is multifaceted and includes extending the astrophysical neutrino flux of IceCube to higher energies, detection of cosmogenic neutrinos, fundamental

neutrino physics, transient source detection, multimessenger astronomy, and sky-coverage both different and complementary to detectors at the South Pole.

RNO-G is designed to be the first observatory to detect astrophysical neutrinos at energies in excess of 10 PeV, extending IceCube's already-measured astrophysical neutrino flux to energies unreachable by optical Cherenkov detectors. Measuring the astrophysical neutrino flux to higher energy will enable the study of production mechanisms in sources at energies inaccessible to any other detector (see Sect. 1.1.3).

RNO-G will target the expected energy scales of cosmogenic neutrinos, neutrinos produced by UHECRs interacting with the CMB. The discovery or null observation of cosmogenic neutrinos will measure or place limits on UHECR composition, source evolution, and source acceleration mechanisms.

An ambitious goal of RNO-G is to participate in multi-messenger astronomy, both in the same manner as and in tandem with IceCube. Source searches will be performed on any neutrino or UHECR candidates found by the detector. Transient sources, due to the recent correlation of UHE neutrinos by IceCube, are of particular interest to RNO-G. Transient sources have been shown to produce sufficiently high UHE neutrino fluxes to be observed in both single-event alerts and neutrino flares in time-analysis [12, 11, 31].

Above the PeV scale, the earth becomes opaque to neutrinos, making detectors most sensitive to downward-going and horizon-skimming neutrinos. Since RNO-G is near to the opposite pole as IceCube, a combined UHE neutrino analysis could continuously monitor all sources in the sky. Sources near to the horizon for both detectors, including the Texas Blazar TXS 0506+056, would be monitored by both, while RNO-G would be sensitive to Northern sky sources, such as TA's hotspot in its UHECR spectrum [23, 170]. RNO-G's skymap sensitivity with a few sources of interest is plotted in Fig. 1.12.

With sufficient neutrino osbservations, RNO-G will be able to make fundamental physics measurements of neutrinos. No other experiment under construction will be able to probe

neutrinos at such high energies, giving the detector a unique ability to measure cross sections [97, 155], flavor mixing [56, 231], and neutrino lifetime [231, 74].

While RNO-G has ambitious science goals of its own, it is also a a test bed for future, still larger scale neutrino experiments, specifically the IceCube-Gen2 Radio detector, described in Sect. 1.5.3. The systems, measurements, and simulation being developed for RNO-G are currently being folded into the development of the baseline design of IceCube-Gen2 Radio.

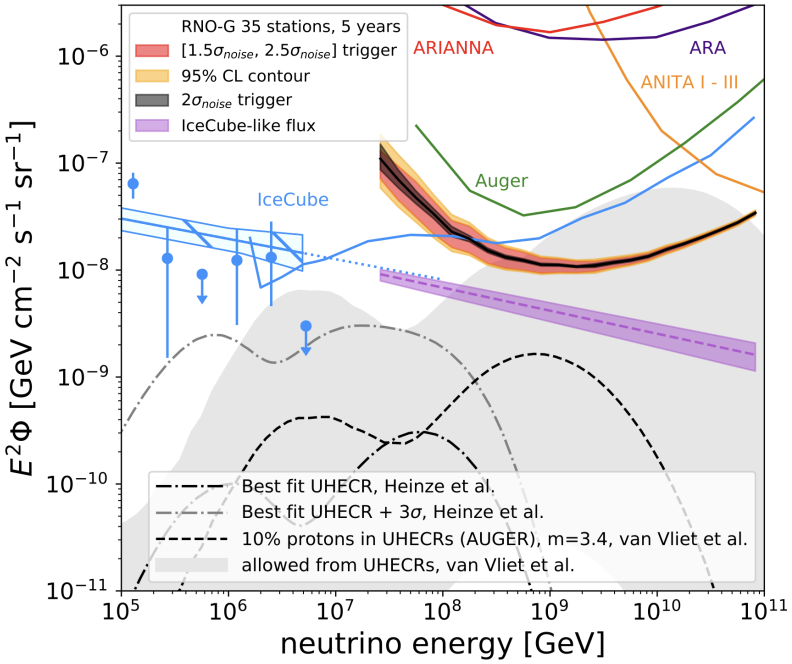

Figure 1.11: Preliminary five-year, 35 station sensitivity (90% CL upper limits) of RNO-G to the all-flavor diffuse flux compared against existing experiments and predicted fluxes [31]. Contours around the RNO-G sensitivity represent different trigger hypotheses. IceCube's current measured flux is in points with error bars in blue, and IceCube's current limit at higher energy is in blue. In purple is the integrated sensitivity (90% CL upper limits) for the astrophysical neutrino flux measured by IceCube extrapolated forward, given a range of trigger hypotheses. Figure from [31].

1.5.2 IceCube

The IceCube Neutrino Observatory is an ice Cherenkov detector with 1 km^3 of detector volume, located near to the Amundsen-Scott South Pole Station in Antarctica. The detector

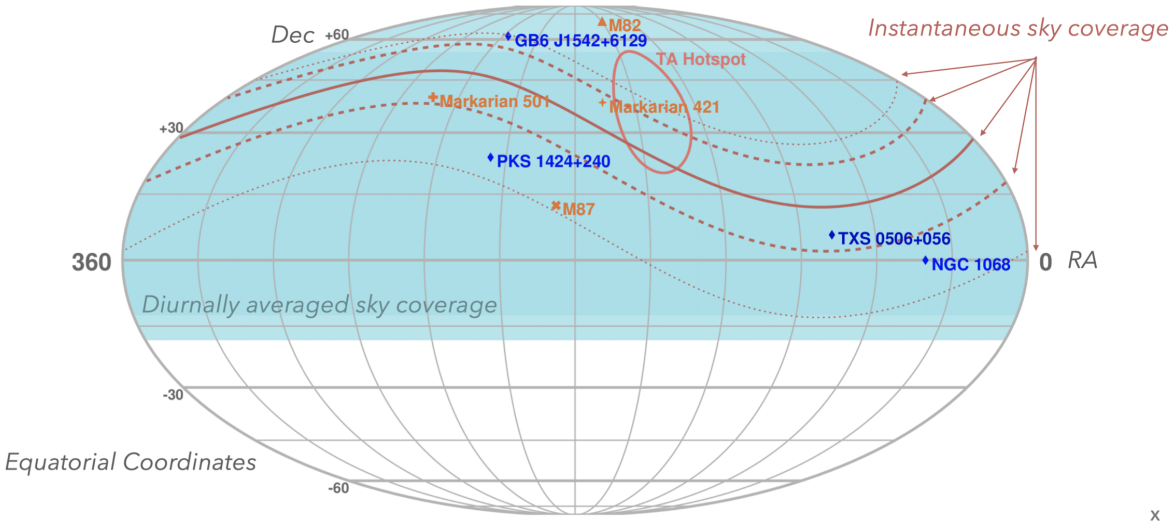

Figure 1.12: Map of sky coverage of the RNO-G array, including the time-integrated sensitivity (blue shade), an instantaneous sky coverage for a particular day (red lines), potential sources of interest (blue and orange plots), and the TA UHECR hotspot (red circle). Figure from [30].

is composed of 86 strings, each with 60 optical detectors (DOMs), deployed in the ultra-pure ice above the bedrock at the South Pole. The detector records the optical Cherenkov light from charged particles produced in or passing through the detector. IceCube has been hugely successful, being the first detector to measure a flux of astrophysical neutrinos and the first with a high likelihood of association between a astrophysical neutrino and its source, among many other physics results. Completed in 2010, IceCube continues to run and collect data, increasing statistics on the astrophysical neutrino flux while waiting for more neutrino-source correlations.

Of particular interest to this thesis is IceCube's public release of muon track data. The muon track data can be used to run time-integrated source searches (looking for sources that produce a constant flux of neutrinos, a signal that would increase with increased statistics). A description of one such search is described in Chapter 4.

1.5.3 *IceCube-Gen2*

IceCube-Gen2 is the planned upgrade to the IceCube experiment [20]. Along with an extended ice optical Cherenkov detector, there is a planned co-located radio array, called IceCube-Gen2 Radio and plotted in Fig. 1.13. While the design for the detector is still preliminary, it is projected to have instruments distributed over ~ 500 km^2 of the area near to the South Pole Station. This radio array has matching science goals to the RNO-G experiment but with more than an order of magnitude increase in detector sensitivity. Discussion of the simulations, planned array, and projected science results of the array are presented in Chapter 5.

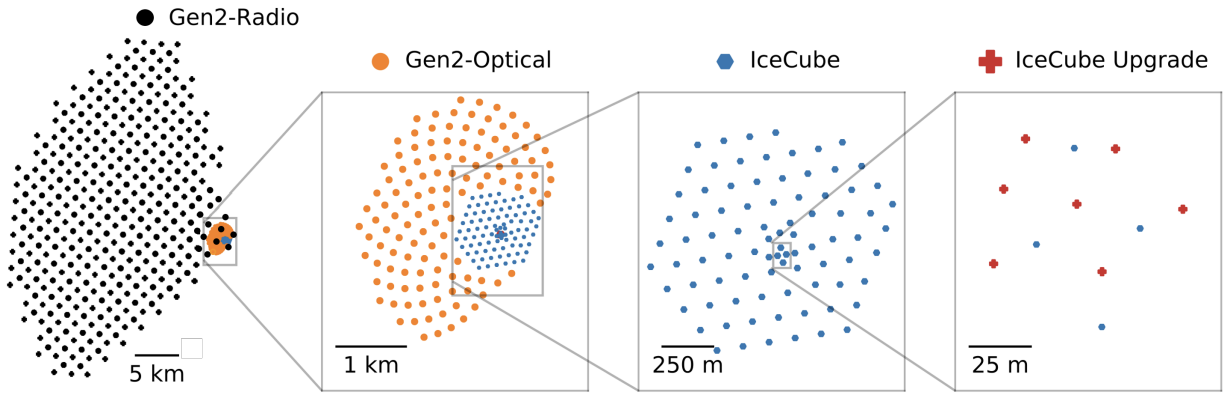

Figure 1.13: Top down view of the preliminary plan of IceCube-Gen2 along with the current IceCube array. **First on left:** IceCube-Gen2 Radio component. Note that here 361 stations are shown, a preliminary number. **Second from left:** Optical improvement of the Gen2 upgrade, with 120 new strings of deep optical detectors. **Third from left:** The original IceCube detector. **Fourth from left:** Layout of the IceCube Upgrade, added to increase IceCube's sensitivity to lower energy neutrinos. Figure adapted from [20].

1.5.4 *ANITA*

The Antartic Impulsive Transient Antenna (ANITA) experiment [133] is a series of balloon-borne detectors designed to detect UHE neutrinos via Askaryan radiation produced by neutrino interactions in the Antarctic Ice Sheet. ANITA has flown four times (ANITA-I through

ANITA-IV), each with an improved but overall similar payload. The payload is a series of highly directional horn antennas pointed down and towards the Earth. The balloon, provided by NASA [133], caries the payload to $\sim$ 35 km above the ice. At such altitudes, the horizon is at approximately $\sim$ 700 km and the instantaneous detector volume is the largest in the world, at O(10^6 km^3). A picture of the ANITA-4 payload is shown in Fig. 1.14.

The experiment suffers from a short flight period. After set aloft from near to McMurdo Station, the payload follows the air currents over Antarctica, spiraling until right before it reaches the ocean, at which point the payload is released and falls to the Earth, arrested by a parachute. All data is collected from hard drives at the crash site. ANITA-I flew for 35 days [160], ANITA-II for 30 days [134], ANITA-III for 22 days [137], and ANITA-IV for 28 total days [138].

Since the payload is O(100 km) from a neutrino vertex in the ice, the signal suffers extensive path loss. For that reason, ANITA is most sensitive to the highest energy neutrinos, with world-leading diffuse neutrino flux limits at energies above 10^{20} eV [134, 137], as can be seen in Fig. 1.11.

ANITA was constructed for the detection of cosmogenic neutrinos. The null observation of UHE neutrinos from the flights have ruled out many cosmogenic models (predominately models that assume proton-only UHECR composition with an erroneously high flux measured by Fly's Eye [109]), leading to the suppressed models that we have today.

Along with the planned science case, ANITA observed UHECRs from the geomagnetic emission of UHECR-induced EASs. ANITA is also sensitive to τ neutrinos via geomagnetic emission from the EAS created in the decay of a τ lepton. A ν_τ undergoes a charged current interaction near the Earth's surface, producing a τ lepton that is so boosted that it escapes the Earth, passes through the ice, and decays in flight [256]. This signal would appear to be "up-going", separating it from the normal "down-going" UHECR signals.

Of most interest to this thesis is ANITA's two 'anomalous' events, impulsive signals that

appear to have been made from a particle that has a cross section much smaller than any Standard Model particle. The mystery events are discussed in Chapter. 6.

Figure 1.14: Picture of the ANITA-4 payload prior to launch near to McMurdo Station. For scale, each of the horn antennas are 0.8 m across. The solar panels on the bottom drop down after taking flight to expose another ring of antennas. Figure from [95], available under Creative Commons licensing.

1.6 Thesis Layout

Over the last four years, I have worked on topics of astroparticle physics that span the field, from detector development to astrophysical analysis. That work is documented in this thesis as follows:

- In Chapter 2 and Chapter 3, I discuss the RNO-G detector, on which I worked through

the simulation development, detector construction, and commissioning. I give particular attention to the vertically polarized antenna, which I designed and constructed for the first season of deployment of the detector, and RNO-G's ice attenuation measurement at Summit Station, an analysis that I lead.

- In Chapter 4, I use publicly available IceCube data to look for correlations between potential neutrino events and AGN sources, demonstrating the current status of neutrino astronomy and an example of analyses that will be performed in RNO-G and IceCube-Gen2 Radio.

- In Chapter 5, I discuss simulation results for the future IceCube-Gen2 Radio array, showing the future of the radio detection of neutrinos and the current best design for the future design.

- In Chapter 6, I discuss a challenge for current and future ice detectors, the simulation of the ice that may impact the over-all sensitivity of the array, focusing on the two 'anamolous' events from ANITA as motivation to run large-scale, high resolution simulations of the ice.

CHAPTER 2

RADIO NEUTRINO OBSERVATORY IN GREENLAND (RNO-G)

2.1 Instrumentation Overview

This chapter serves as an overview of RNO-G's system electronics and deployment, as well as an in-depth description of the vertically-polarized (VPol) antenna design, simulation, and *in situ* performance.

RNO-G is planned to be composed of 35 autonomous stations situated in a 1 km grid pattern north west of Summit Station, Greenland, as can be seen in Fig. 2.1. Each station has a surface array of antennas and an array of antennas in the ice inside of three, 100 m deep boreholes.

The surface array of antennas is made up of nine directional, log-periodic dipole antennas (LPDAs) buried immediately below the surface, with three pointing up and six cantered down. They are used for cosmic ray tagging, veto of background events from the surface, and energy and polarization reconstruction of neutrino signals. The deep array is composed of 15 in-house developed vertically-polarized (VPol) and horizontally-polarized (HPol) antennas (11 VPol and 4 HPol antennas per station) deployed on three strings. There is one 'power string' with a dense cluster of VPol antennas for triggering and two 'helper strings' used for signal arrival direction reconstruction and, with the use of two *in situ* RF pulsers, as a calibration source. The main signal trigger of the array is a phased-array trigger [42, 168, 63, 31] on the four deepest VPol antennas on the power string. The depths of the antennas allow for monitoring of greater ice volume, away from the changing index of refraction of the firn that shadows large volumes of ice.

The station electronics, plotted in Fig. 2.2 and in Fig. 2.3, are deployed in an environmental enclosure at the surface in the center of each station. The bulk of the station electronics,

including the front-end amplifiers, RF-over-fiber system, power control, digitization, data acquisition and telemetry, were produced in-house to meet the low-power constraints of the system.

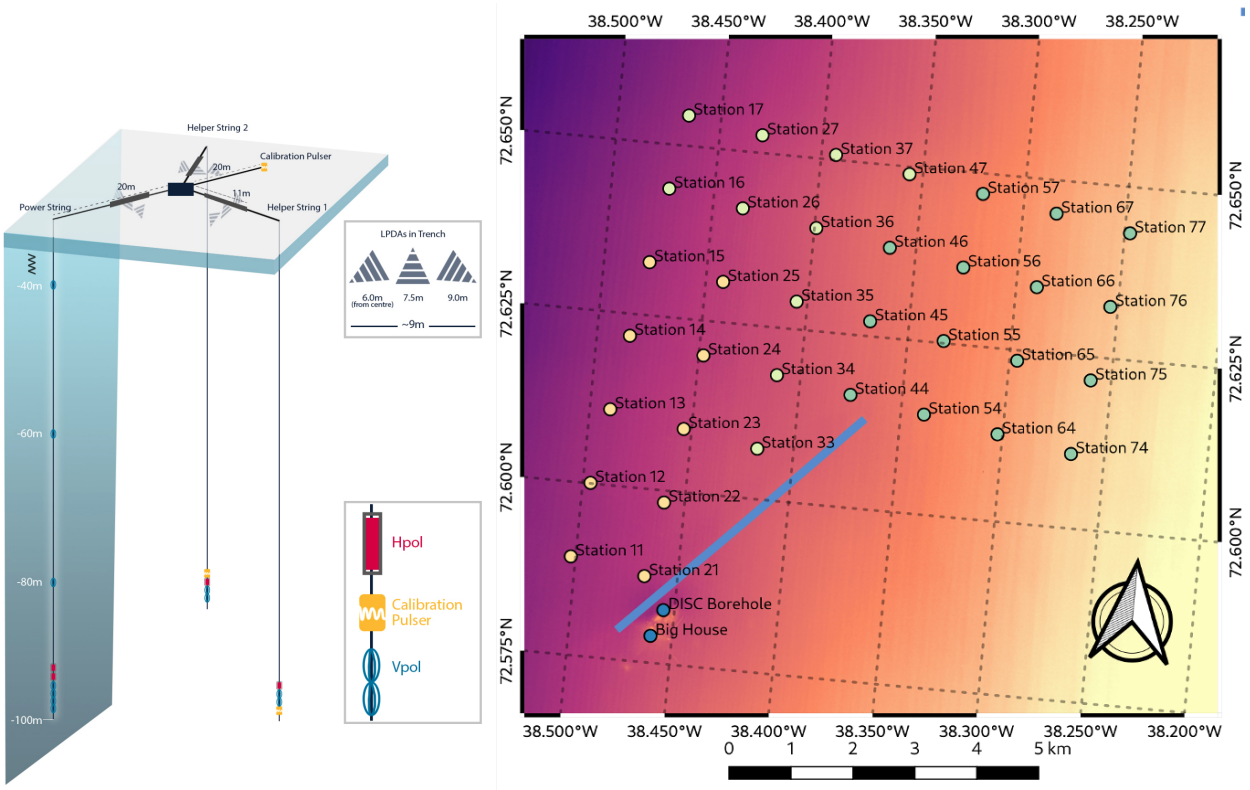

Figure 2.1: **Left:** Diagram of a single station with surface antennas, deep antennas, calibration pulser, and environmental enclosure labeled. Figure from [31]. **Right:** Map of current and planned station locations for RNO-G. Stations 11, 21, and 22 were deployed Summer 2021. All stations are north of Summit Station (labeled as Big House) to avoid a clean-air sector to the south. The skiway, labeled as a blue line, is 4.5 km in length. Figure by Cosmin Deaconu.

2.2 Signal Detection Concept

A schematic of the event geometry from a neutrino in one station is shown in Fig. 2.4. The Askaryan emission from a neutrino-induced particle shower propagates through the ice and to the antennas in the station. The radio signal propagates in a straight line in deep ice but has a curved trajectory in the top $\sim$ 150 m of ice due to refraction in the firn [129, 235, 149].

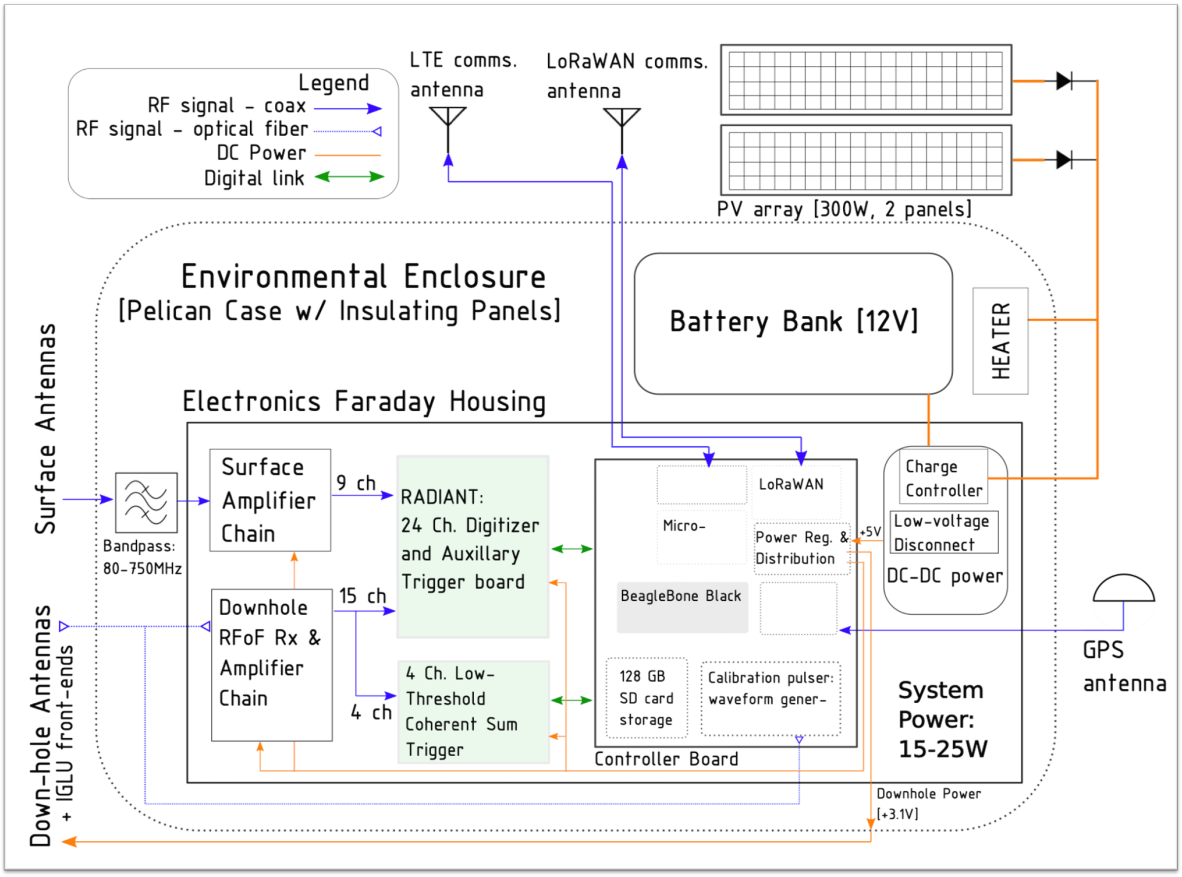

Figure 2.2: Diagram of the electronics in each station, including front-end amplifiers, power control, digitization, data acquisition, telemetry. Figure from [31].

The firn is the top of the glacial ice that has a density (and thus index of refraction) that is dependant on depth. Over time and snow accumulation, the weight of the light snow at the top compresses the snow below, leading to a gentle gradient from $n \approx 1.4$ snow at the surface to $n \approx 1.78$ ice below $\sim$ 150 m (the firn is deeper in Antarctica). The change in density is usually modeled as an exponential function in the form $n(z) = A + Be^{z/z_0}$, where A, B, and z_0 are derived from fits of measurements of ice density [129]. The firn can cause multiple propagation paths to the same antenna. In Fig. 2.4, the direct and refracted signals from the neutrino vertex arrive at the deep antenna array while only the direct ray arrives at the surface array.

Propagation geometries can be more complicated than what is seen in Fig. 2.4. For

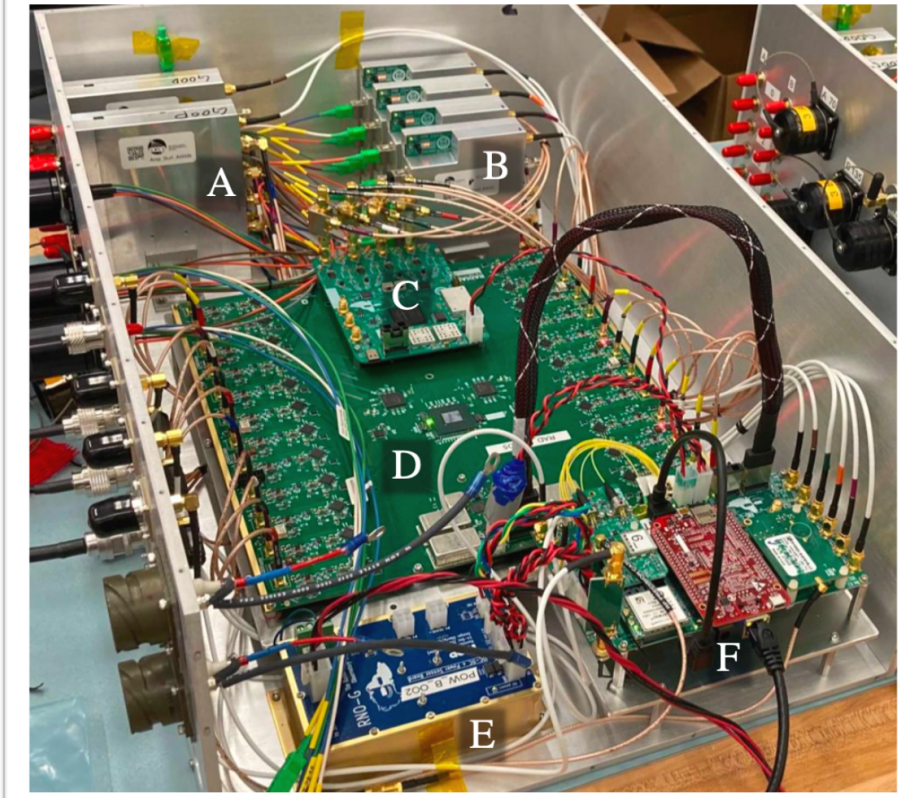

Figure 2.3: Nearly complete DAQ box, with **A** Surface amplifiers (`SURFACE` boards, Sect. 2.6), **B** Deep amplifiers and RFoF reciever (`DRAB` boards, Sect. 2.6), **C** Low-threshold trigger (`FLOWER` board, Sect. 2.9), **D** Digitizer (`RADIANT` board, Sect. 2.8), **E** Power regulation board (Sect. 2.7), **F** Controller board with single board computer (Sect. 2.10), GPS unit, and calibration pulser source daughter board (Sect. 2.11).

example, the deep antennas have a larger effective detector volume than surface antennas due to the firn 'shadowing' parts of the ice, 'shadowing' referring to paths that would be forbidden by propagation described by a ray tracer. This creates a set of events that have signals in the deep antennas but no expected signal in the surface. Signals that originate in the 'shadow zone' have been observed [73, 101], but such signals would be difficult to reconstruct due to the propagation path that is not predicted by a ray tracer and the low signal quality from decoherence in this region.

Using the surface array of antennas, RNO-G will also detect cosmic rays from the geomagnetic emission of UHECR-induced EASs. Three of the surface LPDA antennas are pointed up to tag UHECR signals. Radio propagation in air is much simpler than in ice due to the $n \approx 1$ of air: signals will propagate along straight lines between the EASs and the stations.

2.3 Noise Sources

RNO-G has four predominant noise sources: thermal, anthropogenic, mis-tagged UHECRs, and other natural radio-frequency interference (RFI) sources.

Thermal noise is the incoherent signal produced from the thermal agitation of charge carriers (electrons and holes) in the 50 Ω transmission line, inside of the first stage of amplification, and produced from the black body radiation of the environment observed by the antenna [128, 243]. Thermal noise is typically quantified as a temperature and related to a voltage RMS via,

$$V_{RMS} = \sqrt{4k_B T R \Delta f}, \tag{2.1}$$

where k_B is Boltzmann's constant, R is resistance (50 Ω), Δf is the bandwidth of the system, and T is the temperature of the system. For the deep array, the noise temperature

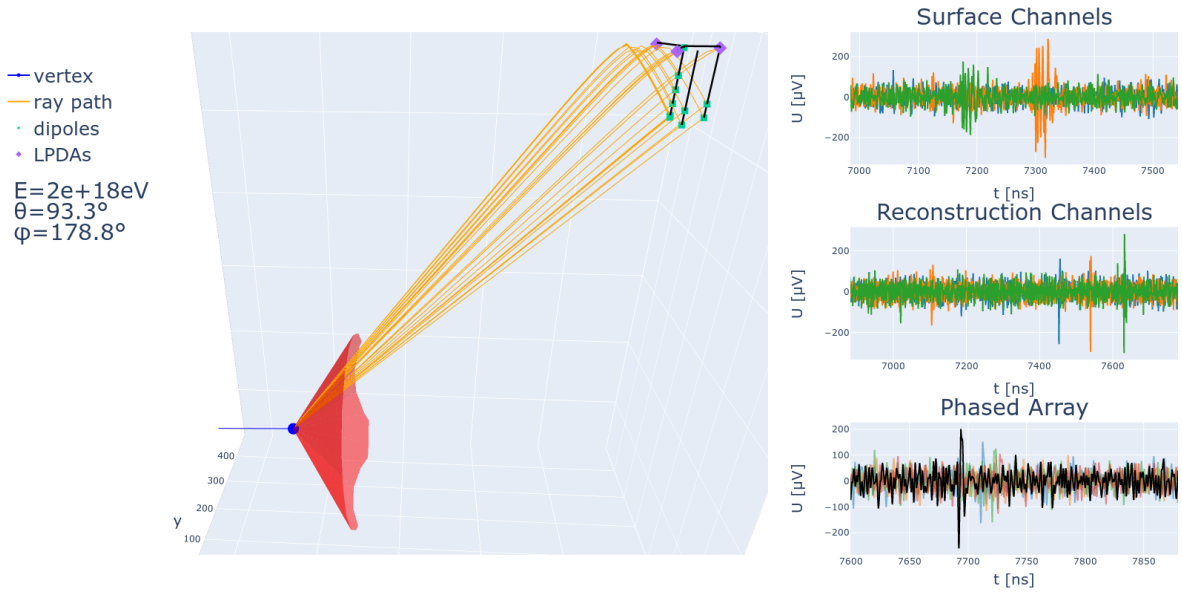

Figure 2.4: Diagram of an example simulated neutrino event with signal paths and measured signals in the array shown. **Left:** a neutrino vertex (blue) produces an Askaryan cone (red) with allowed ray tracer signal paths (orange) to the 11 simulated deep antennas and 3 simulated surface antennas. Note that this is a simplified version of a typical RNO-G station. **Right top:** The signals after the electronics chain on the three surface channels. **Right middle:** The signals after the electronics chain on the 4 deepest VPol antennas. **Right bottom:** The signals after the electronics chain on the 4 deepest VPol antennas after phasing, demonstrating the increased SNR from the phased array technique, discussed in Sect. 5.2. Figure by Christoph Welling.

contribution from the ice is expected to be ~ 250 K and the electronics temperature to be < 100 K. [31, 42].

RNO-G is a trigger-limited detector, meaning the majority of signals from UHE neutrinos are expected at or slightly above the trigger level of the detector. To increase the sensitivity of the detector, the trigger level is lowered until the number of thermal noise triggers equals a predetermined rate (between 1–10 Hz in RNO-G depending on power conditions). In this regime, thermal noise represents the majority ($> 99\%$) of triggers. In hardware, there are minimal ways to reduce thermal noise: it can be reduced by lowering component temperatures and by tuning amplifiers to reduce noise figure, but the noise contribution from the temperature of the ice observed by the antenna is irreducible. In triggering and analysis,

antennas are phased together to suppress noise. Summing antenna signals increases the magnitude of incoherent noise by $\sqrt{n_{ant}}$ while increasing coherent signals by n_{ant}, resulting in a boost to SNR of $\sqrt{n_{ant}}$, where n_{ant} is the number of antennas phased together. A further description of the phased array trigger used in RNO-G is available in Sect. 5.2.

Anthropogenic noise is radio signals created by human activity. Example noise sources include:

- Handheld VHF radios used by Summit Station staff
- Large electric generator used by Summit Station
- Internal combustion engines of snowmobiles and heavy equipment
- Overflying airplanes
- From a station electronics itself

The VHF radios and electric generator create constant wave (CW) signals, or signals composed of only a single frequency. CW events are relatively easy to remove in analysis. However, due to the volume of events, future versions of the hardware or firmware may include a notch filter to reject such events at the trigger level.

While Summit Station, Greenland is an isolated location, it is located below a commonly used flight corridor connecting Europe and North America. RNO-G has deployed a plane tracker at Summit Station, a small antenna that collects the tracking information broadcast by all commercial airlines, that can be used to reject airplane events in analysis.

Analysis is currently underway to determine sources of internally-produced RFI. So far, there are notable increases in trigger rates from the surface array during times of high battery charge, presumably due to the solar panels. Internally-produced RFI will be relatively easy to tag: events that the surface array reconstruct as originating from the detector itself must be noise.

It is important to note that anthropogenic noise will be significantly lower amplitude in the deep array than the surface array due to more path loss, the surface interface, and less directional antennas. As can be seen in Fig. 2.40 and described in Sect. 2.2, the SNR of signals in the surface array are significantly higher than in the deep component, making the surface array an effective approach to tag anthropogenic noise. Moreover, the direction of anthropogenic background events can be reconstructed and used to reject all events originating from the surface of the ice and from known background sources (e.g., overflying airplanes).

The UHECR events are a background for UHE neutrino searches, while being useful for calibration and as a measurement of the UHECR flux, a science result in its own right. UHECR-induced EASs that penetrate the ice may produce radio signals in the ice that are similar to the expected signal from UHE neutrino interactions, leading to a potential background for future UHE neutrino searches. Tagging the UHECR using the surface array is a natural way to remove the background from the neutrino search. Moreover, many UHECR events are expected to be bright, inducing large SNR signals on both the surface and deep arrays simultaneously, potentially serving as a calibration source of the array.

Besides UHECRs, other sources of natural RFI exist. Windstorms have been shown to create static discharges on the detector and on the surface of the snow, called the tribo-electric effect [234]. The discharges appear as a higher-than-normal thermal noise trigger rate. Wind data is collected to be used in analysis to remove wind-induced RFI events. Other possible natural RFI sources include lightening and solar flares, which are sufficiently rare as to not to be a concern to RNO-G.

The expected background rate for RNO-G's UHE neutrino flux measurement remains to be quantified. The ARA experiment, representing the current cutting edge of in-ice radio UHE neutrino analyses, reports a background of $0.10^{+0.06}_{-0.04}$ events over 208.7 days of livetime for one station and a 68% analysis efficiency [44]. RNO-G can expect to improve upon

the ARA experiment by improving the surface background rejection. The majority of loss in ARA's analysis efficiency is due to a harsh surface cut made necessary due to ARA's lack of surface antennas. RNO-G, with the directional surface antennas, will better reject anthropogenic noise from the surface, increasing analysis efficiency while performing with the same background event rate.

2.4 Antennas

Each station is deployed with deep and shallow science antennas, each with their own design constraints, science goals and trigger configuration.

The shallow antennas are commercially available, high-gain, log-periodic dipole antennas (LPDAs), seen in Fig. 2.5 [99]. These antennas are deployed in slots in the snow that are back-filled, directly coupling the antennas to the snow. The surface antennas are large, broadband, have high resolution polarization reconstruction ability [54], and have been extensively calibrated by the ARIANNA collaboration [70]. Surface antennas will be used primarily for UHECR tagging, noise rejection, and improved event reconstruction for deep-triggered events.

The deep antennas are the primary sensing component of RNO-G. Deep antennas are deployed 100 m into the ice to avoid the loss of effective detector volume caused by the firn [102, 129]. Antenna design is a challenge due to the constrained geometry of the $11.2''$ diameter ice borehole. Simulation is a challenge due to the air/ice interface created by the borehole that exists in the near-field of the antenna.

The vertically polarized (VPol) antenna, seen in Fig. 2.6, takes the form of a fat-dipole antenna, iterating on the GNO and RICE antenna designs [176]. The design is sensitive in the band 150–600 MHz and has a VSWR < 3 over its entire band. The antenna is 60 cm tall, $5''$ in diameter, and constructed in stock aluminum to reduce material and machining costs. The opening angle and design of the antenna feed were optimized for 50 Ω matching

in the time-domain antenna simulation software package xFDTD. *In situ* measurements of the antenna response are ongoing using *in situ* calibration pulsers as well as calibration campaigns made by mobile RF pulsers (*i.e.* on snowmobiles). An extended discussion of the process to create, test, verify simulation, and ultimately produce 150 VPol antennas for Summer 2021 deployment is available in Sect. 2.5.

Constructing a horizontally polarized (HPol) antenna inside of a borehole is a challenge since the 11.2″ diameter is much smaller than the wavelengths of interest, O(m). RNO-G design is an iteration of the ARA collaboration design. The antenna, seen in Fig. 2.7, is a quadslot antenna, effectively a loop antenna with four feeds to improve azimuthal symmetry and extended in the direction of the borehole to improve bandwidth. The four feeds are phased together and passed through a matching network to increase bandwidth. The antenna's usable band is 250–500 MHz with a VSWR < 10 in band. *In situ* calibration is ongoing as well as studies of other HPol designs, including a turnstile antenna.

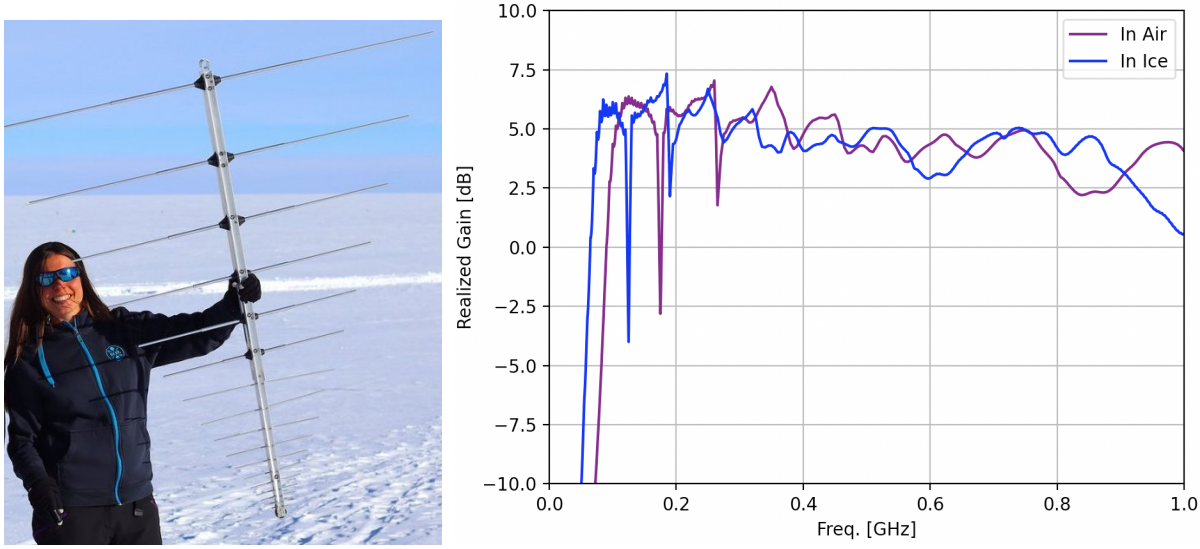

Figure 2.5: **Left:** Image of the LPDA antenna, with Ilse Plaisier for scale. Photo by Cosmin Deaconu. **Right:** Simulated realized gain as a function of frequency on boresight. Since the antenna has no azimuthal symmetry, I have only plotted boresight for simplicity. Simulations performed in xFDTD, and includes an LPDA in $n = 1.4$ ice without the air / ice surface interface.

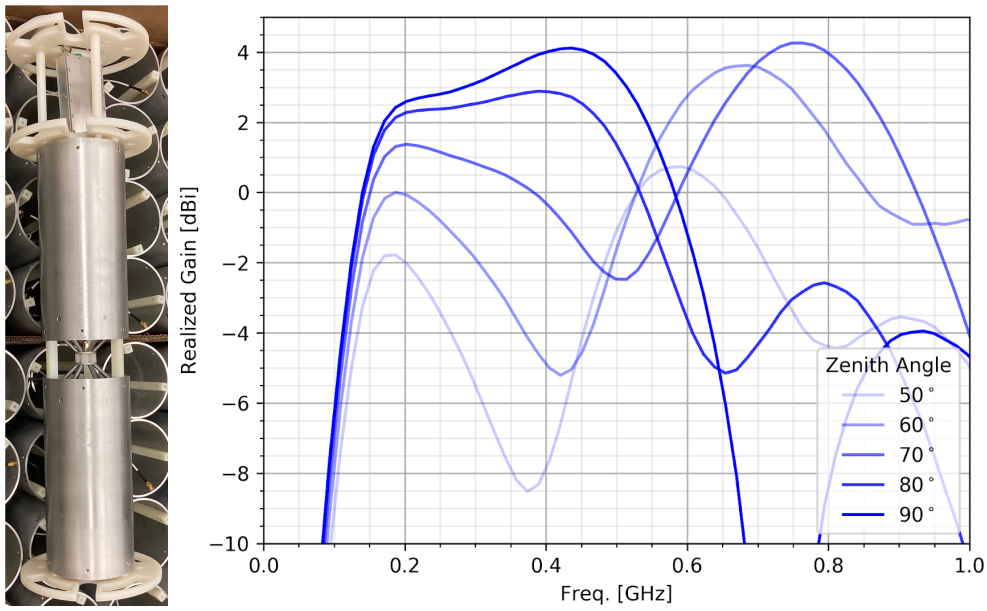

Figure 2.6: **Left:** Image of the VPol antenna, including the front-end amplifier. **Right:** Simulated realized gain as a function of frequency for several different zenith angles. Simulation performed in xFDTD, and includes a VPol inside of a borehole in deep ($n(z = 100\text{ m}) = 1.75$) ice.

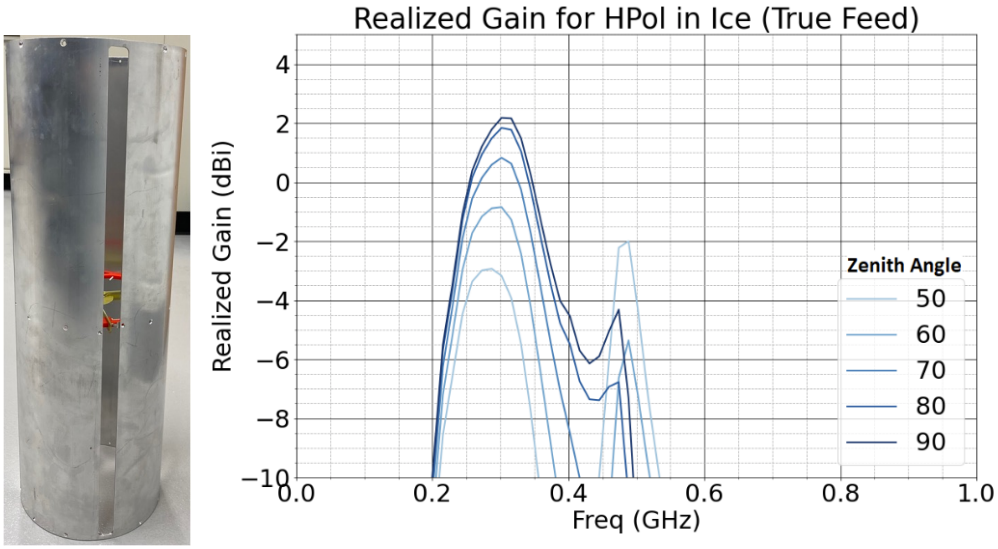

Figure 2.7: **Left:** Image of the HPol antenna. **Right:** Simulated realized gain as a function of frequency for several different zenith angles. Simulation performed in xFDTD, and includes an HPol frozen into deep ($n(z = 100\text{ m}) = 1.75$) ice, without a simulated borehole. Simulations that include the borehole are forthcoming.

2.5 Vertically Polarized Antenna (VPol)

The VPol antenna is the primary sensing element of RNO-G. Its design and characteristics are critical for the operation of the detector. For that reason, I spent roughly a year designing the antenna and another year improving simulations of the antenna. That work, from initial design tests to mass production and deployment, is detailed below.

2.5.1 Antenna Theory

One all-encompassing characteristic of an antenna is the realized vector effective length (VEL, $\boldsymbol{\mathcal{H}}_{rl}$). The VEL directly converts an incoming electric field to voltage, folding in losses at the feed. It is a function of frequency and arrival direction. We determine an antenna's VEL in the antenna simulation software xFDTD and pass the result to the radio neutrino detector simulation software NuRadioMC, which is described in more detail in Sect. 5.1.

For NuRadioMC, the VEL should follow the definition listed in the note [128]. Two other helpful resources to understand VEL are the ARIANNA experiment's antenna calibration in Ref. [70] and an explanation of antenna response in air by Farr Fields, L.C. in Ref. [115]. Note that each reference uses slightly different definitions of VEL and its relation to realized gain. To remain compatible with NuRadioMC, I use the definition in [128].

NuRadioMC converts the incident electric field produced in an in-ice or in-air shower, after propagation effects, to recorded voltage on the 50 Ω coax connected to the antenna feed, $\mathcal{V}_L(t)$, via,

$$\mathcal{V}_L(t) = \boldsymbol{\mathcal{H}}_{rl}(t) \circledast \boldsymbol{\mathcal{E}}(t) = (\mathcal{H}_{rl})_\theta(t) \circledast \mathcal{E}_\theta(t) + (\mathcal{H}_{rl})_\phi(t) \circledast \mathcal{E}_\phi(t), \tag{2.2}$$

where both the electric field ($\boldsymbol{\mathcal{E}}(t)$) and VEL are vector quantities for the two polarizations of an electromagnetic field. The subscript $_{rl}$ stands for 'realized' and denotes that matching losses at the coaxial cable are already included. The subscript $_L$ denotes the voltage is on

a 50 Ω transmission line. NuRadioMC works in spherical coordinates meaning that, in the far field and due to Maxwell's equations, $(\mathcal{H}_{rl})_r = \mathcal{E}_r = 0$.

In the context of the antenna simulation software xFDTD, the feed of the antenna is excited and then the electric field in the far field is recorded. Under these conditions, and moving into the frequency domain, the result from Ref. [128] becomes,

$$\boldsymbol{\mathcal{H}}_{rl}(\omega) = \frac{\lambda(1+S_{11})}{-iV_{OC}} \frac{Z_L}{Z_0} R\boldsymbol{\mathcal{E}}(\omega), \tag{2.3}$$

where λ is wavelength, R is the distance between the antenna and the receiving point in the far field, Z_L is the impedance of the transmission line (50 Ω), V_{OC} is the open circuit voltage, Z_0 is the impedance of free space ($\sim 120\pi$ Ω), and S_{11} is the value of the scattering matrix at the feed, equivalent to the loss at the feed. Note that often the antenna match is the easiest or only measurable of an antenna since gain measurements (as defined below) require complicated setups of multiple antennas. The S_{11} can be quickly measured using a network analyzer. We often quote the S_{11} as a voltage standing wave ratio (VSWR), equal to,

$$VSWR = \frac{1+\Gamma}{1-\Gamma}, \tag{2.4}$$

where Γ is S_{11}.

Eq. 2.3 can be rewritten into a slightly more useful form:

$$\boldsymbol{\mathcal{H}}_{rl}(\omega) = 2\pi R \frac{c}{n} \frac{\boldsymbol{\mathcal{E}}(\omega)}{\dot{\mathcal{V}}_L(\omega)} \frac{Z_L}{Z}, \tag{2.5}$$

where $2\pi Rc/n$ is a path loss correction, Z_L/Z is from coupling of the 50 Ω coax with the environment Z, and the derivative is due to being a transmitted signal instead of received. See the Farr Note [115] for a derivation of this equation. Note that $Z = Z_0/n$, where Z_0 is the impedance of free space and Z is the impedance of a material. Eq. 2.5 differs from Eq.

2.3 in the NuRadioReco note in only the sign, given how an open circuit voltage relates to a 50 Ω load voltage:

$$\mathcal{V}_L(\omega) = \frac{V_{OC}(\omega)}{(1 + S_{11})}. \tag{2.6}$$

The VEL is related to realized gain via,

$$G_{rl}(\omega) = 4\pi \left| \frac{fn}{c} \boldsymbol{\mathcal{H}}_{rl}(\omega) \right|^2 \frac{Z}{Z_L} = 4\pi \left| \frac{f}{c} \boldsymbol{\mathcal{H}}_{rl}(\omega) \right|^2 n \frac{Z_0}{Z_L}. \tag{2.7}$$

2.5.2 xFDTD Simulations

To maximize precision for neutrino detector simulations, the antennas deployed in RNO-G must be simulated in a manner that most closely represents its deployed state, which includes ice, borehole, and power feed-through N-type cable. Given such an antenna simulation, an optimized antenna design can be created by sweeping through the available phase space of antenna geometries. As well, the output of the antenna simulations will need to be compatible with NuRadioMC so that full detector simulations can be run.

A well suited antenna simulation program is xFDTD, a time-domain solver that relies on the Finite Difference Time Domain method for solving Maxwell's equations. The method solves for Maxwell equations by taking numerical derivatives on a 3D grid and stepping initial conditions through time over the grid. The FDTD method is described in more detail in Sect. 6.1. While more time and memory intensive than method-of-moment solvers like HFSS or NEC, the xFDTD can capture transient behavior and can run in an arbitrary environment, allowing for the simulation of the ice, the borehole, and complicated behavior of a fast impulse interacting with the environment.

Below is a detailed explanation of the xFDTD simulation used to develop and simulate the VPol and HPol antennas in RNO-G. The simulation setup, shown in Fig. 2.8, includes the antenna of interest, an antenna feed, a block of ice with borehole, power feedthrough

cable, and electric field sensors (called `Near Field Sensors` in the software even though they are in the approximate far field).

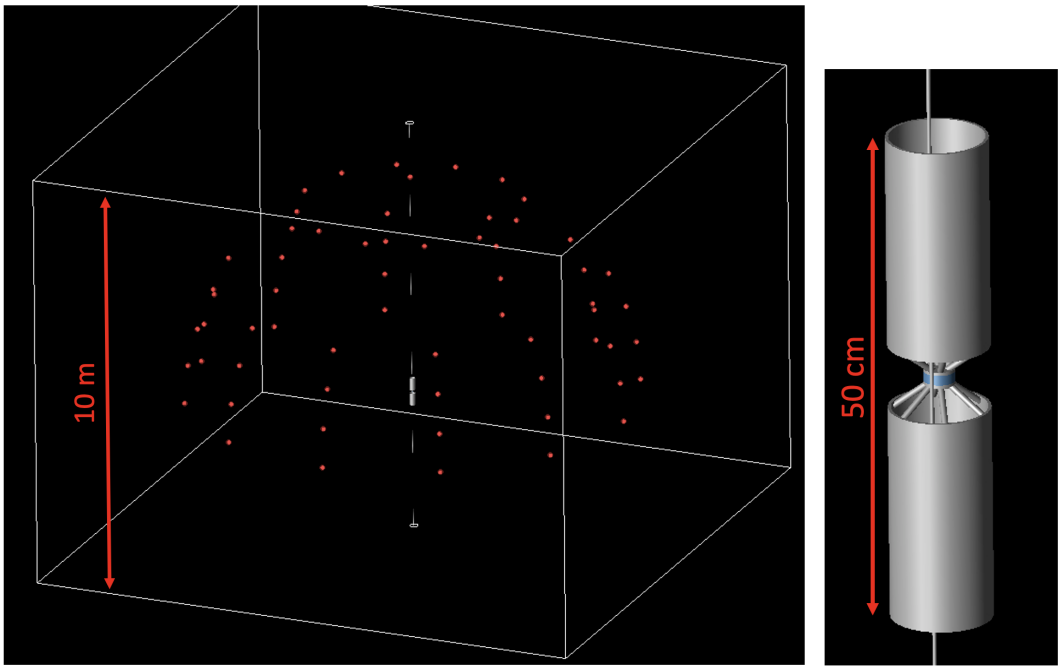

Figure 2.8: **Left:** Simulation Setup, with block of ice, borehole, antenna, and power feedthrough cable. Electric field sensors are highlighted in red.
Right: Zoom-in of VPol antenna.

Components of Simulation

Antenna: The antenna is an idealized version of the real-world antenna. All metal components are set to be perfect conductors, which decreases simulation time due to assuming that fields are exactly zero inside of the metal components. This is a good approximation since aluminum has negligible loss over the distance scales of the VPol.

Feed: The feed is simulated as a simple line of integration connecting the top half to the bottom half of the antenna, as seen in Fig. 2.9. In the context of xFDTD, the line of integration is defined as `Component` under the `Ports` tab in the `Sensors` definitions. The behavior of the `Component` is defined by a `Component Definition`, which can be found under the `Circuit Components` definition. The `Component Definition` is a 50Ω `Voltage Source`, made to

simulate a 50 Ω coaxial cable without any matching networks. The excitation used is the `Automatic` waveform, which is simply a Gaussian pulse meant to approximately stimulate all frequencies of interest given the resolution of the project.

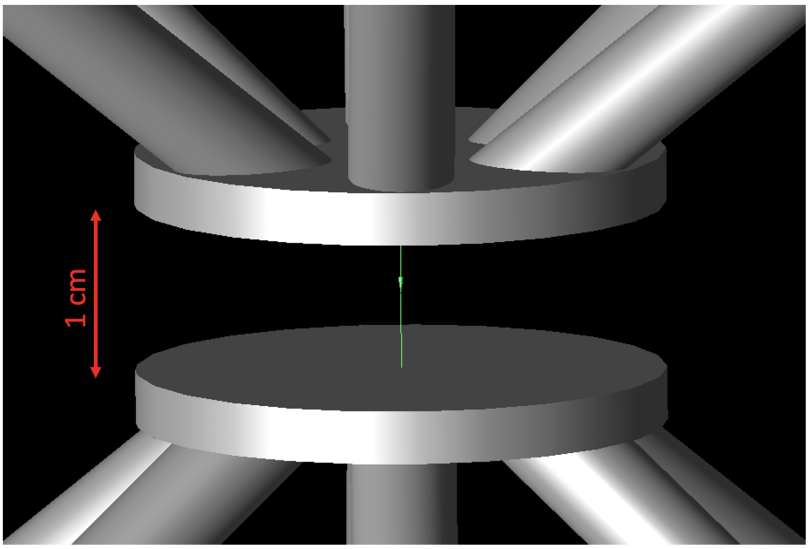

Figure 2.9: The line of integration that makes up the feed component of the VPol antenna.

The simple line of integration is a very good approximation of a full coaxial cable and SMA connector simulation. Removing the small, highly conductive components decreases resolution requirements and greatly decreases simulation time.

To ensure optimal simulation of the feed, the simulation includes two `Fixed Points` of the FDTD grid at the beginning and end of the line of integration of the feed.

Ice & Borehole: The environment of the antenna is approximated as a constant index of refraction block of ice with a cylinder of air to act as the borehole. While the constant index of refraction is a good approximation for deep antennas, such an approach would most likely need to be modified for surface antennas where the index of refraction is changing more rapidly.

Results in Sect.2.5.4 show that the presence of the borehole is essential to accurately capture the response of the antenna. One might be tempted to not include the borehole since all wavelengths of interest will be larger or of order the size of the borehole. However,

interactions at the ice / air interface and matching of the antenna necessitate the inclusion of the borehole.

xFDTD has a native near-to-far propagation calculator, where fields are collected in the near field and propagated using a Green's function to the far field. This cannot be used because it assumes propagation in a vacuum. Instead, the ice block in xFDTD is made large enough to approximately encompass the far field and is instrumented with electric-field sensors at desired angles in the volume. The block of ice will need to be sufficiently large to have electric field sensors approximately in the far field. At 1000 MHz, the Fraunhofer distance is ~ 3 m.

Electric Field Sensors: As discussed in the previous bullet, xFDTD's native far field outputs cannot be used to find the in-ice far electric field. Instead, the ice block is expanded at expense of computational resources and the electric field is read out of the simulation using so-called `Near Field Sensors`. To measure the antenna response as a function of incident angle, near field sensors are placed in even steps of ϕ and θ over a hemisphere of the antenna. For all antenna setups considered, the antenna response is not necessarily azimuthally symmetric but the response is symmetric over $\phi = 90°$.

Power FeedThrough: The N-Type power feed-through cable runs through the inside of each VPol antenna to power the front-end electronics. This large conductive cable will impact the antenna response, including inducing azimuthal asymmetry. xFDTD simulations have shown that the cable raises the band up in frequency and makes realized gain much less flat in frequency. However, in-lab measurements have confirmed ferrite beads on the cable isolate the cable from the antenna. The deployed antennas include the ferrite beads on the power feedthrough and the final simulation results of the VPol and HPol antenna do not include the feedthrough cable.

Simulation Outputs

The outputs of the simulation needed to calculate the VEL, $\boldsymbol{\mathcal{H}}_{rl}$, are:

- Electric Field, $\boldsymbol{\mathcal{E}}$. The electric field as picked out of the simulation at `Near Field Sensors`. This output is a vector quantity in Cartesian coordinates.
- S_{11}. Can be derived from the complex S-Parameters at the antenna feed.
- Voltage, V_{OC}.
- Distance to `Near Field Sensors`, R. Needed to correct for path losses. In my simulation, the radius of the sphere where the points are located is parameterized to the value `points_r`.
- Index of the ice, n. The material index of refraction is also parameterized to the value `n_ice`.

To be explicit, the realized VEL is,

$$\boldsymbol{\mathcal{H}}_{rl}(\omega) = -iR\lambda\boldsymbol{\mathcal{E}}(\omega)\frac{1+S_{11}}{V(\omega)}\frac{Z_L}{Z_0}, \tag{2.8}$$

where V is the Voltage at the feed as measured by xFDTD, S_{11} is the complex S-parameter as measured by xFDTD, $\boldsymbol{\mathcal{E}}$ is the vector value of the electric field from a `Near Field Sensor`, and R is the distance to the near field sensors as defined by `points_r`. Z_L is the impedance of the transmission line, 50 Ω, and Z_0 is the impedance of free space, $\sim 120\pi$ Ω. The realized gain is then,

$$G_{rl}(\omega) = 4\pi\left|\frac{f}{c}\boldsymbol{\mathcal{H}}_{rl}(\omega)\right|^2 n\frac{Z_0}{Z_L}, \tag{2.9}$$

where n is the index of the ice as defined by `n_ice`.

The realized VEL is best represented in spherical coordinates. To calculate a spherical coordinate VEL, the electric field vector needs to be transformed from Cartesian to spherical coordinates. In the true far field, the r component of the spherical electric field will go to zero. Since we are forced to use electric field sensors in the approximate far field, there remains a small but non-zero r component of the electric field. For all angular points, this r component is > 20 dB down in power from the other angular components, making it a fair approximation to set the r component to exactly zero.

2.5.3 Design Requirements

The design requirements of the VPol are defined by their constrained environment in the borehole, frequency content of Askaryan emission, station triggering, and neutrino vertex distribution within the ice. As the antennas are stationed in a borehole and used for an interferometric phased array trigger, they are constrained radially by the borehole diameter, 11.2", and length-wise by resolution requirements of the phased array trigger, ~ 1 m.

Askaryan radiation is expected to be brighter at lower frequencies, making a longer antenna favored. However, the VPol needs to be broadband for direction and energy reconstruction. A longer antenna needs to be wider to meet broadband requirements (a broadband antenna is a bicone while a single frequency antenna is a simple dipole). There is an ill-defined optimization problem between length and bandwidth.

To optimize for detector volume, the antennas need to have azimuthal symmetry (omnidirectional in the polar direction) and with maximum gain at boresight (90° in zenith). The zenith requirement is due to the angular distribution of neutrino events: more ice is visible radially than straight down and events are bent by the changing of the index of the firn towards boresight so the majority of neutrino events arrive at the antenna between 30° above and below the horizon.

Due to the size of the array, harsh conditions during deployment, and issues reported

by the ARA detector with antenna-to-antenna variations [41], the VPol must be robust and simple to manufacture.

To meet all requirements, a fat dipole with a biconical feed design was chosen. The antenna is made from stock aluminum materials and easy-to-machine shapes such as those made on a water-jet CNC machine. The final design takes inspiration from the GNO experiment [63] and RICE experiment [176] antenna designs.

2.5.4 VPol Antenna, V1

Initial deployment in Summer 2020 called for boreholes with a diameter of $5.75''$ created by an auger drill called the ASIG drill. With that diameter in mind, the VPol was initially designed to be $4''$ in diameter. This size was a compromise between antenna bandwidth (the wider the antenna, the closer it is to a bicone instead of a dipole, thus more broadband) while still being easy to deploy (a wider antenna has a higher chance of snagging on the borehole wall, creating many deployment logistics issues). As well, $4''$ aluminum tube stock is readily available.

After the delayed season due to COVID-19, a new drill technology was picked for Summer 2021 based on an auger design created by the British Antarctic Survey (BAS). The new drill creates an $11.2''$ diameter borehole, allowing for a wider VPol. The second version of the VPol (called VPol V2) uses $5''$ diameter aluminum stock and a slightly redesigned feed. A discussion of the final design that was mass produced for the Summer 2021 season can be found in Sect. 2.5.5.

While the final design for the VPol uses larger stock and a larger borehole, the initial designs and simulations using the smaller design and borehole are still illustrative as verification of simulation performance and general behavior of antennas both in air and in ice. For this reason, results for VPol V1 are documented below.

Prototypes

There were two physical prototypes produced at the early stages of VPol development, seen in Fig. 2.10. Each is of maximal length (1 m) and diameter (at the time, $4''$) of the physical constraints of the borehole. The simulation software HFSS was used to optimize the design of the feed to match the 50 Ω transmission line. The length of the antenna was maximized because HFSS simulations erroneously suggested that that an antenna of maximal length would still have $\sim$ 400 MHz of bandwidth while deployed in an ice borehole. Time domain simulations in xFDTD (and now *in situ* measurements at Summit Station) have shown that HFSS, a method of moments simulator without the ability to change the material properties of the far field, cannot realistically simulate the in-ice antenna response. Regardless of the flaws in the motivating in-ice simulations, the in-air simulations are still useful.

One of the prototypes had an asymmetric feed, as can be seen in Fig. 2.10. The asymmetry improves the antenna's match to 50 Ω while creating asymmetry in the zenith beam pattern. The original motivation of the asymmetry was to create an antenna that has a beam pattern that is better matched to the expected arrival distribution of neutrino events. While most signals arrive within 30° above and below the horizon, more signals are expected to arrive from below than from above due to the large ice volume below the detector and the relatively small number of events that will have a refracted signal. This design was shelved due to fear of modeling the more complicated beam pattern. The improvement that such an asymmetric antenna can bring to a detector's effective volume remains to be seen. This can be quantified using a neutrino detector simulation software package such as NuRadioMC, which was unavailable at the time of initial prototyping. I include measurements of the beam pattern in Fig. 2.12.

The initial prototype data is most useful in verifying the in-air gain of the antenna and comparing the result against simulation. A system diagram of the in-air gain measurement can be seen in Fig. 2.11. The beam pattern measurements were performed in a large cargo

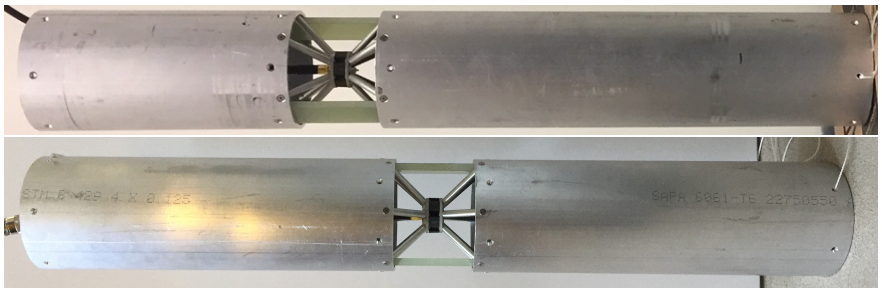

Figure 2.10: Prototype VPol antennas. Note that the top image shows an antenna with a asymmetric feed, used to increase antenna match and point antenna gain downward. The bottom image shows a symmetric feed, which is the design used for the deployed VPol antennas.

bay. A directional horn antenna from the ANITA experiment was used to broadcast an impulse at the VPol prototype. The impulse was generated by an Avtech pulse generator, and was O(1 ns) in duration, ensuring that it was a broadband pulse up to 1 GHz. The feed of the prototype was connected to an 2 GHz-bandwidth Tektronix MSO5204B oscilloscope. The oscilloscope was triggered by the `TRG OUT` of the Avtech pulse generator, which was self-triggering at 1 kHz. Data was collected in runs of the average of 1,000 triggers. The prototype was on a swivel so that it could be rotated 10° between runs. The impulse response of the antenna was derived from deconvolving the horn antenna impulse response, signal pulse generator shape, and path loss from the saved data runs for each angle. The environment was very reflective, requiring the time selection of the initial pulse and the potential of unknown systematic biases in the final result. The results for the asymmetric and symmetric antennas are plotted in Fig. 2.12 and Fig. 2.13 respectively.

To date, these prototypes are the only VPol designs with a full beam pattern measurement, albeit a relatively rough measurement. The final designs of the VPol antenna are being verified *in situ* at Summit Station and there are plans for full anechoic chamber measurements. The relatively simple design of the antenna and the promising results from measurements of the prototypes give us confidence in the simulation results and dropped the priority of the full measurement over commissioning of other RNO-G systems.

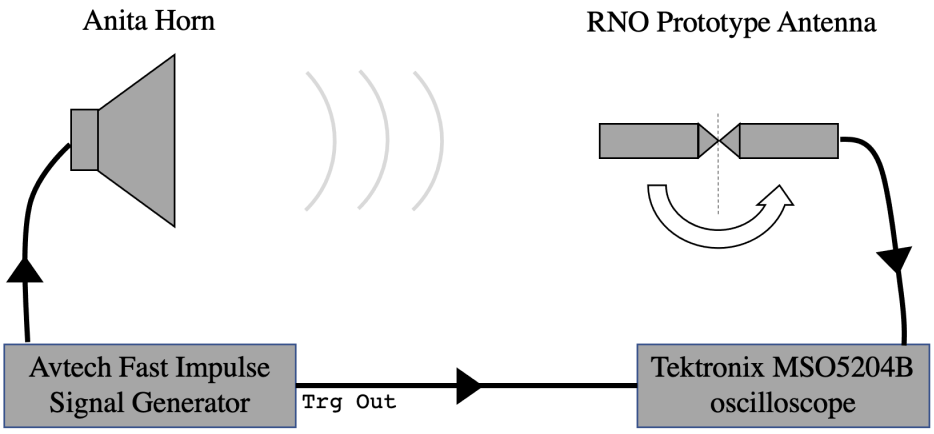

Figure 2.11: Diagram of the beam pattern measurement of the VPol prototype antennas. The measurement was performed in a cargo loading bay, resulting in potential systematic biases in the final measurement from reflections.

Settled Design & Machining

After the prototyping phase and the transition to xFDTD to simulate the antenna, the design of VPol V1 was finalized. The final dimensions of the antenna were chosen to optimize bandwidth and gain band flatness. It was found that, due to the air-ice interface at the borehole, there is focusing of the beam pattern at boresight for higher frequency (as seen in 2.15). This can be cancelled out by making the VPol longer since a longer VPol has worse high-frequency response. The two effects cancel and lead to a relatively flat gain at approximately $20''$ in length for a $4''$ diameter antenna in a $5.75''$ diameter borehole. The feed opening angle was then optimized for minimized VSWR while embedded in ice.

The schematic of finalized design of the VPol V1 can be seen in Fig. 2.14.

This design was mass produced for the scheduled first year of deployment. 80 antennas were ordered and approximately half were assembled before COVID-19 shut down operations. Parts were ordered from B.A.P. Enterprises, Inc. for long-lead time items, Zero Hour Parts for small and fast turn around rates, and FedTech for parts that could be waterjet machined.

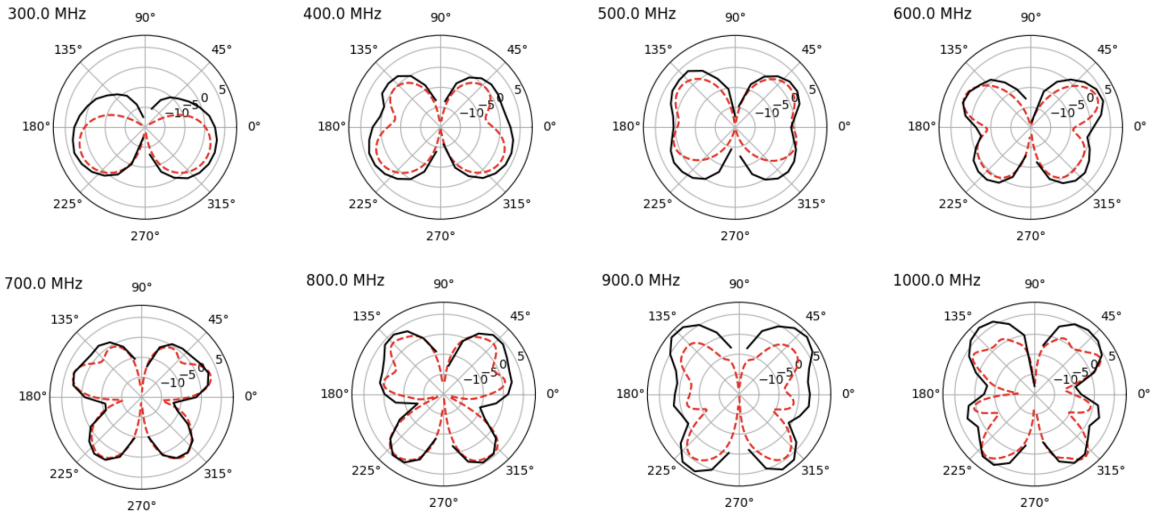

Figure 2.12: Gain pattern of the asymmetric prototype antenna. Black is data and dashed red is HFSS simulation. While not plotted here, the in-air HFSS simulation results are very similar to xFDTD results, the simulation packaged used for the current antenna design. Differences between data and simulation are due to the reflective environment used during data collection and imprecision in the measured zenith angle.

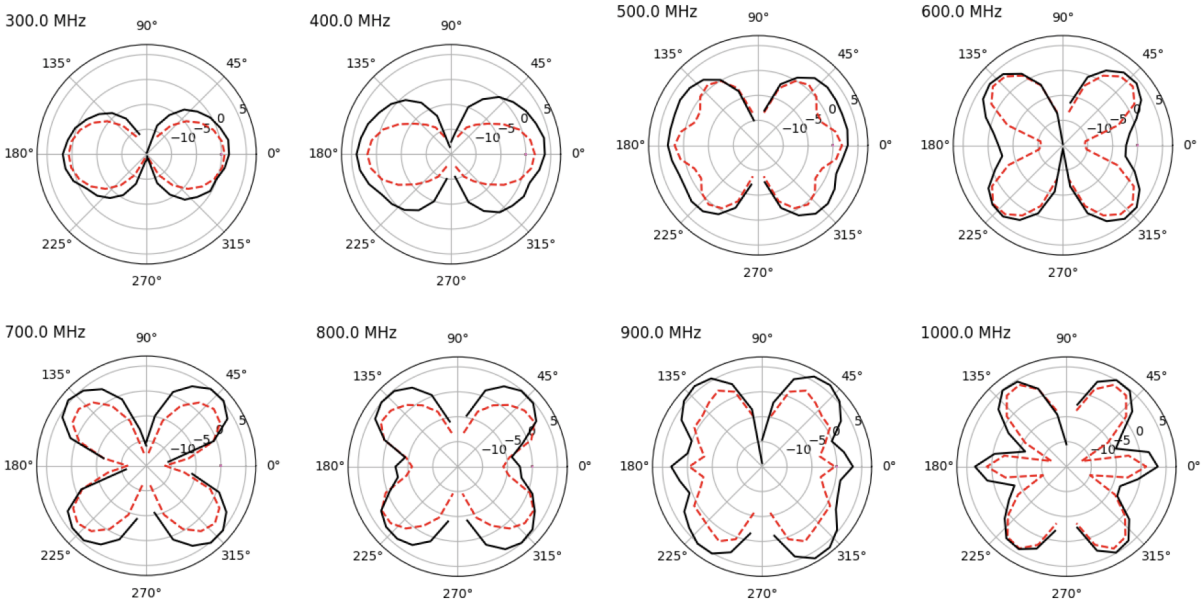

Figure 2.13: Gain pattern of the symmetric prototype antenna. Black is data and dashed red is simulation. While not plotted here, the in-air HFSS simulation results are very similar to xFDTD results, the simulation packaged used for the current antenna design. Differences between data and simulation are due to the reflective environment used during data collection and imprecision in the measured zenith angle.

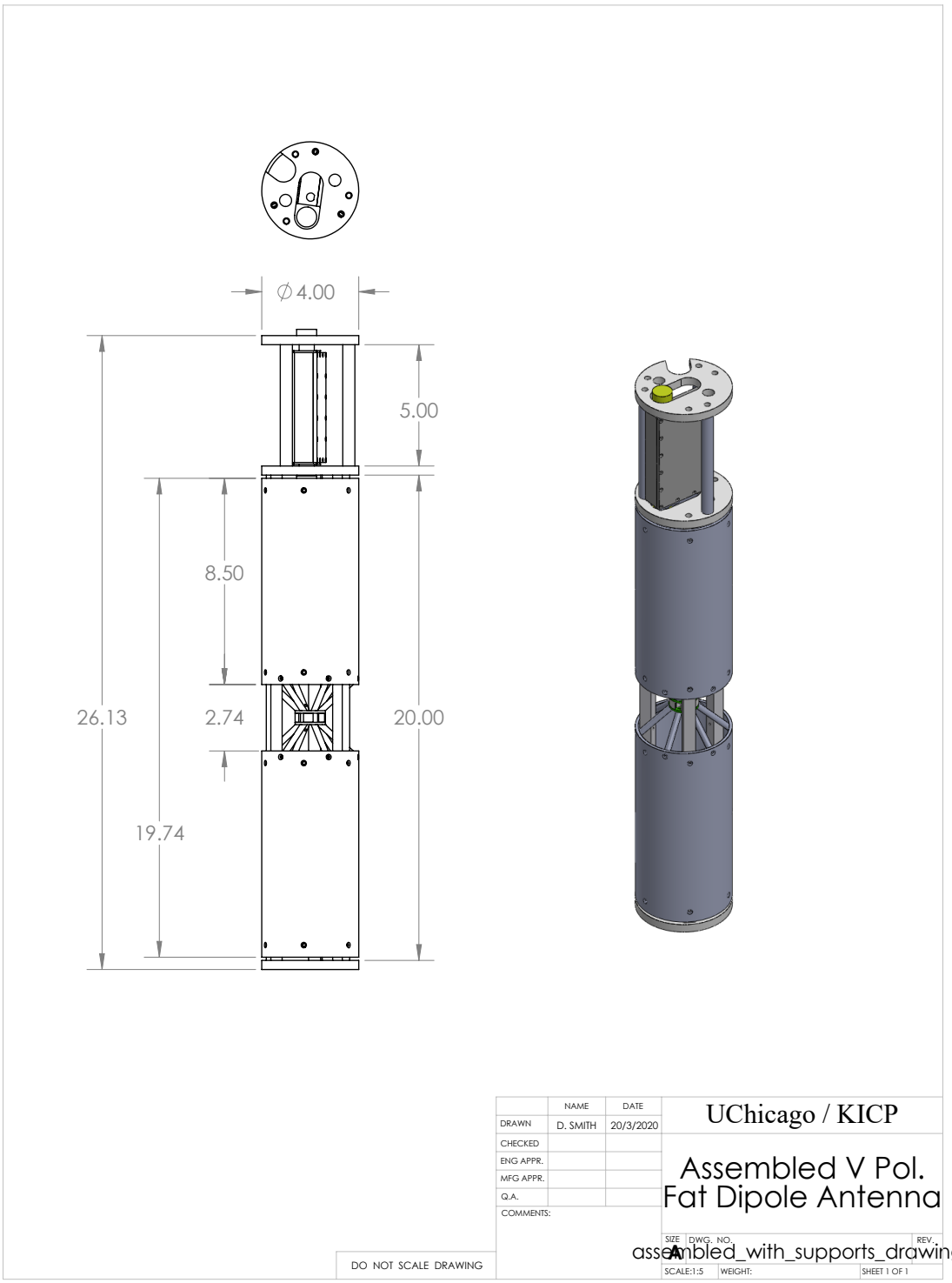

Figure 2.14: Schematic of the assembled finalized design of the VPol V1, including the front-end amplifier.

Borehole Radius

With the change in drill type, RNO-G was tasked with determining how the borehole radius impacts antenna response. The VPol V1 was simulated in xFDTD using different size boreholes to determine the overall change to the realized gain of the antenna. The results of the simulation can be seen in Fig. 2.15 and Fig. 2.16. There is a transition in bandwidth between frozen-in and in-air simulations with larger borehole radius. Notably, this means that a wider borehole will result in an increase in the low frequency turn-on, losing bandwidth that are essential for triggering and detector effective volume. For this reason, the second iteration of the VPol is longer to compensate for the change in turn-on frequency and wider to compensate for lost bandwidth from the longer antenna. For a 11.2″ borehole, the VPol needs to be 1.3 times longer, or 65 cm long, to have the same high-pass frequency as the original VPol in a 5.75″ borehole, as can be seen in Fig. 2.16.

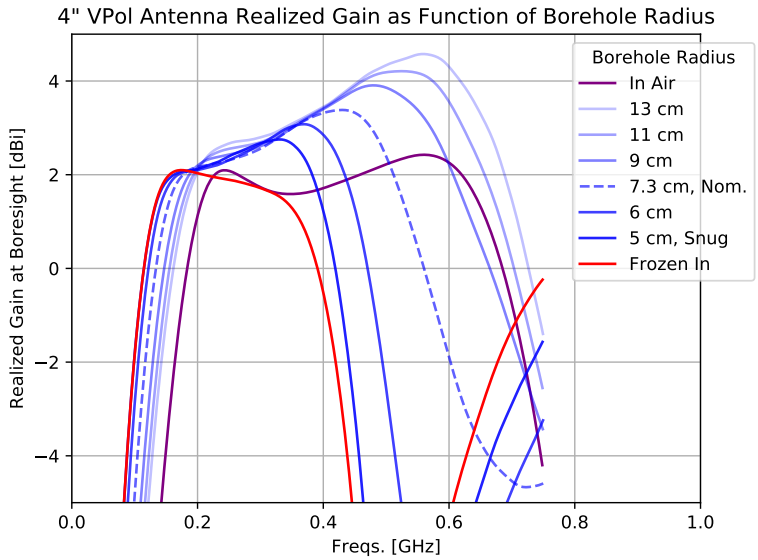

Figure 2.15: Broadsight Realized Gain for different values of borehole radius. Results are for a VPol V1 antenna, and simulations are performed in xFDTD. Results plotted include an antenna frozen in ice (red), in air (purple), and an antenna in an ice borehole with changing diameters (blue). The dashed blue line denotes the 'nominal' borehole from the 2020 season at 5.75″.

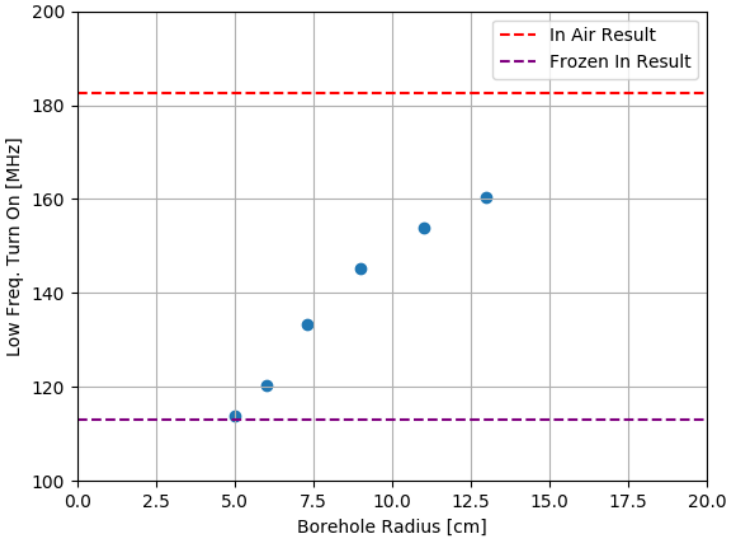

Figure 2.16: Frequency at which realized gain at boresight crosses 0 dBi. Results are for a VPol V1 antenna, and simulations were performed in xFDTD.

Centering Study

Any displacement of the antenna from the center of the borehole will induce azimuthal asymmetry, an asymmetry that would be very difficult to calibrate. Any azimuthal asymmetry will create an uncertainty in the reconstruction of electric field and thus energy and direction of a neutrino event. Depending on the magnitude of this effect and the ability to remove the uncertainty through detailed *in situ* calibrations, asymmetry from a displaced antenna may represent the dominant uncertainty for electric field reconstruction for RNO-G and future radio neutrino detectors.

To study this, I ran simulations using the original $5.75''$ borehole and VPol V1 with two separate displacements from center: $0.4375''$ displacement, with the antenna half way between the center and the borehole wall, and $0.875''$ displacement, with the antenna resting on the wall. The results can be seen in Fig. 2.17. There is a transition from in-ice-like to more in-air-like at higher frequencies, with the realized gain in the direction of the displacement looking more like it is frozen in ice and the realized gain in the direction opposite of the

displacement looking more like it is in air. This makes intuitive sense, as there is more or less air between the antenna and the borehole depending on the viewing angle from the displacement, resulting in worse or better coupling to the ice.

To counter-act the uncertainty generated from an uncentered antenna, a support structure was added to the design of VPol V2 that has a wider radius than the antenna itself. The structure acts as a standoff from the wall, reducing the possible absolute offset from center by about half. A perfectly snug fit is not possible due to the potential of the antenna becoming stuck in the borehole during deployment. For the second season of deployment, a spring system is being tested that has the potential to reduce the offset from the center (and thus reduce the induced electric field uncertainty) further.

The best solution to remove the uncertainty from an uncentered antenna would be to backfill the borehole with water, freezing the antennas in place and removing the ice / air interface. Freezing the antenna would also greatly simplify antenna simulations and modeling. Such a plan would require extensive testing of the antennas and front end electronics to confirm that they would no be destroyed during the freezing process. For this reason, backfilling will not be performed in RNO-G, but remains a possibility for IceCube-Gen2 Radio.

2.5.5 VPol Antenna, V2

The design of the VPol V2 can be seen in Figs. 2.18 and 2.6. Schematics for all components of the VPol V2 are available on GitHub[1]. The simulated results of the antenna effective height are plotted in Figs. 2.19 and 2.20, for the θ and ϕ effective height respectively. The bands in the figures represent the maximum and minimum effective height of the antenna given a maximal offset from the center of the borehole, where the antenna offsets are touching the wall. The bands do not represent a standard deviation. It is interesting to note the VPol

1. `https://github.com/dansmithphysics/rnog_vpol_fat_dipole`

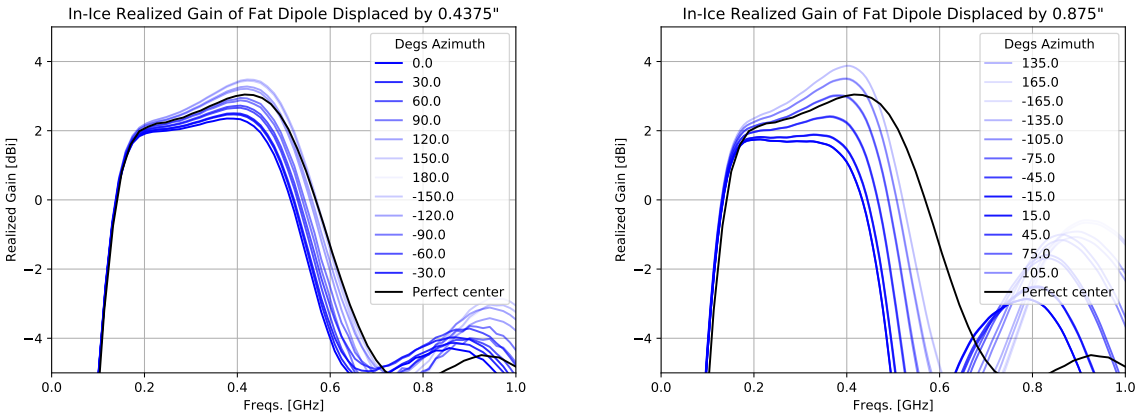

Figure 2.17: Results of a VPol V1 in a 5.75″ diameter borehole, displaced from the center of the borehole in the $\theta = 0°$ direction. **Left:** Realized gain for different azimuth directions for an antenna displaced by 0.4375″, or half way to a 5.75″ diameter borehole wall. **Right:** The same as the left but displaced 0.875″, all the way to the borehole wall.

ϕ dependence: an antenna offset from the center of the borehole can have significantly larger cross-polarization response. If physical, this strong response may be used to calibrate the position of an antenna within a borehole, reducing systematic uncertainties and systematic biases via calibration.

2.5.6 Machining and Mass Production

For the Summer 2021 deployment season, 150 VPol V2 antennas were ordered and assembled (shown in Fig. 2.22), 145 of which were shipped to Summit Station. Parts were ordered from B.A.P. Enterprises, Inc. for long-lead time items, Zero Hour Parts for small and fast turn around rates, and FedTech for parts that could be waterjet machined.

Before deployment, a VSWR measurement was taken for all 145 assembled antennas as a pass-fail test. Those measurements for the antennas deployed are plotted in Fig. 2.21. Out of the 145 tested antennas, one failed, which was the first antenna assembled. The failure was due to a lack of electrical connection between the two halves of the antenna at the feed. The two halves are connected by a copper wire soldered to the SMA connector. This solder

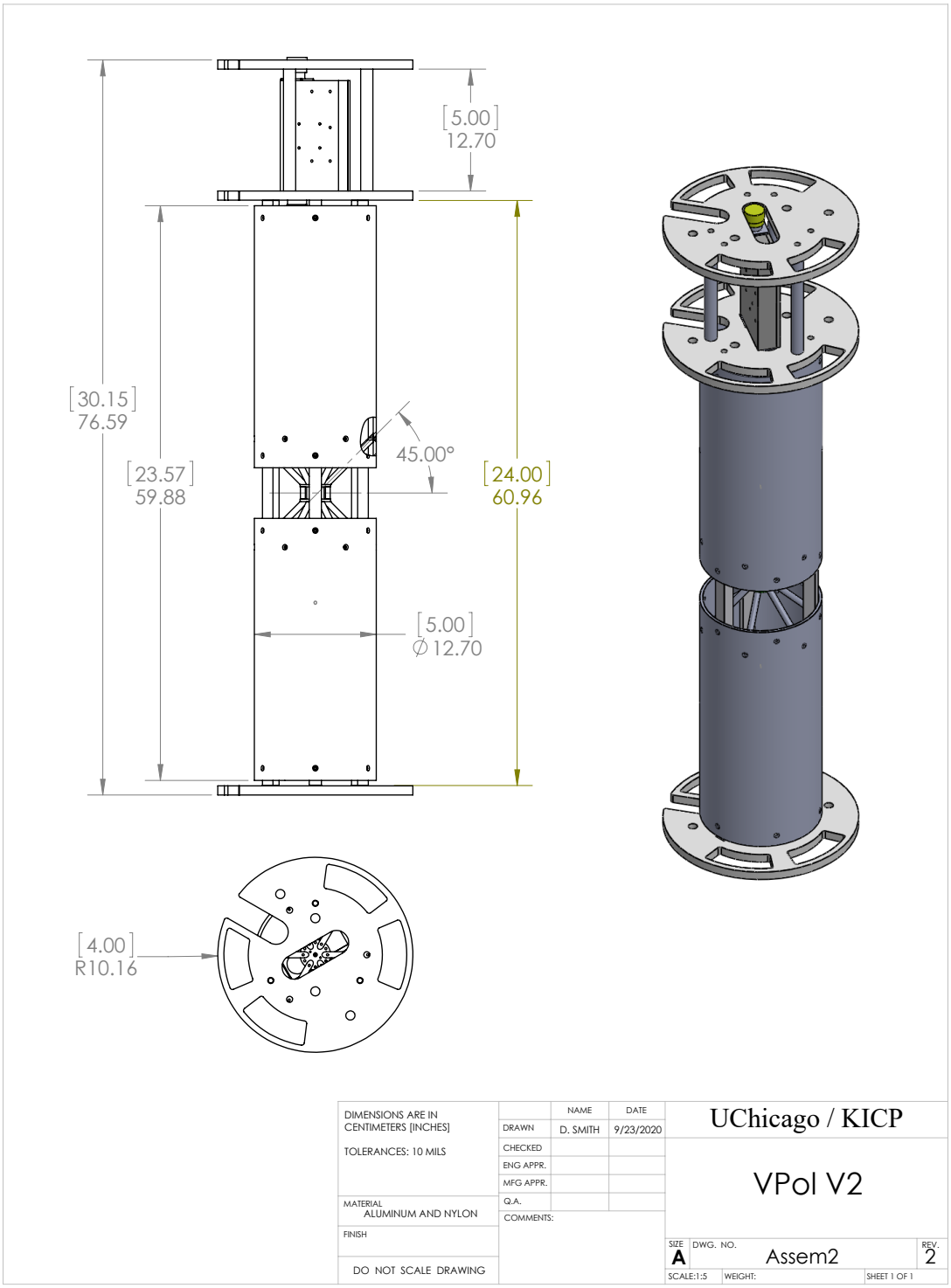

Figure 2.18: Schematic of the assembled finalized design of the VPol V2, including the front-end amplifier and standoffs.

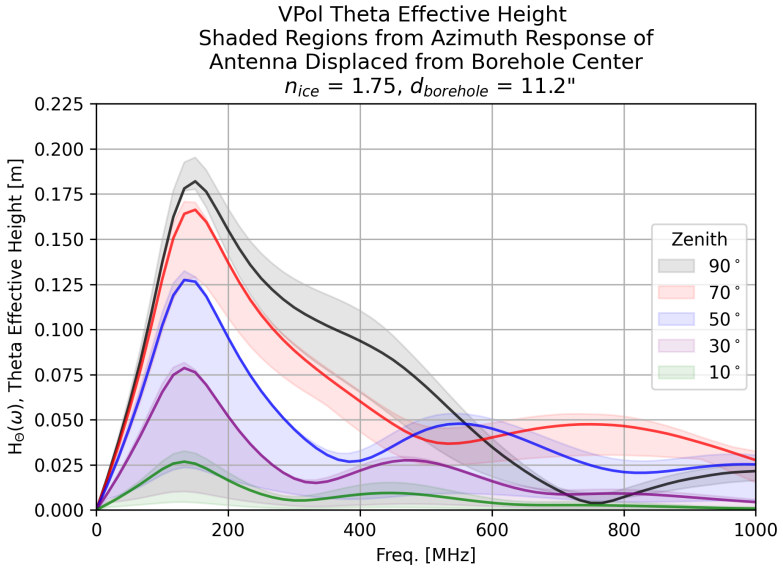

Figure 2.19: In-Ice Effective Height of θ result from VPol V2 from xFDTD. Shaded region from range of values allowed from the azimuth dependency of the antenna when displaced from the center of the borehole.

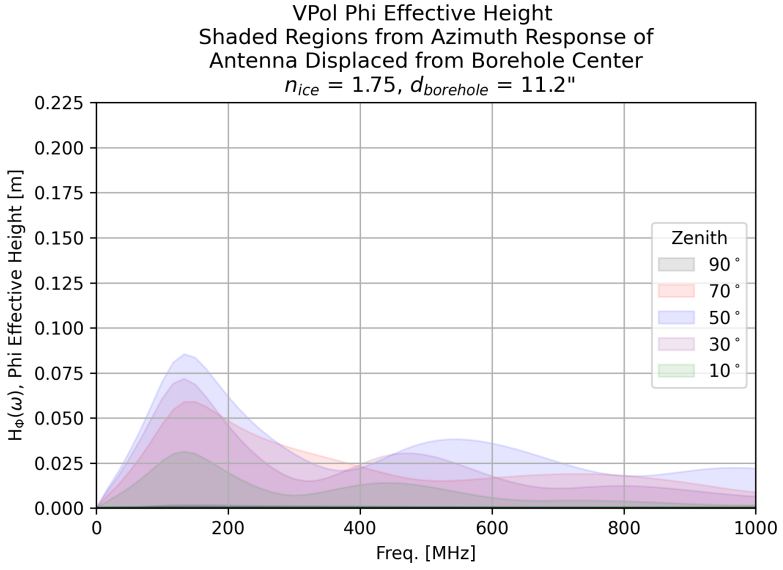

Figure 2.20: In-Ice Effective Height of ϕ result from VPol V2 from xFDTD. Shaded region from range of values allowed from the azimuth dependency of the antenna when displaced from the center of the borehole. It is interesting to note that the ϕ dependency of the antenna in the center of the borehole is near zero but much higher for a displaced antenna.

point is the most likely failure point for the VPol antenna. After assembly, there is no stress on the solder point itself, so the failure was due to a weak solder joint that broke during assembly. This solder joint could be improved or replaced in future iterations of the antenna to improve the robustness of the design.

Assembly time, not including the front-end amplifier, was $\sim$ 90 hours for the 150 antennas assembled, or $\sim$ 40 minutes per antenna. The time to perform the VSWR measurement was $\sim$ 5 minutes per antenna.

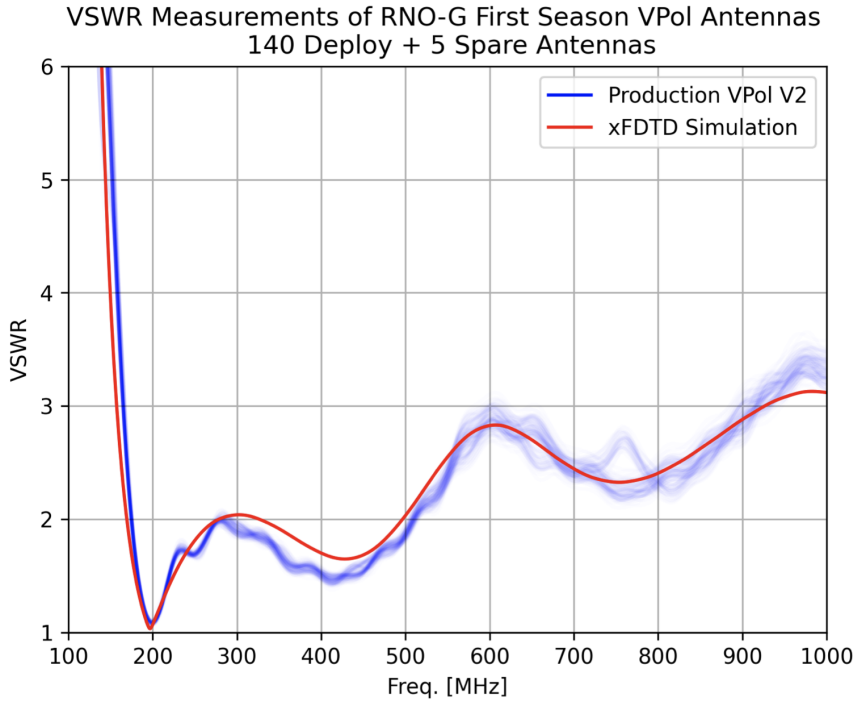

Figure 2.21: In-Air VSWR for the VPol V2. xFDTD simulated results are red. 145 assembled VPol antennas that were deployed to Summit Station in Summer 2021 are in blue.

Preliminary *In-situ* Studies

After deployment in Summer 2021, calibration data for each station was collected, including data from the two deep calibration pulsers (described in Sect. 2.11). These pulsers represent an optimal calibration source for gain measurements since their pulse shape has been mea-

Figure 2.22: Picture of the 145 VPol V2 antennas assembled before shipment to Summit Station.

sured and the transmitting antenna is a VPol V2, allowing for a classic two antenna gain calibration, as described in [115].

There are caveats preventing a quick *in situ* calibration. The front-end amplifier, RFoF, and digitizer board all have behavior different from what was expected from in-lab studies. There are large channel-to-channel variations and digitizer effects (discussed in Sect. 2.5.6 and 2.6) that first need to be understood and measured before an antenna calibration study can be performed in earnest.

With all caveats in mind, I perform a preliminary analysis of the in-ice response of the

VPol V2 compared with simulation. I neglect digitizer effects. To correct for amplitude variations between channels, I normalize data to simulation within the frequency range 200–400 MHz. To avoid deconvolutions of the data, I manipulate the simulation to approximate the data. The simulated in-ice antenna responses are convolved with the *in situ* calibration pulse shape, front-end amplifier response, path-loss corrections, and with itself to capture the full chain of Pulser → Transmitting Antenna → Geometric Path Loss → Receiving Antenna → Front-end Amplifiers.

The result of the preliminary comparison for Station 21 is plotted in Fig. 2.23, generated from the data plotted in Fig. 2.38. The boresight agreement is good up to 400 MHz. The divergence at higher frequency may be due to an offset of the antenna from the borehole center. The agreement remains relatively the same for steeper zenith angles, with the exception of a growing discrepancy of the high-pass frequency, with data having a lower frequency turn-on than simulation. This divergence may be due to the front-end amplifiers: the amplifiers have an out-of-band ripple that causes power below the low-pass filter of the amplifier, as discussed in Sect. 2.6.

While much work remains to be done, this is promising evidence that design goals of the VPol antenna have been met. The bandwidth of the antennas matches expectation from xFDTD simulations and the complicated behavior of an in-ice and in-borehole antenna seems to be approximately captured by the simulations. The robustness and antenna-to-antenna reproducibility goals have also been met: all deployed antennas in Summer 2021 (39 in total) survived shipment and deployment and have visibly similar impulse responses.

2.6 Radio Frequency (RF) Signal Chain

The RF signal chain takes two forms, one each for the deep and surface antennas.

For surface antennas, RF is fed over $\sim$ 20 m coaxial cables to custom, low-power and low-noise amplifiers (LNAs) on the so-called `SURFACE` boards that are deployed inside of the

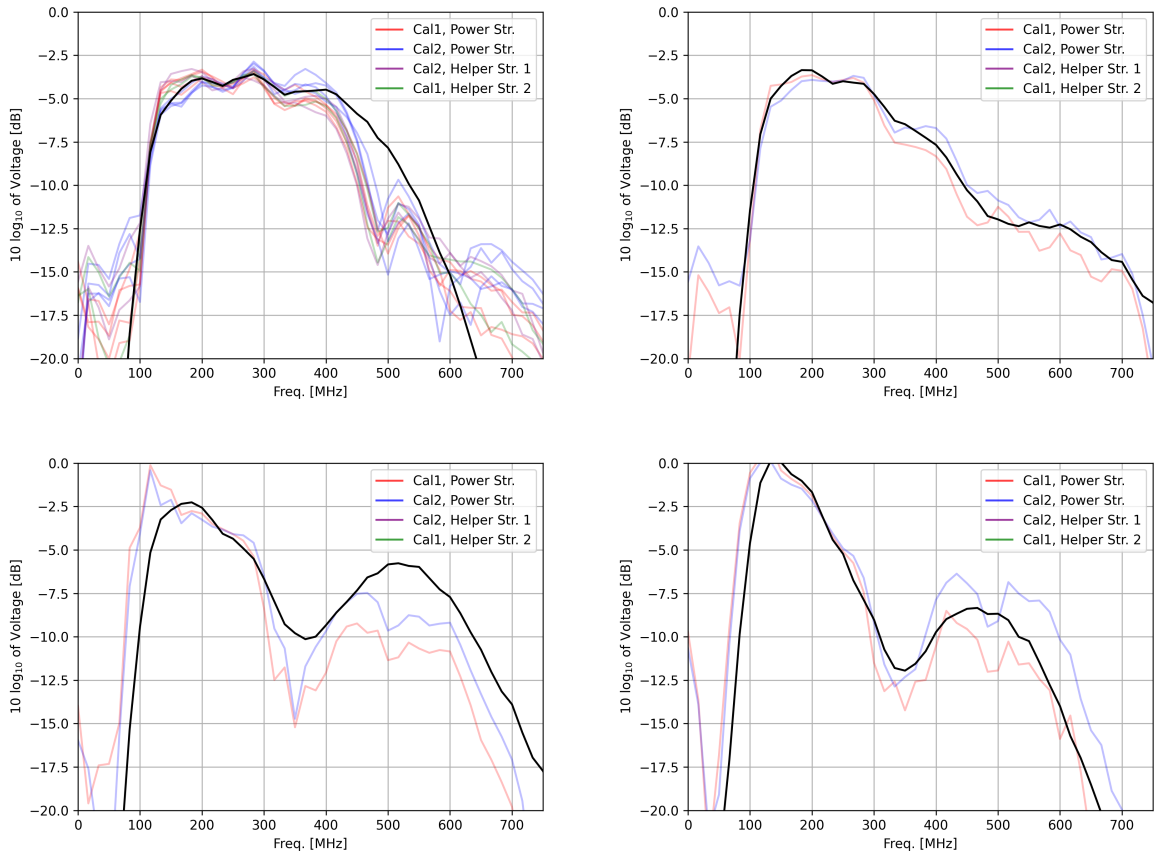

Figure 2.23: *In situ* calibration pulser data (in red, blue, purple and green) plotted against simulation manipulated to approximately match the data signal (in black). Data taken Summer 2021 for Station 21. **Top Left:** The boresight responses for the 6×2 different combinations of receiving and transmitting VPols. **Top right:** The response at Channel 5, $\sim 45^\circ$ elevation arrival angle. **Bottom left:** The response at Channel 6, $\sim 25^\circ$ elevation arrival angle. **Bottom right:** The response at Channel 7, $\sim 18^\circ$ elevation arrival angle.

DAQ environmental enclosure. The signals are amplified by ∼60 dBm before being fed into the digitizer and surface trigger on the `RADIANT` board (Sect. 2.8). The `SURFACE` board has a bandwidth, defined as the frequencies with a gain > 55 dB, of 80–750 MHz. Two `SURFACE` boards, each with five channels, are deployed in each station to amplify the signals from the nine surface LPDA antennas. The remaining channel is a spare in the case one of the other nine channels fails. A digital render of the `SURFACE` board and gain of the electronics channel are shown in Fig. 2.24.

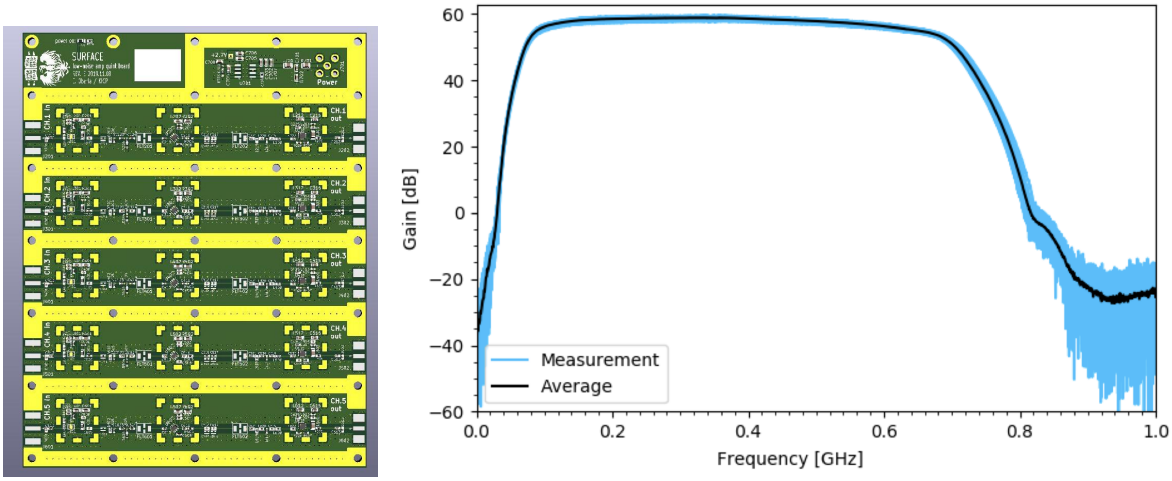

Figure 2.24: The SURFACE amplification board, used for surface channels in each station. **Left:** Digital render of the SURFACE before being populated and shown without its RF enclosure and shields. **Right:** The gain of the system for all 100 channels tested for Summer 2021 deployment as measured by Nora Feigl and the Erlangen group [117]. There is a measured 10% variation from the mean.

For deep antennas, RF is fed directly into an LNA and RF-over-fiber optical transmitter (RFoF) (on the IGLU board) that is co-deployed in the borehole with each antenna. The now optical signals travel ∼120 m in a fiber optic cable before entering an optical receiver. The RFoF receiver, within the DAQ environmental enclosure on the so-called DRAB board, converts the signal back to analog and amplifies it again before inserting the signal into the digitizer board (Sect. 2.8) and low-threshold triggering FLOWER board (Sect. 2.9). RF from the deep component has a total of ∼55 dBm amplification before the digitizer. The combined IGLU and DRAB chain has a bandwidth, defined as the frequencies with a gain $>$ 50 dB, of 120–550 MHz, a narrower range to better match the high pass frequency of downhole antennas. Four DRAB boards, each with four channels, are deployed in each station to amplify the signals from the 15 deep antennas. The remaining channel is a spare in the case one of the other 15 channels fails. 15 IGLU boards are deployed in each station, one for each deep VPol and HPol antenna deployed. A digital render of of the DRAB board and gain of the electronics channel are shown in Fig. 2.24. An image of the IGLU board is shown in

Fig. 2.26.

The RFoF system removes the need for deploying coaxial cables down to each antenna, which minimizes weight and amount of dielectric material running through upper antennas while minimizing noise temperature (< 150 K). The front-end LNA and RFoF system on the IGLU boards were developed in-house to optimize for noise figure and power, with the final design consuming ~ 140 mW per channel.

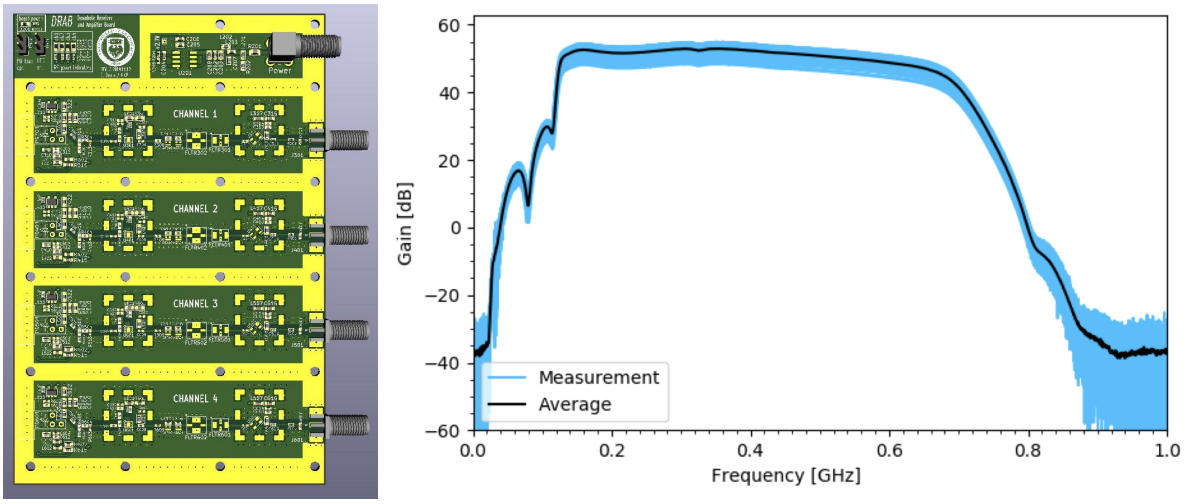

Figure 2.25: The DRAB amplification board, used as the receiver for deep channels in each station. **Left:** Digital render of the DRAB before being populated and shown without its RF enclosure. **Right:** The gain of the DRAB & IGLU chain for all 150 channels tested for Summer 2021 deployment as measured by Nora Feigl and the Erlangen group [117]. There is 20% variation from the mean as measured in the lab, and significantly larger variation measured in the field.

The custom RFoF system required extensive prototyping to meet low-power, low-noise figure, and bandwidth requirements. Iterations of the design included different laser types, laser matching networks, and front-end amplifiers. Plotted in Fig. 2.27 is the result of one such board iteration, showing temperature tests on Rev. G IGLU with different two types of lasers. The production version for Summer 2021, plotted *en masse* for all deployed IGLU boards in Fig. 2.25, has issues that required repair in the field and modifications to the design for future years. At borehole temperatures ($-40°$C), a reflection between the front-end amplifier and laser causes a large 30 MHz oscillatory mode in the channel, swamping

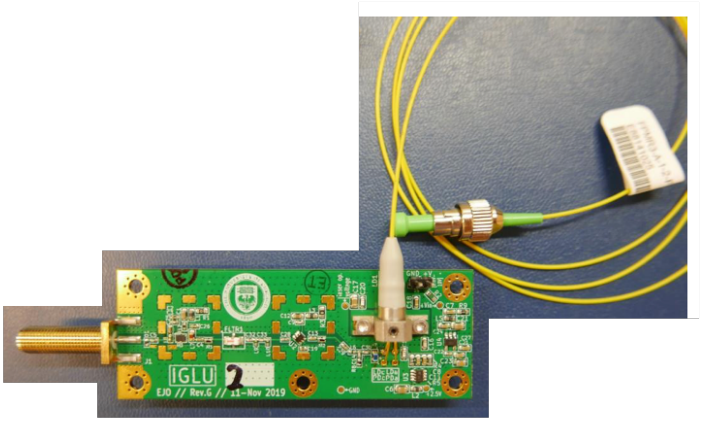

Figure 2.26: An image of a Rev. G `IGLU` front-end amplifier and RFoF transmitter for the deep science antennas. Note that the board is shown without its RF enclosure or surface-mount RF shields attached.

any signal and rendering the channel useless. This was repaired in the field by adding an attenuator after the amplifier, cutting down any reflections. There is also insufficient high pass filtering resulting in 'spurs' in the data at low frequency, as can be seen in Fig. 2.25 below 100 MHz. There are also large, ~ 4 dB channel-to-channel gain variance due to a yet-unknown reason. The most likely culprit is the fiber-to-fiber connectors in the RFoF system, which have been shown to have inconsistent S_{21}. As of Winter 2022, studies and calibration are forthcoming to diagnose and mend this issue for future seasons. While increasing electric field reconstruction uncertainty, the channel-to-channel variations do not significantly impact the over-all sensitivity of the detector.

2.7 Power and Communication Systems

The detector will be composed of 35 autonomous stations deployed in a grid. Each station must operate autonomously: Summit Station cannot logistically support cabling each station together for power and data transfer.

For power, each station is equipped with two solar panels with a total power output of

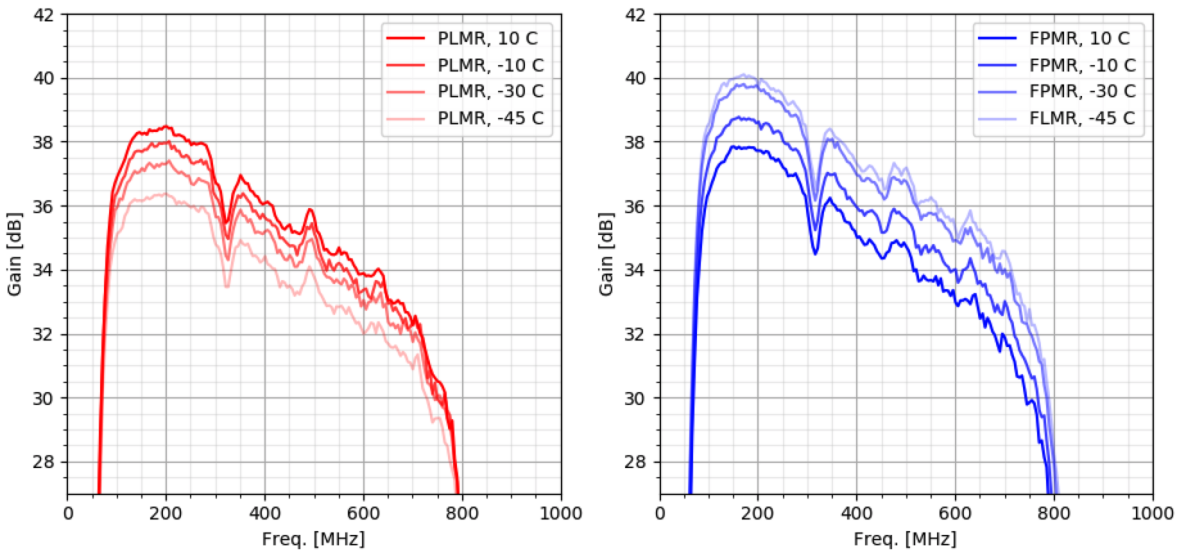

Figure 2.27: Temperature tests of the Rev. G `IGLU` board with two different laser types. Note the opposite slope between gain vs. temperature for each laser. Note one front-end amplifier is missing from this measurement setup to reduce variables in the measurement, resulting in significantly reduced system gain. The sharp dip at 300 MHz was due to a poorly matched filter which was repaired for the production version of the amplifier.

300 W and a 5 kWh sealed lead-acid battery bank. A wind power system is being developed to produce power for the stations during the winter months and may be deployed in a future season. Wireless communication is performed using two systems: a LoRAWAN and LTE network. LoRAWAN is an ultra-low power system for slow control and housekeeping data during the winter season. Commercial LTE offers high data bandwidth over large distances at the expense of power and is used for data telemetry to a server at Summit Station. Commercial LTE can only be used during the Summer, when stations are producing sufficient power.

The stations operate on three energy modes to optimize scientific up-time and detector longevity. Due to the lack of sun during arctic winter and before wind turbine deployment, stations will be left in a minimum low-power mode during the winter (∼30% of the year), with the only system online being an on-board micro-controller sending housekeeping data over LoRAWAN. During the time before and after the winter, called the 'shoulder seasons,'

the stations will be set to a low-power mode where thermal trigger rates and data transfer are minimized to extend the productive up-time of the station. During the arctic summer, each station produces surplus power and can operate at high thermal trigger rates (10 Hz) and can operate over LTE continuously. During summer operation mode, each station has a power budget of ∼25 W.

2.8 Digitizer

Due to the specific power constraints of RNO-G, digitization of antenna signals is performed on an in-house developed board, the RAdio DIgitizer and Auxiliary Neutrino Trigger (`RADIANT`) board. The `RADIANT` is a 24 channel board that uses the LAB4D, a custom ASIC that is a single channel, switched-capacitor array with 12-bit sampling [217]. For the purposes of RNO-G, the LAB4Ds are operated at 3.2 GSa/s with two buffers of 2048 samples each, giving a total 1280 ns recorded window per channel. An example digitized trace from a generated fast impulse passed through the signal chain can be see in Fig. 2.28.

The LAB4D ASIC was developed by Jarred M. Roberts *et al.* [217] specifically for the low-power and digitizer frequencies of radio neutrino detectors, iterating on the LABRADOR ASIC design used by the ANITA experiment [247]. The LAB4D has tunable capacitance for each sample in the switched-capacitor array to minimize the sample-to-sample timing variations that are inherently large in this digitization technology. The LAB4D also has tunable window timing to reduce window-to-window timing variations. A properly tuned LAB4D has been shown to reduce the need for post-processing and correction of digitizer effects. The LAB4Ds have been demonstrated to have sample-to-sample timing of O(10 ps) [217], and O(20 ps) variations have so far been achieved in RNO-G.

At start up, the `RADIANT` performs the calibration necessary to tune the LAB4Ds. The calibration is an iterative process that starts with the collection of thousands of triggers of sine wave signals created by an on-board sine wave generator. The triggers are processed

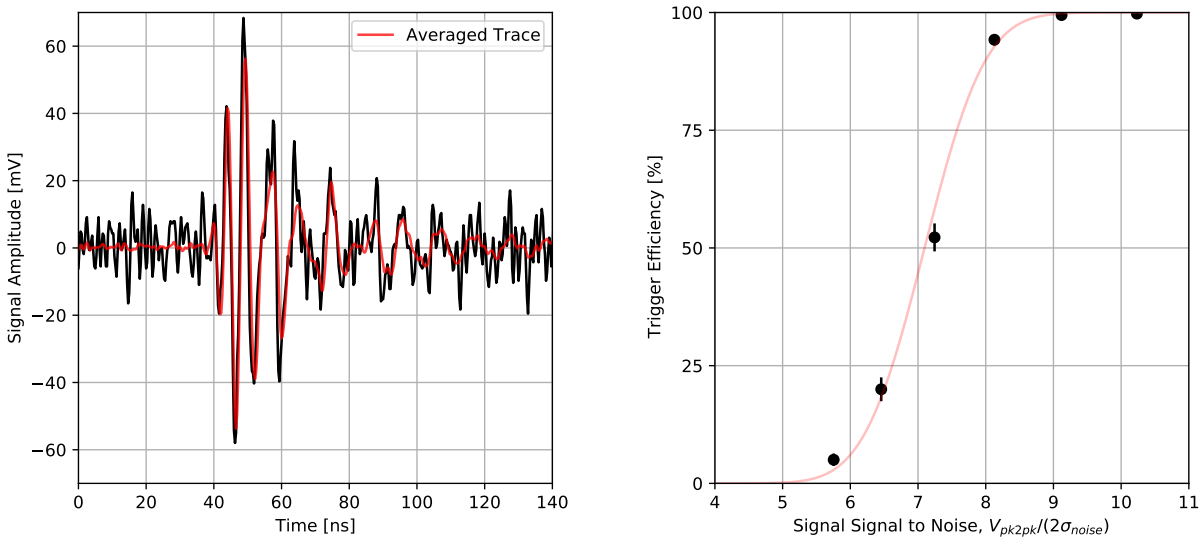

Figure 2.28: **Left:** Digitized trace of an SNR = 9, 100–225 MHz band-passed impulse passed through the surface amplifiers and recorded by the `RADIANT` board. Red is the average of 1k triggers and the black is a single trigger. **Right:** Preliminary trigger efficiency vs. SNR for the surface / air-shower trigger. Measurement taken in lab and before deployment. The trigger level results in a thermal noise trigger rate of < 1 Hz. The trigger for the deep component is expected to have a 50% trigger efficiency rate of ~ 3.5 SNR.

in real time by an FPGA on the RADIANT board to count the number of zero crossings per sample. For a perfectly tuned system, the zero crossings should be equal on all samples. The values of the tunable capacitance on the samples are slightly changed to bring the number of zero crossings on a given sample closer to the mean expected value. After tuning, more sine wave data is collected, iterating until the desired sample-to-sample timing is met, O(20 ps) in the case of RNO-G. Due to power issues and the complexity of the RADIANT board, the tuning process is still preliminary with improved firmware forthcoming to bring the LAB4Ds to their demonstrated low sample variation.

RNO-G saves both pedestal data at the start of each data run and performs a pedestal sweep at station start up. Pedestals are the average ADC of each sample, used to subtract the baseline from the signal in post-processing. Pedestals are measured by averaging many triggers of thermal noise. Pedestal sweeps are used to determine the ADC-to-voltage conversion of each sample, a required quantity for electric field reconstruction. The sweep is performed by taking pedestal data as a function of pedestal bias voltage, which is tunable from 0–2.5 V. An example pedestal sweep taken from lab data for all 24 LAB4Ds on a RADIANT board is plotted in Fig. 2.29.

2.9 Trigger

The primary science trigger for each station will occur on the low-threshold trigger board, the so-called FLOWER board. The low-threshold board is a 4-channel board with its own streaming, 8-bit, 500 MSa/s digitizers that feed into an FPGA. The FPGA will calculate, in real time, the expected delays between the four deep, VPol antennas for incident plane waves of various arrival directions, subtracting the delays from the channels and summing the channels together. This technique amplifies signal by n_{ant} while amplifying noise by $\sqrt{n_{ant}}$, increasing the single-channel SNR. RNO-G's trigger design is a lower-power version of that deployed in ARA [42] and identical in theory to the trigger described in Sect. 5.2.

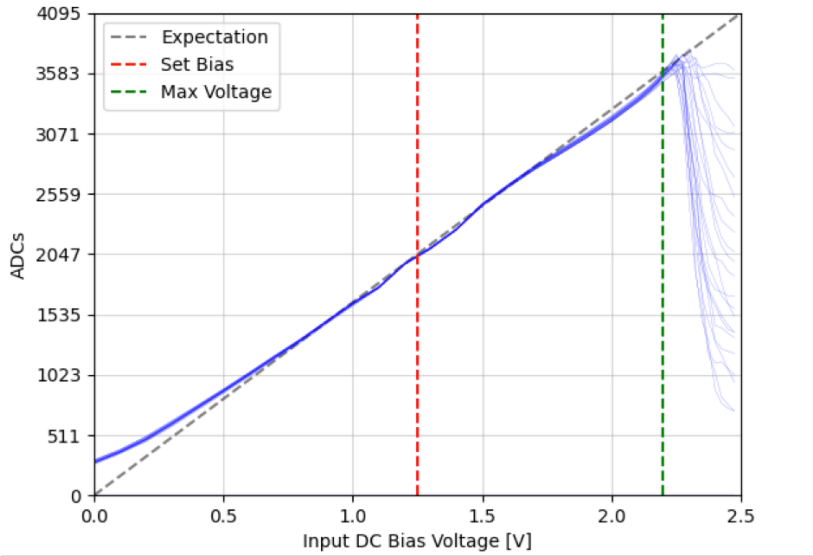

Figure 2.29: Pedestal scale for all 24 LAB4Ds on a RADIANT, from lab data. Blue is the result of the sweep. The grey dashed line is an expected result if the samples had completely linear response. The red dashed line is the set bias for each station, set to maximize dynamic range and local linearity. The green dashed line is the maximum bias voltage before roll-over effects, making the effective highest measurable voltage ~ 2.1 V.

By operating with four channels instead of the seven used in ARA and using a 500 MSa/s digitizer instead of the 2 GSa/s on the RADIANT, the trigger board is able to consume ~ 2.4 W while reaching a 50% trigger efficiency of 3–4 SNR while maintaining a O(10 Hz) thermal noise trigger rate. The phased array trigger technique has proven to improve low SNR triggering and thus increasing detector volume [42].

Each channel on the RADIANT board comes deployed with a low-power, Schottky diode detector circuit. The enveloped signal produced by the Schottky diode is compared between a definable DC voltage level and fed to the on-board FPGA to build a combinatoric trigger. The final combinatoric trigger will have a higher overall threshold than the primary science trigger (the phased array trigger) and will be used for the surface array. A preliminary trigger efficiency vs. SNR can be seen in Fig. 2.28. The trigger efficiency is lower than expected due to poor coupling to the 50 Ω signal chain and is due to be repaired in future seasons.

The firmware for the FLOWER board is still in development. The trigger used for the first

season of deployment is the diode trigger on the digitizer board. In the future, the diode trigger will only be used in surface channels where the expected SNR for RFI and cosmic ray signals is very high, negating the need for a low-threshold trigger.

2.10 DAQ and Data Handling

The electronics of each station are housed in the environmental enclosure, a large, insulated pelican case. Within the environmental enclosure is the data acquisition system (DAQ), composed of the receiving side of the electronics chains described in Sect. 2.6, the digitizer board described in Sect. 2.8, the battery system and power control described in Sect. 2.7, and a central controller board. The controller board is itself controlled by a commercial BeagleBone Black, a single board computer (SBC) run by a Unix operating system. Communication over commercial LTE allows for connection to the stations via `ssh` from the local Summit Station network. The SBC can toggle power systems, change trigger configurations, re-flash the `RADIANT` boards, set calibration pulser settings, and handle all data telemetry.

As of 2021, data is collected in runs which are saved on the station as binary files. RNO-G's server at Summit Station periodically queries each station for new event data and transfers the data over the network if available. On the server, the data is converted to a `ROOT` format, creating three files for each run, a `daqstatus.root` file with meta-information like station temperatures, a `headers.root` file for information like trigger configuration, run number, and time, and a `waveforms.root` file for the digitized signals. Summit Station has continuous satellite internet connection that RNO-G uses to transfer data south for further analysis at a rate of 5 GB/day to avoid overwhelming Summit's internet budget.

2.11 Fast RF Pulse Generator

Each RNO-G station is equipped with a fast RF pulse generator that is used to drive the two deep ($\sim$ 100 m), VPol calibration pulser antennas (one on each helper string), and the one surface VPol calibration pulser antenna. The calibration pulser antennas are used to perform *in situ* characterizing of the science antennas, electronics chains, ice properties, and triggering performance. A discussion of the antenna characterization performed via the deep calibration pulser antennas is in Sect. 2.5.6.

The pulse generator outputs an O(1 ns) pulse to transmit up to 750 MHz, the low-pass frequency of the front-end amplifiers and the highest frequency of interest for the experiment. The generator has a variable output amplitude to allow for SNR scans for trigger studies. Along with the hardware to produce the fast impulse, the pulse generator comes equipped with an RF CW generator with two frequency options, 156.25 MHz and 400 MHz. The CW source may be useful for antenna position calibration, end-to-end electronics response measurements, and as a double check for measurements made by the fast impulse. Triggering of the pulse can either be synced to the GPS PPS (pulse per second) or synced to an output from the station's SBC. The GPS PPS is a very stable timing source provided by the atomic clocks on GPS satellites [251].

The pulse generator is a daughter board of the controller board and is controlled via an I^2C bus connected to the SBC. The control commands include toggling the generator on and off, selecting channel output, selecting trigger type, and selecting the pulse type (fast impulse or CW), and, in the case of CW, selecting the output frequency. There are two output types on the board, an SMA connector for coaxial connection to the surface calibration antenna and two fiber optic outputs for the down-hole calibration antennas. To reduce weight of the string and reduce dielectric material inside of science antennas, the down-hole calibration antennas receive the calibration signal over a custom RFoF system. The RFoF system is effectively the reverse of the `IGLU`–`DRAB` system: the optical transmitter

is on the calibration pulse generator and the optical receiver (called the `IGLU-Cal` board) is down-hole, co-located with the calibration antenna. The signal produced by the pulse generator for both the coaxial and fiber optical signal chains is plotted in Fig. 2.30. Data from the *in situ* pulser in the deployed Station 21 is plotted in Fig. 2.38.

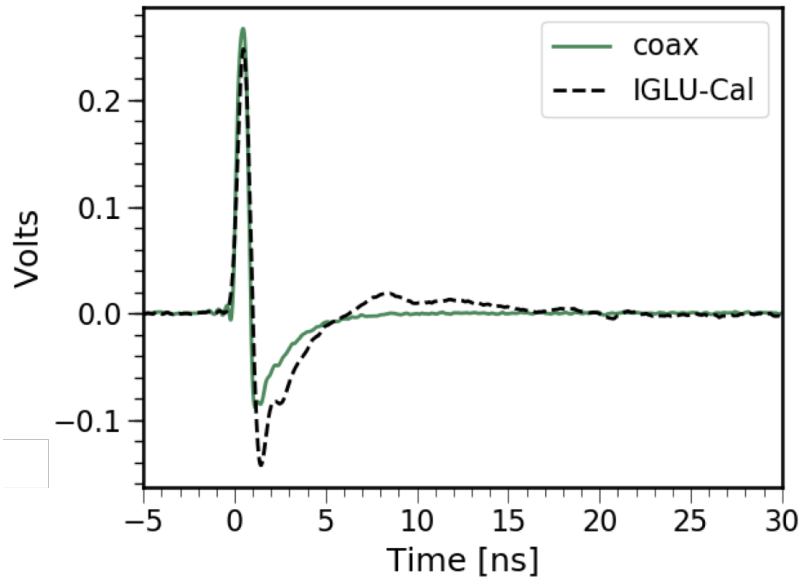

Figure 2.30: The fast output pulse from RNO-G's pulse generator, as seen on the coaxial (in green) and optical (`IGLU-Cal`, in dashed line) outputs of the board. Figure by Eric Oberla.

The prototype of the pulse generator board generated the fast impulse using two fast digital comparators in a race condition. Each comparator is set so that, without a trigger signal, one outputs a low signal and the other a high signal. The outputs of the two comparators are connected to a logical 'and' gate whose output is the output of the pulse generator. When a trigger arrives, it undergoes a slightly longer path to one comparator than the other. The race conditions allows for both comparators to output high for a short period. The 'and' gate outputs high for a controlled, short amount of time, producing a fast RF pulse. The schematic of the prototype of the pulse generator board is shown in Fig. 2.31 and a picture of the manufactured prototype is in Fig. 2.32. The prototype proved to be successful at producing an impulse of desired duration. A version of the prototype pulser with modified filtering is deployed on the production pulse generator board.

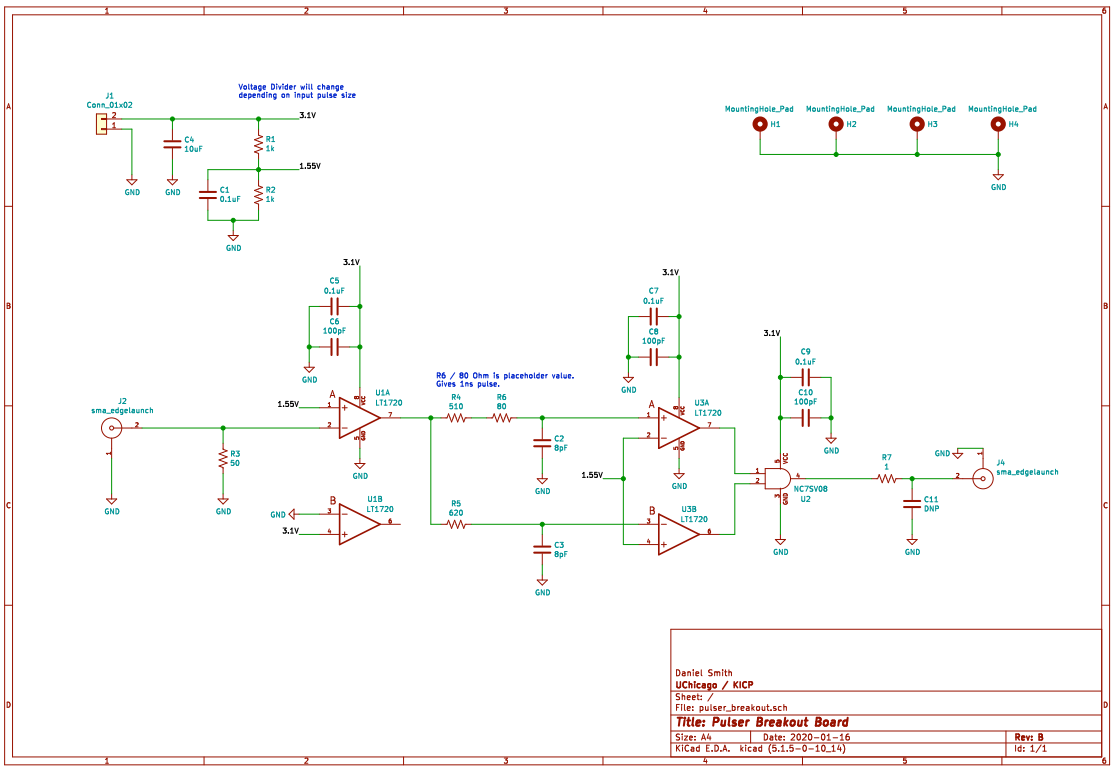

Figure 2.31: The schematic of the prototype of the pulse generator. The prototype only included the hardware to produce the fast impulse. The production model is more complicated to incorporate I^2C control, CW generation, and optical output.

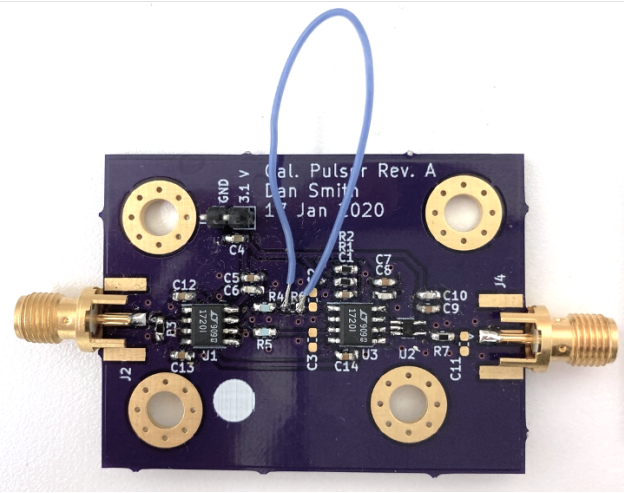

Figure 2.32: An image of the prototype of the pulse generator. Note the large jumper was used to roughly measure the relationship between path length and output pulse length.

2.12 Deployment

The first season of deployment in Summer 2021 saw the construction of the first three stations of RNO-G, Stations 11, 22, and 21. Deployment consisted of three teams arriving at Summit in succession. In order, they were the drilling (arrived in May), deployment (arrived in June) and calibration (arrived in July) teams, with deployment and drilling teams operating in tandem in June.

Deployment at a station began with surveying to flag the predetermined location of boreholes and surface antennas. After that, the drilling team follows to drill the three, 100 m boreholes in a triangle shape, as shown in Fig. 2.1. After drilling, the environmental enclosure with pre-assembled DAQ, science antennas, and deployment shack are brought to the station via snowmobile. The deployment shack is parked over each borehole in sequence, where it is used as a warm space to assemble the antenna strings and winch each down into the boreholes. At the same time, the 9 surface LPDAs are placed into three 2 m deep hand dug trenches. The trenches are back filled to improve the LPDA match with the ice. After the LPDA antenna and down-hole antennas are in place, the station electronics, including cabling, power systems, and communications, are assembled and the station is remotely powered on to confirm successful commissioning.

The original plan for the deployment of 10 stations was pared back for contingent set-backs, first in the drill technology and then in hardware. The successful deployment of three stations is an accomplishment unto itself due to the hardships faced in the field and hardships faced due to COVID-19.

The drill, named the Rapid Access Isotope Drill (RAID) and designed by the British Antarctic Survey (BAS), was designed to create one borehole a day, including the setup, drilling, disassembly and transportation of the drill. The RAID drill was tested by drilling a smaller diameter hole in Antarctica, and operated as predicted. The larger diameter hole required for RNO-G, as well as the warmer conditions in Greenland, caused the anti-torque

mechanism to fail and several instances of drill bit freeze-in (luckily at shallow depths where the bit could be extracted). Drilling was substantially slowed down to avoid damage to the drill, meaning only 3 stations could be drilled (9 holes and a test hole).

Besides drilling issues, hardware malfunctions reduced the number of deployable stations. The issues in the down-hole, front-end amplifier system, as described in Sect. 2.6, and missing jumper cables on the digitizer board, an oversight in construction, were repaired using scavenged parts from other stations, reducing the number of usable station hardware to three.

After deployment, a different failure mode was found: the commercial LTE modem fails on reset when at temperatures within its designated operating range, rending communication to one of the stations and potentially other stations in the future impossible. The three stations deployed in Summer 2021 will be repaired in Summer 2022, and future stations will be deployed with a different LTE modem, and further in-lab freezer tests will be performed to assure deployed hardware operates within manufacturer's defined specifications.

2.13 Calibration Data

During the deployment season in Summer 2021, the second science team, composed of Christoph Welling, Bryan Hendricks and myself, was tasked with collecting calibration data of the newly minted stations. Presented here is the data collected and preliminary analyses, where available.

The calibration campaign for each station is drawn in Fig. 2.34. For each station, four types of calibration data were collected: *in situ* pulsing, 'berm-top' pulsing, local surface pulsing in four cardinal directions around stations, and RFI produced by a snowmobile with GPS tracking. The meta information of the calibration data collected in Summer 2021 is shown in Tab. 2.1, 2.2, 2.3 for Stations 21, 11, and 22 respectively. The averaged event display from the *in situ* pulsing runs for Station 21 is plotted in Fig. 2.38, the surface *in*

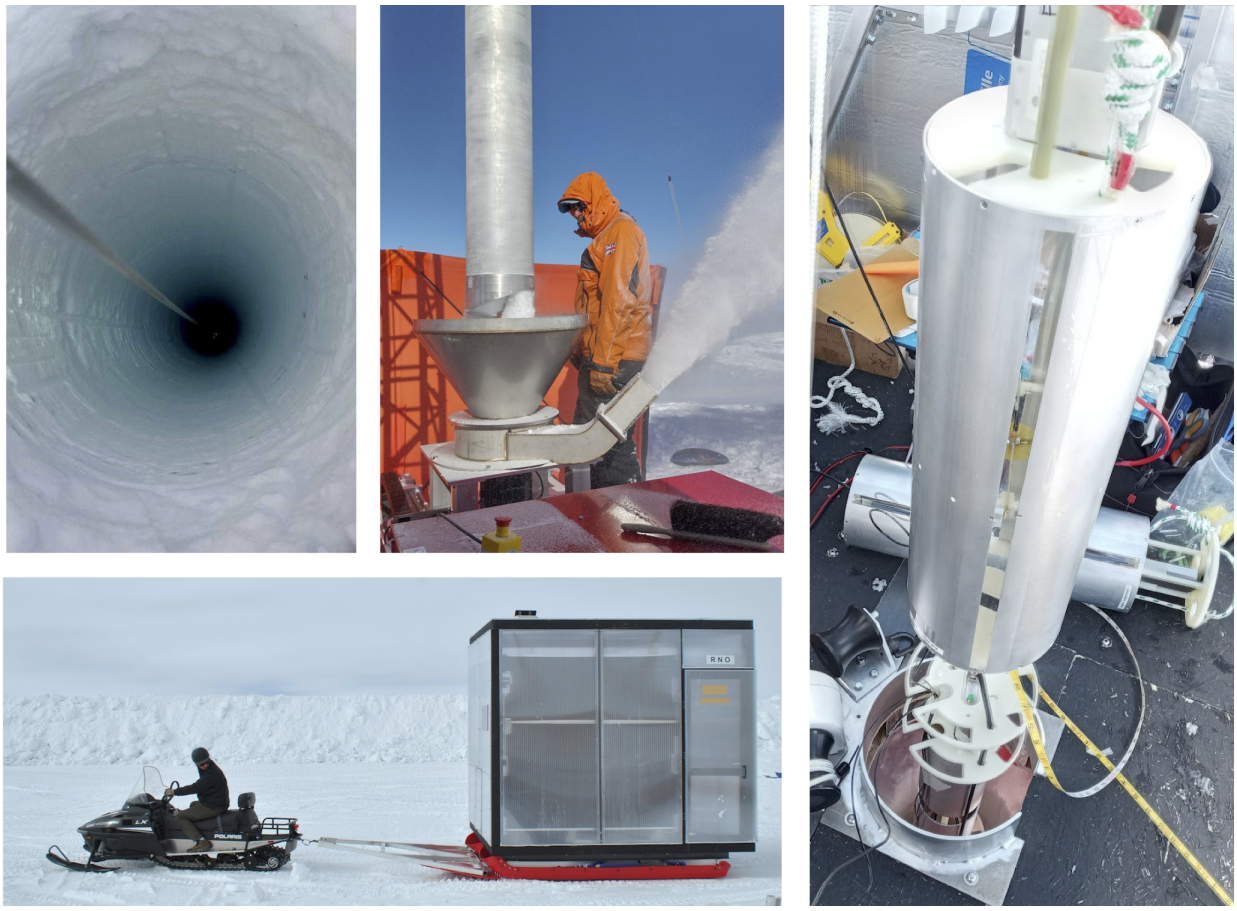

Figure 2.33: Photos from construction and deployment of the first stations in the 2021 season. Photos by Eric Oberla, Cosmin Deaconu, and Delia Tosi.
Top, Left: Finished borehole.
Top, Middle: ASIG borehole drill in operation.
Right: A VPol and HPol antenna being deployed down a borehole inside of the deployment shack.
Bottom, Left: Deployment shack being transported into position over borehole.

situ pulsing runs for Station 21 is plotted in Fig. 2.39, and the averaged event display from the local surface pulsing for Station 21 is plotted in Fig. 2.37.

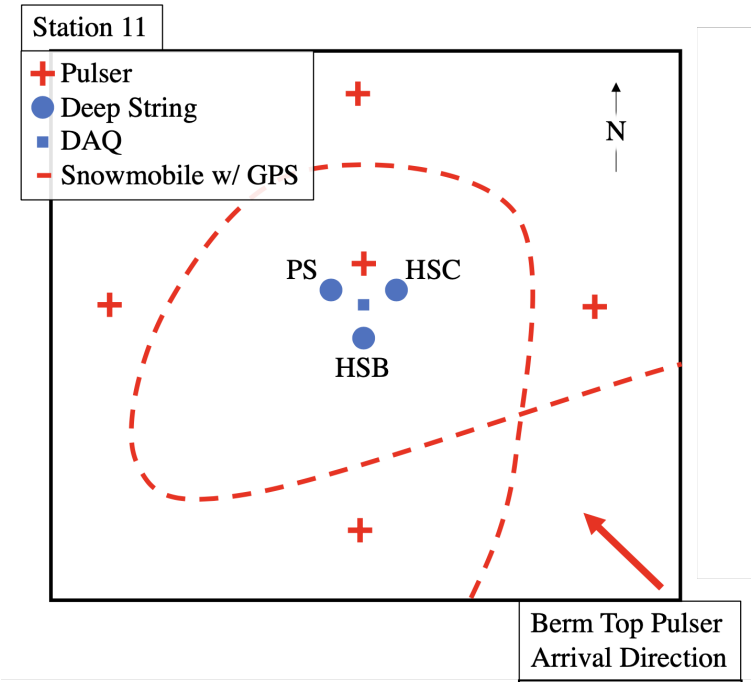

Figure 2.34: Diagram of calibration data collected for each station. Data was collected from 1) the three *in situ* pulsers, 2) a 'berm-top' pulser, an LPDA suspended ∼10 m in the air broadcasting a signal to all three stations, 3) local surface pulsing in all four cardinal directions, and 4) snowmobile data with GPS tracking data. The deep strings are the power string (PS), and helper strings B and C (HSB and HSB).

'Berm-top' pulsing, an iteration of 'roof-top' pulsing that was done for ARA, is primarily useful for station-to-station timing and inter-station position calibration. As can be seen in Fig. 2.35, an LPDA positioned on top of a man-made snow berm, ∼10 m above the ice surface, was used to broadcast a bright (+5 kV) impulse, produced by a FID pulse generator. The pulse was sufficiently bright to produce triggers in all stations. Several such berm-top pulsers, permanently installed at Summit Station and controlled remotely, would be a powerful tool to calibrate a detector for future potential coincident detections of a neutrino event in multiple stations. The only other option for inter-station calibration would be from a yet unavailable deep (O(km)) pulser.

Figure 2.35: Photo of 'berm-top' pulsing, showing an LPDA broadcasting to the three stations deployed in Summer 2021.

Local surface pulsing in the four cardinal directions around each station is useful for antenna position calibration and ice property measurements, mainly the index of refraction of the firn. The data was collected using a VPol antenna, buried ~ 0.5 m into the firn and ~ 100 m away from a station, that was connected to a self-triggering AVTECH AVIR-1-C signal generator. The antenna was positioned vertically, broadcasting vertically-polarized radio to the station. The apparatus was powered using a battery and inverter, and kept warm in a pelican case. A picture of the setup is shown in Fig. 2.36. The GPS coordinate of each calibration site was recorded, and data was collected for ~ 10 minutes, allowing for O(1000) triggers in the station. The surface amplifiers and trigger were turned off during pulsing to avoid damaging amplifiers. The data collected at Station 21 is plotted in Fig. 2.37. This calibration run could be improved in the future by also performing horizontal-polarized pulsing.

While not the optimal calibration route, the data from local surface pulsing alone may be sufficient to constrain both the antenna positions and a model of the ice index of refraction. If

we consider only deep VPol antennas, there are 11 antennas, each with 3 unknown positions in space ($\hat{x}$, $\hat{y}$, and $\hat{z}$), equally 33 unknowns. Each calibration source adds 3 more unknowns from its location. For calibration purposes, the difference of arrival time for pairs of antennas is used, removing the unknown time of the original calibration pulse, unknown time of propagation to the array, and unknown trigger time jitter. Each pair is a known and the number of pairs is equal to the binomial coefficient $\binom{11}{2} = 55$. Naively, from one calibration pulser on one station, there are 36 unknowns and 55 knowns, allowing for the addition of an ice model with 19 free parameters. Using four calibration pulsers, there are 45 unknowns and 220 knowns, making for a very constrained system.

Obviously, there are caveats to this approach and the usefulness of the local pulser data. Since each antenna has a different cable length and signal delay to the DAQ that may diverge from the cable measurements taken in the lab, there may be the additional unknowns from the antenna delay, adding 11 more unknowns. It is possible these cable delays are degenerate with antenna position, with additional cable delay appearing like additional depth into the ice. There may also be fewer knowns than expected because signals may have identical arrival direction at the deep antennas due to the phenomenon of Snell's window. In reality, the best antenna position calibration will be derived from many calibration sources including local surface pulser data.

The local surface pulsing data can be used to measure the directional dependence of the ice response due to birefringence from the local ice crystal structure and local ice flow. Due to the shallow depth of the array, it is unlikely that birefringence will be a measurable quantity, but the surface pulser data can be used to set limits on birefringence. Birefringence can be measured either by differences in the time of arrival of signals as a function of arriving azimuth angle (from a polarization-dependant index of refraction) or from differences in the amount of horizontal vs. vertical polarization as a function of arriving azimuth angle due to the rotation of the signal in polarization [147, 166]. A further description of birefringence

and future measurements of birefringence are available in Sect. 3.2.

The RFI from a snowmobile, while not very precise or repeatable, is useful both as a double check of antenna position calibration and RFI rejection efficiency. The GPS location along the path of the snowmobile was recorded to compare with arrival direction reconstruction.

Figure 2.36: Photos of different stages of calibration studies. Photos by Bryan Hendricks. **Left:** on-site pulsing, showing the pelican case containing the signal generator and the location of the buried antenna. **Middle:** Image of an RFI site survey, using a spectrum analyzer to diagnose rough amplitude and direction of RFI at the stations. **Right:** The process of burying two LPDA antennas for birefringence measurements, described in Sect. 3.2.

Date	Pulser Type	Run Num.	Description
4 Aug 2021	'Berm-top'	270–287	Test runs
6 Aug 2021	Snowmobile	307–316	
7 Aug 2021	Local Surface	326–341	Test runs
8 Aug 2021	'Berm-top'	343–378	Stable trigger
10 Aug 2021	Local Surface	409–416	
18 Aug 2021	*in situ*	472–480	

Table 2.1: Calibration data runs from 2021 in Site 1 / Station 21

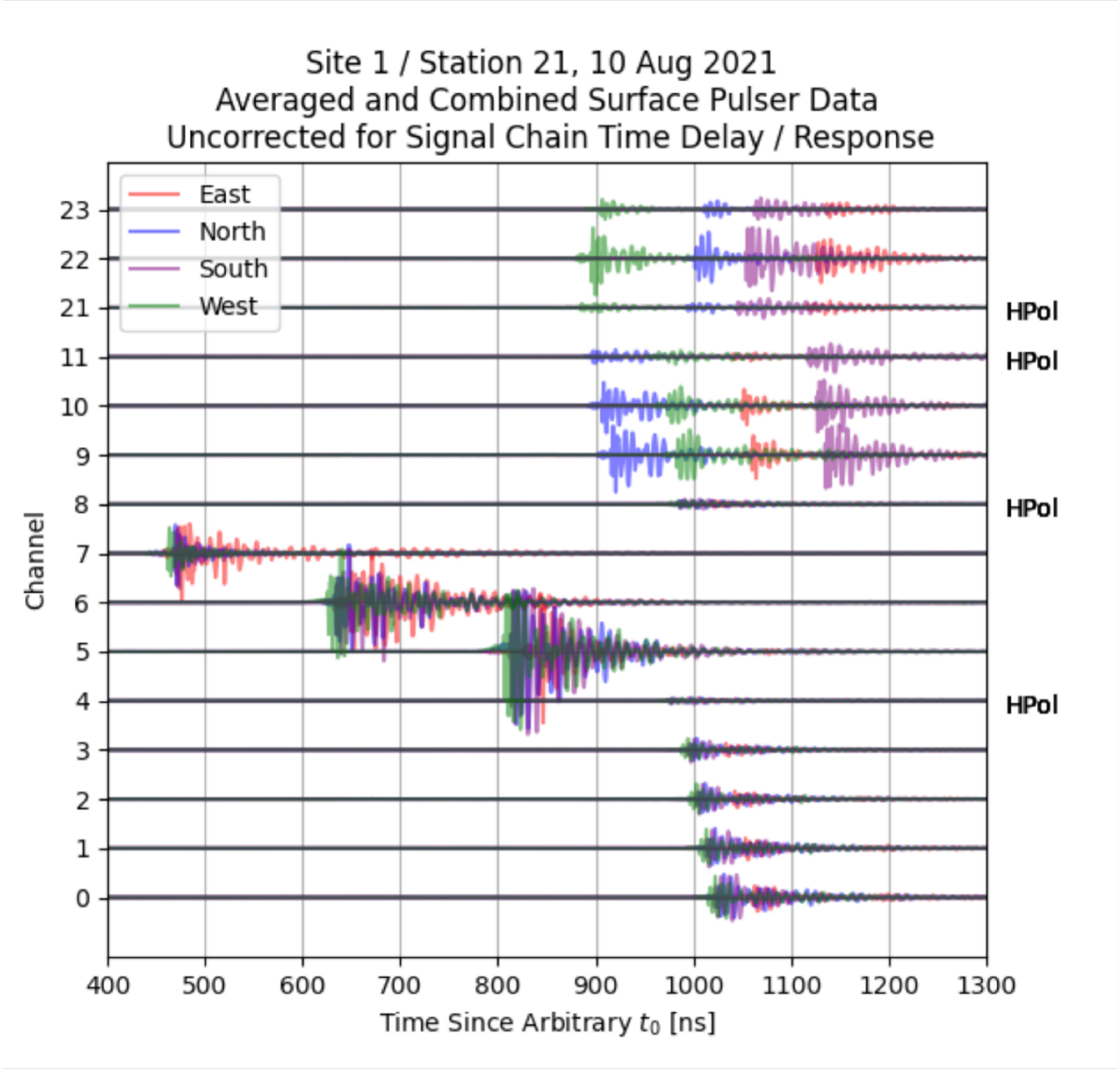

Figure 2.37: Averaged signals on all deep antennas for the four calibration pulsing directions for Station 21. The relative time delay of t_0 is set by the trigger configuration.

Date	Pulser Type	Run Num.	Description
4 Aug 2021	'Berm-top'	148–155	Test runs
6 Aug 2021	Snowmobile	174–179	
8 Aug 2021	'Berm-top'	201–224	Unsuccessful due to trigger glitches
11 Aug 2021	Local Surface		

Table 2.2: Calibration data runs from 2021 in Site 2 / Station 11

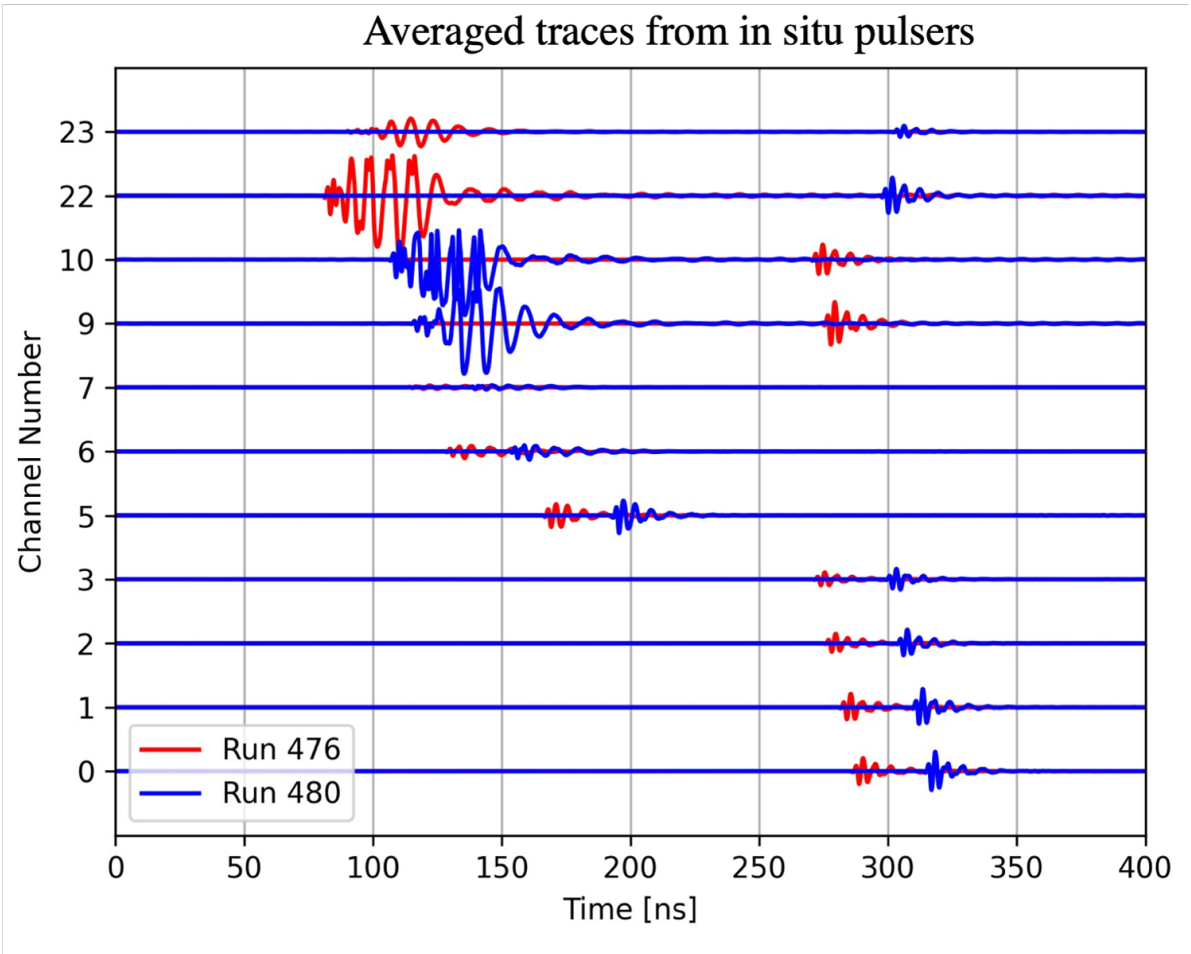

Figure 2.38: Averaged signals on all deep VPol antennas for the two deep *in situ* calibration pulsers for Station 21. The relative time delay of t_0 is set by the trigger configuration. Note that the antenna directly above or below the calibration pulser antenna has a saturated signal and would be unusable in calibration.

Date	Pulser Type	Run Num.	Description
4 Aug 2021	'Berm-top'	187–193	Test runs
6 Aug 2021	Snowmobile	212–217	
8 Aug 2021	'Berm-top'	234–264	Stable trigger
11 Aug 2021	Local Surface		

Table 2.3: Calibration data runs from 2021 in Site 3 / Station 22

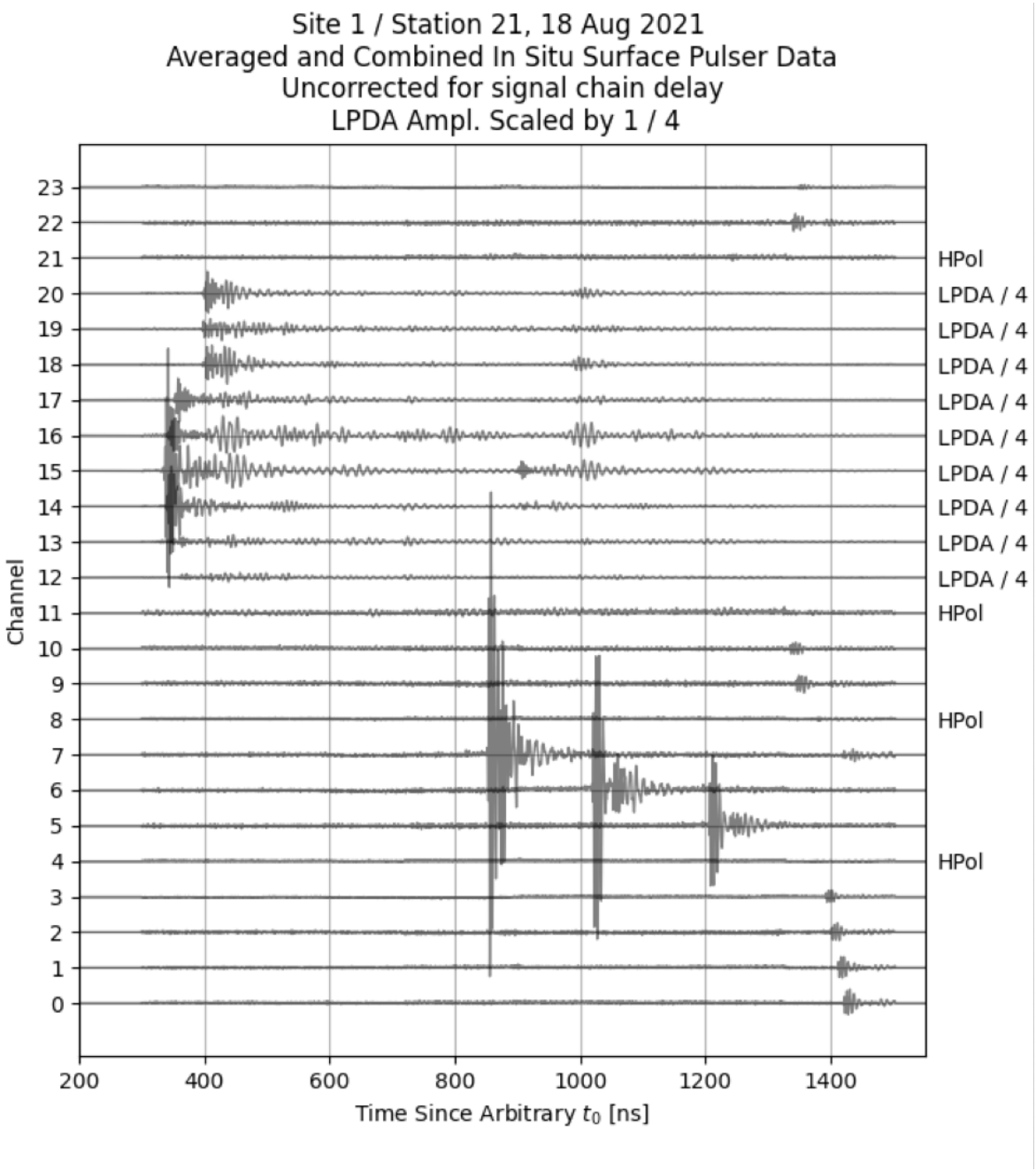

Figure 2.39: Averaged signals on all antennas for the surface *in situ* calibration pulsers for Station 21. The relative time delay of t_0 is set by the trigger configuration. Note that the surface array signal is scaled by 1/4 to show details of both the surface and deep component.

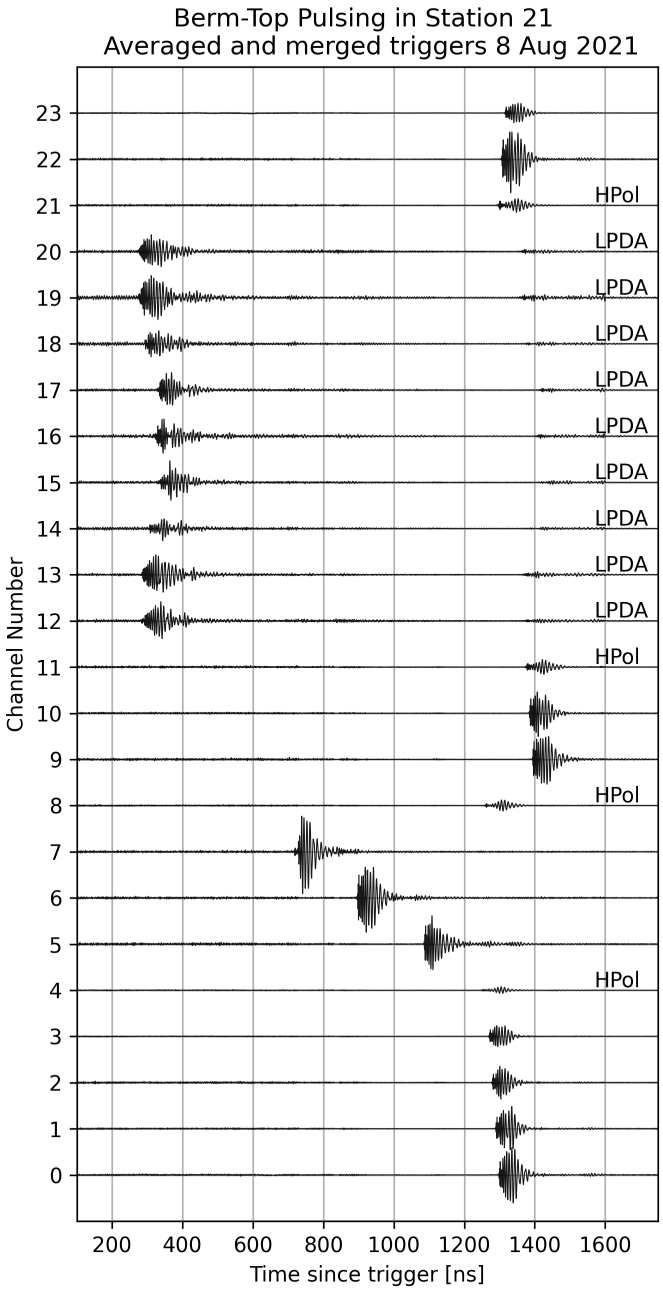

Figure 2.40: Averaged signals on all antennas for the berm top calibration pulser for Station 21. The relative time delay of t_0 is set by the trigger configuration.

CHAPTER 3

ICE PROPERTIES AT SUMMIT STATION, GREENLAND

During RNO-G's Summer 2021 deployment season, there was a campaign, lead by Christoph Welling, Bryan Hendricks and myself, to collect calibration data to measure the properties of ice most of interest to RNO-G's science case, mainly radio frequency attenuation length, birefringence, and subsurface layers. This chapter presents an extended discussion of the attenuation measurement along with an overview of the data collected for birefringence and subsurface layer measurements.

The content in Sect. 3.1 has been submitted for review to the Journal of Glaciology, cited as J. A. Aguilar et al. *In situ*, broadband measurement of the radio frequency attenuation length at Summit Station, Greenland [32]. Reuse is permitted according to the Creative Commons Attribution (CC-BY) licence used by the journal.

3.1 *In Situ*, Broadband Measurement of the Radio frequency attenuation length at Summit Station, Greenland

We report a measurement of the radio frequency electric field attenuation length of deep glacial ice at the US National Science Foundation's Summit Station in Greenland. This measurement is of interest to the ultra-high energy neutrino (UHEN) community due to the development of the Radio Neutrino Observatory in Greenland (RNO-G), a particle astrophysics experiment that uses the ice as a target material in the search for astrophysical and cosmogenic neutrinos [31].

The IceCube experiment has placed a flux upper limit for astrophysical neutrinos of $E^2\phi \lessapprox 2 \times 10^{-8}$ GeV/(cm^2 s sr) at E_ν =1 EeV [17]. At such fluxes, a particle detector requires an active volume of O(10 km^3) or larger for a discovery-level detection within a detector's lifetime. A sparsely instrumented array of radio antennas, deployed in and on

an extensive dielectric medium can satisfy this volume requirement. An UHEN interaction creates an extensive electromagnetic shower that produces impulsive radio emission via the Askaryan effect [60]. If the interaction occurs in an environment of low radio attenuation, a relatively small number of radio antennas can probe target volumes at the scale needed for UHEN observations.

Glacial ice has been measured to have long radio attenuation lengths due to low temperature and relatively high purity [69, 77, 40, 62, 67, 146]. This, combined with the volume of glacial ice available in Greenland and Antarctica, makes polar ice sheets attractive sites for the construction of a radio neutrino detector.

RNO-G is one such experiment based on radio detection of UHEN in glacial ice [31], among others in Antarctica [40, 43, 52, 175, 133, 138]. RNO-G is being constructed near NSF's Summit Station at the highest point of the Greenland Ice Sheet. The planned detector will ultimately be composed of 35 autonomous stations separated by 1.25 km in a grid pattern. Each station is instrumented with radio antennas, with good response over the range 100–600 MHz, deployed both just below the surface and at depths down to 100 m in boreholes. Construction of the detector began during the summer of 2021 with the installation of the first three stations.

Previous measurements of radio attenuation lengths in Antarctica [69, 77, 40, 67, 146] and Greenland [62, 185, 208] have demonstrated that radio attenuation lengths vary at different ice locations, due primarily to differences in ice temperature and impurity levels. Since electric field attenuation length is a primary determinant of the expected number of observed UHENs at energies greater than 1 EeV, a precise, *in situ* measurement is required at Summit Station to assess RNO-G's science potential.

Our work builds upon one previous *in situ* measurement of the bulk ice electric field attenuation length performed at Summit Station by [62]; that effort reported a depth-averaged attenuation length $\langle L_\alpha \rangle = 947^{+92}_{-85}$ m at 75 MHz. We herein quantify the attenuation length

at higher frequencies to better match RNO-G's frequency range of 100-600 MHz. In addition to that prior analysis, there have been several previous measurements of the radio ice properties at Summit Station, including radar attenuation length measurements from air-borne radio sounding in the Greenland Ice Sheet Project [185] and *in situ* radio sounding to investigate layering in the ice [208]. We include a comparison of our reported attenuation with previous measurements at Summit Station and Antarctica in the **Discussion and Summary** section.

3.1.1 Experimental Approach

Our approach is similar to previous work in the astro-particle physics field [62, 67, 77, 146, 69].

We transmit an impulsive, broadband radio signal downwards into the ice via a wideband, directional antenna, and measure the return signal as a voltage versus time trace on a second, identical antenna. The transmitted signal propagates through the ice sheet, reflects off of the bedrock, and returns to the receiving antenna on the surface. After correcting for geometric path loss, bedrock coefficient of reflection, and electric field amplification from the focusing effect of the firn, the remaining power loss is attributed to absorption and scattering in the ice. Note that, experimentally, we do not distinguish between the two – our quoted attenuation length implicitly includes both effects. (Possible dispersive effects at the bedrock are quantified in the **Bedrock Echo** section.) To reduce systematic uncertainties, we remove the system response of the electronics (initial impulse, antenna response, cables, amplifiers, filters) by normalizing against a second measurement run in air. We recreate the through-ice setup (same initial impulse, antenna polarization, cables, amplifiers, and filters but additional attenuators) for two antennas transmitting over a short distance in air and thereby largely cancel dependence on the system response from the in-ice data run.

We take the reflection off the bedrock to be specular. Motivation for this decision is described in the **Bedrock Echo** section below. Given a specular reflection, the radar range

equation reduces to the Friis equation [121], and the direct through-air transmission formalism is applicable to our observed bedrock echoes. In that case, following the notation used by [62], the ratio of recorded voltages for each configuration (through-air vs. through-ice) as a function of frequency ν is,

$$\frac{V_{\nu,ice}}{V_{\nu,air}} = \sqrt{F_f R} T_{ratio} \frac{d_{air}}{d_{ice}} \exp\left(-\frac{d_{ice}}{\langle L_\alpha \rangle}\right), \tag{3.1}$$

where d_{air} and d_{ice} are the distances the ice and air signals travel between antennas, R is the power reflection coefficient of the bedrock, F_f is a focusing factor from the changing index of refraction in the firn [239, 238], T_{ratio} corrects for the change of transmission coefficient at the antenna feed between the antenna operating in air and in ice, and $\langle L_\alpha \rangle$ is the depth-averaged electric field attenuation length over the entire depth of the ice. Solving for the attenuation gives,

$$\langle L_\alpha \rangle = d_{ice} / \ln\left(\sqrt{F_f R} T_{ratio} \frac{V_{\nu,air}}{V_{\nu,ice}} \frac{d_{air}}{d_{ice}}\right). \tag{3.2}$$

This equation differs from that in [62] by the inclusion of the focusing factor, which arises from the amplification of field strength from propagation in the firn [235]. The addition of the focusing factor modifies the [62] bulk attenuation result from 947^{+92}_{-85}m to 913^{+85}_{-79}m. We assume that the firn has an index of refraction varying linearly with the ice density profile $\rho(z)$ at Summit Station [174]. The density profile has been experimentally measured [59, 148, 38, 39] and fit to a double exponential [101], leading to a refractive index varying between $n \sim 1.4$ at the surface and $n \sim 1.78$ in deep (< 100 m) ice. The changing index of refraction focuses power from the transmitter on the downwards path, such that the Fresnel zone radius at the bedrock is reduced relative to the constant refractive index case. After reflection at the bedrock, signal is partially de-focused on the return path, however the electric field areal flux density at the surface receiver is still amplified compared to the

n=constant case. The focusing factor is equivalent to a correction to the expected $1/R^2$ geometric spread factor, mathematically formalized by [263]. The focusing factor is present in [185], [189], and [239], among others. We have used the finite-different time domain electrodynamics simulation software MEEP [205] to confirm this effect.

3.1.2 Experimental Setup

A system diagram of the experiment is presented in Fig. 3.1. This measurement was performed in August 2021 at Summit Station, Greenland, using a separation distance of 244 meters between the transmitter (coordinates 72.5801°N, 38.4569°W) and receiver (coordinates 72.5786°N, 38.4527°W) sites. The large separation distance assured that direct propagation from the transmitting antenna to the receiving antenna did not saturate the receiving amplifier. All antennas used were commercially available Create CLP-5130-2N [99] log-periodic dipole antennas (LPDA) with ~ 8 dBi in-air forward gain over the band 105–1300 MHz.

Due to the large distance between stations, two parallel electronics signal chains are used, for triggering and the bedrock echo measurement, respectively. The bedrock echo electronics signal chain starts with the self-triggered high voltage FID Technology[1] model FPG6-1PNK pulse generator, which delivers a +5 kV signal to a 50Ω coaxial feed. After the FID output, we apply a 100 MHz high pass filter using a Minicircuits[2] NHP-100 filter. Following the filter, the signal is conveyed over 12 m of LMR-400 50Ω coaxial cable to an LPDA buried in the ice and pointed vertically downwards towards the bedrock; the bedrock-reflected return signal is then measured by a similarly-buried, downwards-pointing, receiver LPDA. The receiving antenna, located 244 m away along the surface of the ice, is aligned with the antenna tines parallel and collinear to the ones of the transmitting antenna, so that each antenna is in the gain null of the other to minimize contamination from horizontal ray

1. http://www.fidtechnology.com

2. https://www.minicircuits.com/products/RF-Filters.html

paths. After measurement in the receiving antenna, the signal travels over a 10 m LMR-400 cable, bandpass filtered from 145-575 MHz using Minicircuits VHF-145+ and VLF-575+ filters, and then amplified by a custom RNO-G design low-noise amplifier with +59 dB of gain over the band 80–750 MHz. After the amplifier, the signal is bandpass filtered again using Minicircuits NHP-200 and VLF-575+ filters, and then recorded on a 2 GHz-bandwidth Tektronix MSO5204B oscilloscope.

The oscilloscope is triggered by the second electronic signal chain, ensuring a stable trigger over the distance between transmitter and receiver. The second chain begins with an AVTECH AVIR-1-C pulse generator triggered by the FID pulse generator `TRG OUT`, producing an impulsive, O(1 ns) pulse. The pulse generator is connected over a 12 m LMR-400 cable to an elevated, in-air LPDA pointed at a similarly elevated receiver LPDA located 244 m away and viewing the transmitter on boresight. The received in-air signal is then attenuated by 20 dB to prevent saturation, bandpass filtered using Minicircuits VHF-145+ and VLF-575+ filters, amplified by +59 dB using the RNO-G low-noise amplifier, bandpass filtered again using Minicircuits VHF-145+ and VLF-575+ filters and finally captured by the oscilloscope. This in-air signal was used to trigger the oscilloscope, and therefore provides the reference t_0 for our measurements.

The oscilloscope was set to collect data over a 50 μs window; 10,000 individual triggers are averaged to suppress incoherent noise contributions and that average is written to scope memory. Twenty 10,000-event runs were collected, and then again averaged in post-processing, bringing the total number of triggers to 200,000.

To perform the air $\rightarrow$ air normalization run, we swapped the cables for the in-ice antennas with those from the in-air antennas. On the receiving side, two modifications were made: we added a 46 dB attenuator to prevent amplifier saturation and, for this configuration, we self-triggered on the arriving signal.

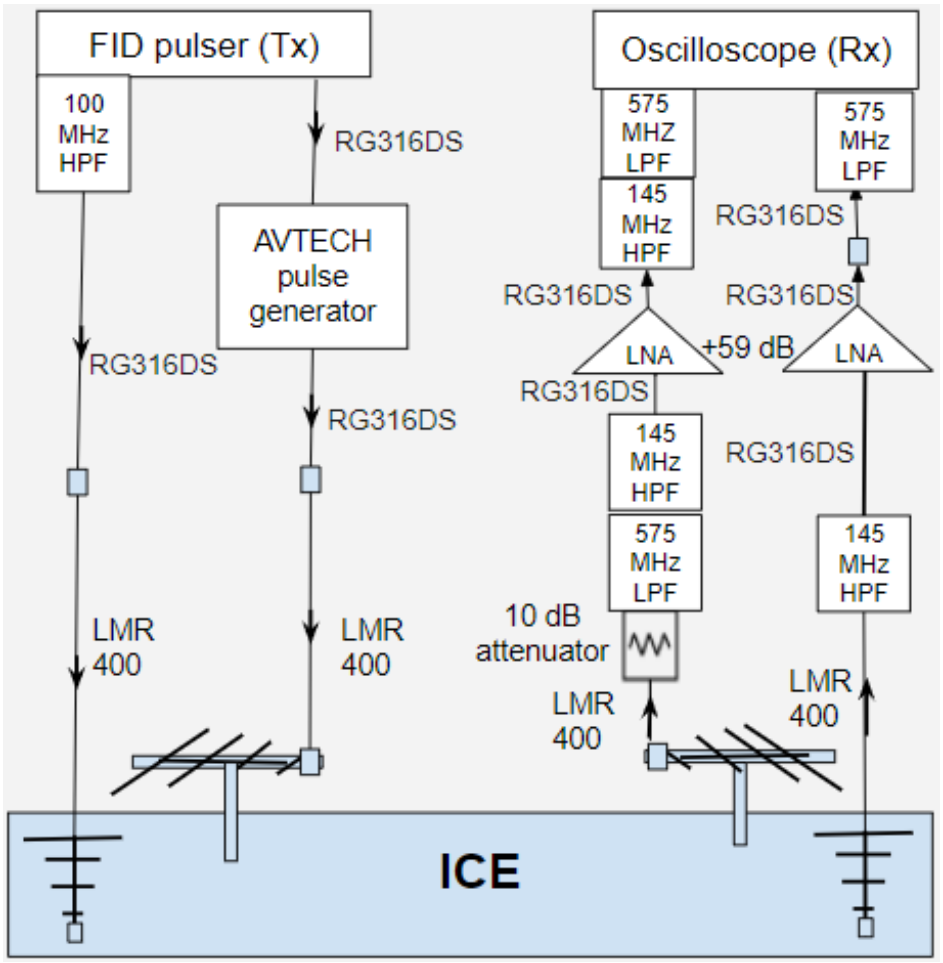

Figure 3.1: Diagram of experimental setup for bedrock reflection. On the transmitting side, we use a self-triggering FID Technologies +5 kV high voltage pulse generator connected to a buried log-periodic dipole antenna (LPDA); an AVTECH fast pulse generator triggered by the FID pulser is connected to an in-air LPDA. On the receiving side, both the buried downward-pointing, and the in-air LPDAs are connected to a +59 dB low noise amplifier; those outputs are then recorded on a Tektronix digital oscilloscope, triggered by the in-air signal.

3.1.3 Experimental Results

Bedrock Power Reflection Coefficient

The power reflection coefficient at the ice-rock interface is not well-known and constitutes the largest uncertainty in our measurement of attenuation length. Taking an approach similar to [62], we take the power reflection coefficient to have a mean value of 0.215, a typical value for ice-bedrock interfaces as derived from radio sounding experiments [91, 69]. For uncertainty analysis, we assume the reflection coefficient can be drawn from a probability density function, uniformly distributed in the log of the reflection coefficient over the range from 0.01 to 1.0, which represent plausible extrema for the interface, from a frozen bedrock with high water content to an underlying layer of water [91].

The observed return echo, in principle, could include both coherent and also incoherent contributions. Whereas the former sum linearly with the number of average triggers, the latter will scale as the square root of the number of events averaged N_{avg} [207]. We have explicitly verified that our final results are insensitive to N_{avg}, consistent with the assumption that the observed specular return echo, after subtracting the contribution from noise, is dominated by coherent scattering.

Bedrock Echo

The reflection from the bedrock is visible above thermal noise in the time domain voltage trace of the receiving antenna, at a signal onset time of 35.55 μs after the oscilloscope trigger (Fig. 3.2). The bedrock echo is observed to include two components: a predominantly-specular, sharp, faster impulse (of duration $\sim 500ns$), and a long ($> 2\mu s$) extended signal which we associate with more diffuse, multi-path reflections off irregular features, both on the surface of, and within, the underlying bed reflector. For the purposes of the bulk radio attenuation measurement, and since an extended tail is not present for the in-air normalization

run, we restrict consideration to the fast, specular component.

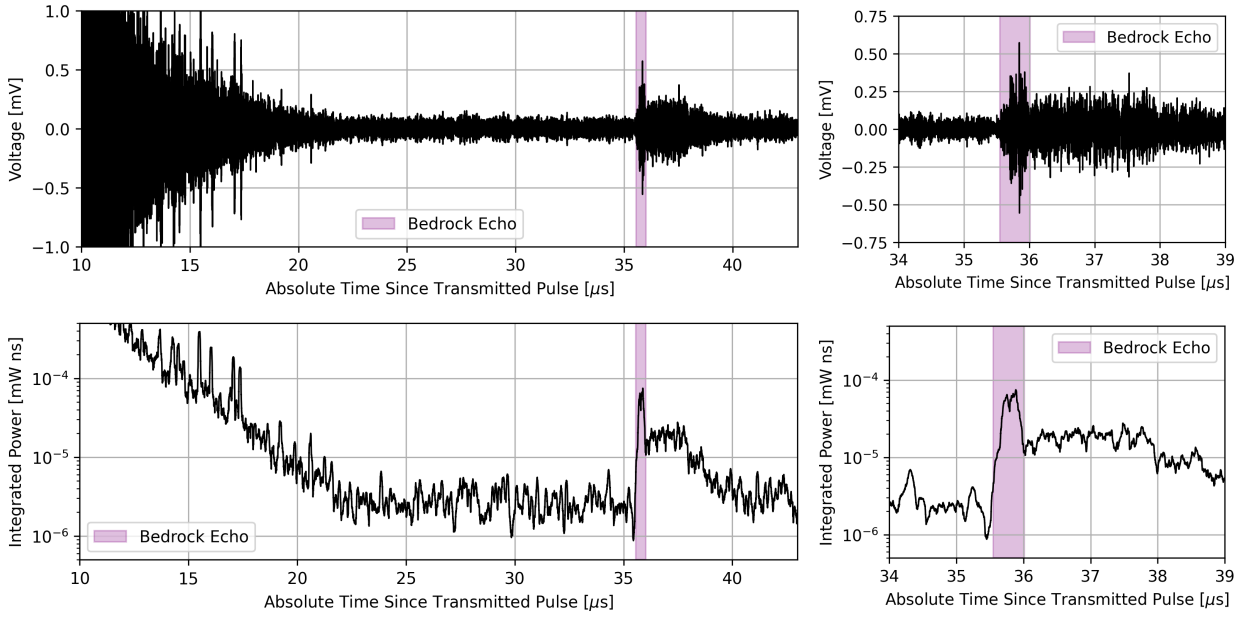

Figure 3.2: Top: Recorded voltage as a function of time for the receiving in-ice antenna. Bottom: Recorded power, integrated in a sliding window of 100 ns to account for the group delay of the LPDA antennas. The specular component of the bedrock echo 'signal' is highlighted in magenta. Sub-surface internal layer reflections are visible at times earlier than 22 μs, after which noise dominates up to the point at which the bedrock echo is evident.

The uncertainty in the time window of the specular reflection is of $O(10ns)$, dominated by noise fluctuations at the edges of the window. This uncertainty is neglected since it is sub-dominant relative to the other systematic uncertainties in our final measurement. The final window start and end times are therefore defined to be 35.55 and 36.05 μs, respectively.

To determine the impact of neglecting the diffuse component of the bedrock echo on our final measured value of bulk attenuation, we investigate the dependence of our numerical result on the window length used in our analysis. We expect the measured attenuation to increase with increased window length due to the extended integration of power returning from the bedrock; at frequencies below 250 MHz, we obtain a $\sim$10% larger attenuation length, but with increased uncertainty, as seen in Fig. 3.3. At frequencies above 250 MHz, there is a negligible increase in attenuation length with increased window length. We note

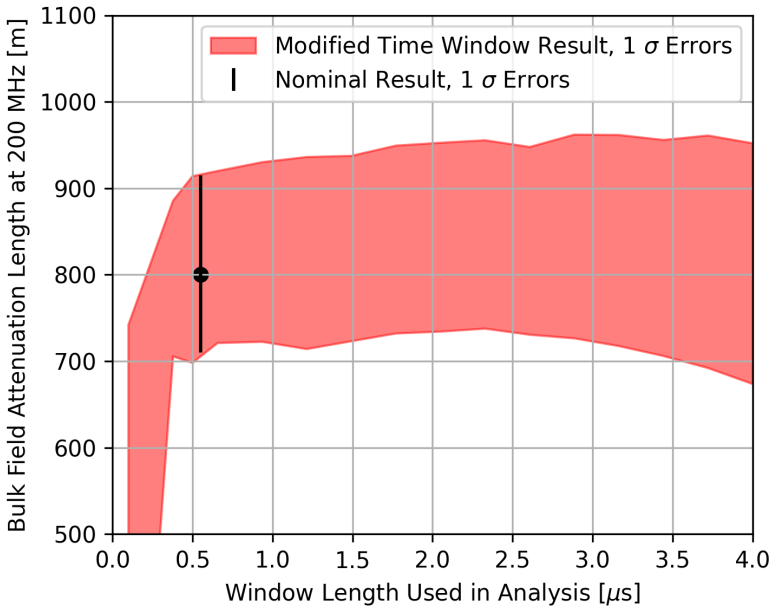

Figure 3.3: Measurement of the depth-averaged electric field attenuation at 200 MHz as a function of the window length used to select the bedrock echo. We note that including the entire diffuse component of the reflection into the final attenuation calculation increases the final result by no more than 10%.

that the additional attenuation length is within the systematic uncertainties of our stated result due to the large bedrock reflection coefficient uncertainty.

The relationship between bulk ice attenuation and received power is different for the specular vs. diffuse components. We define attenuation from the Friis transmission equation (implicit in Eq. 3.1) [121]. The Friis transmission equation is applicable for a specular reflection as it assumes direct line-of-sight propagation without interference within the first Fresnel zone, leading to a geometric path loss $\propto d_{ice}^2$. The radar range equation is more applicable to the diffuse component since it includes power contributions from a rough surface via the definition of a radar cross section and a geometric path loss $\propto (d_{ice}/2)^4$ [66]. We find that use of the radar range equation instead of the Friis equation over the combined specular and diffuse components also increases the measured attenuation length at lower frequencies by a maximum of 10%, albeit introducing more model dependence from the unknown value of bedrock radar cross section.

Based on the relatively small increase in obtained attenuation length from including the diffuse component, we quote our final result based on the Friis equation; this choice is consistent with previous similar measurements [69, 77, 67, 146, 62, 208].

Bedrock Depth

The bedrock depth can be derived from the absolute time of flight of the transmitted pulse and a model for the index of refraction of the ice as a function of depth. To reduce systematic biases (from location extrapolation and bedrock radio properties) and also as a cross check of our absolute timing calibration, we measure the bedrock depth from these data, rather than relying on previous measurements . The relationship between time of flight (Δt) and bedrock depth (half of the total distance propagated by the transmitted signal, d_{ice}) can be found by solving for d_{ice} in the integral:

$$\Delta t = \frac{2}{c} \int_0^{d_{ice}/2} n(z) dz, \tag{3.3}$$

where $n(z)$ is the model for the index of refraction as a function of depth [m]. Index of refraction is related to dielectric constant (ϵ') via $n(z) = \sqrt{\epsilon'(z)}$. The value of $\epsilon'(z)$ is derived from its relationship with measured ice density (ρ, [kg / m^3]) [174, 73]:

$$\epsilon'(z) = (1 + 0.854\rho(z))^2 . \tag{3.4}$$

The parameterization of the dependence of ice density on depth follows [101], who performed a double exponential fit with a critical density at a depth of 14.9 m [149]:

$$\rho(z) = \begin{cases} 0.917 - 0.594 e^{-z/30.8} & z \leq 14.9 \text{ m} \\ 0.917 - 0.367 e^{-(z-14.9)/40.5} & z > 14.9 \text{ m} \end{cases} \tag{3.5}$$

The uncertainty on the depth determination arises primarily from the uncertainty in the

asymptotic index of refraction of deep glacial ice, which we take to be $n = 1.78 \pm 0.03$ [81] for ice below the firn (deeper than 100 m at Summit Station). Using this refractive index profile, we calculate the bedrock to be at a depth of 3004^{+50}_{-52} m, corresponding to $d_{ice} = 6008^{+100}_{-104}$ m for the through-ice bedrock echo total travel distance.

We note that, while our transmitting and receiving antennas were separated by 244 m, the through-ice signal approximately propagates vertically and Eq. 3.3 holds true. Over the measured 6 km propagation distance, horizontal propagation results in 4 m extra path length.

This bedrock depth is consistent with previous measurements of the bedrock depth from [139], at 3053.5 m in 1993, and from [62], at 3014^{+48}_{-50} m in 2015.

Antenna Coupling

The antenna transmission coefficient is defined as the quantity of power transmitted by the antenna from an incident radio frequency signal on a 50 Ω transmission line at the antenna feed point (S_{21} in the scattering matrix). The transmission coefficient depends upon the dielectric properties of the antenna's embedded environment [128, 70]. To increase the power transmitted into the ice, we buried our antennas so that all active conductors were at least $\sim$ 20 cm below the surface, thereby embedding them in an environment of $n \approx 1.4$. The antennas used for the normalization are in air, for which $n \sim 1.0$. To correct for the change in match, we calculate a T_{ratio} from the measured reflection coefficient (S_{11} as shown in Fig. 3.4) of the four antennas, two in air and two in ice, taken in the field. Assuming that all power not reflected at the feed is transmitted, the ratio becomes, in terms of the reflection coefficient S_{11} in dB,

$$T_{ratio} = \frac{1 - 10^{S_{11,ice}/10}}{1 - 10^{S_{11,air}/10}}. \tag{3.6}$$

The antennas were found to transmit nearly all incident power in the frequency range

of interest (150–550 MHz) in both the in-air and in-ice cases, resulting in a small T_{ratio} correction. Averaged over frequency in the range of interest, $T_{ratio} = 1.00 \pm 0.05$, with the uncertainty assessed empirically from the variance of the measured match over the band. Our result is consistent with T_{ratio} measured by other groups using the same or similar antennas [67, 62].

In situ measurements, as well as simulations [70, 128], have shown that the frequency-dependent antenna gain G_0, measured in air, also changes when the antenna is embedded in a dielectric medium. This change can be modeled as a down-shift in frequency, by the index of refraction of the medium ($G'(\nu) = G_0(\nu/n)$). For the LPDA used in this work, the gain over the frequency band of interest is uniform to < 0.5 dBi [99], rendering the shift between in-air and in-ice measurements a subdominant systematic bias. The down-shift in frequency will cause a corresponding shift in low-frequency cutoff both in the gain and in the S_{11} (as shown in Fig. 3.4), but the cutoff in both environments is below the high-pass filter of our analysis.

We note that there will be different contributions from the ice surface in both the in-air and in-ice antenna responses. We neglect these effects because they are likely to be small so long as the directional antennas (front-to-back [F/B] ratio of the LPDA $\sim$-15 dB) are pointed away from the surface [70].

Firn Focusing

There is a geometric amplification of the bedrock echo electric field at the surface of the ice due to the changing index of refraction of the firn. To calculate the power focusing factor, for a negligibly thin firn layer, straightforward application of Snell's law prescribes that the electric field flux density measured at the surface, after bedrock reflection, follows:[239]:

$$F_f = \left(\frac{n(z=0)}{n(z=d_{ice}/2)} \right)^2 . \tag{3.7}$$

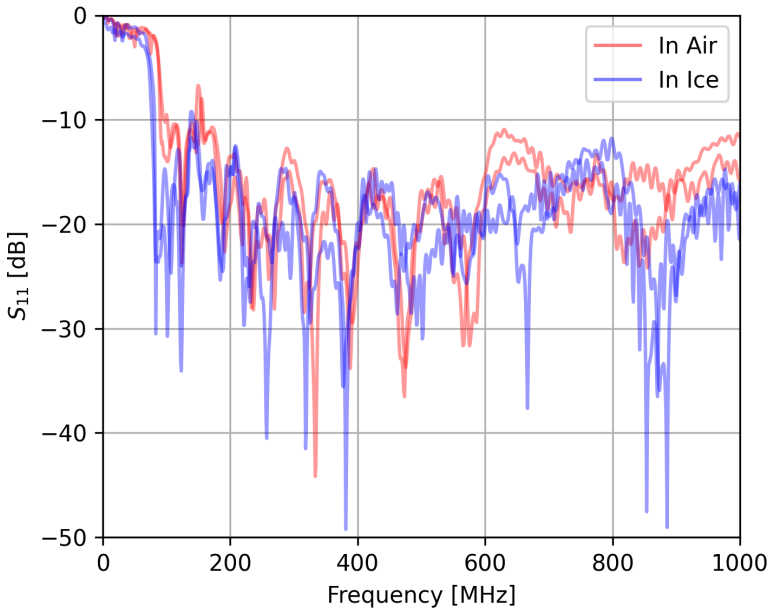

Figure 3.4: Measured S_{11} of each antenna used in the experiment. The difference in the low-frequency cutoff of the antenna when it is embedded in the ice compared to in air is due to the different indices of refraction of the two environments.

We have verified that this equation agrees with a ray tracing simulation and 3D FDTD simulation. The uncertainty on the focusing factor arises from the uncertainty in the index of refraction model. Using $n = 1.78 \pm 0.03$ [81] (as described previously in the **Bedrock Depth** section), and $n = 1.4 \pm 0.1$ for the surface ice [81], we obtain a final focusing factor of $F_f = 1.61 \pm 0.24$.

In-Air Normalization Amplitude

The amplitude of the signal from the in-air normalization run can be systematically biased from reflections off of the ice surface, increasing or decreasing the recorded power observed from the direct line-of-sight signal. Given the antenna heights above the ice (1.5 m) and distance between antennas (244 m), the first Fresnel zone is comprised by a nearly uniform, planar surface ice reflector, at all frequencies of interest. This leads to potential interference from reflections, depending on geometry: direct rays will interfere destructively/constructively

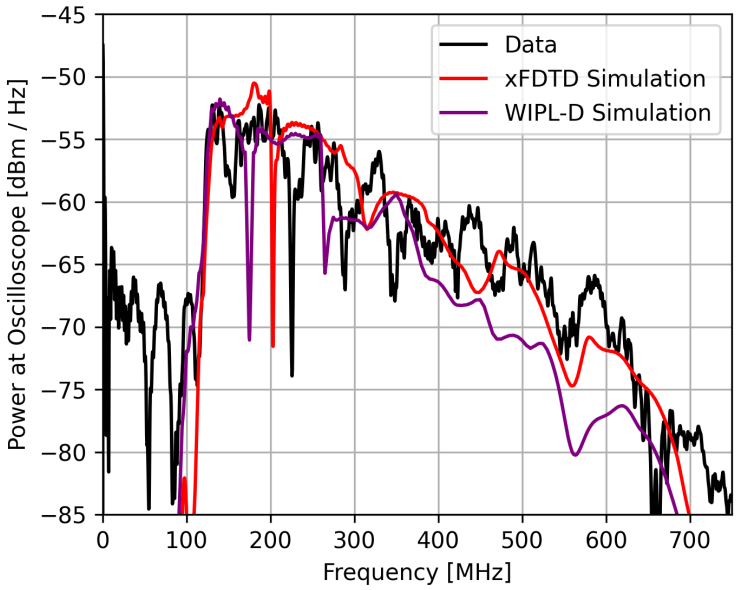

Figure 3.5: Comparison of data from the in-air normalization run compared against an absolute amplitude expectation as derived from two separate LPDA simulations. No systematic bias is evident within the ±10% voltage uncertainty in the antenna model [72, 70], over the frequency band of this analysis. The sharp dip between 180-220 MHz seen in data and simulations is most likely due to fine details in tine length and separation, which may be difficult to accurately simulate [72].

with rays at the center/periphery of the Fresnel zone. To quantify any possible systematic bias, we compare the data against the absolute amplitude expectation of the signal from simulation. The absolute amplitude is derived from a measurement of the FID pulse shape, amplifier response, filter response, free space path loss, and two independent simulations of the LPDA antenna response. Our simulations use either the Method of Moments software WIPL-D[3] or Finite Difference Time Domain software xFDTD[4], and have been found to agree with anechoic chamber measurements to 10% uncertainty [72, 70]. The comparison of the simulated result with our data, seen in Fig. 3.5, demonstrates that any possible systematic bias is not greater than 10% in voltage, consistent with previous results [72, 70].

3. `https://wipl-d.com`

4. `https://www.remcom.com/xfdtd-3d-em-simulation-software`

Result and Error Analysis

The measured depth-averaged field attenuation length is presented in Fig. 3.6. The previous *in situ* measurement reported by [62] is included for comparison, adjusted to remove the systematic bias from firn focusing not previously included in that analysis, resulting in a correction of their published result (from 947^{+92}_{-85}m to 913^{+85}_{-79}m). We report the measurement only within the bandpass limits of our system, over which we have the highest sensitivity and lowest systematic biases from antenna modeling and filter response. Beyond the system bandpass limits, we have checked that our procedure yields an attenuation length numerically consistent with zero as expected for a noise-dominated regime.

Contributions of different sources of uncertainty are calculated using a Monte Carlo method. We numerically calculate the estimated probability density distribution (PDF) of the bulk electric field attenuation within each frequency bin by repeatedly drawing random values of each component of the final measurement from their respective PDFs. For systematic uncertainties, we assume that each measured quantity used in the calculation of bulk field attenuation is uncorrelated and has a PDF either of a normal distribution (as is the case for F_f, T_{ratio} and d_{ice}) or the distribution already described in the text (as is the case for R). The main component of statistical uncertainty is due to fluctuations in the power contributions from thermal noise in the recorded oscilloscope trace. In the 150-300 MHz band, the uncertainty from noise statistical fluctuation is sub-dominant to systematic uncertainties, contributing less than 10% to the quoted uncertainty of each frequency bin. The final measurement is reported as a central value with one standard deviation (statistical plus systematic) error bars for those frequency bins that yield statistically significant results. For all other frequency bins, we report a 95% confidence level upper limit.

It is important to note that the majority of uncertainties are correlated in each frequency bin of the final measurement, with the primary contributions to the uncertainty arising from finite noise statistics and small systematic biases from the difference in LPDA response in

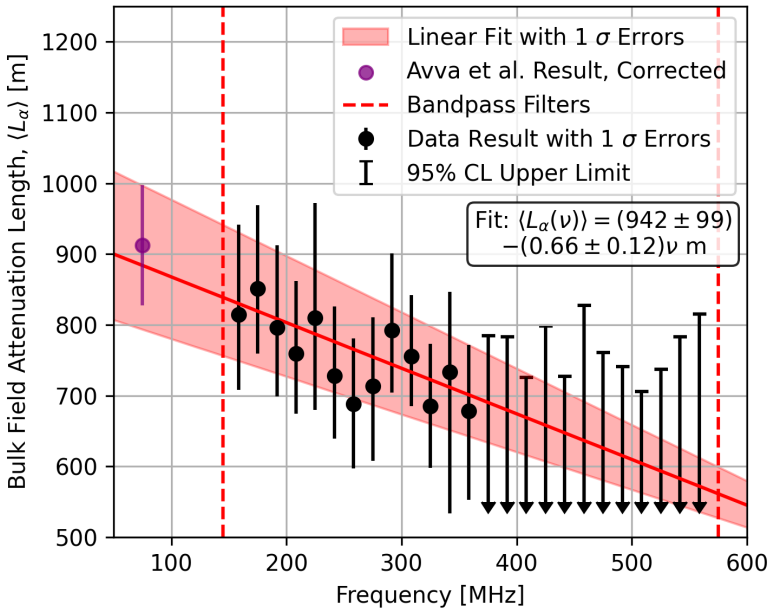

Figure 3.6: Measurement of the depth-averaged electric field attenuation as a function of frequency at Summit Station, within the system bandpass (shown as red dashed lines). Definitions of the error bars (and displayed upper limits) are provided in the text. The corrected result from [62] is shown for comparison. The frequency ν in the fit has units of MHz.

ice vs. air. For the linear fit presented below, the visibly high goodness of fit is due to this correlation of uncertainties between frequency bins.

The reported bulk attenuation length includes losses from layer scattering. While expected to be a subdominant effect for vertical propagation due to the low reflection coefficient of the observed layers [208], quantifying effects due to layer scattering for the more horizontal neutrino geometries must account for the larger Fresnel reflection coefficients at more glancing layer incidence angles [33].

Birefringence of the ice can result in rotation of the signal that is dependent on polarization, leading to apparent loss of power at the co-polarized receiver. Measurements of the crystal orientation at Summit Station indicate uniaxial fabric at all depths [244], unlike South Pole [188, 69], indicating that birefringence will matter less for the Greenland site, though this remains to be quantified.

Discussion and Summary

We derive the electric field attenuation length as a function of depth using a model of the field attenuation dependence on temperature and chemical impurities, as described in detail in [184, 185, 258]. For a medium with non-zero intrinsic conductivity, the attenuation length can be expressed as:

$$L_\alpha(f,z) = A(f)\frac{\epsilon_0\sqrt{\epsilon'_r(z)}c}{\sigma_\infty(z)}, \tag{3.8}$$

where c is the speed of light, ϵ_0 is the permittivity of free space, $\epsilon'_r(z)$ is the real component of the relative permittivity at a given depth z (defined in Eq. 3.4), $\sigma_\infty(z)$ is the infinite frequency limit of the electrical conductivity at a given depth, and the parameter $A(f)$ is extracted experimentally, by requiring that the integrated, depth-dependent attenuation match our measured value of full-path attenuation, at each frequency f. [122] suggest that the infinite frequency limit conductivity is valid at radio frequencies, since the molar conductivity does not change from low frequency (the frequency at which reference conductivity was measured, 0.3-3 MHz, [258]) to our frequency band (VHF/UHF, 150-550 MHz). The infinity frequency conductivity is related to chemical impurities and temperature via,

$$\begin{aligned}\sigma_\infty(z) = \sigma_{\text{pure}}\exp&\left[\frac{E_{\text{pure}}}{k}\left(\frac{1}{T_r}-\frac{1}{T(z)}\right)\right]\\ &+\mu_{\text{H}^+}[\text{H}^+](z)\exp\left[\frac{E_{\text{H}^+}}{k}\left(\frac{1}{T_r}-\frac{1}{T(z)}\right)\right]\\ &+\mu_{\text{Cl}^-}[\text{Cl}^-](z)\exp\left[\frac{E_{\text{Cl}^-}}{k}\left(\frac{1}{T_r}-\frac{1}{T(z)}\right)\right]\\ &+\mu_{\text{NH}_4^+}[\text{NH}_4^+](z)\exp\left[\frac{E_{\text{NH}_4^+}}{k}\left(\frac{1}{T_r}-\frac{1}{T(z)}\right)\right],\end{aligned} \tag{3.9}$$

where k is Boltzmann's constant, $T(z)$ is in-ice temperature at a given depth as measured at

Symbol	Description	Unit	Value
T_r	Reference temperature	°C	-21
σ_{pure}	Conductivity of pure ice	μS/m	9.2 ± 0.2
μ_{H^+}	Molar conductivity of H^+	S/m/M	3.2 ± 0.2
μ_{Cl^-}	Molar conductivity of Cl^-	S/m/M	0.43 ± 0.07
$\mu_{NH_4^+}$	Molar conductivity of NH_4^+	S/m/M	0.8
E_{pure}	Activation energy of pure ice	eV	0.51 ± 0.01
E_{H^+}	Activation energy of H^+	eV	0.20 ± 0.04
E_{Cl^-}	Activation energy of Cl^-	eV	0.19 ± 0.02
$E_{NH_4^+}$	Activation energy of NH_4^+	eV	0.23
T(z)	Ice temperature at depth z	°C	See 5
$[H^+](z)$	Molar concentration of H^+	μM	See 6
$[Cl^-](z)$	Molar concentration of Cl^-	μM	See 7
$[NH_4^+](z)$	Molar concentration of NH_4^+	μM	See 7

Table 3.1: Values of parameters used in the conductivity model of ice at Summit Station. Compiled from [184, 185] and from the GRIP borehole [139]. Molar concentrations and ice temperature are tables of data measured at the GRIP borehole, and are available at the corresponding links in the footnotes.

the GRIP borehole [139][5], T_r is a reference temperature, σ_{pure} is the conductivity of pure ice, μ_{H^+}, μ_{Cl^-}, and $\mu_{NH_4^+}$ are molar conductivities, E_{pure}, E_{H^+}, E_{Cl^-}, and $E_{NH_4^+}$ are activation energies, and $[H^+](z)$[6], $[Cl^-](z)$[7] and $[NH_4^+](z)$[7] are depth dependent molar concentrations as measured at the GRIP borehole [139, 177, 257]. The values of molar conductivities, conductivity of free ice, and activation energies as measured by [184, 185] and used in this analysis are given in Table 3.1. Note that, in this formulation, the temperature dependence of the attenuation length is explicitly absorbed into the conductivity dependence on temperature - the zero conductivity limit would correspond to no absorption and, correspondingly, no attenuation, for any temperature.

5. ftp://ftp.ncdc.noaa.gov/pub/data/paleo/icecore/greenland/summit/grip/physical/griptemp.txt

6. ftp://ftp.ncdc.noaa.gov/pub/data/paleo/icecore/greenland/summit/grip/ecm/gripdep.txt

7. ftp://ftp.ncdc.noaa.gov/pub/data/paleo/icecore/greenland/summit/grip/chem/gripion.txt

Using the model of electric field attenuation length as a function of depth, we then unfold and solve for the parameter $A(f)$, requiring that the depth-integrated attenuation matches our measured depth-averaged attenuation. The result reported at 300 MHz is plotted in Fig. 3.7. We note a conspicuous enhancement in the L_α(z) profile at depth $\gtrsim$1600 m; this feature tracks a similarly precipitous drop in the tabulated GRIP H^+ and NH_4^+ molar concentrations at z$\sim$1600 m, resulting in a corresponding enhanced radio-frequency transparency at those depths.

[62] derived the electric field attenuation length as a function of depth using a simplified model of the field attenuation dependence on temperature. They assume a linear relationship between the log of the attenuation versus the temperature of the ice:

$$L_\alpha(T(z)) = A \cdot 10^{mT(z)}. \tag{3.10}$$

The parameter m is taken to be the average of the two sites measured by [81] and set equal to -0.017 $(^\circ C)^{-1}$. The parameter A is derived from measured value of bulk field attenuation at each frequency and set equal to 200–280 m. For comparison, our result using the simplified model as reported at 300 MHz is plotted in Fig. 3.7.

The average electric field attenuation length of the top 1500 m of ice is of particular interest to RNO-G as the majority of neutrino interactions detectable by the experiment occur in this region [33]. It can be extracted from the bulk result using the field attenuation versus depth relation defined by [184, 185]. The average field attenuation length for the top 1500 m of ice result is shown in Fig. 3.8. For reference, the bulk attenuation measurement at 300 MHz is 756^{+71}_{-87} m ($-11.49^{+1.49}_{-0.99}$ dB / km) while the average attenuation measurement of the top 1500 m of ice is 926^{+107}_{-124} m ($-9.38^{+1.45}_{-0.97}$ dB / km).

Our measurement can be used in simulations that calculate RNO-G's sensitivity to astrophysical neutrinos. For those simulations, we include, for convenience, a linear fit to the average electric field attenuation length for the top 1500 m of ice, shown in Fig. 3.8. We find

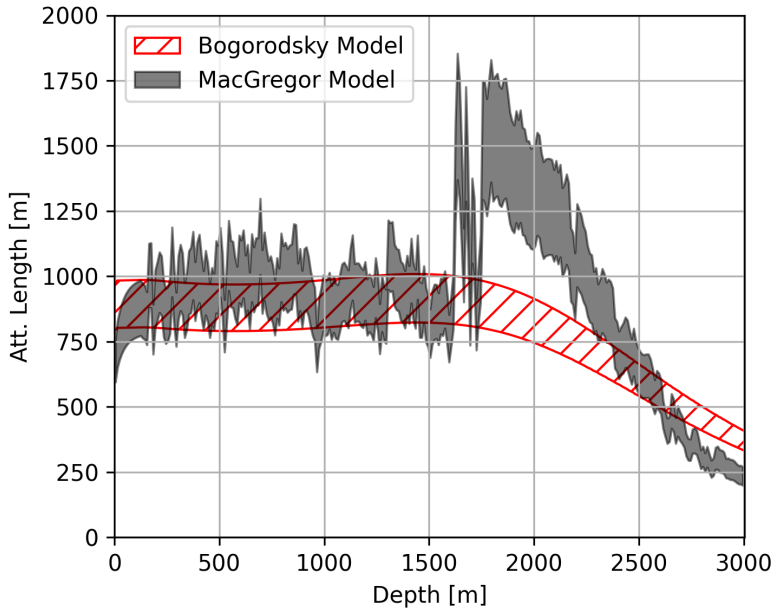

Figure 3.7: Electric field attenuation length as a function of depth at 300 MHz as derived from the two model of ice attenuation, one derived from temperature and chemical impurities [184, 185] (black) from temperature alone [81](red). Hatched and filled regions denotes $\pm 1\sigma$.

a significant correlation between the two parameters of the linear fit, which yields a slope of -0.81 ± 0.14 m / MHz (-0.12 ± 0.02 dB / km / MHz), intercept of 1154 ± 121 m (-7.53 ± 0.72 dB / km), and a correlation coefficient $\rho = -0.95$.

We compare our obtained result of the average electric field attenuation length for the top 1500 m at 300 MHz of 926^{+107}_{-124} m to other similar measurements. [62] extrapolated their results at 75 MHz to 300 MHz and estimated $\langle L_\alpha \rangle = 1022^{+230}_{-253}$ m, consistent (within uncertainty) with the result presented herein. The electric field attenuation length at the South Pole has been measured, with the focusing factor included, to be $\langle L_\alpha \rangle = 1660^{+255}_{-120}$ m at 300 MHz for the top 1500 m of ice [40], consistent with the colder ice at the South Pole ($\sim$–50°C compared to $\sim$–30°C at Summit Station).

Measurements of the bulk radio field attenuation length at Summit Station have also been performed using air-borne radio sounding data. [185] inferred the bulk radio field attenuation by comparing the relative strengths of internal reflectors, obtaining attenuation lengths of

750–850 m at 150–200 MHz around Summit Station, consistent (within uncertainty) with the result presented herein. [239] measured the bulk radio field attenuation using the relative strength of the radio echo from the snow surface and the bedrock, obtaining at an attenuation length of 546 ± 23 m at 150-200 MHz around Summit Station. This measurement is notably lower than our result and the measurement done by [185] potentially due to radiometric calibration issues [185, 239].

The RNO-G experiment, currently under construction at Summit Station in Greenland, is set to be one of the world's largest particle detectors. Our measurement of the bulk electric field attenuation length at Summit Station is consistent with previous measurements, with reduced systematic uncertainties. Our measurement will ultimately increase the precision of RNO-G's UHEN sensitivity estimates, which will either better motivate upper limits in the case of a null result or decrease uncertainties on the measured flux of ultra-high energy neutrinos in the universe in the case of observation.

The average field attenuation length of the top 1500 m of ice will be imported into NuRadioMC [129, 128] to be used in future detector simulations of RNO-G. A comparison of the model currently used in NuRadioMC and the updated measurement is shown in Fig. 3.9. Our updated measurement is within uncertainty of the previous model while significantly reducing the attenuation length uncertainty and acting as a confirmation that the linear extrapolation used by the Avva et al. measurement (and thus all previous RNO-G simulations) is valid. The measurement as derived from the Macgregor model in Fig. 3.9 will be the default model of attenuation used in RNO-G simulations, and updated simulated results of RNO-G's effective volume and electric field reconstruction uncertainty are forthcoming, but we can expect a small decrease in both the effective volume and field uncertainty.

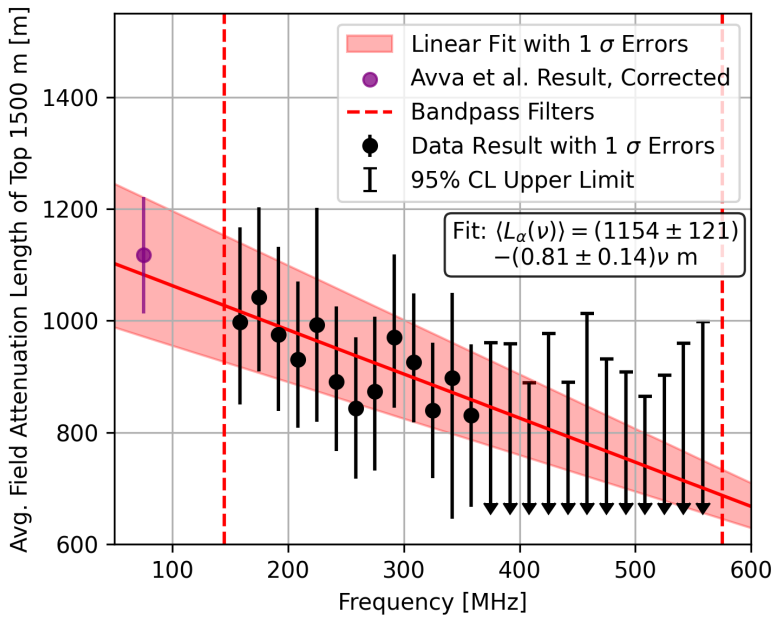

Figure 3.8: Measurement of the average electric field attenuation for the top 1500 m of the ice sheet, as a function of frequency at Summit Station, derived from the measured bulk field attenuation in Fig. 3.6 and the relationship between attenuation and temperature. Overlaid is the $\pm 1\sigma$ confidence interval of a linear fit of the data. Parameters of the fit are described in the text. Frequency ν in the fit is in units of MHz.

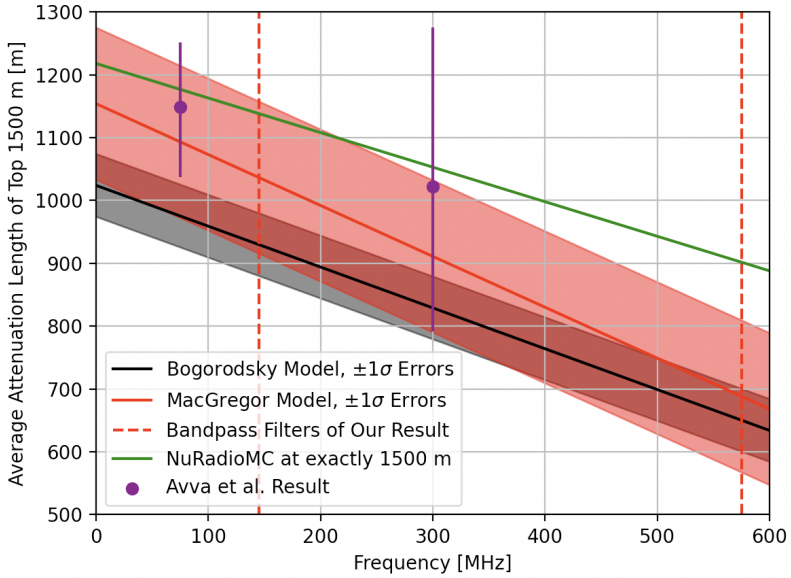

Figure 3.9: A comparison of the average electric field attenuation of the top 1500 m of ice at Summit Station as defined in NuRadioMC (green line) vs. the measurement presented in Fig. 3.8 (red and black shaded regions). The NuRadioMC result is based on an extrapolation of the Avva et. al measurement at 75 MHz [62] (purple line).

3.2 Birefringence

Broadly speaking, birefringence is any response of the ice that is a function of the polarization of the incident electromagnetic field. This behavior is modeled by the dielectric tensor ϵ that is induced by the crystal structure of the ice. Following the notation in [147], the ice is uniaxial and has a principal component (aligned with ice axis) equal to,

$$\epsilon = \begin{pmatrix} a & 0 & 0 \\ 0 & a & 0 \\ 0 & 0 & b \end{pmatrix} \tag{3.11}$$

where a and b are measurables and depend on the crystal structure of the ice. For a given crystal direction defined by the spherical coordinates θ and ϕ, the dielectric tensor will be rotated, creating non-zero off-diagonal components. On-diagonal components will result in a time delay for the given polarization (related to the index of refraction via $n_{ii} = \sqrt{\epsilon_{ii}}$) and off-diagonal components will result in electric field polarization rotation, changing the relative amplitude of the observed polarization. There may also be polarization-dependant loss as determined by the complex component of the dielectric tensor.

Since birefringence can impact reconstruction direction, energy reconstruction, and detector sensitivity, it is important to quantify. Crystal structure is partly determined by the direction of ice flow, which is very small and in the westerly direction at Summit Station [167], leading to birefringence effects that depend on the local ice flow direction. With this in mind, we created a measurement setup similar to that described in Sect. 3.1 that enables the collection of different polarizations of electric field relative to the ice flow direction to quantify birefringence effects at Summit Station.

The expected time delay differences from propagating long distances through the ice for different polarizations is the most straight-forward approach to measure birefringence. We measured the time-of-flight for a pulse transmitted down into the ice that reflects off the

bottom and returns to the surface while keeping the relative orientation of the transmitting and receiving antennas the same but rotated around a central point, as shown in Fig. 3.10. We collected data in four different orientations, thus four different polarizations. The long path length increases the precision of the measurement of differences of time-of-flight for the four polarizations tested.

The setup, seen in Fig. 3.11, differs from the measurement described in Sect. 3.1 by the removal of the air trigger path. To reduce timing uncertainties, we co-located the transmitting and receiving antennas. We elected not to bury the antennas since the increase in transmitted power offered by burying the antennas was no longer important: the signal arrival time rather than the signal amplitude is of most importance for this measurement. Both transmitting and receiving antennas had identical cable lengths which were themselves measured using a network analyzer. The data from the four polarizations takes the form of 20 runs of 10,000 averaged triggers, with the 200,000 averaged triggers (averaged in post-processing) showing the bed rock echo signal for each polarization. The precise position of each antenna in each iteration of data collection was measured to determine the electric field polarization relative to the ice flow. The survey is plotted in Fig. 3.10.

A complete analysis of the birefringence data is forthcoming.

3.3 Subsurface Layers

Subsurface layers are thin, reflective layers within the bulk ice that give rise to internal scattering as can be seen in at times before 20 μs in Fig. 3.2. There are multiple origins of these layers and the most reflective layers can be correlated to ash deposited by volcanic eruptions [141].

These layers are expected to have extremely small reflection coefficients of O(-60 dB) [208]. At more oblique angles, like the angles expected by the geometry of a signal propagating to the station from a neutrino interaction in the ice, the reflection coefficient of the layers

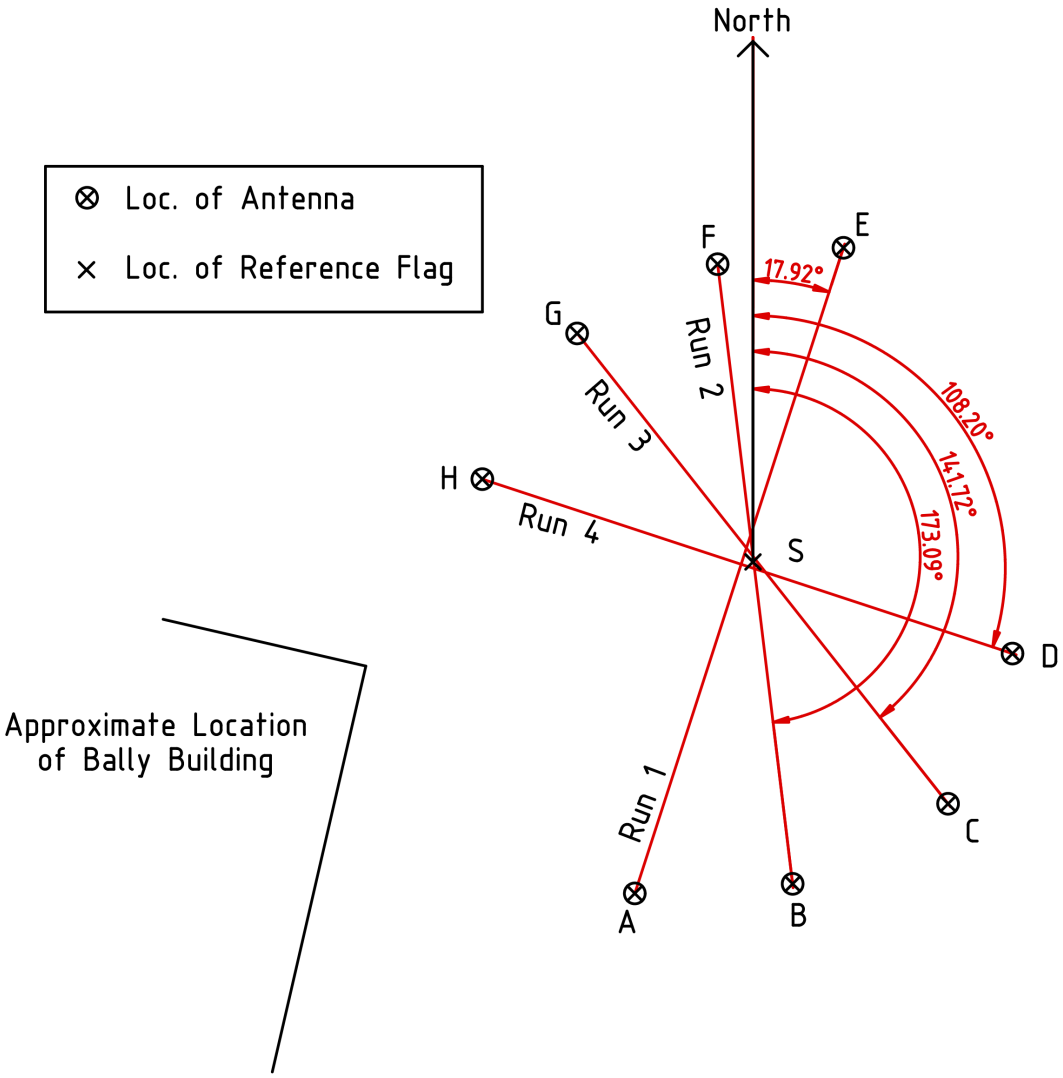

Figure 3.10: A top-down view of the survey of the antennas used in the four runs, including their angle relative to geographic north, used to determine electric field polarization relative to ice flow direction. At Summit Station, ice flow is slow and in the westerly direction [167].

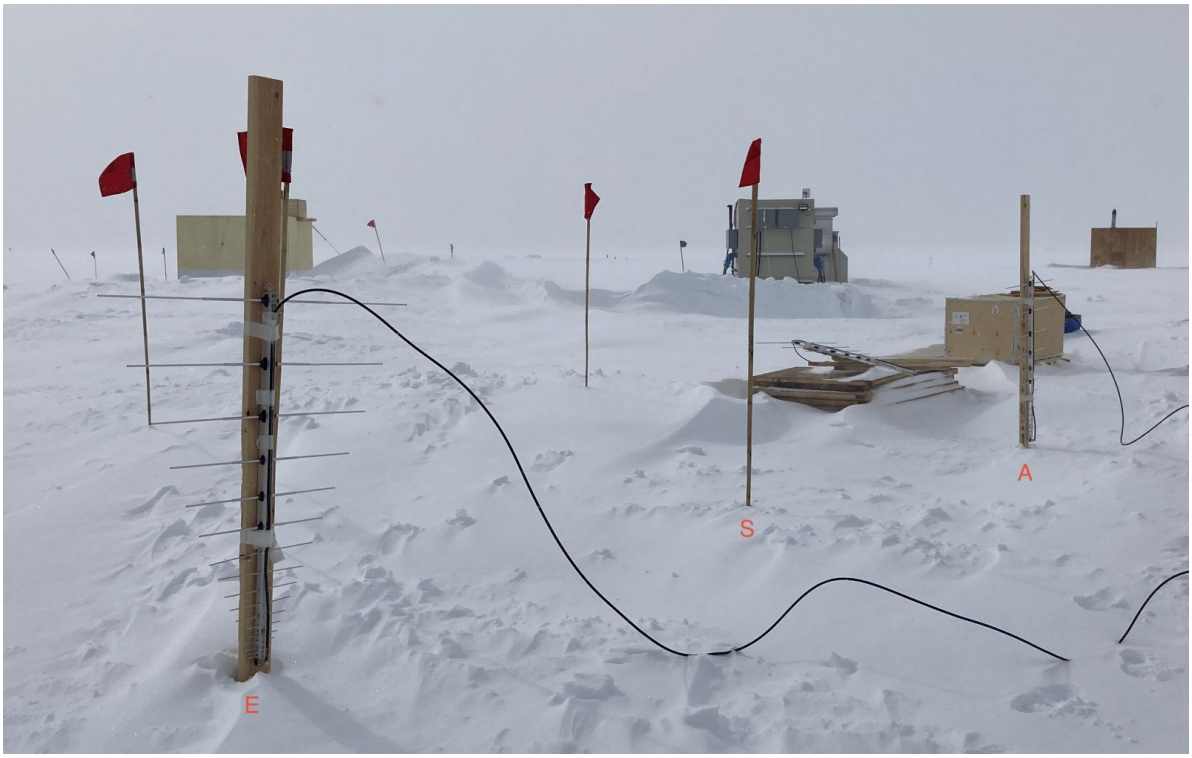

Figure 3.11: A photo of the birefringence measurement setup, showing the two LPDA antennas used for transmitting and receiving. Data collection and transmitting pulsing electronics are in the Bally building, to the right of the photo.

will be larger due to the increased Fresnel reflection coefficient. The subsurface layers may cause unexpected propagation paths for neutrino signals, 'shadowing' of neutrino signals (if the interaction happened below a reflective surface), and may introduce a background from the radio produced by an UHECR-induced EAS that enters the ice, reflects, and arrives at the detector in a direction similar to a neutrino-induced signal. Analysis of the reflection coefficient of subsurface layers in the bed rock echo reflection data is forthcoming to quantify the ultimate effect on detector volume, energy reconstruction uncertainty, and background contribution.

The subsurface layers have an additional potential utility: if their absolute depth can be determined via correlation to layers observed by the near-by GISP2 borehole [141], they can be used to determine the index of refraction of deep ice. The GISP2 borehole was created for deep ice core studies. The data is now freely available [139] and includes information such as the conductivity of the ice at a measured depth. Currently, the best measurement of the index of refraction of deep glacial ice is $n = 1.78 \pm 0.03$ [81]. Given the large number of bright subsurface reflectors at depths below ~ 500 m depth, the measurement of time-of-flight between subsurface layers has the promise to greatly reduce the uncertainty of deep glacial ice and, at the very least, provide a double check of the widely used measurement by Bogordsky [81]. A complete analysis of this data and technique is forthcoming.

CHAPTER 4

SOURCE OF ICECUBE'S DIFFUSE NEUTRINO FLUX

This chapter contains material published as D. Smith *et al.* Revisiting AGN as the Source of IceCube's Diffuse Neutrino Flux, Journal of Cosmology and Astroparticle Physics [233]. Reuse is permitted according to the copyright agreement used by the journal.

In 2013, the IceCube Collaboration reported the detection of a diffuse flux of astrophysical high-energy neutrinos. The spectrum of these neutrinos is consistent with a power-law with an index of $\alpha \approx 2.4 - 2.6$, extending from tens of TeV to several PeV [6], and with flavor ratios that are consistent with those predicted from the decays of charged pions [3]. The angular distribution of this flux shows no significant departures from isotropy [9, 106], and searches for individual point sources in the IceCube data have thus far not resulted in any detections [15, 8, 2] (with the possible exception of the blazar TXS 0506+056 [12, 11]). These results indicate that IceCube's high-energy neutrinos are produced by a large number of extragalactic sources, of which even the brightest contribute only a small fraction of the total flux.

Many varieties of astrophysical objects have been proposed as potential sources of high-energy neutrinos, including gamma-ray bursts [255, 211, 249, 192, 142, 104, 105], star-forming and starburst galaxies [180, 183], both blazar and non-blazar active galactic nuclei (AGN) [236, 143, 61, 186, 193], as well as tidal disruption events [253, 230, 100, 182, 202], fast radio bursts [171, 10, 110], and galaxy clusters [113, 173, 112]. Most of these proposals, however, have since been excluded as the primary source of IceCube's diffuse flux. In particular, the lack of neutrino events observed in coincidence with known gamma-ray bursts has ruled out this class of objects as a major source of IceCube's neutrinos [5, 163, 14] (with the possible exception of low-luminosity gamma-ray bursts [196, 241, 229]). Similarly, the lack of neutrino events from the direction of gamma-ray blazars excludes this class of sources [7, 158]. Starburst and other starforming galaxies are also unable to generate the entirety of IceCube's

signal between 10-100 TeV without simultaneously exceeding the measured intensity of the isotropic gamma-ray background [75, 198, 209, 210].

In this paper, we attempt to measure or constrain the fraction of IceCube's diffuse neutrino flux that originates from blazars and non-blazar AGN. We also consider starburst galaxies and other starforming galaxies within this context. To this end, we follow a procedure similar to that taken in Refs. [2, 7, 158] in searching for correlations between the arrival directions of IceCube's muon track events and the locations of known AGN. We improve and expand upon these previous studies by utilizing the latest (3 year) public release of IceCube muon track data [13], as well as the latest catalog of gamma-ray emitting AGN detected by the Fermi Gamma-Ray Space Telescope (the 4LAC catalog) [36]. The latter update is particularly important in the case of non-blazar AGN, as the current catalog of such sources detected by Fermi is much larger than those used in previous studies (65, compared to 19 non-blazar AGN used in Ref. [158], for example). Despite these advances, we do not identify any statistically significant correlation between IceCube events and known blazars or non-blazar AGN. From this, we are able to conclude that no more than 15% of IceCube's diffuse high-energy neutrino flux can originate from blazars. The constraint we derive on neutrinos from non-blazar AGN is significantly less restrictive, and it remains possible that this class of sources could produce the entirety of the astrophysical flux observed by IceCube. This scenario is expected to be within the reach of IceCube after relatively modest increases in exposure, and with expansions of gamma-ray catalogs of non-blazar AGN. This is particularly interesting given the evidence that non-blazar AGN produce the majority of the isotropic gamma-ray background [157], and are likely to represent the dominant source of IceCube's diffuse neutrino flux [156]. Starburst and other starforming galaxies may also substantially contribute to the signal observed by IceCube, in particular at the lowest detected energies.

4.1 Methods

In this analysis, we make use of IceCube's most recent public data release of muon tracks, consisting of events collected between June 2010 and May 2013 [13].[1] The first year of this data is from the 79-string detector, while the remaining two years are from the complete, 86-string detector. Each year of data contains 93133, 136244, and 105300 events, respectively. Each event has a reported direction, angular resolution, and a quantity known as the "energy proxy", which is related to the energy deposited in the detector. Each year of this dataset includes an effective area for the detector as determined by simulation, as a function of declination and neutrino energy.

To test for evidence of a neutrino signal from an individual point source, we follow the approach outlined in Ref. [83]. The likelihood that a given source results in n_s events, out of a total N recorded in the detector, is given by:

$$\mathcal{L}(n_s) = \prod_i^N \left[\frac{n_s}{N} S_i(|\vec{x}_s - \vec{x}_i|) + \left(1 - \frac{n_s}{N}\right) B_i(\sin\delta_i) \right], \tag{4.1}$$

where S_i and B_i are the signal and background probability distribution functions (PDFs), respectively. These PDFs are defined as follows:

$$\begin{aligned} S_i &= \frac{1}{2\pi\sigma_i^2}\, e^{-\frac{|\vec{x}_s - \vec{x}_i|^2}{2\sigma_i^2}} \\ B_i &= \frac{\mathcal{P}_B(\sin\delta_i)}{2\pi}, \end{aligned} \tag{4.2}$$

where $\vec{x}_s$ is the direction to the source, $\vec{x}_i$ is the reported direction of the event, and σ_i is the angular resolution of the event. The function, P_B, is equal to the fraction of events in the dataset averaged across a band of $\pm 6^\circ$ in declination, δ, around a given source. We only consider sources with declination between $\pm 87^\circ$ due to the limited amount of solid angle

1. https://icecube.wisc.edu/science/data/PS-3years

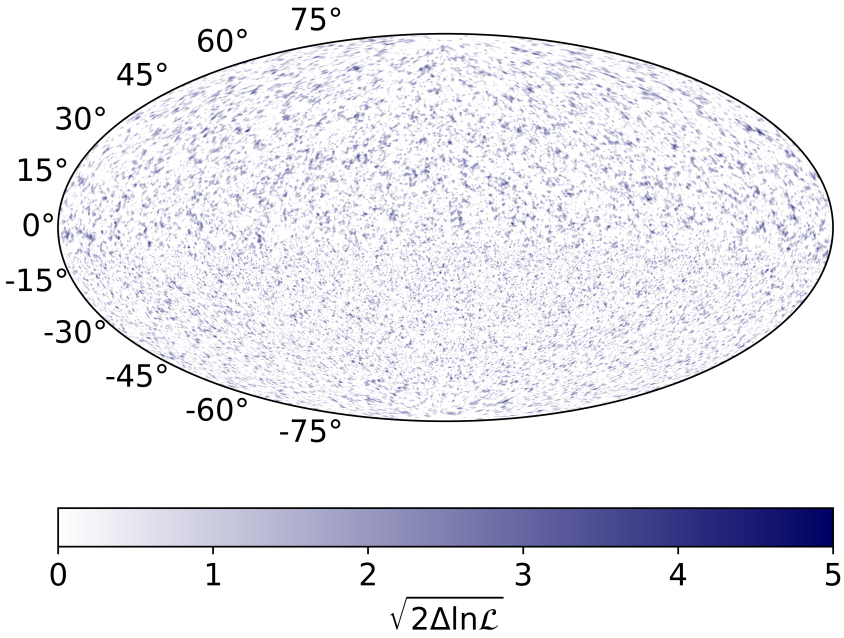

Figure 4.1: An all-sky map of the likelihood of a neutrino point source, $\sqrt{2\Delta \ln \mathcal{L}}$, in RA and Dec in Aitoff projection.

near the poles with which to characterize the background PDF.

The statistical significance in favor of a neutrino point source over a background-only hypothesis is calculated using the following test statistic:

$$2\Delta\mathcal{L}(n_s) = 2\big[\ln \mathcal{L}(n_s) - \ln \mathcal{L}(0)\big], \tag{4.3}$$

where $\mathcal{L}(0)$ is the likelihood for the background-only hypothesis. From this, the p-value can be calculated by performing an integral over a χ^2 distribution with one degree-of-freedom.

In contrast to the analysis performed by the IceCube Collaboration [8], we do not include energy information in our analysis, due to our inability to reliably relate the "energy proxy" provided in the public dataset with the actual energy of the neutrinos without access to the full IceCube detector simulation. The energy enters our analysis only in the form of

IceCube's energy-dependent effective area. This analysis also differs from that of the IceCube Collaboration in that their analysis uses 7 years of data, while our study is limited to the 3 years of data that is publicly available at this time.

In Fig. 4.1, we show an all-sky map of the likelihood of a neutrino point source, $\sqrt{2\Delta \ln \mathcal{L}}$, in terms of right ascension and declination in Aitoff projection. This scan was performed in steps of 0.1°, and at each point we show the result using the value of n_s that maximizes the test statistic defined in Eq. 4.3. In Fig. 4.2, we show that the distribution of this test statistic across the sky is consistent with that expected from Gaussian fluctuations. As in Ref. [158], we identify a slight excess of events in the range of $\sqrt{2\Delta \ln \mathcal{L}} \approx 4-5$. Given that this could quite plausibly be attributed to inaccuracies in the background PDF, we do not consider this to be evidence of a near-threshold point source population. In Table 4.1, we list the six most significant points identified in our all-sky scan. After accounting for an appropriate trials factor, these do not represent statistically significant point sources.

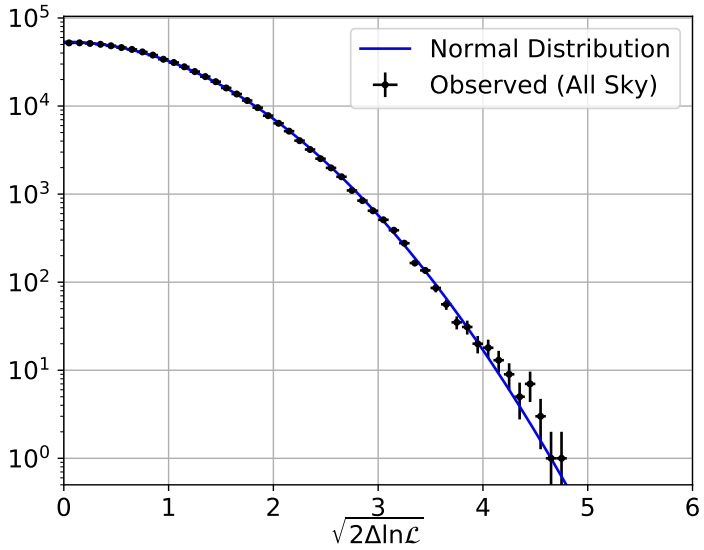

Figure 4.2: The likelihood distribution in favor of a neutrino point source from our all-sky scan. The observed distribution is consistent with background and we identify no evidence of a neutrino point source population. Sky locations with $\Delta \ln \mathcal{L} < 0$, corresponding to a best fit with a negative point source flux, are not shown. The error bars represent the 68% Poissonian confidence interval on each bin.

$2\Delta \ln \mathcal{L}$	Pre-Trial p-value	RA	Dec
22.28	2.36×10^{-6}	174.6	-39.2
21.72	3.15×10^{-6}	296.4	-21.0
20.79	5.12×10^{-6}	67.8	38.8
20.25	6.79×10^{-6}	349.0	31.0
19.80	8.60×10^{-6}	275.6	11.4
19.36	1.08×10^{-5}	42.0	-5.6

Table 4.1: The six most significant independent locations identified by our all-sky scan. After accounting for an appropriate trial factor, these do not represent statistically significant point sources.

Next, we use the public IceCube dataset to measure or constrain the fraction of IceCube's diffuse neutrino flux that originates from known classes of astrophysical objects. The joint likelihood in each case is calculated as the product of the likelihoods for each source, as described in Eq. 4.1, as a function of the total neutrino flux from the entire source population.

In calculating the joint probability, we consider three different hypotheses for the expected neutrino fluxes from the members of a given source class:

1. Gamma-Ray Scaling: The neutrino flux from a given source is taken to be proportional to the gamma-ray flux observed from that source, as reported in the 4LAC catalog [36]. Here we take the gamma-ray flux to be the number of photons between 1-100 GeV per area, per time. Such a proportionality would be expected if the observed gamma-ray emission is produced mostly through hadronic interactions, resulting in a fixed ratio of neutrinos and photons. If the gamma-ray and neutrino luminosity functions are substantially distinct, the limits obtained with this choice of scaling could potentially be violated [261].

2. Geometrical Scaling: The neutrino flux from a given source is taken to be proportional to $1/D_L^2$, where D_L is the luminosity distance of the source. This hypothesis treats the neutrino luminosity of a given source as uncorrelated to other information, and only takes into account the distance from the source. Since this approach can only make

use of sources with a measured redshift, it sometimes requires the use of smaller source catalogs.

3. Flat Scaling: The neutrino flux from a given source is taken to be entirely uncorrelated to any other information under consideration. This hypothesis is maximally conservative, in that it is predicted to produce a constraint that is valid for any distribution of neutrino fluxes from the collection of sources under consideration [7].

These hypotheses were each applied in our previous study [158], as was the case of gamma-ray scaling in Ref. [15]. Here, we expand upon this earlier work by considering a range of updated source catalogs and utilizing the 3-year public data release of IceCube muon track events.

4.2 Searching for Neutrinos from 4LAC Blazars

In this subsection, we consider the blazars contained within the Fourth Catalog of AGN detected by the Fermi Large Area Telescope (the 4LAC catalog). More specifically, of the 2863 sources in this catalog, we consider the 2796 classified as blazars, which includes 658 flat spectrum radio quasars (FSRQs), 1067 BL Lacs, and 1071 other sources classified as "blazars of unknown type". There are three AGN in this catalog that we do not consider due to their location within 3° of the poles (for which we are not able to reliably characterize the background distribution).

We begin by considering each of the 2860 sources in the 4LAC catalog independently (including both blazar and non-blazar AGN). In Table 4.2, we list the 10 of these sources that yielded the highest statistical significance in our analysis, along with their reported gamma-ray flux, redshift, and their source type as classified by the Fermi Collaboration [36]. While we cannot rule out the possibility that one or more of these sources is producing neutrinos, none is statistically significant after accounting for an appropriate trials factor.

4FGL Name	AGN Type	z	$\Phi_{1-100\,\mathrm{GeV}}$	$2\Delta \ln \mathcal{L}$
J2228.6-1636	AGN (unknown type)	0.52	2.86×10^{-12}	12.31
J1211.6+3901	BL Lac	0.60	1.45×10^{-12}	10.79
J2235.3-4836	FSRQ	0.51	1.05×10^{-11}	10.48
J1435.9-8348	AGN (unknown type)	–	4.51×10^{-12}	9.29
J0808.5+4950	FSRQ	1.44	5.16×10^{-12}	8.84
J1027.2+7427	AGN (unknown type)	0.88	9.31×10^{-12}	8.33
J1829.2-5813	FSRQ	1.53	3.13×10^{-11}	8.04
J0532.0-4827	BL Lac	–	4.49×10^{-11}	7.85
J1401.2-0915	FSRQ	0.67	3.13×10^{-12}	7.18
J0928.4-0415	AGN (unknown type)	–	3.46×10^{-12}	7.11

Table 4.2: The 10 sources from the 4LAC catalog with the greatest evidence for neutrino emission, along with their redshift (when available) and gamma-ray flux as measured by Fermi [36]. None of these sources are statistically significant after accounting for an appropriate trials factor.

Furthermore, we have not identified anything about this collection of sources that sets them apart from other representative samples of sources within the 4LAC catalog; they do not appear to be systematically brighter (in gamma rays), nearby, or otherwise notable.

In Fig. 4.3, we show the likelihood distribution of our analysis, for the 2796 sky locations associated with 4LAC blazars. As with the all-sky scan, we observe no significant evidence of any departure from Gaussian fluctuations. Next, we consider the joint probability of neutrino emission from this class of sources. In the left frames of Fig. 4.4, we show how the likelihood changes with the total neutrino flux from 4LAC blazars, for each of the three weighting hypotheses described in Sect. 4.1, and for two choices of the spectral index (2.0 and 2.5). The value of $\alpha = 2.5$ is motivated by the measured shape of IceCube's diffuse neutrino spectrum, whereas $\alpha = 2.0$ is the value naively predicted from Fermi acceleration. For the results shown in the upper frames, we include all 2796 of the blazars in the 4LAC catalog. In the lower frames, we limit our analysis to the 1674 of these blazars (160 FSRQs, 700 BL Lacs, and 814 blazars of unknown type) that do not exhibit significant variability in their gamma-ray emission. More quantitatively, we include in the lower frames only those sources with

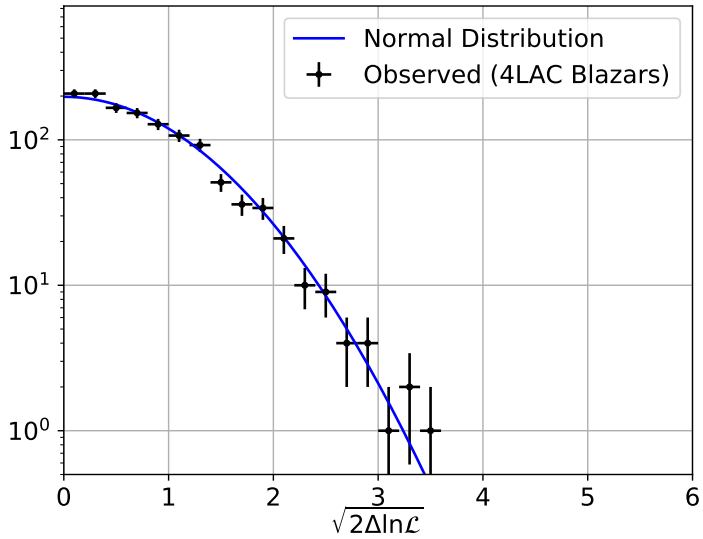

Figure 4.3: The likelihood distribution in favor of a neutrino point source at the locations of 2796 blazars in the 4LAC catalog. The observed distribution is consistent with background and we identify no evidence of neutrino emission from this population of sources. Sky locations with $\Delta \ln \mathcal{L} < 0$, corresponding to a best fit with a negative point source flux, are not shown. The error bars represent the 68% Poissonian confidence interval on each bin.

a variability index below 18.48, as reported by the Fermi Collaboration [25].[2] There is no strong dependence upon variability threshold value and our measured flux limits, suggesting that this classification approach well separates the two source populations. In none of these cases do we obtain any statistically significant evidence for neutrino emission. We then proceed to place a 95% confidence level upper limit (corresponding to $2\Delta \ln \mathcal{L} = -3.84$) on the total neutrino emission from this collection of sources. The limits we obtain are well below the diffuse flux reported by the IceCube Collaboration [6], indicating that these blazars cannot produce a large fraction of the observed neutrinos.

In the right frames of Fig. 4.4, we show the upper limits that we have derived on the neutrino flux from blazars, and compare this to diffuse flux reported by the IceCube Col-

2. The variability index is defined as the difference in the log-likelihood between the flux fitted in each time interval and the average flux over the full catalog interval. Sources with a variability index greater than 18.48 are detected to be variable at the 99% confidence level [25].

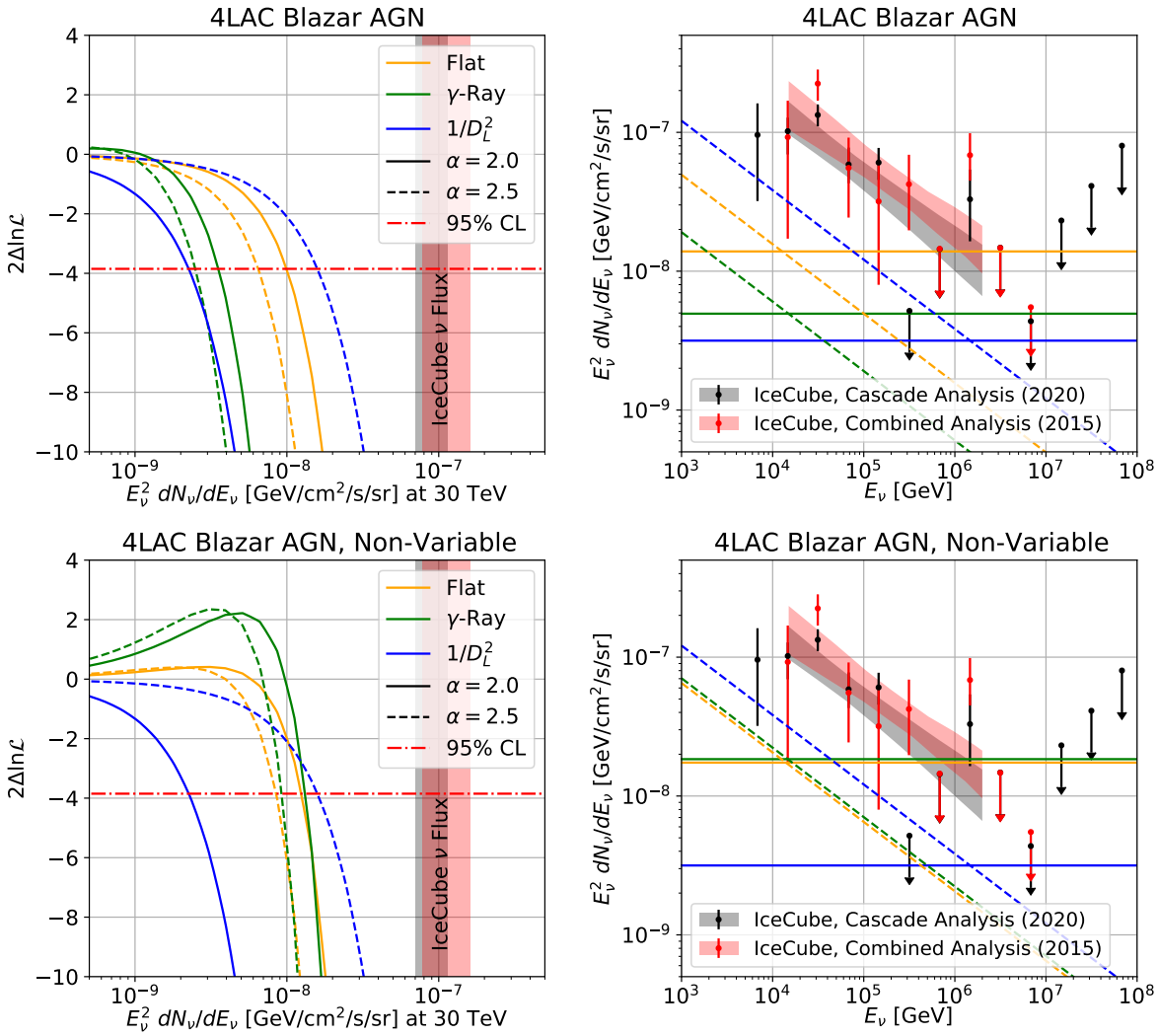

Figure 4.4: **Left figures:** The change to the log-likelihood as a function of the total, all-flavor neutrino emission from the blazars contained in the 4LAC catalog, for two choices of the neutrino spectral index, α, and for the three flux weighting hypotheses described in Sect. 4.1. We do not detect any statistically significant evidence for neutrino emission from this class of sources. **Top figures:** The results based on all of the 2796 blazars contained in the 4LAC catalog. **Bottom figures:** The result from only the 1674 of these blazars that do not exhibit statistically significant variability in their gamma-ray emission. **Right figures:** The 95% confidence level upper limits on the total neutrino flux from these source populations, and compare these constraints to the diffuse neutrino flux as reported by the IceCube Collaboration [4, 18]. We have weakened the constraints by an appropriate completeness factor that accounts for the emission from blazars that are too distant or too gamma-ray faint to be included in the 4LAC catalog. From these results we conclude that no more than $\sim 15\%$ of IceCube's neutrino diffuse flux can originate from blazars.

laboration. Here, we show the all-flavor diffuse flux as reported in IceCube's 2015 analysis of both cascades and muon tracks [4], and their more recent analysis of cascade events in six years of data [18]. In each case, we show the individual error bars associated with the measurement, as well as a shaded band, which represents the range of power-laws (between $\sim$20 TeV and $\sim$3 PeV) that is supported by the data.

In the left frame of this figure, these results specifically apply to the blazars contained in the 4LAC catalog. In order to translate this result to apply to the population of all blazars (including those that are too distant or gamma-ray faint to be included in the 4LAC), we weaken the limits in the right frames by a completeness correction factor of 1.4. Note that this quantity was originally calculated in Ref. [7] in order to account for the fraction of the total gamma-ray emission from blazars that did not come from sources contained in the 2FGL catalog. Since the 4LAC catalog is significantly more complete than the 2FGL, a more accurate completeness factor would be less than 1.4 and closer to unity. In an effort to present a conservative constraint, however, we retain the value of 1.4 in our analysis. There is one caveat with this approach to calculating a completeness factor: the potential anti-correlation between the gamma-ray and neutrino emissions in the potentially optically thick environment of a blazar would result in an erroneously low completeness factor and thus incorrect limits.

From the upper limits presented in this subsection, we conclude (at the 95% confidence level) that blazars can produce no more than $\sim$ 15% of the neutrino flux reported by IceCube. If we were to adopt the flat or gamma-ray scaling hypotheses, the constraints would be even more restrictive. These results are consistent with those presented by the IceCube Collaboration [7], our previous analysis [158] and independent limits obtained from neutrino anisotropy searches [201]. We note that our analysis benefits from the use of the larger 4LAC catalog, which contains approximately $\sim$ 60% more sources than were utilized in our previous study. For completeness, we have also applied the above described procedure to

those blazars categorized in the 4FGL as BL Lacs, or categorized as FSRQs. Again, we find no evidence in favor of neutrino emission from these source populations, allowing us to place limits on their contribution to IceCube's diffuse neutrino flux.

It is important to acknowledge the apparent lack of improvement upon our previous blazar flux limit results [158] regardless of the increased data sample and more complete blazar catalog. Breaking the blazar sources into FSRQs and BL Lacs in Fig. 4.5, the lack of improvement stems from BL Lac sources, suggesting that BL Lac blazars may be associated with the IceCube data. Removing the TXS 0506+056 from the stacking search does not appreciably strengthen limits, suggesting that many yet-to-be-associated BL Lacs can be contributing upwards to $\sim 10\%$ of the reported astrophysical neutrino flux. However, no flux hypothesis nor subset of the BL Lac sources has led to a statistically significant signal.

4.3 Searching for Neutrinos from Non-Blazar AGN

Although blazars cannot produce most of IceCube's diffuse neutrino flux, other types of AGN remain far more promising in this context. In particular, non-blazar AGN (those whose jets are not pointed in the direction of Earth) are less luminous and far more numerous than blazars, making it more difficult to constrain their contribution to the diffuse flux of high-energy neutrinos. Furthermore, it has been demonstrated that the isotropic gamma-ray background, as measured by the Fermi Gamma-Ray Space Telescope [28], is dominated by emission from unresolved non-blazar AGN [157] (see also Refs. [35, 90, 119]). If the gamma-ray emission from these sources is generated through the interactions of cosmic-ray protons with gas in optically thin environments, then they should also produce a spectrum of high-energy neutrinos that is similar to that measured by IceCube [156]. In contrast, if non-blazar AGN do *not* produce the bulk of IceCube's diffuse flux, then the sources of IceCube's neutrinos must produce their neutrino emission in environments that are optically thick to gamma rays, allowing the high-energy photons that are produced in conjunction

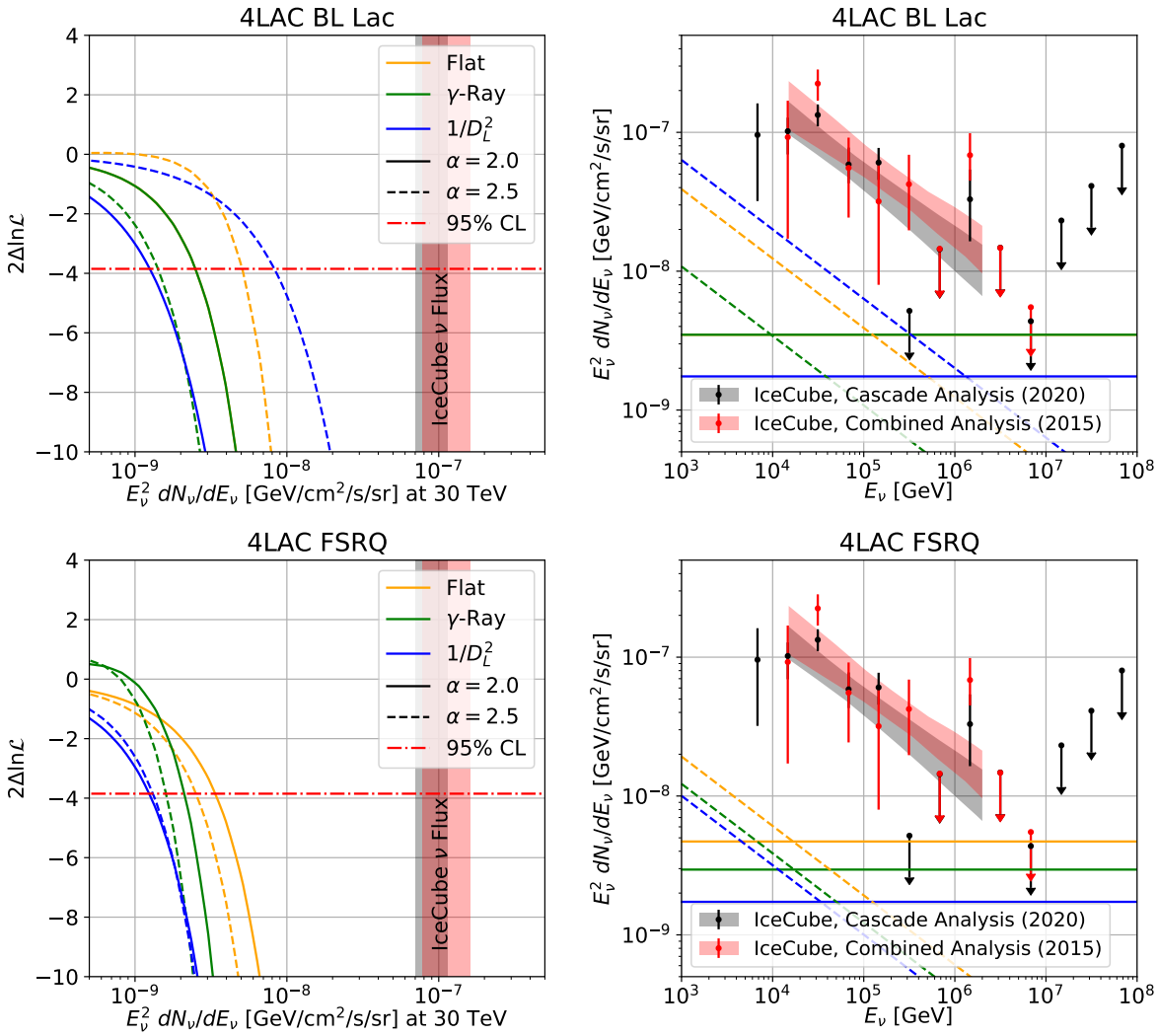

Figure 4.5: **Left figures:** The change to the log-likelihood as a function of the total, all-flavor neutrino emission from the BL Lac and FSRQ sources contained in the 4LAC catalog. We do not detect any statistically significant evidence for neutrino emission from this class of sources. **Right figures:** The 95% confidence level upper limits on the total neutrino flux from these source populations, and compare these constraints to the diffuse neutrino flux as reported by the IceCube Collaboration [4, 18]. We have weakened the constraints by an appropriate completeness factor that accounts for the emission from blazars that are too distant or too gamma-ray faint to be included in the 4LAC catalog. From these results we conclude that no more than $\sim 10\%$ of IceCube's neutrino diffuse flux can originate from BL Lacs and $\sim 5\%$ can original from FSRQs.

with neutrinos through pion decay to be absorbed and thus not excessively contribute to the isotropic gamma-ray background [200, 15, 86].

In this subsection, we consider 65 non-blazar AGN, including the 63 contained in 4LAC catalog, as well as Centaurus B and 3C 411. Note that whereas the core and lobes of Centaurus A are listed as two sources in the 4LAC, we sum these gamma-ray fluxes and treat Centaurus A as a single source in our analysis. This collection of sources includes objects that Fermi classifies as compact steep-spectrum quasars, narrow line Seyfert 1 galaxies, radio galaxies, Seyfert galaxies, soft-spectrum radio quasars, and other non-blazar AGN of uncertain type. Of these 65 sources, 47 are non-variable, following the criteria described in Sect. 4.2.

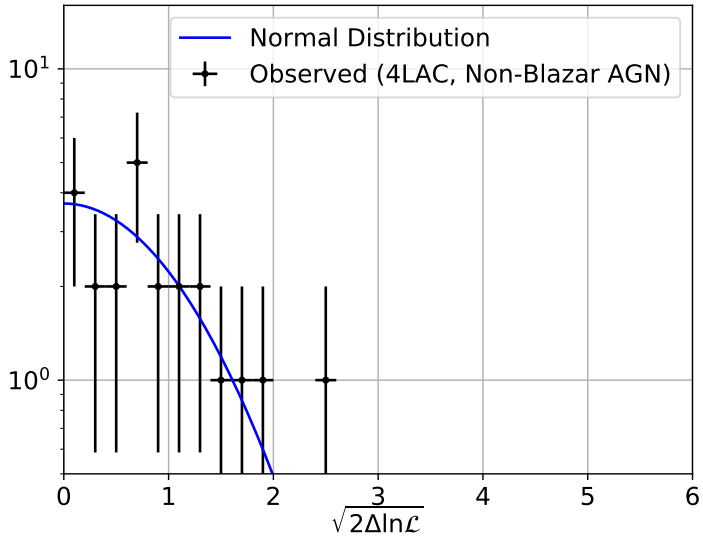

Figure 4.6: The likelihood distribution in favor of a neutrino point source at the locations of 47 non-variable non-blazar AGN in the 4LAC catalog. The observed distribution is consistent with background and we identify no evidence of neutrino emission from this population of sources. Sky locations with $\Delta \ln \mathcal{L} < 0$, corresponding to a best fit with a negative point source flux, are not shown. The error bars represent the 68% Poissonian confidence interval on each bin.

In Fig. 4.6, we plot the likelihood distribution for our sample of 47 non-variable, non-blazar AGN. Here, we have chosen to focus on the non-variable sources, as those AGN that exhibit a high degree of variability are generally throught to produce their gamma-ray emission primarily through leptonic processes. As with our results for the all-sky and blazar

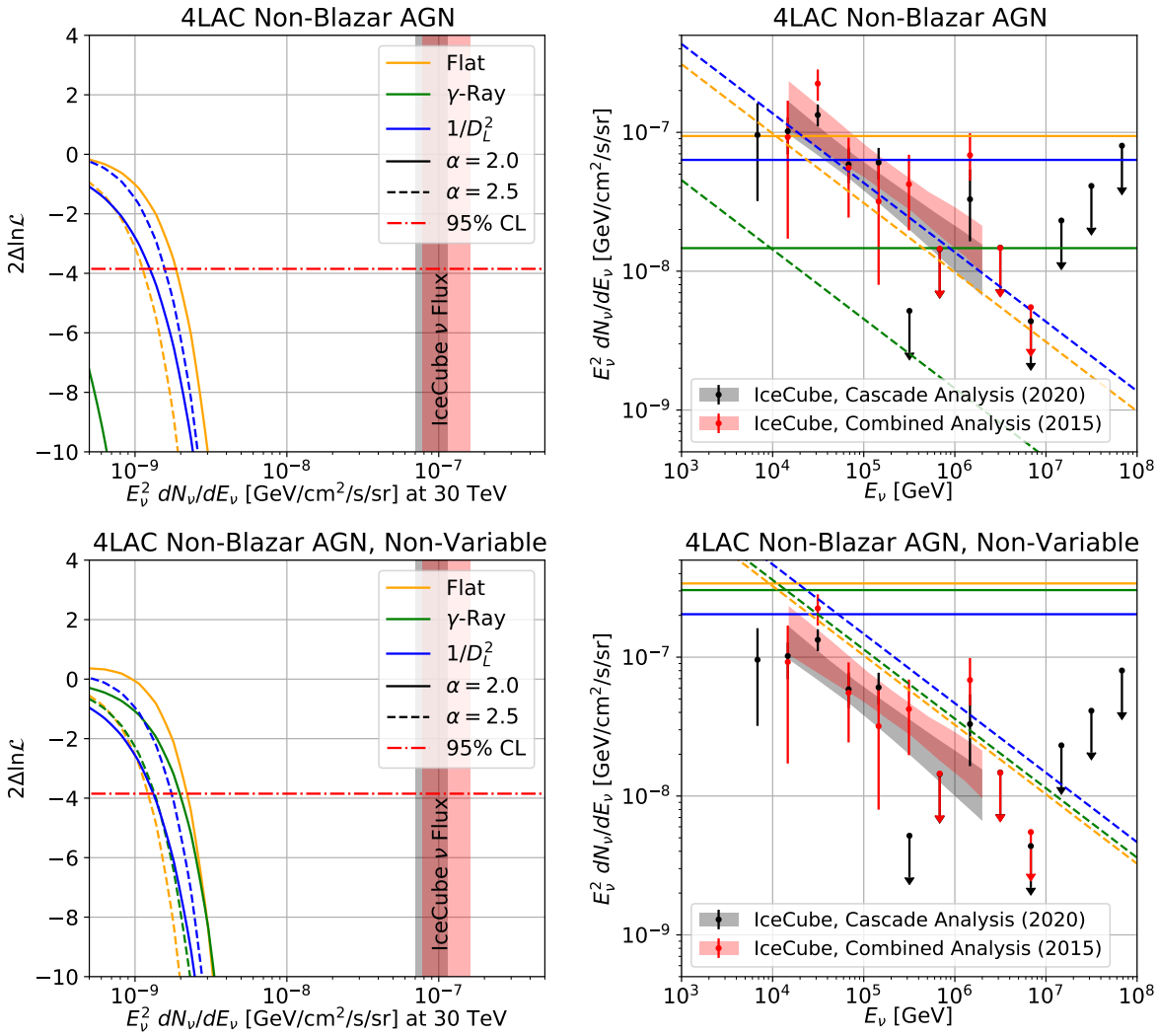

Figure 4.7: **Left figures:** The log-likelihood as a function of the total, all-flavor neutrino emission from our sample of non-blazars AGN, for two choices of the neutrino spectral index, α, and for the three flux weighting hypotheses described in Sect. 4.1. We do not detect any statistically significant evidence for neutrino emission from this class of sources. **Top figures:** The results based on all of the 65 non-blazar AGN contained in our sample. Bottom figures: results from only the 47 sources that do not exhibit statistically significant variability in their gamma-ray emission. **Right figures:** The 95% confidence level upper limits on the total neutrino flux from these source populations, and compare these constraints to the diffuse neutrino flux as reported by the IceCube Collaboration [4, 18]. We have multiplied the constraints by an appropriate completeness factor that accounts for the emission from AGN that are too distant or too gamma-ray faint to be included in our sample. These results indicate that non-variable, non-blazar AGN could potentially generate the entirety of the diffuse neutrino flux reported by the IceCube Collaboration.

searches, this distribution is consistent with Gaussian fluctuations, with no statistically significant indication of neutrino emission.

The joint likelihood in favor of neutrino emission from non-blazar AGN is plotted in Fig. 4.7. In the upper frames, we include all 65 of the non-blazar AGN under consideration, while in the lower frames we limit our analysis to the 47 of these sources that do not exhibit significant variability in their gamma-ray emission. For no combination of spectral index and weighting hypotheses (see Sect. 4.1) do we identify any evidence of neutrino emission.

In the right frames of Fig. 4.7, we have again applied a completeness factor in order to account for those non-blazar AGN that are too distant or gamma-ray faint to be included in the 4LAC [158]. Whereas the blazar completeness factor was not far above unity, a much larger fraction of the total gamma-ray emission from non-blazar AGN remains unresolved. Comparing the total gamma-ray flux from our sample of non-blazar AGN to the total contribution from all non-blazar AGN to the isotropic gamma-ray background [157], we find the appropriate completeness factor to be 50.6 (154.7) in the case of all (all non-variable) non-blazar AGN.

The constraints shown in the upper frames of Fig. 4.7 would appear to rule out the hypothesis that non-blazar AGN (including those that exhibit significant variability) produce the entirety of IceCube's reported signal. This conclusion is especially stark if we take the neutrino emission from a given source to be proportional to the observed gamma-ray flux. In this case, however, the limit is being driven in large part by a single source, NGC 1275. We excluded this source in our previous study [158], noting that the highly variable nature of NGC 1275's gamma-ray emission suggests that it is dominated by leptonic emission mechanisms. When this source is excluded from our analysis, the resulting constraint relaxes by a factor of approximately four, reducing the tension substantially.

After accounting for the lack of completeness in our catalog, we find that non-variable, non-blazar AGN could potentially generate the entirety of the diffuse neutrino flux reported

by the IceCube Collaboration. It is encouraging to note, however, that these constraints are within a factor of ∼2-3 of the flux measured by IceCube. As IceCube accumulates and releases more data, and as gamma-ray catalogs of non-blazar AGN accumulate larger numbers of sources, we expect that it will become possible to definitively test the hypothesis that the majority of IceCube's signal originates from non-blazar AGN.

4.4 Searching for Neutrinos from Starburst and Starforming Galaxies

Starburst and other starforming galaxies are often discussed as a potential class of sources for IceCube's diffuse neutrino flux. Although these sources cannot produce the entirety of IceCube's signal without exceeding the measured intensity of the isotropic gamma-ray background [75], it remains entirely plausible that they could generate a non-negligible fraction (up to ∼10%) of the neutrinos observed by IceCube below 100 TeV and greater fractions at energies above 100 TeV [179, 209]. As they are even more numerous and less luminous than non-blazar AGN, it is expected to be very difficult to detect neutrinos from individual starforming galaxies.

For the analysis performed in this subsection, we make use of a catalog of 45 nearby radio- and infrared-bright starburst galaxies, as described in Ref. [183]. Once again, we find no evidence of neutrino emission from this class of sources. In the right frame of Fig. 4.8, we have applied a completeness factor of 650, which is significantly larger than in the case of blazar or non-blazar AGN due to the significantly lower luminosities of these sources. Once again, we estimate this factor by comparing the intensity of the isotropic gamma-ray background to the combined gamma-ray emission from our sample of 45 sources. We determine this later quantity using the reported measurements of the far-infrared emission from these sources, which we relate to their gamma-ray emission by applying the empirical correlation described in Refs. [178, 27, 218]. We note that there are significant uncertainties

associated with the determination of this correction factor for starburst and starforming galaxies, and the constraints presented in the right frame of Fig. 4.8 could plausibly be inaccurate at the level of a factor of $\sim$2-3.

By making use of the Fermi 4LAC catalog in our analysis, we are intrinsically limiting ourselves to gamma-ray emitting sources. To test the hypothesis that IceCube's diffuse flux could be produced by gamma-ray faint AGN, one could perform a similar analysis that that described here, but utilizing radio or other multiwavelength catalogs [158].

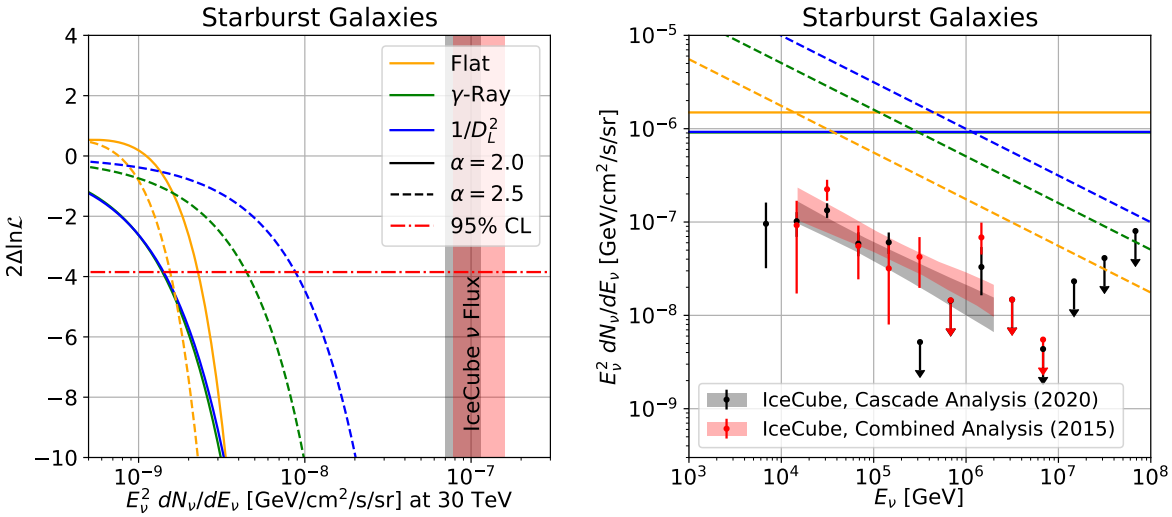

Figure 4.8: **Left:** The change to the log-likelihood as a function of the total, all-flavor neutrino emission from our sample of 45 nearby radio- and infrared-bright starburst galaxies [183], for two choices of the neutrino spectral index, α, and for the three flux weighting hypotheses described in Sect. 4.1. We do not detect any statistically significant evidence for neutrino emission from this class of sources. **Right:** The 95% confidence level upper limits on the total neutrino flux from this source population, and compare these constraints to the diffuse neutrino flux as reported by the IceCube Collaboration [4, 18]. We have multiplied the constraints by an appropriate completeness factor that accounts for the emission from starburst and starforming galaxies that are too distant or too gamma-ray faint to be included in our sample.

4.5 Summary and Conclusions

The origin of IceCube's diffuse flux of high-energy neutrinos remains one of the most interesting and important open questions in the field of high-energy astrophysics. In an effort to shed light on this mystery, we have used 3 years of publicly available IceCube data to measure or constrain the fraction of IceCube's flux that originates from blazars, non-blazar AGN, and starforming galaxies.

Our analysis did not identify any statistically significant neutrino emission from any of the source classes under consideration. Instead, our results force us to conclude that no more than 15% of IceCube's diffuse high-energy neutrino flux can originate from blazars. In contrast, it remains possible that non-blazar AGN could produce the entirety of the neutrino flux observed by IceCube. We expect such a scenario to be testable in the relatively near future, as a result of additional IceCube data and increasingly complete catalogs of gamma-ray AGN. Our constraints on starburst and other starforming galaxies remain quite weak, and we cannot significantly test the hypothesis that such sources contribute significantly to IceCube's signal.

CHAPTER 5

ICECUBE GEN-2 SIMULATIONS

IceCube-Gen2 is the planned upgrade to the IceCube experiment [20]. Along with an extended ice optical Cherenkov detector, there is a planned co-located radio array, called IceCube-Gen2 Radio, with the science goal of extending the detector sensitivity to energies and fluxes inaccessible to optical Cherenkov detectors. More explicitly, IceCube-Gen2 Radio plans to extend the already-measured astrophysical neutrino flux to higher energies and to measure or place limits on the cosmogenic neutrino flux, as can be seen in Fig. 5.1.

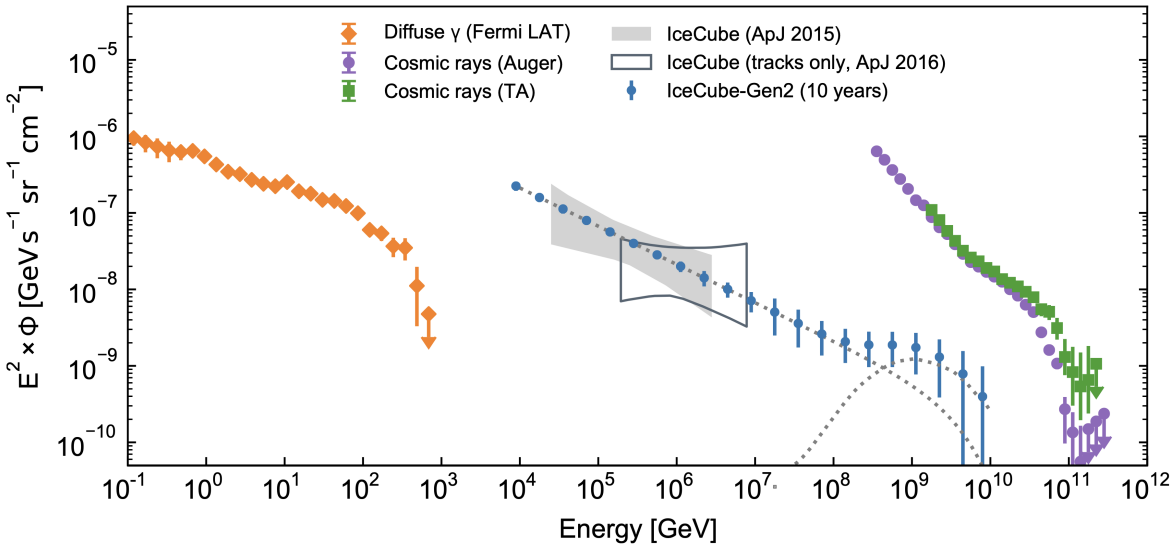

Figure 5.1: The expected neutrino flux measured by IceCube-Gen2 after 10 years of detector run time and given a neutrino flux with spectrum that goes as $\phi \propto E^{-2.5}$ and a cosmogenic neutrino flux from a UHECR spectrum with 10% proton fraction. Also plotted is the γ ray spectrum measured by Fermi-LAT [25] and the UHECR spectrum measured by the Telescope Array [165] and the Pierre Auger Observatory [1]. The grey band and black outline are the reported fits on IceCube's already measured astrophysical neutrino flux. IceCube-Gen2 Radio has a larger detector effective volume and becomes the primary detection channel at energies above $\sim 10^{17}$ eV. Figures from [20].

Large-scale neutrino detector simulations are underway to determine the design of the future IceCube-Gen2 Radio array. The optimal design will be a trade-off between detector effective volume and energy and pointing resolution, since a more sparse array can instru-

ment more ice but a denser array will have lower reconstruction uncertainties. The free parameters of the optimization problem in simulation include station separation, station type (shallow only vs. deep, shown in Fig. 5.3), deep antenna depth, deep antenna phased array composition (4 antenna vs. 8 antenna), and absolute station number.

Presented herein is the first baseline array of the IceCube-Gen2 Radio array, shown in Fig. 5.2. The simulations were performed using the simulation software NuRadioMC and the results were presented at an internal IceCube review in February 2021. The baseline array represents a baseline for sensitivity projection, while further optimization on station layout is ongoing.

5.1 NuRadioMC

NuRadioMC is a Monte Carlo simulation package designed for radio neutrino detectors [129]. NuRadioMC includes all software components necesary to turn an expected flux of UHE neutrinos into simulated digitized traces in the detector electronics. The software package is used by other experiments in the field, including RNO-G [31] and ARIANNA [71].

NuRadioMC produces results through four steps of simulation: event generation, signal generation, signal propagation, and detector simulation.

Event generation starts with randomly placed neutrino vertices from a uniform distribution inside of a designated volume of ice. Each initial neutrino has a flavor, energy, inelasticity, direction, and interaction type (NC or CC) drawn randomly from underlying probability density functions. The energy distribution is taken to be a falling power law, the flavor distribution is taken to be equal parts ν_e, ν_μ, and ν_τ due to the distance scales to UHE neutrino sources (discussed in Sect. 1.1.4 and Sect. 1.2.2), and the inelasticity and interaction type are determined by models of neutrino cross sections at high energy [97]. After the initial vertex simulation, the probability of a neutrino interacting at the given location in the ice is folded into the simulation via a weight, calculated from expected neutrino absorption

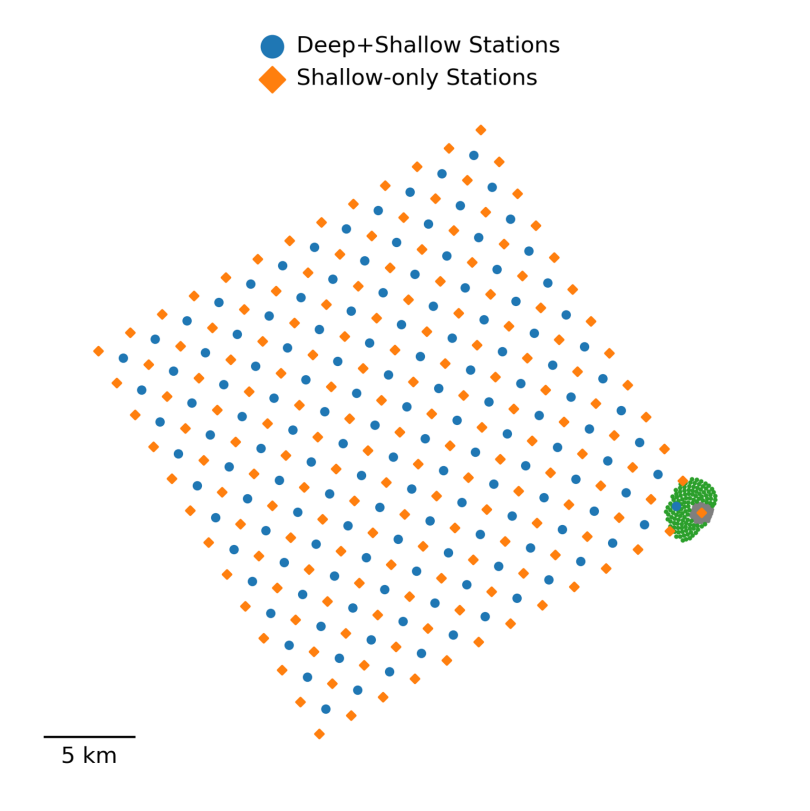

Figure 5.2: A top-down view of the baseline array for IceCube-Gen2 radio. In blue are stations with both deep and shallow antennas, in orange are stations with only a shallow component, in green is the upgrade IceCube-Gen2 Optical, and in grey (hidden on the right corner of the array) is the current IceCube array. Note that this figure shows a different baseline array to that shown in Fig. 1.13. The array has changed in shape to match spatial restrictions around IceCube (clean air sector, radio quiet zone, etc.) and to minimize cabling between stations.

over its given pathlength through the earth and ice.

Signal generation starts with the primary particles generated from the initial neutrino event generator. These primaries are fed into the `PROPOSAL` software package to track secondary particle paths and energy losses.

PRopagator with Optimal Precision and Optimized Speed for All Leptons (`PROPOSAL`) [172] is a Monte Carlo simulation software package that calculates the energy losses and interactions of charged leptons propagating through a medium. The package, used by both IceCube and NuRadioMC, improves the accuracy of the particle shower simulation by ex-

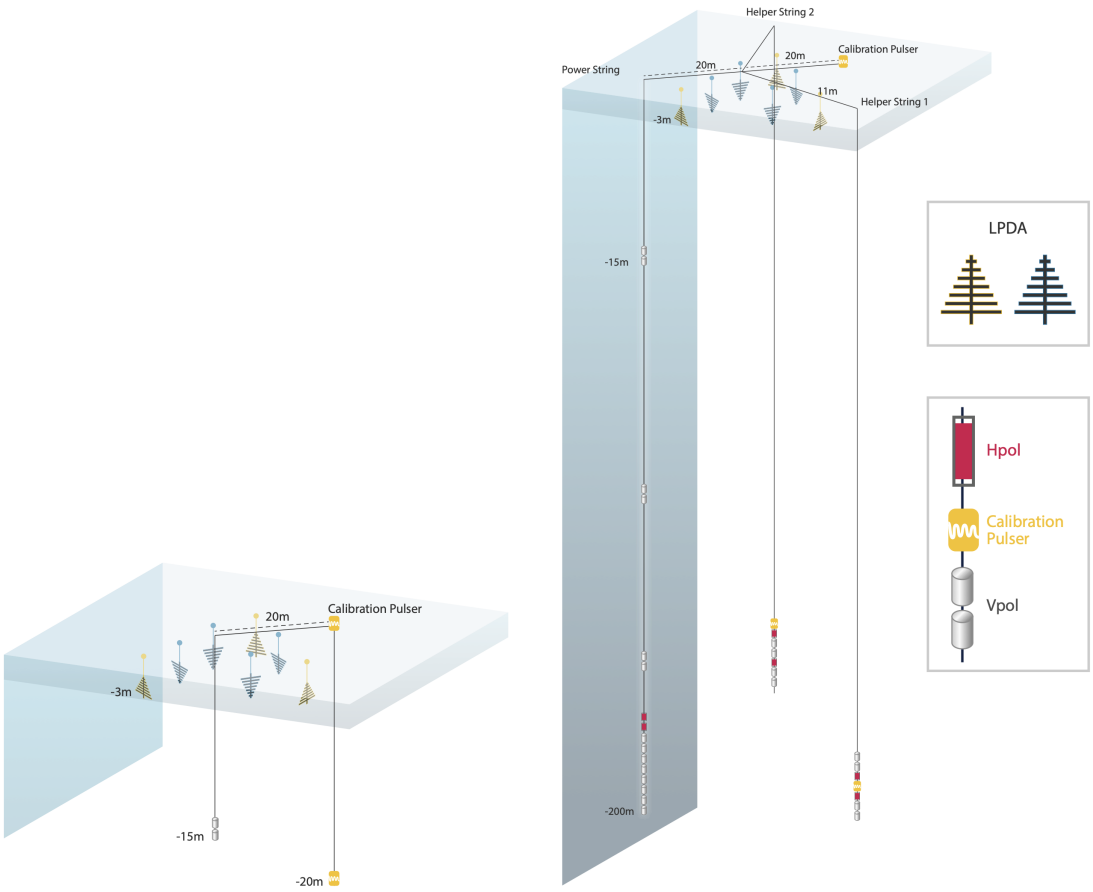

Figure 5.3: **Left:** Layout of a shallow detector station, which consists of four downward facing LPDAs and a vertically polarized dipole antenna at 15 m deep. There are also three upward facing LPDAs to measure and veto cosmic rays as well as anthropogenic noise. **Right:** Layout of a hybrid station with a shallow and a deep component. The deep component consists of a 200 m deep phased array of vertically polarized antennas for triggering and vertically and horizontally polarized antennas for reconstruction. Figures from [21].

plicitly calculating the energy contributions from secondary particles. In the case of a ν_e, `PROPOSAL` increases the precision of the shape and radio output of the initial particle shower by including the elongation of the shower due to the Landau-Pomeranchuk-Migdal effect (LPM effect). The LPM effect is the reduction of energy loss due to bremsstrahlung and pair production at high energies in dense medium, creating a shower that is longer than one would expect from the radiation length of the material alone. In the case of ν_μ, `PROPOSAL` simulates energetic muons that can propagate long distances through the ice before interacting,

introducing uncertainties on energy construction, direction reconstruction and potentially increasing detector volume. In the case of ν_τ, `PROPOSAL` will simulate the out-going τ lepton which then will propagate a long distance before decaying or interacting in flight. The 'double bang' signature, two radio signals from two large showers in the ice, is a powerful signature of the neutrino type.

Moreover, muons produced from air showers can propagate deep into the ice before interacting, creating a potentially irreducible background. NuRadioMC coupled with `PROPOSAL` allows us to understand these backgrounds and how they impact neutrino measurements.

With the given energy losses from primary and secondary particles as calcalated by `PROPOSAL`, NuRadioMC then simulates the expected Askaryan radio emission. The emission is modeled using the ARZ2019 parameterization [47, 46]. Following the notation in [46], the vector potential of the radio emission is equal to,

$$\boldsymbol{A}(r,z,t) = \frac{\mu}{4\pi}\int_{-\infty}^{\infty} dz' \frac{Q(z')}{\sqrt{r^2+(z-z')^2}}\boldsymbol{p}(z')F_p\left(t-\frac{n}{c}z'-\frac{n}{c}\sqrt{r^2+(z-z')^2}\right), \quad (5.1)$$

where z' is the shower depth, Q is the charge excess profile, $\boldsymbol{p}$ is the polarization vector, F_p is a form factor, and r and z are the cylindrical coordinate distances between the observer and the shower. The form factor gives the time dependence of the shower and captures interference effects due to the lateral distribution of the shower. Both the form factor and the charge excess profiles are interpolated from a library of fully simulated showers performed in ZHAireS, described in more detail in Sect. 6.1. Three types of showers are simulated and included in the library: electromagnetic for charge current interactions, hadronic for neutral current interaction that destroys a nucleon, and tau-induced hadronic showers. The ARZ2019 model agrees with full numerical simulations and other Askaryan emission parameterizations to a few percent [47, 46, 129].

After shower production and radio emission calculations, the radio must be propagated

from the shower location to the detector array. NuRadioMC primarily performs propagation using an analytical ray tracer in lieu of an numerical ray tracer to decrease simulation run time. An analytical ray tracer solution exists if the index of refraction of the ice takes the exponential form,

$$n(z) = n_{ice} - \Delta_n e^{z/z_0}, \tag{5.2}$$

where z is the depth into the ice (taken to be negative) and n_{ice}, Δ_n, and z_0 are parameters of the model which roughly correspond to the index of refraction of deep ice, the difference of the index of refraction at the surface and deep ice ($\Delta_n = n_{deep} - d_{shallow}$), and the exponential rate of change between the shallow and deep, respectively. The analytic solution, given the model ice, is equal to:

$$y(z) = \pm z_0 \left(\sqrt{n_{ice}^2 C_0^2 - 1}\right) \ln\left(\gamma \left[2\sqrt{c(\gamma^2 - b\gamma + c) - b\gamma + 2c}\right]^{-1}\right) + C_1, \tag{5.3}$$

where $\gamma = \Delta_n e^{z/z_0}$, $b = 2n_{ice}$ and $c = n_{ice}^2 - C_0^{-2}$. The parameters C_0 and C_1 uniquely describe the ray between a neutrino vertex and observer (antenna location) and must be solved analytically and numerically, respectively. The number of solutions of C_0 determines the number of rays between vertex and antenna, between zero for a completely shadowed vertex and two for a position with both a direct and refracted solution, described in Sect. 2.2.

At the detector, the propagated radio electric field is converted to a voltage by convolving the radio signal with the vector effective length (defined in Sect. 2.5) of a given antenna,

$$V_L = \mathcal{H}_{rl} \circledast \mathcal{E}, \tag{5.4}$$

where V_L is the voltage on a 50 Ω transmission line, $\mathcal{H}_{rl}$ is the realized VEL of the antenna,

and $\mathcal{E}$ is the incident electric field. The VEL of the antenna is derived from simulation, described for the VPol antenna in Sect. 2.5. After the antenna response, the electronics response (filters, amplifiers, cable delays, ect.) are convolved into the signal and thermal noise, based on the given bandwidth and temperature of the detector as described in Sect. 2.3, is added.

After the detector simulation is complete for a given shower (of many potential showers from an incident neutrino) and all antennas in an array, a simulation of the array trigger is performed. A description of the software implementation of the phased array trigger planned to be used in IceCube-Gen2 Radio array is available in the next section.

5.2 Phased Array Trigger

For a sparse array of antennas, the majority of detector volume, and thus the majority of neutrino vertices, is at the limits of the sensitivity of the trigger of the detector. The further away from the detector, the more volume but the smaller the signal due to path loss and attenuation in the ice. It is paramount to increase detector volume in IceCube-Gen2 Radio to increase the probability of neutrino detections. One way to increase the sensitivity of the array is by implementing a phased array trigger.

First proposed for neutrino detection by [248] and demonstration by [42], a phased array trigger actively sums signals from antennas, suppressing the incoherent thermal noise and amplifying the coherent signal expected from a neutrino vertex. The signal amplitude goes as the number of antennas in the arrive N while the noise goes as noise goes as $\sqrt{N}$, making the relative signal-to-noise ratio go as $\sqrt{N}$. Effectively, the phase array merges many antenna elements into one large antenna with gain of,

$$G_{array}(\theta = \pi/2) = NG_{ant}(\theta = \pi/2), \tag{5.5}$$

where $G_{ant}(\theta = \pi/2)$ is the gain of a single antenna at boresight. For the example of four ideal dipole antennas in a vertical line in a borehole, the gain of a single antenna is equal to 2.15 dBi and the gain of the array would be $N \times 2.15$ dBi = 8.6 dBi.

In the case of RNO-G, ARA, and IceCube-Gen2 Radio, the deep VPol antennas inside of the boreholes will be used for a phased array trigger system. There are several trade-offs to consider with the phased array trigger. While the gain of the array is very high, it also becomes very directional. Following [42] and [65], the zenith width of the gain is equal to,

$$AF(\psi) = \frac{\sin(N\psi/2)}{\sin(\psi/2)}, \tag{5.6}$$

where $\phi = 2\pi d \cos\theta/\lambda$ and d is the separation between antennas. $AF(\theta)$ is an 'array factor' which can be be used to define the array gain by $G_{array}(\theta) = AF(\theta)G_{ant}(\theta = \pi/2)$.

To counteract narrowing of the effective gain width, the signal from each antenna in the array can be delayed to point the high gain lobe in a specific direction in a procedure called beamforming, shown in Fig. 5.5. The delays added to each antenna correspond to the delays between each antenna from a plane wave incident upon the array in the desired direction. In theory, the entire space can be filled with beams to make the array identical to $G_{array} = 10\log_{10} N + G_{ant}$ in all space. However, with each additional beam, there is a trials factor: each additional beam contributes to the thermal noise trigger rate, reducing the effectiveness of the technique for each additional beam considered.

Moreover, many beams is difficult to implement in hardware. The IceCube-Gen2 array plans to implement the phased array trigger on an FPGA that will process the digitized signals from the array. In this scenario, the only directions that a beam can be created, θ_m, is determined by the digitizer step, equal to,

$$\theta_m = \sin^{-1}\left(\frac{cm\Delta t}{nd}\right), \tag{5.7}$$

where n is the index of refraction of the ice, m is the beam number, and Δt is the sampling interval of the digitized signals.

After phasing signals together, there is an additional step to determine a trigger. The phased signal for each beam is digitally squared and summed in time windows of the length expected for a neutrino signal after the antenna and electronics response, O(10 ns). There is a threshold level set on these power sums for each beam. The dark rate, or trigger rate on pure thermal noise, is kept stable on each beam by moving the threshold to match the desired rate. A figure of the power sum is shown in Fig. 5.5.

Ultimately, the ideal phased array trigger would have as many antennas phased together as possible to increase SNR, with antennas as close to each other as possible to increase beam width, and a firmware implementation of the phased array trigger that minimizes the number of beams in the analysis.

In the context of the IceCube-Gen2 Radio array, the hardware setups being considered are a four and eight antenna phased array at a depth of 200 m, with signals bandpassed to 80–250 MHz and digitized at 500 MHz. To cover $\pm 60^\circ$ of elevation angle from boresight, there are 11 and 21 digital beams, corresponding to 1 ns and 0.5 ns steps time offsets between channels, for four and eight antenna arrays respectively. For each case, the signal is digitally upsampled by a factor of two and four, respectively, to allow for the desired in beam time offsets. The beams of the arrays, plotted against an idealized antenna with gain of NG_{ant}, is shown in Fig. 5.4. The eight antenna array has narrower beams due to the over-all larger span of the array, requiring more beams to cover the same solid angle as the four antenna array. At the power integration stage of the trigger, each is integrated for 16 ns, with steps in window size of 8 ns, meaning there is 8 ns overlap with the windows before and after any given window.

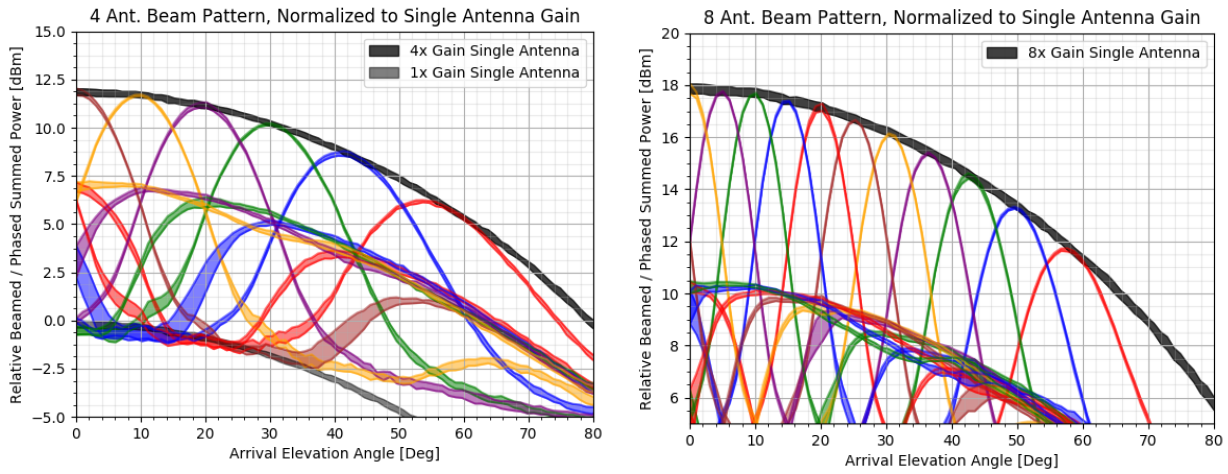

Figure 5.4: The beams of the four antenna (left) and eight antenna (right) arrays used in the IceCube-Gen2 Radio simulations. Plotted in black is an 'ideal' antenna. The lower gain between beam maximums reduces the over-all sensitivity of the array compared to the 'ideal' response.

5.3 IceCube-Gen2 Radio Simulation Results

The simulated baseline array of IceCube-Gen2 Radio extends over an area of ~ 500 km^2 on top of and near to both IceCube and IceCube-Gen2 Optical, as can been seen in Fig. 5.2. The array is composed of two types of radio stations: a station with only surface antennas that will be used for reconstruction and is quick to commission, and a station with a hybrid surface and deep antenna array (similar to stations in RNO-G, described in Sect. 2.1) that will have a larger effective volume. The two station types are shown in Fig. 5.3. The hybrid stations are in a 12×12 grid, spaced by 2 km. The shallow-only stations are in a 13×13 grid, also spaced 2 km and positioned between the hybrid stations. The array is planned to be cabled, allowing for 100% detector up-time.

The deep array is simulated with antennas down three 200 m boreholes, in a similar but more densely instrumented setup as the RNO-G stations. At 200 m, the deep antennas are below the firn, increasing the visible ice volume, as discussed in Sect. 2.2. The main science trigger of the station is a phased array trigger on the deepest VPol antennas. The noise trigger rate vs. trigger threshold is shown in Fig. 5.6. The trigger efficiency vs. SNR at a

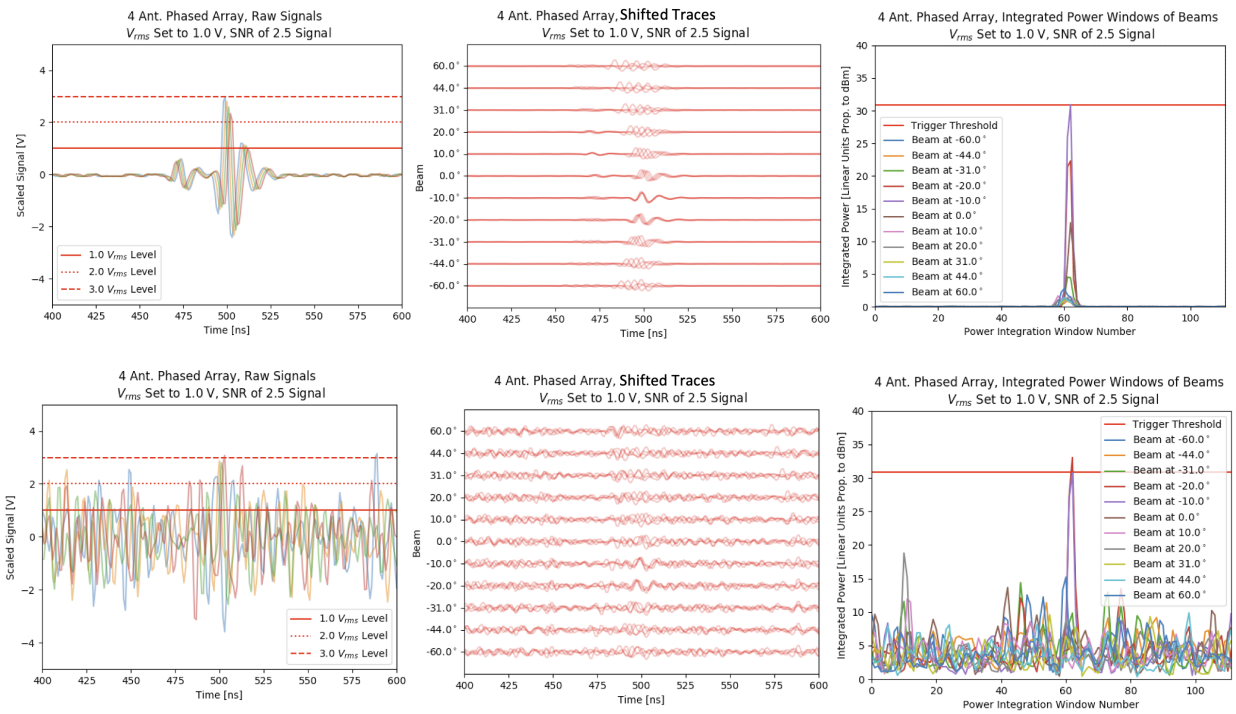

Figure 5.5: Demonstration of the phased array concept from the simulation of a 4 antenna array at a depth of 200 m. **Top row:** A noiseless simulation. **Bottom row:** Simulation with $V_{rms} = 1$. **Left column:** The signals from the four antennas, showing the direct and refracted rays. **Middle column:** The four signals after being delayed by the defined amount for each of the 11 beams. **Right column:** the power, summed in windows of 16 ns, of each beam. On the bottom right, the very low SNR signal still is above the trigger threshold, demonstrating the increased sensitivity from the phased array technique.

noise rate of 100 Hz is shown for the array in Fig. 5.7, which is the noise rate used for the baseline detector.

The projected 90% CL sensitivity to a diffuse all-flavor neutrino flux for the simulated IceCube-Gen2 Radio array is shown in Fig. 5.8. The figure shows a trigger level sensitivity with zero background events and 10 years of detector up-time. The simulated results show that the baseline array will, after ten years, have sensitivity to astrophysical neutrinos with energies that follow the projected diffuse astrophysical neutrino flux from IceCube, as can be seen in the expected number of detected events in Fig. 5.9. The array will also have sensitivity well into the flux expected from many cosmogenic models, one of which is shown in Fig. 5.9.

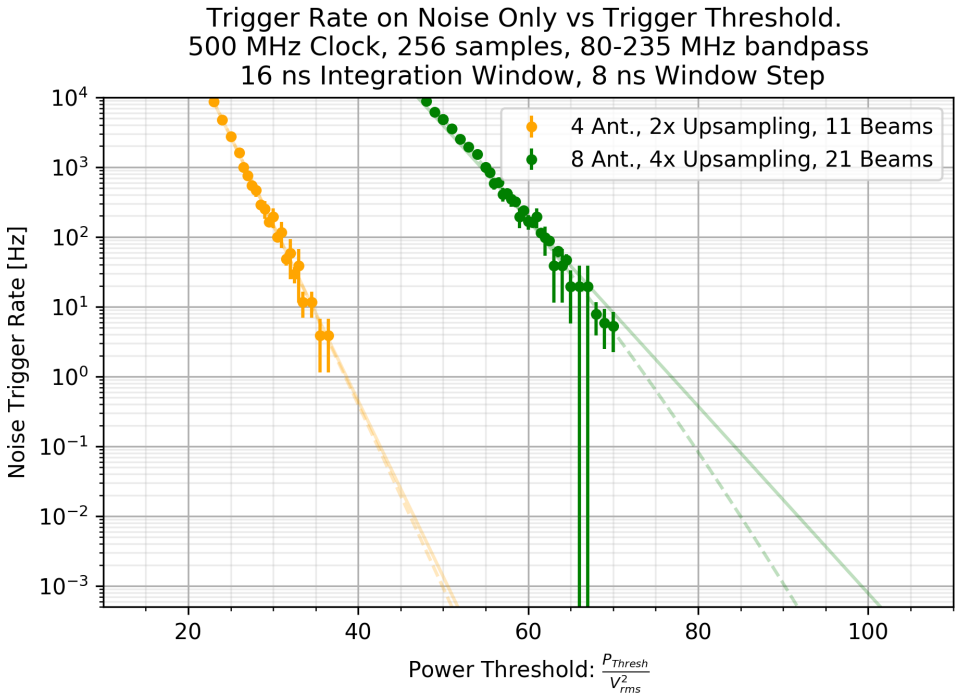

Figure 5.6: The noise trigger rate vs. threshold for the four and eight antenna phased array triggers in the baseline IceCube-Gen2 Radio array, as calculated by the NuRadioMC software package.

The analysis level sensitivity and expected background event rate remain open questions. Simulation results on thermal backgrounds and backgrounds from misidentified cosmic rays are forthcoming. Estimates for the hybrid and shallow stations are available from current results from the ARA and ARIANNA experiments. ARA reports a thermal background rate of < 1 event for 10 years of detector uptime while retaining 68% and 83% at 10^{17} eV and 10^{18} eV of triggered neutrino signals, respectively [44]. ARIANNA reports a thermal and anthropgenic background rate of 0.5 events for 4.5 years of detector uptime while retaining $\sim$ 79% of all triggered neutrino signals [55]. Fig. 5.9 was produced using the estimated analysis level sensitivity from ARA and ARIANNA, and represents a pessimistic projected number of detected events.

As can be seen in the top of Fig. 5.9, there are large variations in the expected number of astrophysical neutrino events due to the large uncertainty on the spectral index of the

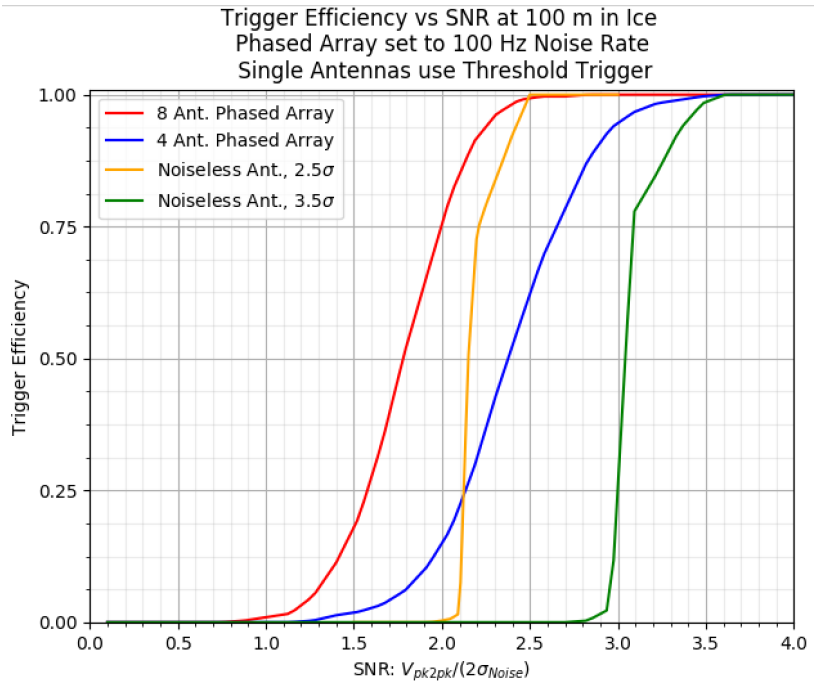

Figure 5.7: The trigger efficiency vs. SNR of the four and eight antenna phased array triggers in the baseline IceCube-Gen2 Radio array, given a noise trigger rate of 100 Hz and as calculated by the NuRadioMC software package. Before the full implementation of the phased array trigger in NuRadioMC, a simple threshold trigger on noiseless antenna was used as a proxy, shown in orange and green for the proxy of the eight and four antenna phased array respectively.

IceCube's measured diffuse astrophysical neutrino flux. The most optimistic model of $\gamma = 2.37$ is the projected line in Fig. 5.8. An equally large variation is presented in the predicted number of cosmogenic neutrinos detected due to the the disparity between the UHECR flux measured by Auger and TA. The bottom of Fig. 5.9 was produced using a UHECR flux measured by the Pierre Auger Observatory [228]. A similar figure produced using the UHECR flux measured by the Telescope Array [145] yields a number of detected neutrinos nearly ten times higher. It is clear that even a single observed neutrino event by IceCube-Gen2 Radio will greatly reduce uncertainty on the diffuse cosmogenic and astrophysical neutrino fluxes, and an ensemble of events will produce a flux measurement in their own right.

The coincident detection of a single neutrino event in multiple stations or in both the

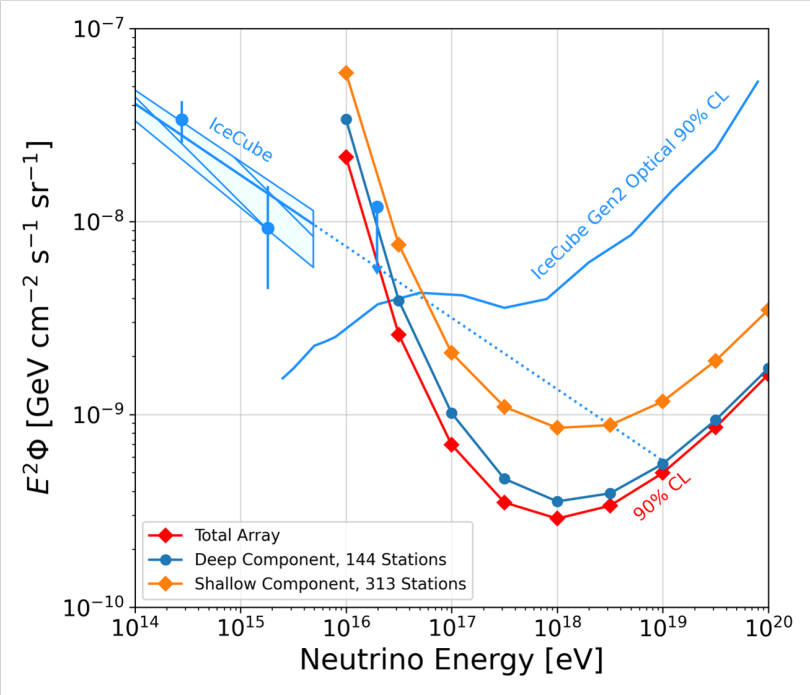

Figure 5.8: Projected 90% CL sensitivity to a diffuse neutrino flux for the shallow (yellow), deep (blue) and combined array (red) of the IceCube-Gen2 Radio array plotted against the current IceCube astrophysical neutrino flux measurement projected forward in energy (dotted light blue line) and the estimated sensitivity of the IceCube-Gen2 Optical array (light blue line).

deep and shallow component of the same station will reduce reconstruction uncertainties. For example, a low SNR signal triggered in the deep array would have very little polarization information since the signals on the horizontally polarized antennas may be below the thermal noise level. With vertically polarized information alone, the allowed signal arrival direction is a half cone up to $\sim$800 deg^2 in size on the sky. However, if there is a coincident detection with a surface or another deep station, the additional information would reduce polarization uncertainty and thus pointing resolution greatly, down to a O(10 deg^2) area on the sky. Moreover, the coincidence detection of an event that produces multiple spatially separated showers is a powerful determinate of flavor identification, specifically for 'double bang' events from ν_τ [22, 31] and extended showers from ν_μ.

Coincidence rates can be increased by decreasing the space between stations. However,

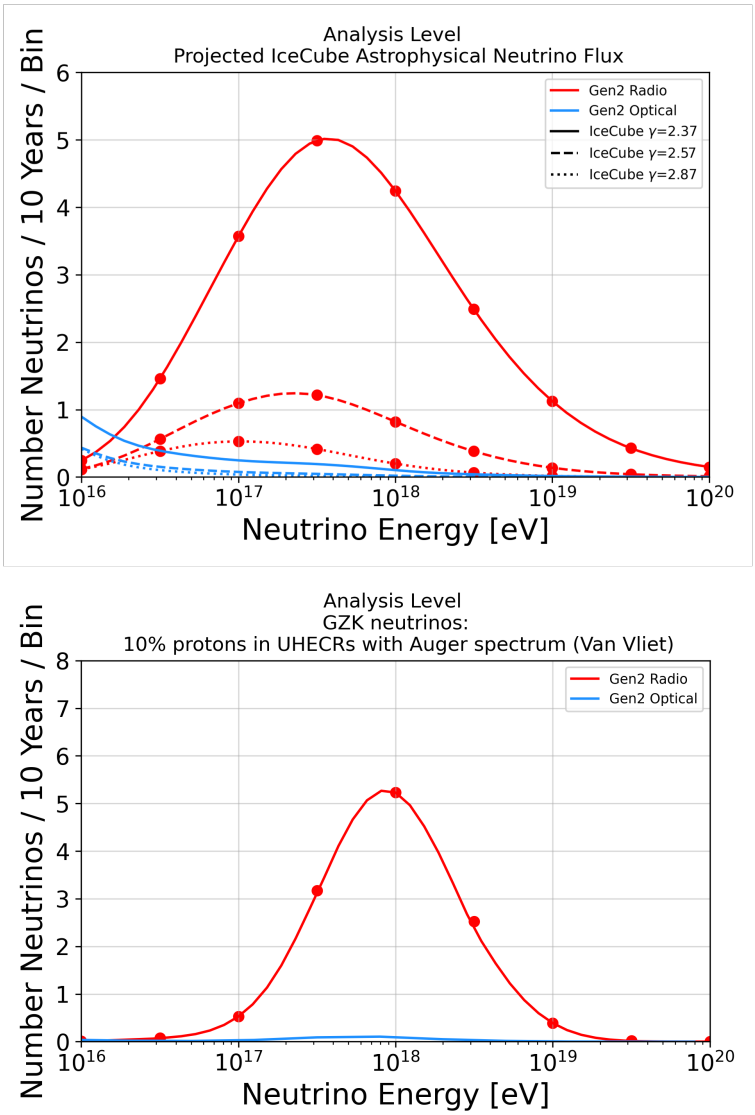

Figure 5.9: **Top:** The expected number of astrophysical neutrinos detected by the baseline array after a ten years of detector up-time and different hypotheses of neutrino flux spectrum. Also plotted in blue is the expected number of detected neutrino the IceCube-Gen2 Optical array. **Bottom:** The expected number of cosmogenic neutrinos detected by the baseline array after ten years of detector up-time and assuming a 10% proton composition of UHECRs that follow the spectrum measured by Auger [228]. The production mechanism is taken to follow [246]. Also plotted in blue is the expected number of detected neutrino the IceCube-Gen2 Optical array.

this decreases the overall sensitivity of the detector. The spacing of 2 km between hybrid stations is a compromise between maximizing sensitivity and coincidence rate in the detector. The rate of coincidences for the baseline array is shown in the left of Fig. 5.10.

The 90% CL fluence sensitivity for the IceCube-Gen2 Radio array for transient sources is plotted in the right of Fig. 5.10. The detector is most sensitive at declinations between $-40-0°$ due to attenuation through the Earth. For comparison against a source class potentially interesting for multimessenger astronomy, Fig. 5.10 includes the expected neutrino flux given a model for a binary neutrino stars merger [111].

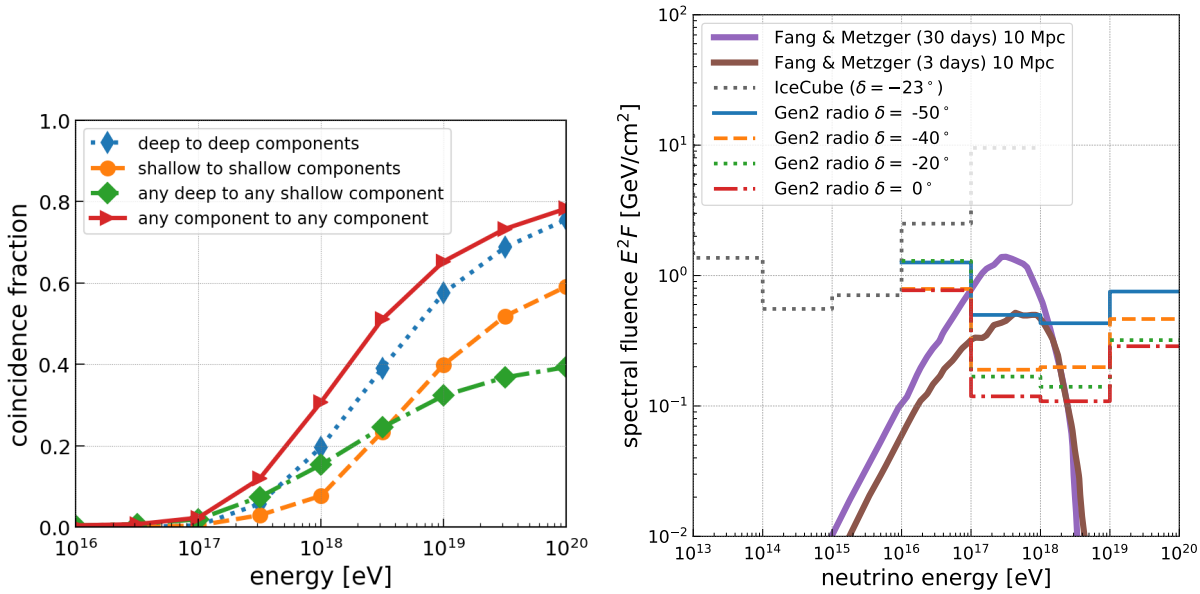

Figure 5.10: Figures from [21].
Left: Coincidence fraction vs. neutrino energy for four different coincidence conditions. Coincidences for the 'deep to deep' and 'shallow to shallow' are from a single event that produces triggers in more than one station. A coincidence detection reduces systematic uncertainties on energy and neutrino direction.
Right: 90% CL fluence sensitivity for the IceCube-Gen2 Radio array for transient point sources located in four different declination bins in the sky. Fluence predictions of neutron star – neutron star mergers as detected by gravitational wave observations [111] are plotted for comparison. IceCube's current sensitivity is also plotted.

Studies to settle the design of IceCube-Gen2 Radio array are on-going, and an incomplete list of such studies includes:

- Station antenna layout to minimize electric field reconstruction uncertainties
- Cosmic ray background calculations and vetos, including the physics of a UHECR EAS

penetrating the ice and reflecting off of a sub-surface reflector to produce a signal with an arrival direction compatible with neutrino events.

- Station separation and deep/hybrid ratio with the inputs of fully simulated reconstruction performance and background rejection as motivators.
- Optimize station layout to avoid restricted sectors (for example, a clean air sector)
- Minimize cabling requirements between stations, including studies on the viability of autonomous stations in case cabling becomes impossible.

It is clear from the simulated baseline array design that there are many parameters in the detection design that are open to optimization. Quantities like energy resolution, pointing resolution, multi-station coincidences, and noise suppression techniques drive the detector design in different directions. Regardless of the optimization chosen, the array must meet the basic science case requirement of extending the neutrino observation sensitivity of IceCube to higher energies. As shown herein, the baseline array will create measurements of all but the most pessimistic astrophysical neutrino flux spectral indices and cosmogenic models. The final design of IceCube-Gen2 Radio will be motivated by further simulation studies, but the radio technique has already been demonstrated to meet science goals and to act as a powerful compliment to the already hugely successful IceCube detector.

CHAPTER 6

MYSTERY EVENTS IN THE ANTARCTIC IMPULSIVE TRANSIENT ANTENNA (ANITA) EXPERIMENT

The ANITA experiment [133] is a balloon-borne experiment designed to detect UHE neutrinos via radio Askaryan emission produced by an in-ice electromagnetic shower [60]. A diagram of the experiment in flight and all noise and data sources is shown in Fig. 6.1. Besides UHE neutrino searches, the ANITA flights have detected radio emission from EASs produced from the interaction of UHECRs [160, 138]. Over ANITA's four flights, the experiment has detected ~ 70 cosmic ray candidates [160, 138].

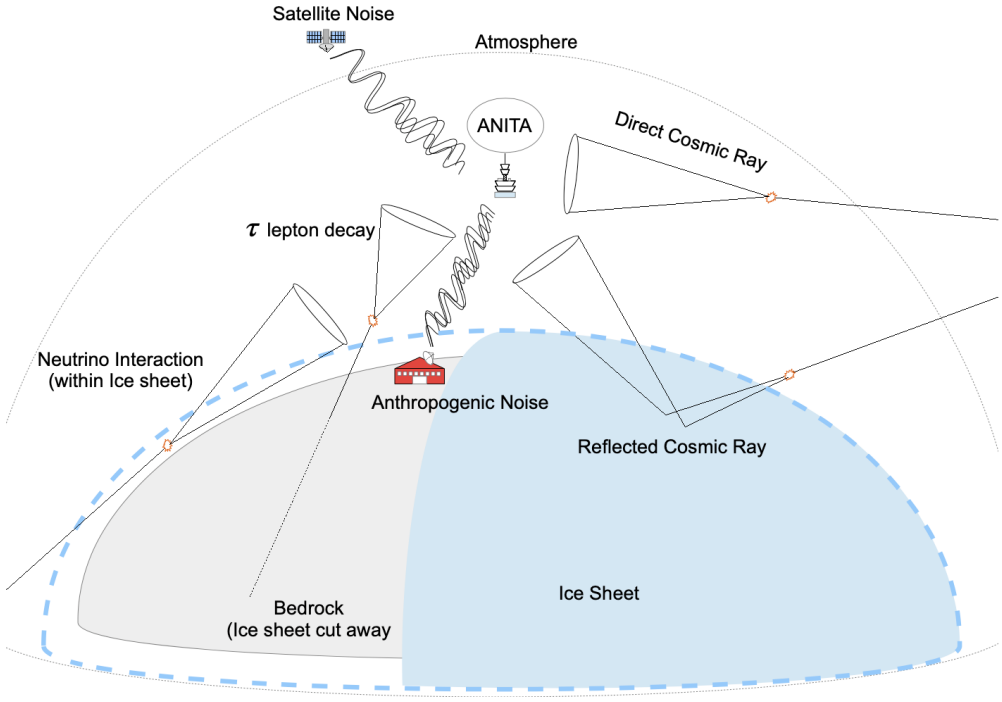

Figure 6.1: Diagram of the ANITA payload, as well as all neutrino detection channels and background sources. Note that cosmic rays can be detected both from radio signal that propagates directly to the payload and from radio signal that reflects off the ice before arriving at the payload. The ν_τ channel shown produces a similar geometry so the 'anomalous' events but with a shorter chord length through the Earth. Figure from Ben Rotter's PhD thesis [221].

Of the EAS detections, there are two anomalous signals, one each from ANITA-I [135] and ANITA-III [136]. These signals appear to have come from an upward-going (25-30° relative to the horizon) EAS that was produced from a particle that traversed through the Earth and erupted out of the ice before interacting with the air or decaying in flight. No Standard Model particle has a cross section compatible with the chord length through the Earth at the energies necessary to produce the EAS. These anomalous events have produced a flurry of papers [89, 50, 161, 98, 120, 94, 87, 151, 159, 93, 51] and media attention.

The best Standard Model candidate is an astrophysical ν_τ. A ν_τ could traversed through the Earth and have a charged-current interaction that produces a highly boosted τ lepton which then decays in the atmosphere to produce the EAS. Analysis by the ANITA [219] and IceCube [19] collaborations disfavor this hypothesis due to the considerably suppressed ν_τ cross section that would be required.

Glaciology may supply a more benign explanation for the anomalous signals. Of the radio signals produced in EASs that ANITA detected, the majority arrived at the balloon at upward-going angles similar to the anomalous events. The EASs produced from downward-going cosmic ray will emit a radio signal that propagates to the ice, reflects, and propagates back up to the ANITA payload. The resulting signal has an upward-going arrival angle and a polarity inversion from the original signal due to the Fresnel coefficient on reflection at the ice surface. Based on empirical observation, the reflection is thought to be specular due to the similarity between the reflected events and the set of events produced from radio emission that propagated directly to the payload without a reflection, as can be seen in Fig. 6.2[136]. However, the two anomalous signals could be explained by an ice surface that creates a non-specular reflection without the expected polarity inversion.

I. M. Shoemaker *et al.* [232] explores different ice properties that may explain the lack of a signal inversion. Herein, I discuss two of the proposed explanations: wind/ablation crusts in Sect. 6.3 and firn density inversions in Sect. 6.4. For both sections, I deploy finite

difference time domain electromagnetic simulations of the ice environment, as described in Sect. 6.1. A subset of the work described therein was published in the ANITA collaborations paper D. Smith *et al.* [234] in direct response to I. M. Shoemaker *et al.* [232]. This chapter contains material published as D. Smith *et al.* Experimental tests of sub-surface reflectors as an explanation for the ANITA anomalous events, Journal of Cosmology and Astroparticle Physics [234]. Reuse is permitted according to the copyright agreement used by the journal.

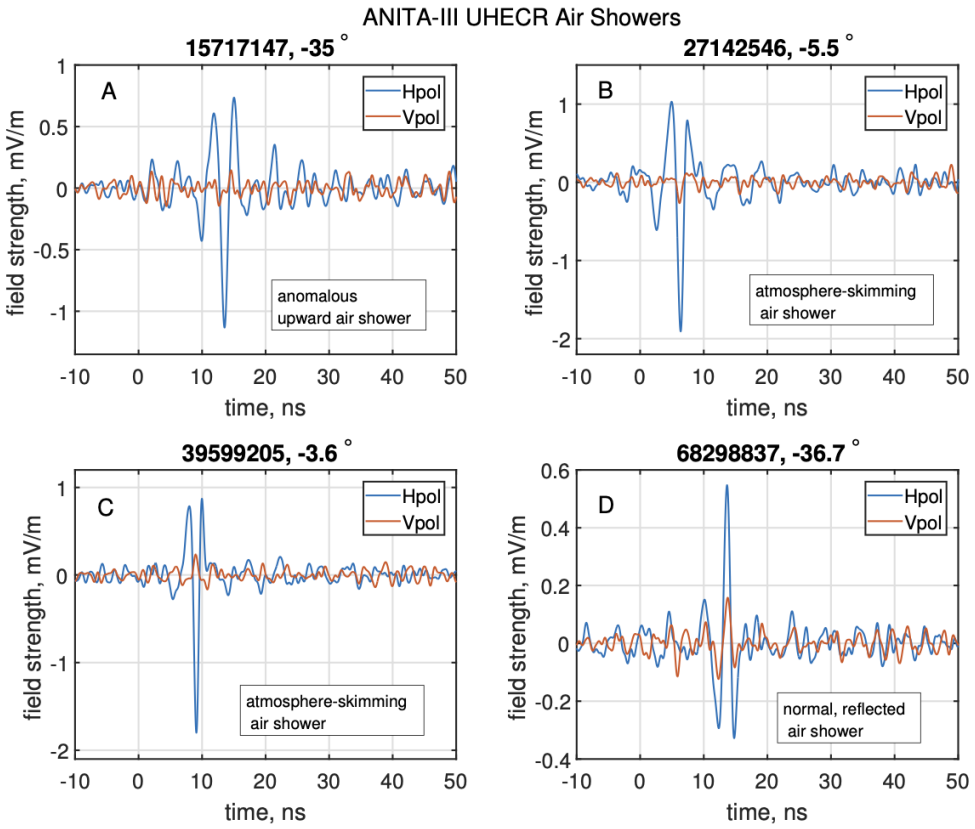

Figure 6.2: Three non-inverted polarity events along with the anomalous event from ANITA-III. Panel A is the anomalous event. Panel B and C are direct events and do not have a polarity flip because their radio signal did not reflect off the ice. Panel D is an event with an arrival direction similar to the anomalous event but with the expected signal polarity flip. Figure from [136].

6.1 Finite Difference Time Domain Method

The finite difference time domain (FDTD) method is a numerical approach to solving Maxwell's Equation given arbitrary initial electric field, magnetic field, and dielectric environment. FDTD simulations are useful for wide frequency band, time-domain applications. With the electric and magnetic fields found on a grid, FDTD simulations can perform with arbitrary precision by decreasing the spatial and time steps of a simulation but are limited by computer memory since all grid points need to be held in memory during the simulation.

A given simulated environment is broken into an evenly spaced grid, with the dielectric constant, and initial electric and magnetic fields determined at each grid point within the space. From the initial conditions, the environment is numerically progressed forward via a discrete time step, with Maxwell equations being numerically solved using central-difference approximations of the space and time derivatives at each grid point. The fields are solved using the 'leapfrog' method, which involves solving the electric field given a frozen-in-time magnetic field for a given time tick, then solving the magnetic field given a frozen-in-time electric field for the next time tick, and so on until the desired end time of the simulation.

To demonstrate the numerics of the FDTD method, I derive the numerical equations of Maxwell's equations within a 1d environment. Written out in their entirety, Maxwell's equations are defined to be,

$$\frac{\partial \mathbf{B}}{\partial t} = -\nabla \times \mathbf{E}, \tag{6.1}$$

and,

$$\frac{\partial \mathbf{D}}{\partial t} = +\nabla \times \mathbf{H} - \mathbf{J}, \tag{6.2}$$

where $\mathbf{B}$ is the magnetic field, $\mathbf{E}$ is the electric field, $\mathbf{D}$ is the displacement field which is related to $\mathbf{E}$ via $\mathbf{D} = \epsilon\mathbf{E}$ where ϵ is the dielectric constant, $\mathbf{H}$ is magnetizing field which is

related to $\mathbf{B}$ via $\mathbf{B} = \mu\mathbf{H}$ where μ is the magnetic permeability, and $\mathbf{J}$ is the current density.

Given no charge current, an electric field that only has a $\hat{z}$ component, and a magnetic field that only has a $\hat{y}$ component, the equations simplify down to the 1D case of [226, 181],

$$-\mu\frac{\partial H_y}{\partial t} = \frac{\partial E_z}{\partial z}, \tag{6.3}$$

and,

$$-\epsilon\frac{\partial E_z}{\partial t} = \frac{\partial H_y}{\partial z}. \tag{6.4}$$

The derivatives now are replaced with their numerical counterparts. Given Eq. 6.3, the magnetization field will experience a time derivative while the spatial component is held constant and the electric field will experience a spacial derivative with the temporal component held constant, leading to:

$$-\frac{\mu(z)}{\Delta t}\left(H_y(z, t+\Delta t) - H_y(z,t)\right) = \frac{1}{\Delta z}\left(E_z(z+\Delta z, t) - E_z(z,t)\right) \tag{6.5}$$

Since these equations are solved on a discretized space, we can replace Δs with coordinates, given that n is the time step and k is the node number of the electric field:

$$-\frac{\mu\left(k+\frac{1}{2}\right)}{\Delta t}\left(H_y\left(k+\frac{1}{2}, n+\frac{1}{2}\right) - H_y\left(k+\frac{1}{2}, n-\frac{1}{2}\right)\right) = \frac{1}{\Delta x}\left(E_z(k+1,n) - E_z(k,n)\right). \tag{6.6}$$

The location of H_y is offset by half a grid spacing from E_z to allow for second-order accuracy while using the leapfrog method. This was first proposed and proved as stable by [260]. H_y becomes,

$$H_y\left(k+\frac{1}{2},n+\frac{1}{2}\right)=H_y\left(k+\frac{1}{2},n-\frac{1}{2}\right)-\frac{1}{\mu\left(k+\frac{1}{2}\right)}\frac{\Delta t}{\Delta x}\left(E_z(k+1,n)-E_z(k,n)\right). \quad (6.7)$$

From initial conditions, Eq. 6.7 is used to update H_y at all magnetic field points in the environment. After that, Eq. 6.6 is performed to update E_z on all electric field points for the next time step. This process is repeated until the desired simulation end time.

While far from a simple operation, the process to solve for the FDTD result in 1D can be expanded to a 3D simulation. In a 3D environment, the smallest component of the grid, called a "Yee Lattice", can be thought of as a cube. The electric field is solved for the $\hat{x}, \hat{y}$, and $\hat{z}$ directions along the edges of the cube while the magnetic field is solved for the $\hat{x}, \hat{y}$, and $\hat{z}$ normal vectors of the cube faces, as can be seen in Fig. 6.3.

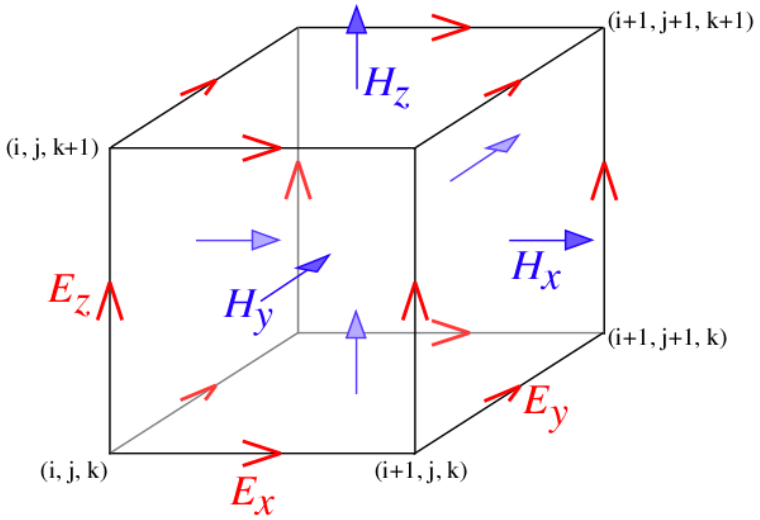

Figure 6.3: The Yee Lattice used in FDTD, with the components of the electric and magnetic field defined on the cube. Figure from [205].

The FDTD simulation software used for this analysis is MEEP [1]. MEEP is an open-source library available for Python that handles all aspects of the FDTD simulation and includes definitions of boundaries (including the perfectly matched layer (PML) boundary), materials,

1. https://meep.readthedocs.io/

sources, coordinates, and exploitations of symmetries. Unlike some FDTD software packages (for example, REMCOM's xFDTD [2]), the grid spacing in MEEP is uniform over all space, increasing the memory intensity.

6.2 Simulation Setup

The simulation setup used to test different ice hypothesis takes three steps: EAS radio emission modeling in the ZHAires software package, ice reflection in MEEP, and post-processing to emulate the ANITA analysis. A diagram of the simulation setup is shown in Fig. 6.4.

The incident radio-frequency electric field from the EAS is simulated using the ZHAireS software package [48], a radio emission simulator widely-used within the UHECR community. ZHAireS is a combination of the AIRES package, which simulates the particle interactions in an EAS, and ZHS, which calculates the electric field emitted by particles in dense media showers. The $\hat{z}$ component of the electric field from an example EAS with an incidence angle compatible with the anomalous event propagated ~ 7 km to the ice surface is shown in Fig. 6.4.

The MEEP simulations used to test difference ice hypothesis only include enough ice volume to encapsulate the first Fresnel zone of the reflection in order to reduce memory intensity. The incident electric field that is pre-calculated by ZHAires is inserted into the simulated volume immediately above the ice surface. The out-going electric field after the reflection is collected and post-processed via a near-to-far field propagation Green's function to the ANITA payload. The final simulated volume can be as small as 100 m^3, as opposed to the tens of cubic kilometers that would be required to encapsulate the EAS and ANITA payload.

The flux of the out-going, reflected electric field is collected at the boundary of the MEEP simulation and used to calculate the far field response of the reflection using the

2. https://www.remcom.com/xfdtd-3d-em-simulation-software

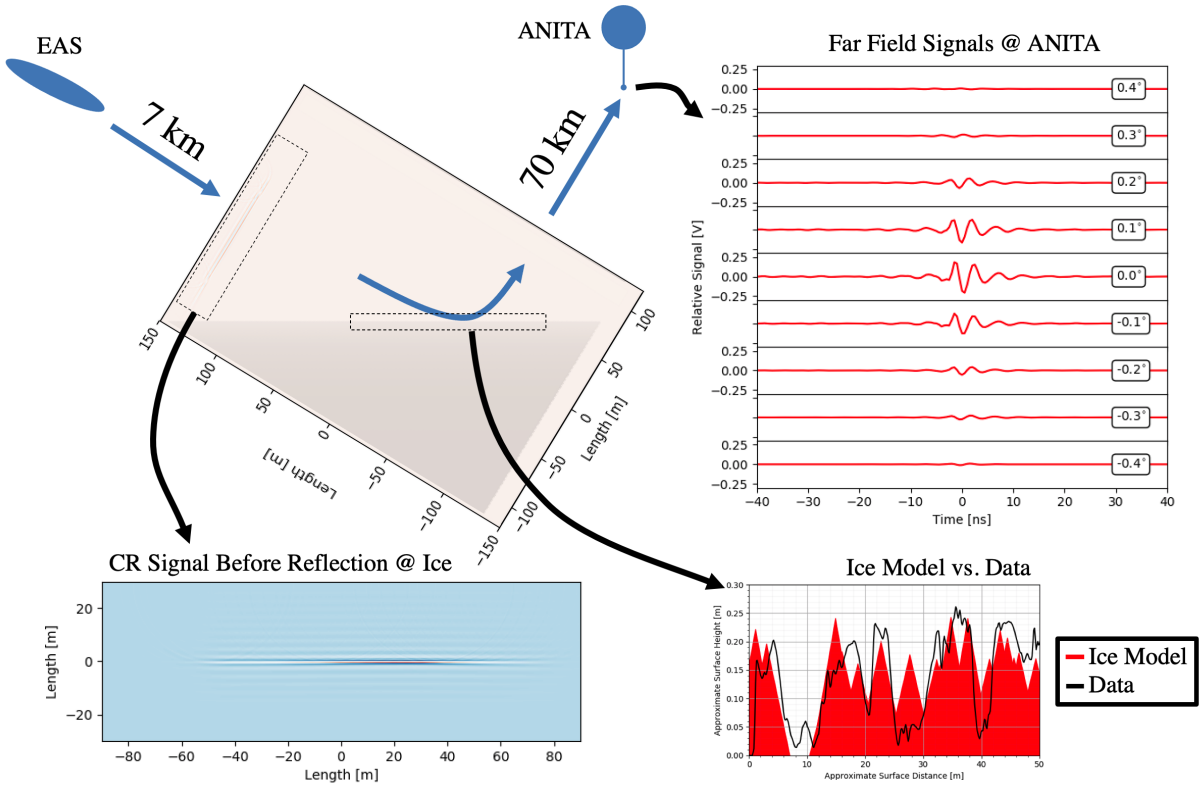

Figure 6.4: Diagram of the simulation used to test ice structures as an explanation of the ANITA anomalous events. The radio-frequency electric field produced in the EAS is propagated $\sim$ 7 km (lower left figure) and inserted into the MEEP simulation volume (tilted upper left figure). The simulation environment is tilted to minimize simulation size while optimizing ice surface length. The definition of the ice, shown as gray in the upper left figure, is altered to meet the ice properties hypothesis. Shown here is one iteration of a simulated ice surface with Sastrugi (lower right figure). After the reflection, the signal is propagated to the payload $\sim$ 70 km away using the free-space Green's function of flux transport. The resulting signal at the payload can be seen in the upper right figure for different off-cone angles.

Green's function for far field propagation in free space. The far field propagator calculates the radio signal at the ANITA payload, roughly $\sim$ 70 km away from the reflection point. The far field propagator operates in the frequency-domain, inducing an over-all unknown phase component. This unknown phase can be solved via comparison: for any given simulation where a non-specular reflection is tested, the expected phase at the payload is calculated by running a corresponding simulation with a specular surface. In the case of surface features,

the simulated signals at the payload will be compared against the signals produced from the reflection off a perfectly flat surface. In the case of subsurface layers, the simulated signals at the payload will be compared against the signals produced from a layer-free ice body.

At the payload, the signal is convolved with the ANITA antenna and electronics response to create a proxy for the signals recorded in the field by the detector. After this, the signal is passed through an approximation of the analysis performed in the UHECR searches that ultimately discovered the anomalous events [135, 136]. The only two observables that can be reconstructed using the simulated signal are a max correlation with a empirically derived UHECR signal template and the so-called peak-to-sidelobe ratio. The peak-to-sidelobe ratio is the the magnitudes of the largest positive and negative peaks of the correlation of the signal with the UHECR template and is a measure of the signal polarity. In analysis, values of max correlation above 0.7 were marked as signal events while peak-to-sidelobe ratios below 1.0 were compatible with specular reflection and above 1.0 were compatible with direction UHECR signal.

6.3 Ice Surface and Sastrugi

Shoemaker *et al.* [232] posited that reflections from a surface covered in wind / ablation crusts and sastrugi could give rise to the conditions necessary to produce a non-inverted signal. Many regions of Antarctica experience little precipitation and near constant wind, creating a layer of dense ice at the surface with features that have been named sastrugi [118], as can be seen in Fig. 6.5. The density inversion could lead to a reflection at the sastrugi-snow interface that does not have the expected phase inversion. To suppress detection of the air-sastrugi reflection while still detecting a sastrugi-snow reflection, there must be a slope difference between the air-sastrugi and sastrugi-snow interfaces, so that the air-sastrugi reflection misses the payload while the sastrugi-snow reflection does not. We deployed FDTD simulations to test whether such a situation could occur.

The statistics of such a hypothesis are complicated. Many tens of reflected CR signals have arrived at the payload without polarity inversion. The events that have arrived at the payload are relatively clean and constant, suggesting the ice surface is smooth enough on average to create specular reflections [160]. Any surface feature that could give rise to an anomalous event must simultaneously not create them in too much abundance and must not introduce 'raggedy' events (events created by a non-specular reflection) in such number that they would noticeably enter the sideband of the ANITA CR analysis. For the case of surface crusts, as much as 10% [232, 118] of the continent is covered with sastrugi at any given time, meaning any hypothesis must produce anomalous events only at a low rate to remain consistent with the clean CR sample that ANITA has observed.

Sastrugi development, prevalence, and shape are prominent matters of study within glaciology. For the purposes of this study, we developed a simple model of sastrugi that takes the form of dielectric triangles with randomly distributed heights above the ice surface, distance between triangles, and indices of refraction uniformly distributed from 1.5–1.78 (packed snow to dense ice). We modeled our ice after sample data from [118], as can be seen in Fig. 6.5 and 6.4.

The results presented herein are preliminary. The analysis was not brought to completion due mainly to two reasons:

- Simulations of simplified, 2D geometries failed to produce the mystery events at a sufficiently high rate to be consistent with the rate observed in ANITA flights. Extrapolating to 3D would suppress non-specular reflections further due to additional ray paths in an increased Fresnel zone.

- 3D simulations are memory intensive. A single ice interface iteration takes O(10 hrs) to complete. To create a sample of ice interfaces that captured relatively rare reflections, the collective run times was approaching the multi-week scale.

While results presented herein are preliminary, I hope they can serve as a guide for any future researcher who approaches the problem of ice reflections in FDTD simulations.

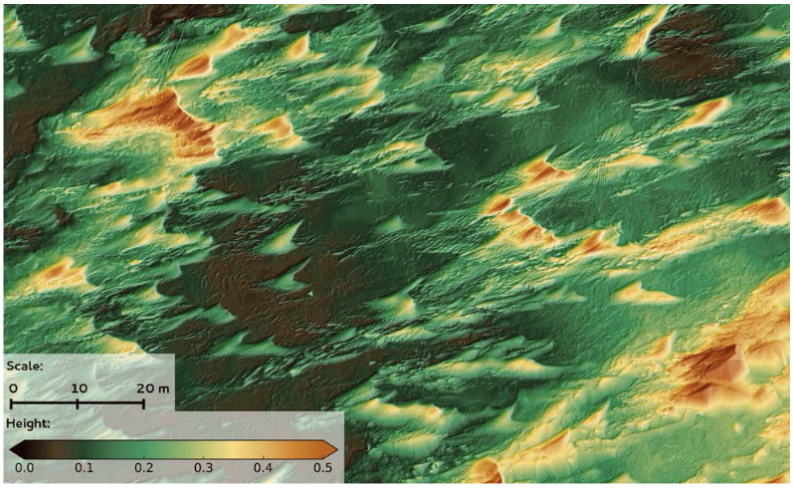

Figure 6.5: Example sastrugi in Antarctica taken from [118]. Colors are height, as measured by laser scanning of the site. The ice models of sastrugi used in this analysis are derived from 2D slices of this image.

6.3.1 2D Results

The first pass of this analysis took a simpler form than that shown in Fig. 6.4. Instead of an incident electric field determined by ZHAireS, the incident electric field was derived from the template of the voltage recorded by ANITA from their sample of UHECR candidates. The signal was taken to be a plane wave at the surface, filling the full width of simulation space seen in Fig. 6.4. Instead of using the far field propagator, the electric field was removed from the simulation at the edge of the simulation volume, approximately 10 m above the ice surface. The 2D results of this very simplified setup for 150 iterations of ice surfaces is plotted in Fig. 6.6.

Fig. 6.6 suggests that sastrugi may readily produce anomalous reflections at a rate compatible with ANITA observations. The rate of production of anomalously events is between 1–10% with few events entering the sideband. Assuming $\sim$ 10% of the continent

is covered with the wind ablated surface [224], one could expected upwards to 1% of the ANITA events to have clean reflections without a polarity inversion, which is compatible with the 2 events out of ~ 70 observed CR events.

However, there are many caveats with the apparently promising result. All simplifying assumptions enhance the anomalous reflection. The use of a 2D simulation and the lack of a far field propagator reduces the size of the Fresnel zone, thus decreasing the number of paths at the payload that could washout the non-specular component of the reflected signal. The plane wave in lieu of the beamed signal reduces the dimensionality of the simulation further.

The 2D results for 150 iterations of ice surfaces after introducing the full electric field as derived by ZHAires and the far field propagator is plotted in Fig. 6.7. The more accurate simulation suppresses the production of anomalous events below 0.1%. The only events with any deviation from the expected phased space for a specular event are signals from far off the center of the signal, which is incompatible with the observed anomalous event frequency spectrum. The 3D results, with additional Fresnel zone area, would also suppress anomalous reflections further, disfavoring the sastrugi hypothesis further.

6.4 Firn Inversion

Shoemaker *et al.* [232] posited that reflections from subsurface layers could give rise to the conditions necessary to produce a non-inverted reflected signal. Internal layers from both thin yearly 'crusts' due to summer surface melt and subsequent refreeze and O(1 mm) scale acidic conductive layers from volcanic activity are common in Antarctic ice [123]. Any individual layer would not be able to produce a reflection of anomalous polarity due to the low reflection coefficient of the sub-wavelength features. However, for wavelengths comparable to the ray path between successive layers, interference maxima may be observed at appropriate viewing angles, creating the conditions necessary for anomalous reflection. The magnitude of such effects has been estimated using FDTD simulations.

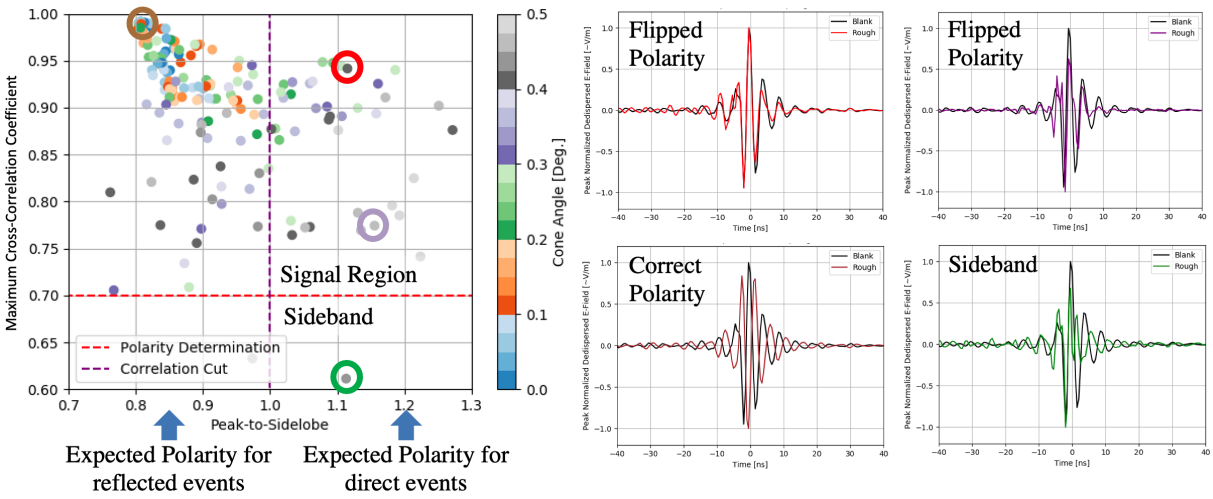

Figure 6.6: **Left:** Max correlation vs. peak-to-sidelobe for signals produced by 150 iterations of a simplified 2D simulation of EAS reflection from a sastrugi surface, which does not include a far-field propagator or fully modeled incident electric field. **Right:** Four example traces which include two anomalous signals (red and purple), a correct polarity signal (brown), a sideband event (green), and the template used for correlation calculations (black). The colors correspond to the circled points in the left figure.

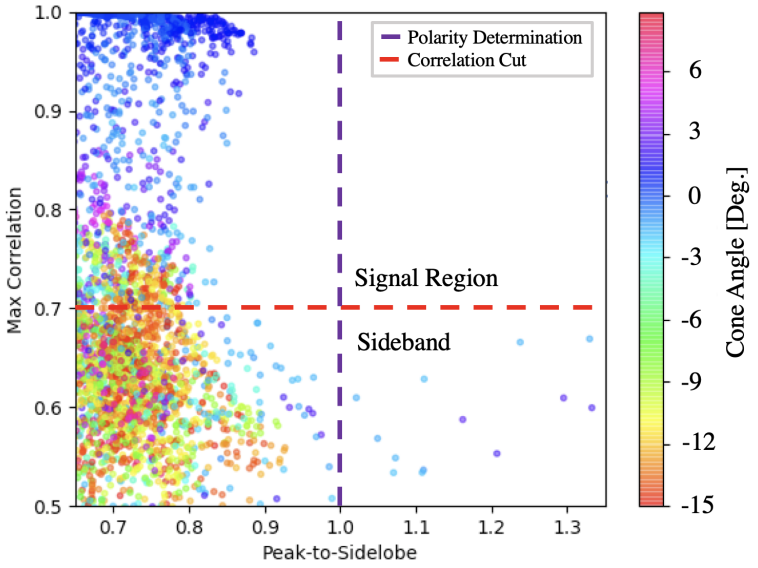

Figure 6.7: Max correlation vs. peak-to-sidelobe for signals produced by 150 iterations of a 2D simulation of EAS reflections from a sastrugi surface. Color shows the off-cone angle of the signal. No signals are classified as 'anomalous,' with zero events entering the signal region (max correlation > 0.7) with an anomalous polarity (peak-to-sidelobe > 1.0). A number of events enter the sideband, but are far off cone so likely have a signal amplitude below ANITA's sensitivity.

Following the specifications for internal reflectors given by Shoemaker *et al.*, the ice is modeled in the MEEP simulation as multiple layers of dielectric with thicknesses randomly ranging from 3 to 15 cm and with indices of refraction alternating between n=1.3 and n=1.6. The thickness range matches typical yearly snow accumulations, and the selected refractive indices correspond to surface-melt refreeze in alternating years. Unlike the simulation of the sastrugi surface described in the previous section, the azimuthal symmetry of ice layers over distances larger than one Fresnel zone in the radio 'foot print' produced by an EAS allow our FDTD simulations to be restricted to 2D with no loss of generality.

The final signal in the far-field is effectively the transfer function of the ice reflection, given a delta function input. The reflection coefficient for a simulation without any subsurface layers is shown in the left of Fig. 6.8. The derived reflection coefficient in the far field is exactly the expected Fresnel reflection coefficient at the air-ice interface. The reflection coefficient for a simulation with perfect layer inversions (alternating between exactly n=1.3 and n=1.6 every 10 cm) is shown in the right figure of Fig. 6.8. The expected high reflection coefficient from the perfect layer inversion in subsurface layers is visible. Fig. 6.8 demonstrates that the MEEP simulations align well with physical expectations.

The reflection coefficient from 20 iterations of randomized ice is plotted in Fig. 6.9. The ice is modeled as multiple layers of dielectric with thicknesses uniformly distributed from 3 to 15 cm and with indices of refraction alternating between n = 1.3 and n = 1.6. While the reflection coefficient is high for certain wavelengths in the ANITA band, this coefficient integrates over all times, and ANITA only records a relatively short window of around 100 ns. We approximate the ANITA trigger window by placing t_0 at 20 ns and truncating the signal at 120 ns, removing the initial reflection at the air-ice interface.

The FDTD simulations indicate that sub-surface reflectors should result in reflected signals with considerably extended tails. Qualitatively, the long duration of the reflection from multiple layers is inconsistent with the comparatively short waveforms in either anomalous

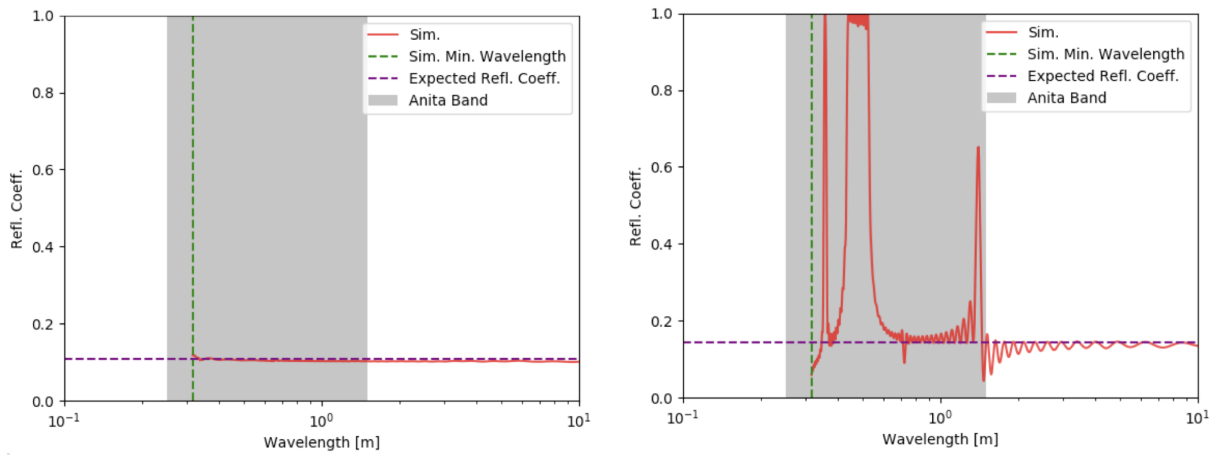

Figure 6.8: **Left:** Reflection coefficient of ice without subsurface layer inversions. The result from FDTD (red) perfectly matches expectation from Fresnel reflection coefficients at the angle of incidence of 60° (shown in purple). **Right:** Reflection coefficient of ice with perfect layer inversion of n=1.3 and n=1.6 every 10 cm. The result from FDTD (red) shows the expected spike in reflection coefficient due to subsurface layer interference.

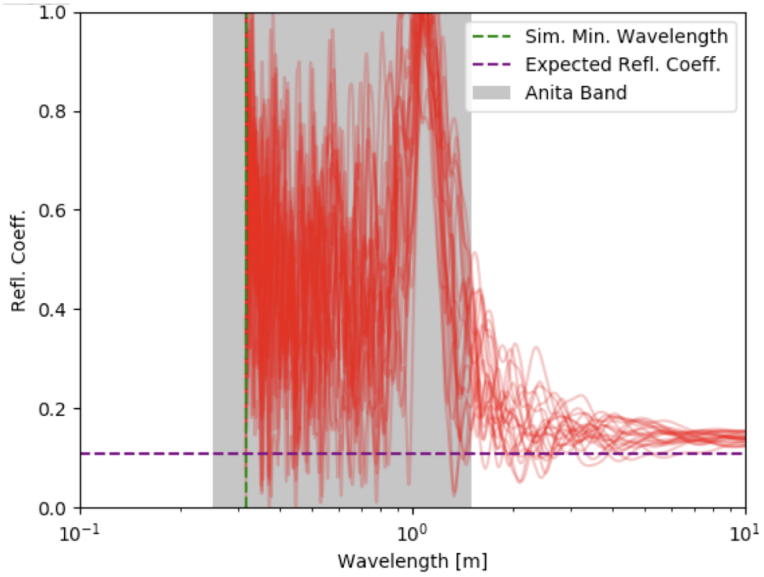

Figure 6.9: The reflection coefficient from 20 iterations of randomized subsurface ice layers, alternating from n=1.3 to n=1.6 and width uniformly distributed from 3 to 15 cm. There is an observed enhancement to reflection coefficient, but the derived impulse response fails to create clean signals with anomalous reflection polarity. Figure from [234].

event. To better quantify the probability that sub-surface layers produce an anomalous reflection, we use data from a high altitude calibration pulser that was released in tandem

with the ANITA flight, called HiCal-2a and HiCal-2b for the two flights from the second generation of the HiCal payload [216]. HiCal data includes signals that propagated directed from the calibration pulser to ANITA and signals that first reflected off the ice surface before arriving at the payload. We convolve the impulse response from the sub-surface reflection simulation iterations with the HiCal direct data to produce an ensemble of emulated reflection data, called Reflected Monte Carlo ANITA waveforms ("RMC"). We then compare the synthetic reflected events with genuine reflected events. To do this, we first define the ratio of the power in the 'tail' (20 ns after the peak signal) relative to the total power of a waveform,

$$\rho = \frac{\sum V_i^2[t_i > t_{peak} + 20 \text{ ns}]}{\sum V_i^2[t > t_{peak}]}. \tag{6.8}$$

For specular reflections, the reflected waveform should be (save for beam pattern effects and Fresnel coefficient contribution) a reproduction of the direct waveform, such that there should be the same fractional power in the tail for both direct and reflected waveforms. Fig. 6.10 compares the ρ distribution for HiCal-2a data (top) vs. HiCal-2b data (bottom). In both cases, we note that the reflected ratio distribution, normalized to the direct distribution, cluster around a value of 1.0, consistent with the naive expectation that the observed reflected waveform should be a reproduction of the observed direct waveform without evidence for an anomalous reflection.

As can be seen in Fig. 6.10, in no cases do we observe a preference for sub-surface reflectors over a single surface reflection in HiCal. ANITA has never observed a reflected HiCal event that is compatible with the sub-surface layer model described herein, strongly disfavoring this model.

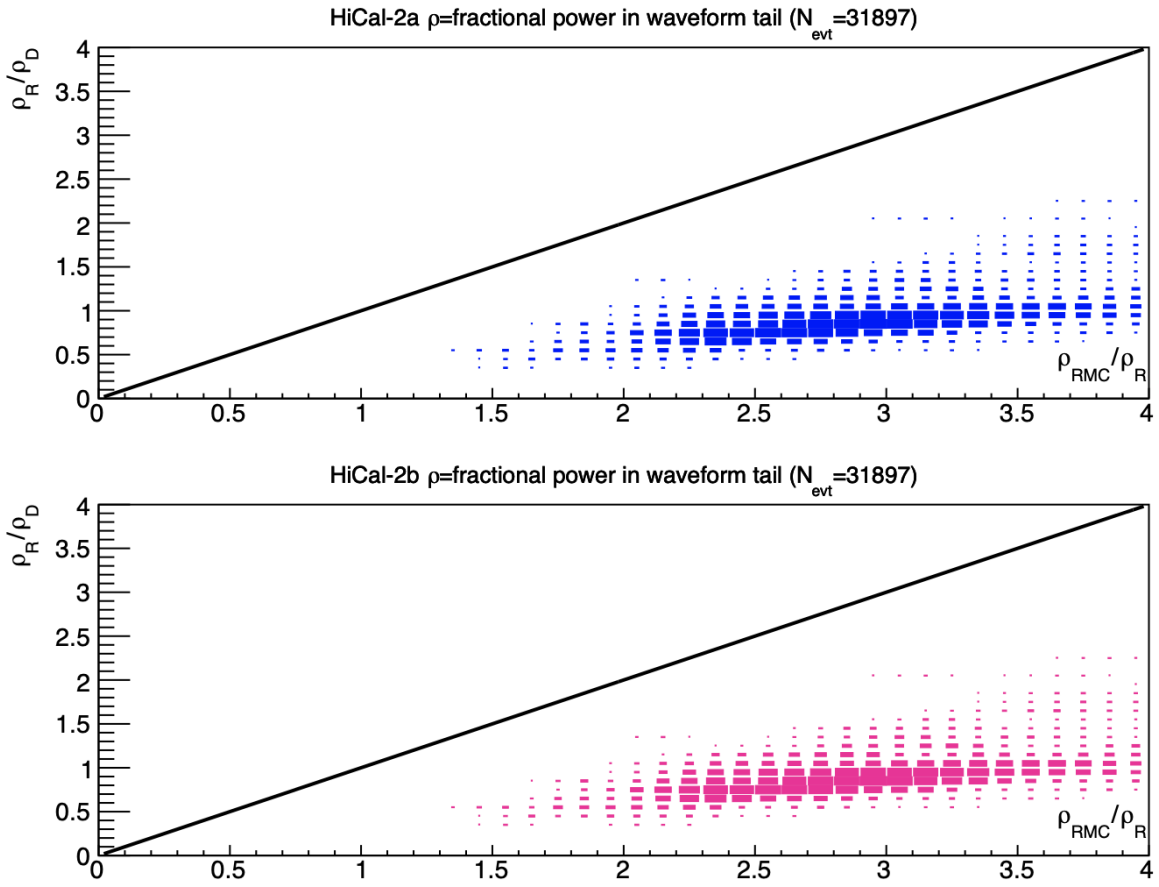

Figure 6.10: Comparison of HiCal-2 reflected (R) data events to data (D) vs. sub-surface reflector (SSR) model. Above and to the left of the diagonal black line, the sub-surface reflector model is favored. Below and to the right of the black line, the sub-surface reflector model is disfavored. Figure from [234].

CHAPTER 7

DISCUSSION

The work presented herein represents a cross section of the current status of the field of UHE neutrino detection. The source search using the already-discovered diffuse neutrino flux from the IceCube experiment represents the current status of neutrino astronomy, with the first single source correlations beginning to be discovered and source class correlations being just out of reach. Design and commissioning of the RNO-G experiment typifies the next generation of radio-based experiments, aimed specifically at higher energies than the IceCube experiment to extend the measured astrophysics neutrino flux measurement and cutting into cosmogenic neutrino models. Along with the development of the next generation of experiments are the challenges to understand our detectors, exemplified by my measurement of the radio frequency attenuation at Summit Station and FDTD simulations for the ANITA experiment. Finally, the large-scale simulations for the IceCube-Gen2 Radio experiment presented herein is a future-looking limit of the technology, being the culmination of the expertise from all previous UHE neutrino experiments and having the highest projected UHE neutrino sensitivity than any previous experiment.

While it has been a long time coming with still more than a decade of work ahead, IceCube-Gen2 Radio simulations show that, even if nature is very unfriendly, the future experiment is at real risk of discovering a flux of both UHE astrophysical and cosmogenic neutrinos. I look forward to seeing the field shift from discovery experiments to precise UHE neutrino observatories, a new paradigm with its own challenges.

REFERENCES

[1] A. Aab et al. The Pierre Auger Cosmic Ray Observatory. *Nucl. Instrum. Meth. A*, 798:172–213, 2015. doi:10.1016/j.nima.2015.06.058.

[2] M. Aartsen et al. Searches for Extended and Point-like Neutrino Sources with Four Years of IceCube Data. *Astrophys. J.*, 796(2):109, 2014. doi:10.1088/0004-637X/796/2/109.

[3] M. Aartsen et al. Flavor Ratio of Astrophysical Neutrinos above 35 TeV in IceCube. *Phys. Rev. Lett.*, 114(17):171102, 2015. doi:10.1103/PhysRevLett.114.171102.

[4] M. Aartsen et al. A combined maximum-likelihood analysis of the high-energy astrophysical neutrino flux measured with IceCube. *Astrophys. J.*, 809(1):98, 2015. doi:10.1088/0004-637X/809/1/98.

[5] M. Aartsen et al. An All-Sky Search for Three Flavors of Neutrinos from Gamma-Ray Bursts with the IceCube Neutrino Observatory. *Astrophys. J.*, 824(2):115, 2016. doi:10.3847/0004-637X/824/2/115.

[6] M. Aartsen et al. Observation and Characterization of a Cosmic Muon Neutrino Flux from the Northern Hemisphere using six years of IceCube data. *Astrophys. J.*, 833(1): 3, 2016. doi:10.3847/0004-637X/833/1/3.

[7] M. Aartsen et al. The contribution of Fermi-2LAC blazars to the diffuse TeV-PeV neutrino flux. *Astrophys. J.*, 835(1):45, 2017. doi:10.3847/1538-4357/835/1/45.

[8] M. Aartsen et al. All-sky Search for Time-integrated Neutrino Emission from Astrophysical Sources with 7 yr of IceCube Data. *Astrophys. J.*, 835(2):151, 2017. doi:10.3847/1538-4357/835/2/151.

[9] M. Aartsen et al. Constraints on Galactic Neutrino Emission with Seven Years of IceCube Data. *Astrophys. J.*, 849(1):67, 2017. doi:10.3847/1538-4357/aa8dfb.

[10] M. Aartsen et al. A Search for Neutrino Emission from Fast Radio Bursts with Six Years of IceCube Data. *Astrophys. J.*, 857(2):117, 2018. doi:10.3847/1538-4357/aab4f8.

[11] M. Aartsen et al. Neutrino emission from the direction of the blazar TXS 0506+056 prior to the IceCube-170922A alert. *Science*, 361(6398):147–151, 2018. doi:10.1126/science.aat2890.

[12] M. Aartsen et al. Multimessenger observations of a flaring blazar coincident with high-energy neutrino IceCube-170922A. *Science*, 361(6398):eaat1378, 2018. doi:10.1126/science.aat1378.

[13] M. Aartsen et al. All-sky point-source IceCube data: years 2010-2012., 2018. URL `https://icecube.wisc.edu/science/data/PS-3years`.

[14] M. Aartsen et al. Constraints on minute-scale transient astrophysical neutrino sources. *Phys. Rev. Lett.*, 122(5):051102, 2019. doi:10.1103/PhysRevLett.122.051102.

[15] M. Aartsen et al. Time-Integrated Neutrino Source Searches with 10 Years of IceCube Data. *Phys. Rev. Lett.*, 124(5):051103, 2020. doi:10.1103/PhysRevLett.124.051103.

[16] M. G. Aartsen et al. Measurement of South Pole ice transparency with the IceCube LED calibration system. *Nucl. Instrum. Meth. A*, 711:73–89, 2013. doi:10.1016/j.nima.2013.01.054.

[17] M. G. Aartsen et al. Differential limit on the extremely-high-energy cosmic neutrino flux in the presence of astrophysical background from nine years of IceCube data. *Phys. Rev. D*, 98(6):062003, 2018. doi:10.1103/PhysRevD.98.062003.

[18] M. G. Aartsen et al. Characteristics of the diffuse astrophysical electron and tau neutrino flux with six years of IceCube high energy cascade data. *Phys. Rev. Lett.*, 125(12):121104, 2020. doi:10.1103/PhysRevLett.125.121104.

[19] M. G. Aartsen et al. A search for IceCube events in the direction of ANITA neutrino candidates. *The Astrophysical Journal*, 892(1):53, mar 2020. doi:10.3847/1538-4357/ab791d.

[20] M. G. Aartsen et al. IceCube-Gen2: the window to the extreme Universe. *J. Phys. G*, 48(6):060501, 2021. doi:10.1088/1361-6471/abbd48.

[21] R. Abbasi et al. Sensitivity studies for the IceCube-Gen2 radio array. *PoS*, ICRC2021: 1183, 2021. doi:10.22323/1.395.1183.

[22] R. Abbasi et al. The IceCube high-energy starting event sample: Description and flux characterization with 7.5 years of data. *Phys. Rev. D*, 104:022002, 2021. doi:10.1103/PhysRevD.104.022002.

[23] R. U. Abbasi et al. Indications of Intermediate-Scale Anisotropy of Cosmic Rays with Energy Greater Than 57 EeV in the Northern Sky Measured with the Surface Detector of the Telescope Array Experiment. *Astrophys. J. Lett.*, 790:L21, 2014. doi:10.1088/2041-8205/790/2/L21.

[24] B. P. Abbott et al. Sensitivity of the Advanced LIGO detectors at the beginning of gravitational wave astronomy. *Phys. Rev. D*, 93(11):112004, 2016. doi:10.1103/PhysRevD.93.112004. [Addendum: Phys.Rev.D 97, 059901 (2018)].

[25] S. Abdollahi et al. *Fermi* Large Area Telescope Fourth Source Catalog. *Astrophys. J. Suppl.*, 247(1):33, 2020. doi:10.3847/1538-4365/ab6bcb.

[26] T. AbuZayyad et al. Auger-TA energy spectrum working group report. *EPJ Web Conf.*, 210:01002, 2019. doi:10.1051/epjconf/201921001002. URL `https://doi.org/10.1051/epjconf/201921001002`.

[27] M. Ackermann et al. GeV Observations of Star-forming Galaxies with *Fermi* LAT. *The Astrophysical Journal*, 755(2):164, Aug 2012. ISSN 1538-4357. doi:10.1088/0004-637x/755/2/164.

[28] M. Ackermann et al. The spectrum of isotropic diffuse gamma-ray emission between 100 MeV and 820 GeV. *Astrophys. J.*, 799:86, 2015. doi:10.1088/0004-637X/799/1/86.

[29] M. Ackermann et al. High-Energy and Ultra-High-Energy Neutrinos. 3 2022.

[30] J. A. Aguilar et al. The Radio Neutrino Observatory Greenland (RNO-G). *PoS*, ICRC2021:001, 2021. doi:10.22323/1.395.0001.

[31] J. A. Aguilar et al. Design and Sensitivity of the Radio Neutrino Observatory in Greenland (RNO-G). *JINST*, 16(03):P03025, 2021. doi:10.1088/1748-0221/16/03/P03025.

[32] J. A. Aguilar et al. In situ, broadband measurement of the radio frequency attenuation length at Summit Station, Greenland. Preprint, 1 2022.

[33] J. A. Aguilar et al. Reconstructing the neutrino energy for in-ice radio detectors: A study for the Radio Neutrino Observatory Greenland (RNO-G). *Eur. Phys. J. C*, 82 (2):147, 2022. doi:10.1140/epjc/s10052-022-10034-4.

[34] Q. R. Ahmad et al. Measurement of the rate of $\nu_e + d \rightarrow p + p + e^-$ interactions produced by ^{8}B solar neutrinos at the Sudbury Neutrino Observatory. *Phys. Rev. Lett.*, 87:071301, 2001. doi:10.1103/PhysRevLett.87.071301.

[35] M. Ajello et al. The Origin of the Extragalactic Gamma-Ray Background and Implications for Dark-Matter Annihilation. *Astrophys. J. Lett.*, 800(2):L27, 2015. doi:10.1088/2041-8205/800/2/L27.

[36] M. Ajello et al. The Fourth Catalog of Active Galactic Nuclei Detected by the Fermi Large Area Telescope. *Astrophys. J.*, 892:105, 2020. doi:10.3847/1538-4357/ab791e.

[37] E. N. Alekseev et al. Possible Detection of a Neutrino Signal on 23 February 1987 at the Baksan Underground Scintillation Telescope of the Institute of Nuclear Research. *JETP Lett.*, 45:589–592, 1987.

[38] R. Alley and B. Koci. Ice-Core Analysis at Site A, Greenland: Preliminary Results. *Annals of Glaciology*, 10:1–4, 1988. doi:10.3189/S0260305500004067.

[39] R. Alley et al. Visual-stratigraphic dating of the GISP2 ice core: Basis, reproducibility, and application. *Journal of Geophysical Research: Oceans*, 102(C12):26367–26381, Nov. 1997. ISSN 2169-9275. doi:10.1029/96JC03837. Publisher Copyright: Copyright 1997 by the American Geophysical Union.

[40] P. Allison et al. Design and Initial Performance of the Askaryan Radio Array Prototype EeV Neutrino Detector at the South Pole. *Astropart. Phys.*, 35:457–477, 2012. doi:10.1016/j.astropartphys.2011.11.010.

[41] P. Allison et al. Measurement of the real dielectric permittivity ϵ_r of glacial ice. *Astropart. Phys.*, 108:63–73, 2019. doi:10.1016/j.astropartphys.2019.01.004.

[42] P. Allison et al. Design and performance of an interferometric trigger array for radio detection of high-energy neutrinos. *Nucl. Instrum. Meth. A*, 930:112–125, 2019. doi:10.1016/j.nima.2019.01.067.

[43] P. Allison et al. Constraints on the diffuse flux of ultrahigh energy neutrinos from four years of Askaryan Radio Array data in two stations. *Phys. Rev. D*, 102(4):043021, 2020. doi:10.1103/PhysRevD.102.043021.

[44] P. Allison et al. A low-threshold ultrahigh-energy neutrino search with the Askaryan Radio Array. Preprint, 2 2022.

[45] M. Altmann et al. Complete results for five years of GNO solar neutrino observations. *Phys. Lett. B*, 616:174–190, 2005. doi:10.1016/j.physletb.2005.04.068.

[46] J. Alvarez-Muñiz et al. Askaryan radiation from neutrino-induced showers in ice. *Phys. Rev. D*, 101(8):083005, 2020. doi:10.1103/PhysRevD.101.083005.

[47] J. Alvarez-Muniz et al. Cherenkov radio pulses from electromagnetic showers in the time-domain. *Phys. Rev. D*, 81:123009, 2010. doi:10.1103/PhysRevD.81.123009.

[48] J. Alvarez-Muñiz et al. Monte carlo simulations of radio pulses in atmospheric showers using zhaires. *Astroparticle Physics*, 35(6):325–341, 2012. ISSN 0927-6505. doi:https://doi.org/10.1016/j.astropartphys.2011.10.005.

[49] L. A. Anchordoqui. Ultra-High-Energy Cosmic Rays. *Phys. Rept.*, 801:1–93, 2019. doi:10.1016/j.physrep.2019.01.002.

[50] L. A. Anchordoqui et al. Upgoing ANITA events as evidence of the CPT symmetric universe. *LHEP*, 1(1):13–16, 2018. doi:10.31526/LHEP.1.2018.03.

[51] L. A. Anchordoqui et al. The pros and cons of beyond standard model interpretations of ANITA events. *PoS*, ICRC2019:884, 2020. doi:10.22323/1.358.0884.

[52] A. Anker et al. Targeting ultra-high energy neutrinos with the ARIANNA experiment. *Adv. Space Res.*, 64:2595–2609, 2019. doi:10.1016/j.asr.2019.06.016.

[53] A. Anker et al. Neutrino vertex reconstruction with in-ice radio detectors using surface reflections and implications for the neutrino energy resolution. *Journal of Cosmology and Astroparticle Physics*, 2019(11):030–030, Nov 2019. ISSN 1475-7516. doi:10.1088/1475-7516/2019/11/030.

[54] A. Anker et al. Probing the angular and polarization reconstruction of the ARIANNA detector at the South Pole. *JINST*, 15(09):P09039, 2020. doi:10.1088/1748-0221/15/09/P09039.

[55] A. Anker et al. A search for cosmogenic neutrinos with the ARIANNA test bed using 4.5 years of data. *JCAP*, 03:053, 2020. doi:10.1088/1475-7516/2020/03/053.

[56] C. A. Argüelles et al. New Physics in Astrophysical Neutrino Flavor. *Phys. Rev. Lett.*, 115:161303, 2015. doi:10.1103/PhysRevLett.115.161303.

[57] W. D. Arnett and J. L. Rosner. Neutrino mass limits from SN1987A. *Phys. Rev. Lett.*, 58:1906–1909, May 1987. doi:10.1103/PhysRevLett.58.1906.

[58] W. D. Arnett et al. SUPERNOVA SN1987A. *Ann. Rev. Astron. Astrophys.*, 27: 629–700, 1989. doi:10.1146/annurev.aa.27.090189.003213.

[59] R. J. Arthern et al. Inversion for the density-depth profile of polar firn using a stepped-frequency radar. *Journal of Geophysical Research (Earth Surface)*, 118(3):1257–1263, Sept. 2013. doi:10.1002/jgrf.20089.

[60] G. A. Askar'yan. Excess negative charge of an electron-photon shower and its coherent radio emission. *Zh. Eksp. Teor. Fiz.*, 41:616–618, 1961.

[61] A. Atoyan and C. D. Dermer. High-energy neutrinos from photomeson processes in blazars. *Phys. Rev. Lett.*, 87:221102, 2001. doi:10.1103/PhysRevLett.87.221102.

[62] J. Avva et al. An *insitu* measurement of the radio-frequency attenuation in ice at Summit Station, Greenland. *J. Glaciol.*, 61:1005–1011, 2015. doi:10.3189/2015JoG15J057.

[63] J. Avva et al. Development Toward a Ground-Based Interferometric Phased Array for Radio Detection of High Energy Neutrinos. *Nucl. Instrum. Meth. A*, 869:46–55, 2017. doi:10.1016/j.nima.2017.07.009.

[64] J. N. Bahcall. Solar models and solar neutrinos: Current status. *Phys. Scripta T*, 121: 46–50, 2005. doi:10.1088/0031-8949/2005/T121/006.

[65] C. A. Balanis. *Antenna Theory*. Wiley, 3rd edition, 2005.

[66] C. A. Balanis. *Antenna Theory: Analysis and Design*. Wiley Interscience, 4th edition, 2016. ISBN 978-1-118-64206.

[67] T. Barrella et al. Ross Ice Shelf (Antarctica) in situ radio-frequency attenuation. *Journal of Glaciology*, 57(201):61–66, 2011. doi:10.3189/002214311795306691.

[68] I. Bartos and M. Kowalski. Multimessenger astronomy. In *Multimessenger Astronomy*, 2399-2891, pages 1–1 to 1–18. IOP Publishing, 2017. ISBN 978-0-7503-1369-8. doi:10.1088/978-0-7503-1369-8ch1. URL `https://dx.doi.org/10.1088/978-0-7503-1369-8ch1`.

[69] S. Barwick et al. South Polar in situ radio-frequency ice attenuation. *Journal of Glaciology*, 51(173):231–238, 2005. doi:10.3189/172756505781829467.

[70] S. Barwick et al. Time Domain Response of the ARIANNA Detector. *Astropart. Phys.*, 62:139–151, 2015. doi:10.1016/j.astropartphys.2014.09.002.

[71] S. W. Barwick et al. Design and Performance of the ARIANNA HRA-3 Neutrino Detector Systems. *IEEE Trans. Nucl. Sci.*, 62(5):2202–2215, 2015. doi:10.1109/TNS.2015.2468182.

[72] S. W. Barwick et al. Radio detection of air showers with the ARIANNA experiment on the Ross Ice Shelf. *Astropart. Phys.*, 90:50–68, 2017. doi:10.1016/j.astropartphys.2017.02.003.

[73] S. W. Barwick et al. Observation of classically 'forbidden' electromagnetic wave propagation and implications for neutrino detection. *JCAP*, 07:055, 2018. doi:10.1088/1475-7516/2018/07/055.

[74] J. F. Beacom et al. Decay of High-Energy Astrophysical Neutrinos. *Phys. Rev. Lett.*, 90:181301, 2003. doi:10.1103/PhysRevLett.90.181301.

[75] K. Bechtol et al. Evidence against star-forming galaxies as the dominant source of IceCube neutrinos. *Astrophys. J.*, 836(1):47, 2017. doi:10.3847/1538-4357/836/1/47.

[76] K. Belov et al. Accelerator Measurements of Magnetically Induced Radio Emission from Particle Cascades with Applications to Cosmic-Ray Air Showers. *Phys. Rev. Lett.*, 116:141103, Apr 2016. doi:10.1103/PhysRevLett.116.141103.

[77] D. Besson et al. In situ radioglaciological measurements near Taylor Dome, Antarctica and implications for ultra-high energy (UHE) neutrino astronomy. *Astroparticle Physics*, 29(2):130–157, 2008. ISSN 0927-6505. doi:https://doi.org/10.1016/j.astropartphys.2007.12.004.

[78] H. A. Bethe. Energy production in stars. *Phys. Rev.*, 55:434–456, Mar 1939. doi:10.1103/PhysRev.55.434.

[79] D. Biehl et al. Tidally disrupted stars as a possible origin of both cosmic rays and neutrinos at the highest energies. *Sci. Rep.*, 8(1):10828, 2018. doi:10.1038/s41598-018-29022-4.

[80] R. M. Bionta et al. Observation of a Neutrino Burst in Coincidence with Supernova SN 1987a in the Large Magellanic Cloud. *Phys. Rev. Lett.*, 58:1494, 1987. doi:10.1103/PhysRevLett.58.1494.

[81] V. V. Bogorodsky et al. *Radioglaciology*. Reidel Publishing Co., 1985. doi:10.1007/978-94-009-5275-1.

[82] D. Boncioli et al. On the common origin of cosmic rays across the ankle and diffuse neutrinos at the highest energies from low-luminosity Gamma-Ray Bursts. *Astrophys. J.*, 872(1):110, 2019. doi:10.3847/1538-4357/aafda7.

[83] J. Braun et al. Time-dependent point source search methods in high energy neutrino astronomy. *Astroparticle Physics*, 33(3):175–181, Apr 2010. ISSN 0927-6505. doi:10.1016/j.astropartphys.2010.01.005.

[84] S. Buson et al. A Unique Messenger to Probe Active Galactic Nuclei: High-Energy Neutrinos. *Bull. Am. Astron. Soc.*, 51:228, 2019.

[85] M. Bustamante et al. High-energy cosmic-ray acceleration. *2009 CERN-Latin-American School of High-Energy Physics, CLASHEP 2009 - Proceedings*, pages 533–539, 01 2010.

[86] A. Capanema et al. New constraints on the origin of medium-energy neutrinos observed by IceCube. *Phys. Rev. D*, 101(10):103012, 2020. doi:10.1103/PhysRevD.101.103012.

[87] B. Chauhan and S. Mohanty. Leptoquark solution for both the flavor and ANITA anomalies. *Phys. Rev. D*, 99(9):095018, 2019. doi:10.1103/PhysRevD.99.095018.

[88] P. A. Cherenkov et al. Visible Emission of Clean Liquids by Action of γ Radiation. *Dokl Akad Nauk SSSR*, 1934.

[89] J. F. Cherry and I. M. Shoemaker. Sterile neutrino origin for the upward directed cosmic ray showers detected by ANITA. *Phys. Rev. D*, 99(6):063016, 2019. doi:10.1103/PhysRevD.99.063016.

[90] I. Cholis et al. Dissecting the Gamma-Ray Background in Search of Dark Matter. *JCAP*, 02:014, 2014. doi:10.1088/1475-7516/2014/02/014.

[91] K. Christianson et al. Basal conditions at the grounding zone of whillans ice stream, west antarctica, from ice-penetrating radar. *Journal of Geophysical Research: Earth Surface*, 121(11):1954–1983, 2016. doi:https://doi.org/10.1002/2015JF003806. URL `https://agupubs.onlinelibrary.wiley.com/doi/abs/10.1002/2015JF003806`.

[92] B. T. Cleveland et al. Measurement of the solar electron neutrino flux with the Homestake chlorine detector. *Astrophys. J.*, 496:505–526, 1998. doi:10.1086/305343.

[93] J. M. Cline et al. Can the ANITA anomalous events be due to new physics? *Phys. Rev. D*, 100(1):015031, 2019. doi:10.1103/PhysRevD.100.015031.

[94] J. H. Collins et al. R-parity Violating Supersymmetric Explanation of the Anomalous Events at ANITA. *Phys. Rev. D*, 99(4):043009, 2019. doi:10.1103/PhysRevD.99.043009.

[95] W. Commons. Anita-4 prior to launch, 2016. URL `https://commons.wikimedia.org/wiki/File:ANITA-4_prior_to_launch.jpg`. File: ANITA-4 prior to launch.jpg.

[96] W. Commons. Sn1987a neutrino events, 2021. URL `https://commons.wikimedia.org/wiki/File:SN_1987A.png`. File: SN 1987A.png.

[97] A. Connolly et al. Calculation of High Energy Neutrino-Nucleon Cross Sections and Uncertainties Using the MSTW Parton Distribution Functions and Implications for Future Experiments. *Phys. Rev. D*, 83:113009, 2011. doi:10.1103/PhysRevD.83.113009.

[98] A. Connolly et al. On ANITA's sensitivity to long-lived, charged massive particles. Submitted to Astropart. Phys. J, 7 2018.

[99] Creative Design Corp. *Instruction Manual CLP5130-2 Create Radio Antenna*, 1994. URL `https://static.dxengineering.com/global/images/instructions/cae-clp-5130-2n.pdf`.

[100] L. Dai and K. Fang. Can tidal disruption events produce the IceCube neutrinos? *Mon. Not. Roy. Astron. Soc.*, 469(2):1354–1359, 2017. doi:10.1093/mnras/stx863.

[101] C. Deaconu et al. Measurements and Modeling of Near-Surface Radio Propagation in Glacial Ice and Implications for Neutrino Experiments. *Phys. Rev. D*, 98(4):043010, 2018. doi:10.1103/PhysRevD.98.043010.

[102] C. Deaconu et al. Measurements and Modeling of Near-Surface Radio Propagation in Glacial Ice and Implications for Neutrino Experiments. *Phys. Rev. D*, 98(4):043010, 2018. doi:10.1103/PhysRevD.98.043010.

[103] O. Deligny. The energy spectrum of ultra-high energy cosmic rays measured at the Pierre Auger Observatory and at the Telescope Array. *PoS*, ICRC2019:234, 2020. doi:10.22323/1.358.0234.

[104] P. B. Denton and I. Tamborra. Exploring the Properties of Choked Gamma-ray Bursts with IceCube's High-energy Neutrinos. *Astrophys. J.*, 855(1):37, 2018. doi:10.3847/1538-4357/aaab4a.

[105] P. B. Denton and I. Tamborra. The Bright and Choked Gamma-Ray Burst Contribution to the IceCube and ANTARES Low-Energy Excess. *JCAP*, 04:058, 2018. doi:10.1088/1475-7516/2018/04/058.

[106] P. B. Denton et al. The Galactic Contribution to IceCube's Astrophysical Neutrino Flux. *JCAP*, 08:033, 2017. doi:10.1088/1475-7516/2017/08/033.

[107] L. O. Drury. Origin of cosmic rays. *Astroparticle Physics*, 39-40:52–60, 2012. ISSN 0927-6505. doi:https://doi.org/10.1016/j.astropartphys.2012.02.006. Cosmic Rays Topical Issue.

[108] A. S. Eddington. *The Internal Constitution of the Stars*. Cambridge Science Classics. Cambridge University Press, 1988. doi:10.1017/CBO9780511600005.

[109] R. Engel et al. Neutrinos from propagation of ultrahigh energy protons. *Phys. Rev. D*, 64:093010, Oct 2001. doi:10.1103/PhysRevD.64.093010. URL `https://link.aps.org/doi/10.1103/PhysRevD.64.093010`.

[110] S. Fahey et al. A search for neutrinos from fast radio bursts with IceCube. *Astrophys. J.*, 845(1):14, 2017. doi:10.3847/1538-4357/aa7e28.

[111] K. Fang and B. D. Metzger. High-Energy Neutrinos from Millisecond Magnetars formed from the Merger of Binary Neutron Stars. *Astrophys. J.*, 849(2):153, 2017. doi:10.3847/1538-4357/aa8b6a.

[112] K. Fang and K. Murase. Linking High-Energy Cosmic Particles by Black Hole Jets Embedded in Large-Scale Structures. *Nature Phys.*, 14(4):396–398, 2018. doi:10.1038/s41567-017-0025-4.

[113] K. Fang and A. V. Olinto. High-energy neutrinos from sources in clusters of galaxies. *Astrophys. J.*, 828(1):37, 2016. doi:10.3847/0004-637X/828/1/37.

[114] K. Fang et al. Testing the Newborn Pulsar Origin of Ultrahigh Energy Cosmic Rays with EeV Neutrinos. *Phys. Rev. D*, 90(10):103005, 2014. doi:10.1103/PhysRevD.90.103005. [Erratum: Phys.Rev.D 92, 129901 (2015)].

[115] E. G. Farr and F. F. Lc. A Standard for Characterizing Antenna Performance in the Time Domain (With Corrections), 2011.

[116] G. R. Farrar and M. S. Sutherland. Deflections of UHECRs in the Galactic magnetic field. *JCAP*, 05:004, 2019. doi:10.1088/1475-7516/2019/05/004.

[117] N. Feigl. Development of a standard test and calibration procedure for the hardware of the Radio Neutrino Detector RNO-G. Masterarbeit, University of Erlangen, 2020. URL `https://bib-pubdb1.desy.de/record/456342`. Masterarbeit, University of Erlangen, 2020.

[118] S. Filhol and M. Sturm. Snow bedforms: A review, new data, and a formation model. *Journal of Geophysical Research: Earth Surface*, 120, 07 2015. doi:10.1002/2015JF003529.

[119] M. Fornasa and M. A. Sánchez-Conde. The nature of the Diffuse Gamma-Ray Background. *Phys. Rept.*, 598:1–58, 2015. doi:10.1016/j.physrep.2015.09.002.

[120] D. B. Fox et al. The ANITA Anomalous Events as Signatures of a Beyond Standard Model Particle, and Supporting Observations from IceCube. Submitted to Physical Review D, 9 2018.

[121] H. Friis. A note on a simple transmission formula. *Proceedings of the IRE*, 34(5): 254–256, 1946. doi:10.1109/JRPROC.1946.234568.

[122] S. Fujita et al. A summary of the complex dielectric permittivity of ice in the megahertz range and its applications for radar sounding of polar ice sheets. In *Physics of ice core records*, pages 185–212. Hokkaido University Press, 2000.

[123] S. Fujita et al. Radio-wave depolarization and scattering within ice sheets: a matrix-based model to link radar and ice-core measurements and its application. *Journal of Glaciology*, 52(178):407–424, 2006. doi:10.3189/172756506781828548.

[124] Y. Fukuda et al. Evidence for oscillation of atmospheric neutrinos. *Phys. Rev. Lett.*, 81:1562–1567, 1998. doi:10.1103/PhysRevLett.81.1562.

[125] Y. Fukuda et al. Measurements of the solar neutrino flux from Super-Kamiokande's first 300 days. *Phys. Rev. Lett.*, 81:1158–1162, 1998. doi:10.1103/PhysRevLett.81.1158. [Erratum: Phys.Rev.Lett. 81, 4279 (1998)].

[126] V. N. Gavrin. Measurement of the solar neutrino capture rate in SAGE and the value of the pp-neutrino flux at the earth. *Nucl. Phys. B Proc. Suppl.*, 138:87–90, 2005. doi:10.1016/j.nuclphysbps.2004.11.021.

[127] C. Glaser. Neutrino direction and energy resolution of Askaryan detectors. *PoS*, ICRC2019:899, 2020. doi:10.22323/1.358.0899.

[128] C. Glaser et al. NuRadioReco: a reconstruction framework for radio neutrino detectors. *The European Physical Journal C*, 79(6), Jun 2019. ISSN 1434-6052. doi:10.1140/epjc/s10052-019-6971-5.

[129] C. Glaser et al. NuRadioMC: Simulating the radio emission of neutrinos from interaction to detector. *Eur. Phys. J. C*, 80(2):77, 2020. doi:10.1140/epjc/s10052-020-7612-8.

[130] P. W. Gorham et al. Accelerator measurements of the Askaryan effect in rock salt: A Roadmap toward teraton underground neutrino detectors. *Phys. Rev. D*, 72:023002, 2005. doi:10.1103/PhysRevD.72.023002.

[131] P. W. Gorham et al. Observations of the Askaryan effect in ice. *Phys. Rev. Lett.*, 99: 171101, 2007. doi:10.1103/PhysRevLett.99.171101.

[132] P. W. Gorham et al. Observations of the Askaryan effect in ice. *Phys. Rev. Lett.*, 99: 171101, 2007. doi:10.1103/PhysRevLett.99.171101.

[133] P. W. Gorham et al. The Antarctic Impulsive Transient Antenna Ultra-high Energy Neutrino Detector Design, Performance, and Sensitivity for 2006-2007 Balloon Flight. *Astropart. Phys.*, 32:10–41, 2009. doi:10.1016/j.astropartphys.2009.05.003.

[134] P. W. Gorham et al. Observational constraints on the ultrahigh energy cosmic neutrino flux from the second flight of the anita experiment. *Phys. Rev. D*, 82:022004, Jul 2010. doi:10.1103/PhysRevD.82.022004.

[135] P. W. Gorham et al. Characteristics of Four Upward-pointing Cosmic-ray-like Events Observed with ANITA. *Phys. Rev. Lett.*, 117(7):071101, 2016. doi:10.1103/PhysRevLett.117.071101.

[136] P. W. Gorham et al. Observation of an Unusual Upward-going Cosmic-ray-like Event in the Third Flight of ANITA. *Phys. Rev. Lett.*, 121(16):161102, 2018. doi:10.1103/PhysRevLett.121.161102.

[137] P. W. Gorham et al. Constraints on the diffuse high-energy neutrino flux from the third flight of ANITA. *Phys. Rev. D*, 98(2):022001, 2018. doi:10.1103/PhysRevD.98.022001.

[138] P. W. Gorham et al. Constraints on the ultrahigh-energy cosmic neutrino flux from the fourth flight of ANITA. *Phys. Rev. D*, 99(12):122001, 2019. doi:10.1103/PhysRevD.99.122001.

[139] Greenland Ice Core Project. ftp://ftp.ncdc.noaa.gov/pub/data/paleo/icecore/greenland/summit/grip/physical/ griptemp.txt, 1994.

[140] K. Greisen. End to the Cosmic-Ray Spectrum? *Phys. Rev. Lett.*, 16:748–750, Apr 1966. doi:10.1103/PhysRevLett.16.748.

[141] K. Grönvold et al. Ash layers from iceland in the greenland grip ice core correlated with oceanic and land sediments. *Earth and Planetary Science Letters*, 135(1):149–155, 1995. ISSN 0012-821X. doi:https://dpi.org/10.1016/0012-821X(95)00145-3. URL `https://www.sciencedirect.com/science/article/pii/0012821X95001453`.

[142] D. Guetta et al. Neutrinos from individual gamma-ray bursts in the BATSE catalog. *Astropart. Phys.*, 20:429–455, 2004. doi:10.1016/S0927-6505(03)00211-1.

[143] F. Halzen and E. Zas. Neutrino fluxes from active galaxies: A Model independent estimate. *Astrophys. J.*, 488:669–674, 1997. doi:10.1086/304741.

[144] W. Hampel et al. GALLEX solar neutrino observations: Results for GALLEX IV. *Phys. Lett. B*, 447:127–133, 1999. doi:10.1016/S0370-2693(98)01579-2.

[145] W. Hanlon and R. Abbasi. Proton-Air Cross Section and Composition of Ultra High Energy Cosmic Rays Observed by Telescope Array. In *17th conference on Elastic and Diffractive Scattering*, 10 2017.

[146] J. C. Hanson et al. Radar absorption, basal reflection, thickness and polarization measurements from the Ross Ice Shelf, Antarctica. *Journal of Glaciology*, 61(227): 438–446, 2015. doi:10.3189/2015JoG14J214.

[147] N. D. Hargreaves. The radio-frequency birefringence of polar ice. *Journal of Glaciology*, 21(85):301–313, 1978. doi:10.3189/S0022143000033499.

[148] R. L. Hawley et al. Rapid techniques for determining annual accumulation applied at Summit, Greenland. *Journal of Glaciology*, 54(188):839–845, 2008. doi:10.3189/002214308787779951.

[149] M. M. Herron and C. C. Langway. Firn Densification: An Empirical Model. *Journal of Glaciology*, 25(93):373–385, 1980. doi:10.3189/S0022143000015239.

[150] V. F. Hess. Über Beobachtungen der durchdringenden Strahlung bei sieben Freiballonfahrten. *Phys. Z.*, 13:1084–1091, 1912.

[151] L. Heurtier et al. Dark matter interpretation of the ANITA anomalous events. *Phys. Rev. D*, 99(9):095014, 2019. doi:10.1103/PhysRevD.99.095014.

[152] A. M. Hillas. The Origin of Ultra-High-Energy Cosmic Rays. *Annual Review of Astronomy and Astrophysics*, 22(1):425–444, 1984. doi:10.1146/annurev.aa.22.090184.002233.

[153] K. Hirata et al. Observation of a Neutrino Burst from the Supernova SN 1987a. *Phys. Rev. Lett.*, 58:1490–1493, 1987. doi:10.1103/PhysRevLett.58.1490.

[154] K. S. Hirata et al. Results from one thousand days of real time directional solar neutrino data. *Phys. Rev. Lett.*, 65:1297–1300, 1990. doi:10.1103/PhysRevLett.65.1297.

[155] D. Hooper. Measuring high-energy neutrino nucleon cross-sections with future neutrino telescopes. *Phys. Rev. D*, 65:097303, 2002. doi:10.1103/PhysRevD.65.097303.

[156] D. Hooper. A Case for Radio Galaxies as the Sources of IceCube's Astrophysical Neutrino Flux. *JCAP*, 09:002, 2016. doi:10.1088/1475-7516/2016/09/002.

[157] D. Hooper et al. Radio Galaxies Dominate the High-Energy Diffuse Gamma-Ray Background. *JCAP*, 08:019, 2016. doi:10.1088/1475-7516/2016/08/019.

[158] D. Hooper et al. Active Galactic Nuclei and the Origin of IceCube's Diffuse Neutrino Flux. *JCAP*, 02:012, 2019. doi:10.1088/1475-7516/2019/02/012.

[159] D. Hooper et al. Superheavy dark matter and ANITA's anomalous events. *Phys. Rev. D*, 100(4):043019, 2019. doi:10.1103/PhysRevD.100.043019.

[160] S. Hoover et al. Observation of ultrahigh-energy cosmic rays with the anita balloon-borne radio interferometer. *Phys. Rev. Lett.*, 105:151101, Oct 2010. doi:10.1103/PhysRevLett.105.151101.

[161] G.-y. Huang. Sterile neutrinos as a possible explanation for the upward air shower events at ANITA. *Phys. Rev. D*, 98(4):043019, 2018. doi:10.1103/PhysRevD.98.043019.

[162] L. Hüdepohl et al. Neutrino Signal of Electron-Capture Supernovae from Core Collapse to Cooling. *Phys. Rev. Lett.*, 104:251101, Jun 2010. doi:10.1103/PhysRevLett.104.251101.

[163] Icecube Collaboration. An absence of neutrinos associated with cosmic-ray acceleration in γ-ray bursts. *Nature*, 484(7394):351–354, Apr. 2012. doi:10.1038/nature11068.

[164] P. A. Čerenkov. Visible Radiation Produced by Electrons Moving in a Medium with Velocities Exceeding that of Light. *Phys. Rev.*, 52:378–379, Aug 1937. doi:10.1103/PhysRev.52.378.

[165] D. Ivanov. Energy Spectrum Measured by the Telescope Array. *PoS*, ICRC2019:298, 2020. doi:10.22323/1.358.0298.

[166] T. M. Jordan et al. Modeling ice birefringence and oblique radio wave propagation for neutrino detection at the south pole. *Annals of Glaciology*, 61(81):84–91, 2020. doi:10.1017/aog.2020.18.

[167] I. Joughin et al. Greenland flow variability from ice-sheet-wide velocity mapping. *Journal of Glaciology*, 56(197):415–430, 2010. doi:10.3189/002214310792447734.

[168] K. Hughes for the ARA Collaboration. Implementing a Low-Threshold Analysis with the Askaryan Radio Array (ARA). *PoS*, ICRC2021:1153, 2021. doi:10.22323/1.395.1153.

[169] H. Kawai et al. Telescope array experiment. *Nucl. Phys. B Proc. Suppl.*, 175-176: 221–226, 2008. doi:10.1016/j.nuclphysbps.2007.11.002.

[170] K. Kawata et al. Updated Results on the UHECR Hotspot Observed by the Telescope Array Experiment. *PoS*, ICRC2019:310, 2020. doi:10.22323/1.358.0310.

[171] A. Kheirandish et al. Searches for neutrinos from fast radio bursts with IceCube. *PoS*, ICRC2019:982, 2020. doi:10.22323/1.358.0982.

[172] J. H. Koehne et al. PROPOSAL: A tool for propagation of charged leptons. *Comput. Phys. Commun.*, 184:2070–2090, 2013. doi:10.1016/j.cpc.2013.04.001.

[173] K. Kotera et al. Propagation of ultrahigh energy nuclei in clusters of galaxies: resulting composition and secondary emissions. *Astrophys. J.*, 707:370–386, 2009. doi:10.1088/0004-637X/707/1/370.

[174] A. Kovacs et al. The in-situ dielectric constant of polar firn revisited. *Cold Regions Science and Technology*, 23(3):245–256, 1995. ISSN 0165-232X. doi:https://doi.org/10.1016/0165-232X(94)00016-Q.

[175] I. Kravchenko et al. Performance and simulation of the RICE detector. *Astropart. Phys.*, 19:15–36, 2003. doi:10.1016/S0927-6505(02)00194-9.

[176] I. Kravchenko et al. Updated results from the rice experiment and future prospects for ultra-high energy neutrino detection at the south pole. *Physical Review D*, 85(6), Mar 2012. ISSN 1550-2368. doi:10.1103/physrevd.85.062004.

[177] M. Legrand et al. Field investigation of major and minor ions along summit (central greenland) ice cores by ion chromatography. *Journal of Chromatography A*, 640(1): 251–258, 1993. ISSN 0021-9673. doi:https://doi.org/10.1016/0021-9673(93)80188-E. URL `https://www.sciencedirect.com/science/article/pii/002196739380188E`. International Chromatography Symposium 1992.

[178] T. Linden. Star-Forming Galaxies Significantly Contribute to the Isotropic Gamma-Ray Background. *Phys. Rev. D*, 96(8):083001, 2017. doi:10.1103/PhysRevD.96.083001.

[179] R.-Y. Liu et al. Can winds driven by active galactic nuclei account for the extragalactic gamma-ray and neutrino backgrounds? *Astrophys. J.*, 858(1):9, 2018. doi:10.3847/1538-4357/aaba74.

[180] A. Loeb and E. Waxman. The Cumulative background of high energy neutrinos from starburst galaxies. *JCAP*, 05:003, 2006. doi:10.1088/1475-7516/2006/05/003.

[181] H. Loui. 1d-fdtd using matlab. *NUMERICAL METHODS IN PHOTONICS*, 2004.

[182] C. Lunardini and W. Winter. High Energy Neutrinos from the Tidal Disruption of Stars. *Phys. Rev. D*, 95(12):123001, 2017. doi:10.1103/PhysRevD.95.123001.

[183] C. Lunardini et al. Are starburst galaxies a common source of high energy neutrinos and cosmic rays? *JCAP*, 10:073, 2019. doi:10.1088/1475-7516/2019/10/073.

[184] J. A. MacGregor et al. Modeling englacial radar attenuation at siple dome, west antarctica, using ice chemistry and temperature data. *Journal of Geophysical Research: Earth Surface*, 112(F3), 2007. doi:https://doi.org/10.1029/2006JF000717. URL `https://agupubs.onlinelibrary.wiley.com/doi/abs/10.1029/2006JF000717`.

[185] J. A. MacGregor et al. Radar attenuation and temperature within the greenland ice sheet. *Journal of Geophysical Research: Earth Surface*, 120(6):983–1008, 2015. doi:https://doi.org/10.1002/2014JF003418. URL `https://agupubs.onlinelibrary.wiley.com/doi/abs/10.1002/2014JF003418`.

[186] K. Mannheim. High-energy neutrinos from extragalactic jets. *Astropart. Phys.*, 3: 295–302, 1995. doi:10.1016/0927-6505(94)00044-4.

[187] B. G. Marsden. SUPERNOVA 1987A IN THE LARGE MAGELLANIC CLOUD, 1987. URL `http://www.cbat.eps.harvard.edu/iauc/04300/04316.html`.

[188] K. Matsuoka et al. Crystal orientation fabrics within the antarctic ice sheet revealed by a multipolarization plane and dual-frequency radar survey. *Journal of Geophysical Research*, 108:2499, 2003. doi:https://doi.org/10.1029/2003JB002425.

[189] K. Matsuoka et al. Ice-flow-induced scattering zone within the antarctic ice sheet revealed by high-frequency airborne radar. *Journal of Glaciology*, 50(170):382–388, 2004. doi:10.3189/172756504781829891.

[190] R. Mbarek and D. Caprioli. Espresso and Stochastic Acceleration of Ultra-high-energy Cosmic Rays in Relativistic Jets. *Astrophys. J.*, 921(1):85, 2021. doi:10.3847/1538-4357/ac1da8.

[191] P. Meszaros. Astrophysical Sources of High Energy Neutrinos in the IceCube Era. *Ann. Rev. Nucl. Part. Sci.*, 67:45–67, 2017. doi:10.1146/annurev-nucl-101916-123304.

[192] P. Meszaros and E. Waxman. TeV neutrinos from successful and choked gamma-ray bursts. *Phys. Rev. Lett.*, 87:171102, 2001. doi:10.1103/PhysRevLett.87.171102.

[193] A. Muecke et al. BL Lac Objects in the synchrotron proton blazar model. *Astropart. Phys.*, 18:593–613, 2003. doi:10.1016/S0927-6505(02)00185-8.

[194] K. Murase. *Active Galactic Nuclei as High-Energy Neutrino Sources*, pages 15–31. World Scientific, 2017. doi:10.1142/9789814759410_0002.

[195] K. Murase and J. F. Beacom. Neutrino Background Flux from Sources of Ultrahigh-Energy Cosmic-Ray Nuclei. *Phys. Rev. D*, 81:123001, 2010. doi:10.1103/PhysRevD.81.123001.

[196] K. Murase and K. Ioka. TeV–PeV Neutrinos from Low-Power Gamma-Ray Burst Jets inside Stars. *Phys. Rev. Lett.*, 111(12):121102, 2013. doi:10.1103/PhysRevLett.111.121102.

[197] K. Murase et al. Gamma-Ray and Neutrino Backgrounds as Probes of the High-Energy Universe: Hints of Cascades, General Constraints, and Implications for TeV Searches. *JCAP*, 08:030, 2012. doi:10.1088/1475-7516/2012/08/030.

[198] K. Murase et al. Testing the Hadronuclear Origin of PeV Neutrinos Observed with IceCube. *Phys. Rev. D*, 88(12):121301, 2013. doi:10.1103/PhysRevD.88.121301.

[199] K. Murase et al. Diffuse Neutrino Intensity from the Inner Jets of Active Galactic Nuclei: Impacts of External Photon Fields and the Blazar Sequence. *Phys. Rev. D*, 90 (2):023007, 2014. doi:10.1103/PhysRevD.90.023007.

[200] K. Murase et al. Hidden Cosmic-Ray Accelerators as an Origin of TeV-PeV Cosmic Neutrinos. *Phys. Rev. Lett.*, 116(7):071101, 2016. doi:10.1103/PhysRevLett.116.071101.

[201] K. Murase et al. Blazar Flares as an Origin of High-energy Cosmic Neutrinos? *Astrophys. J.*, 865(2):124, 2018. ISSN 1538-4357. doi:10.3847/1538-4357/aada00.

[202] K. Murase et al. High-Energy Neutrino and Gamma-Ray Emission from Tidal Disruption Events. *Astrophys. J.*, 902(2):108, 2020. doi:10.3847/1538-4357/abb3c0.

[203] H. Nagakura et al. Core-collapse supernova neutrino emission and detection informed by state-of-the-art three-dimensional numerical models. *Mon. Not. Roy. Astron. Soc.*, 500(1):696–717, 2020. doi:10.1093/mnras/staa2691.

[204] K. Nakazato et al. Supernova Neutrino Light Curves and Spectra for Various Progenitor Stars: From Core Collapse to Proto-neutron Star Cooling. *Astrophys. J. Suppl.*, 205:2, 2013. doi:10.1088/0067-0049/205/1/2.

[205] A. F. Oskooi et al. Meep: A flexible free-software package for electromagnetic simulations by the FDTD method. *Computer Physics Communications*, 181(3):687–702, 2010. ISSN 0010-4655. doi:https://doi.org/10.1016/j.cpc.2009.11.008.

[206] E. O'Connor and C. D. Ott. The progenitor dependence of the pre-explosion neutrino emission in core-collapse supernovae. *The Astrophysical Journal*, 762(2):126, Dec 2012. ISSN 1538-4357. doi:10.1088/0004-637x/762/2/126.

[207] J. Paden. *Synthetic aperture radar for imaging the basal conditions of the polar ice sheets*. PhD thesis, Department of Electrical Engineering and Computer Science, University of Kansas, Lawrence, Kansas, 2006. URL `http://proxy.uchicago.edu/login?url=https://www.proquest.com/dissertations-theses/synthetic-aperture-radar-imaging-basal-conditions/docview/305320854/se-2?accountid=14657`.

[208] J. Paden et al. Wideband measurements of ice sheet attenuation and basal scattering. *IEEE Geoscience and Remote Sensing Letters*, 2(2):164–168, 2005. doi:10.1109/LGRS.2004.842474.

[209] A. Palladino et al. IceCube Neutrinos from Hadronically Powered Gamma-Ray Galaxies. *JCAP*, 09:004, 2019. doi:10.1088/1475-7516/2019/09/004.

[210] E. Peretti et al. Contribution of starburst nuclei to the diffuse gamma-ray and neutrino flux. *Mon. Not. Roy. Astron. Soc.*, 493(4):5880–5891, 2020. doi:10.1093/mnras/staa698.

[211] T. Piran. Gamma-ray bursts and the fireball model. *Phys. Rept.*, 314:575–667, 1999. doi:10.1016/S0370-1573(98)00127-6.

[212] O. Pisanti. Astrophysical neutrinos: theory. *J. Phys. Conf. Ser.*, 1263(1):012004, 2019. doi:10.1088/1742-6596/1263/1/012004.

[213] I. Plaisier et al. Direction Reconstruction for the Radio Neutrino Observatory Greenland (RNO-G). *PoS*, ICRC2021:1026, 2021. doi:10.22323/1.395.1026.

[214] M. Plum. Measurements of the Mass Composition of UHECRs with the Pierre Auger Observatory. *JPS Conf. Proc.*, 19:011011, 2018. doi:10.7566/JPSCP.19.011011.

[215] B. Pontecorvo. Mesonium and anti-mesonium. *Sov. Phys. JETP*, 6:429, 1957.

[216] S. Prohira et al. HiCal 2: An instrument designed for calibration of the ANITA experiment and for Antarctic surface reflectivity measurements. *Nucl. Instrum. Meth. A*, 918:60–66, 2019. doi:10.1016/j.nima.2018.11.092.

[217] J. M. Roberts et al. LAB4D: A Low Power, Multi-GSa/s, Transient Digitizer with Sampling Timebase Trimming Capabilities. *Nucl. Instrum. Meth. A*, 925:92–100, 2019. doi:10.1016/j.nima.2019.01.091.

[218] C. Rojas-Bravo and M. Araya. Search for gamma-ray emission from star-forming galaxies with Fermi LAT. *Mon. Not. Roy. Astron. Soc.*, 463(1):1068–1073, 2016. doi:10.1093/mnras/stw2059.

[219] A. Romero-Wolf et al. Comprehensive analysis of anomalous ANITA events disfavors a diffuse tau-neutrino flux origin. *Phys. Rev. D*, 99(6):063011, 2019. doi:10.1103/PhysRevD.99.063011.

[220] B. Rotter. *Cosmic Ray and Neutrino Astrophysics with the ANITA III Telescope*. PhD thesis, University of Hawai'i at Manoa, Honolulu, Hawaii, 2017.

[221] B. J. Rotter. *Cosmic Ray and Neutrino Astrophysics with the ANITAIII Telescope*. PhD thesis, University of Hawai'i at Manoa, Jan. 2017.

[222] D. Saltzberg et al. Observation of the Askaryan effect: Coherent microwave Cherenkov emission from charge asymmetry in high-energy particle cascades. *Phys. Rev. Lett.*, 86:2802–2805, 2001. doi:10.1103/PhysRevLett.86.2802.

[223] K. Sato and H. Suzuki. Analysis of neutrino burst from the supernova 1987A in the Large Magellanic Cloud. *Phys. Rev. Lett.*, 58:2722–2725, Jun 1987. doi:10.1103/PhysRevLett.58.2722.

[224] T. Scambos et al. Extent of low-accumulation 'wind glaze' areas on the east antarctic plateau: implications for continental ice mass balance. *Journal of Glaciology*, 58(210): 633–647, 2012. doi:10.3189/2012JoG11J232.

[225] A. Schneider. Characterization of the Astrophysical Diffuse Neutrino Flux with IceCube High-Energy Starting Events. *PoS*, ICRC2019:1004, 2020. doi:10.22323/1.358.1004.

[226] J. B. Schneider. Understanding the finite-difference time-domain method, 2010. URL `www.eecs.wsu.edu/~schneidj/ufdtd`.

[227] K. Scholberg. Supernova neutrino detection. *Annual Review of Nuclear and Particle Science*, 62(1):81–103, 2012. doi:10.1146/annurev-nucl-102711-095006.

[228] F. G. Schröder. News from Cosmic Ray Air Showers (Cosmic Ray Indirect - CRI Rapporteur). *PoS*, ICRC2019:030, 2020. doi:10.22323/1.358.0030.

[229] N. Senno et al. Choked Jets and Low-Luminosity Gamma-Ray Bursts as Hidden Neutrino Sources. *Phys. Rev. D*, 93(8):083003, 2016. doi:10.1103/PhysRevD.93.083003.

[230] N. Senno et al. High-energy Neutrino Flares from X-Ray Bright and Dark Tidal Disruption Events. *Astrophys. J.*, 838(1):3, 2017. doi:10.3847/1538-4357/aa6344.

[231] I. M. Shoemaker and K. Murase. Probing BSM Neutrino Physics with Flavor and Spectral Distortions: Prospects for Future High-Energy Neutrino Telescopes. *Phys. Rev. D*, 93(8):085004, 2016. doi:10.1103/PhysRevD.93.085004.

[232] I. M. Shoemaker, A. Kusenko, P. Kuipers Munneke, A. Romero-Wolf, D. M. Schroeder, and M. J. Siegert. Reflections on the anomalous anita events: the antarctic subsurface as a possible explanation. *Annals of Glaciology*, 61(81):92–98, 2020. doi:10.1017/aog.2020.19.

[233] D. Smith, D. Hooper, and A. Vieregg. Revisiting AGN as the source of IceCube's diffuse neutrino flux. *JCAP*, 03:031, 2021. doi:10.1088/1475-7516/2021/03/031.

[234] D. Smith et al. Experimental tests of sub-surface reflectors as an explanation for the ANITA anomalous events. *JCAP*, 04:016, 2021. doi:10.1088/1475-7516/2021/04/016.

[235] M. S. Sodha et al. Focusing factor in a stratified medium. *BRIT. J. APPL. PHYS.*, 2(2), 1969.

[236] F. Stecker et al. High-energy neutrinos from active galactic nuclei. *Phys. Rev. Lett.*, 66:2697–2700, 1991. doi:10.1103/PhysRevLett.66.2697. [Erratum: Phys.Rev.Lett. 69, 2738 (1992)].

[237] R. Stein et al. A tidal disruption event coincident with a high-energy neutrino. *Nature Astron.*, 5(5):510–518, 2021. doi:10.1038/s41550-020-01295-8.

[238] M. Stockham. *Bulk and Surface Radio-Frequency Response of Ice*. PhD thesis, University of Kansas, Lawrence, Kansas, 2018.

[239] M. Stockham et al. Radio Frequency Ice Dielectric Permittivity Measurements Using CReSIS Data. *Radio Science*, 51:194–212, 2016.

[240] Y. Suwa et al. Observing Supernova Neutrino Light Curves with Super-Kamiokande: Expected Event Number over 10 s. *Astrophys. J.*, 881:139, 2019. doi:10.3847/1538-4357/ab2e05.

[241] I. Tamborra and S. Ando. Diffuse emission of high-energy neutrinos from gamma-ray burst fireballs. *JCAP*, 09:036, 2015. doi:10.1088/1475-7516/2015/9/036.

[242] I. Tamm. *Radiation Emitted by Uniformly Moving Electrons*, pages 37–53. Springer Berlin Heidelberg, Berlin, Heidelberg, 1991. ISBN 978-3-642-74626-0. doi:10.1007/978-3-642-74626-0_3. URL `https://doi.org/10.1007/978-3-642-74626-0_3`.

[243] M. T. Thompson. Chapter 16 - noise. In M. T. Thompson, editor, *Intuitive Analog Circuit Design (Second Edition)*, pages 617–643. Newnes, Boston, second edition edition, 2014. ISBN 978-0-12-405866-8. doi:https://doi.org/10.1016/B978-0-12-405866-8.00016-4.

[244] T. Thorsteinsson. Textures and fabrics in the grip ice core, in relation to climate history and ice deformation. *Berichte zur Polarforschung (Reports on Polar Research)*, 205, 1996.

[245] H. Tokuno et al. New air fluorescence detectors employed in the telescope array experiment. *Nuclear Instruments and Methods in Physics Research Section A: Accelerators, Spectrometers, Detectors and Associated Equipment*, 676:54–65, 2012. ISSN 0168-9002. doi:https://doi.org/10.1016/j.nima.2012.02.044. URL `https://www.sciencedirect.com/science/article/pii/S0168900212002422`.

[246] A. van Vliet et al. Determining the fraction of cosmic-ray protons at ultra-high energies with cosmogenic neutrinos. *Phys. Rev. D*, 100(2):021302, 2019. doi:10.1103/PhysRevD.100.021302.

[247] G. S. Varner et al. The large analog bandwidth recorder and digitizer with ordered readout (LABRADOR) ASIC. *Nucl. Instrum. Meth. A*, 583:447–460, 2007. doi:10.1016/j.nima.2007.09.013.

[248] A. G. Vieregg et al. A Technique for Detection of PeV Neutrinos Using a Phased Radio Array. *JCAP*, 02:005, 2016. doi:10.1088/1475-7516/2016/02/005.

[249] M. Vietri. Ultrahigh-energy neutrinos from gamma-ray bursts. *Phys. Rev. Lett.*, 80: 3690–3693, 1998. doi:10.1103/PhysRevLett.80.3690.

[250] F. L. Villante and A. Serenelli. The relevance of nuclear reactions for Standard Solar Models construction. *Front. Astron. Space Sci.*, 7:112, 2021. doi:10.3389/fspas.2020.618356.

[251] P. Vyskocil and J. Sebesta. Relative timing characteristics of gps timing modules for time synchronization application. In *2009 International Workshop on Satellite and Space Communications*, pages 230–234, 2009. doi:10.1109/IWSSC.2009.5286378.

[252] C. W. Walter. *The Super-Kamiokande Experiment*, pages 19–43. World Scientific, 2 2008. doi:10.1142/9789812771971_0002.

[253] X.-Y. Wang and R.-Y. Liu. Tidal disruption jets of supermassive black holes as hidden sources of cosmic rays: explaining the IceCube TeV-PeV neutrinos. *Phys. Rev. D*, 93 (8):083005, 2016. doi:10.1103/PhysRevD.93.083005.

[254] A. A. Watson. The discovery of Cherenkov radiation and its use in the detection of extensive air showers. *Nuclear Physics B - Proceedings Supplements*, 212-213:13–19, Mar 2011. ISSN 0920-5632. doi:10.1016/j.nuclphysbps.2011.03.003.

[255] E. Waxman and J. N. Bahcall. High-energy neutrinos from cosmological gamma-ray burst fireballs. *Phys. Rev. Lett.*, 78:2292–2295, 1997. doi:10.1103/PhysRevLett.78.2292.

[256] S. Wissel et al. Prospects for high-elevation radio detection of >100 PeV tau neutrinos. *JCAP*, 11:065, 2020. doi:10.1088/1475-7516/2020/11/065.

[257] E. W. Wolff et al. Long-term changes in the acid and salt concentrations of the greenland ice core project ice core from electrical stratigraphy. *Journal of Geophysical Research: Atmospheres*, 100(D8):16249–16263, 1995. doi:https://doi.org/10.1029/95JD01174. URL https://agupubs.onlinelibrary.wiley.com/doi/abs/10.1029/95JD01174.

[258] E. W. Wolff et al. Factors controlling the electrical conductivity of ice from the polar regionsa summary. *The Journal of Physical Chemistry B*, 101(32):6090–6094, 1997. doi:10.1021/jp9631543. URL https://doi.org/10.1021/jp9631543.

[259] L. Yacobi et al. Implication of the Non-detection of gzk Neutrinos. *Astrophys. J.*, 823 (2):89, 2016. doi:10.3847/0004-637X/823/2/89.

[260] K. Yee. Numerical solution of initial boundary value problems involving Maxwell's equations in isotropic media. *IEEE Transactions on Antennas and Propagation*, 14(3): 302–307, 1966. doi:10.1109/TAP.1966.1138693.

[261] C. Yuan et al. Complementarity of Stacking and Multiplet Constraints on the Blazar Contribution to the Cumulative High-Energy Neutrino Intensity. *Astrophys. J.*, 890: 25, 2020. doi:10.3847/1538-4357/ab65ea.

[262] G. T. Zatsepin and V. A. Kuzmin. Upper limit of the spectrum of cosmic rays. *JETP Lett.*, 4:78–80, 1966.

[263] V. Červený et al. Computation of Geometric Spreading of Seismic Body Waves in Laterally Inhomogeneous Media with Curved Interfaces. *Geophysical Journal International*, 38(1):9–19, 07 1974. ISSN 0956-540X. doi:10.1111/j.1365-246X.1974.tb04105.x. URL https://doi.org/10.1111/j.1365-246X.1974.tb04105.x.